MAX-PLANCK-INSTITUT FÜR EXTRATERRESTRISCHE PHYSIK

The ROSAT Users' Handbook

A guide to the Astronomical X-Ray Satellite ROSAT

Intended to provide ROSAT users with an overview
of all technical aspects of ROSAT

With special emphasis on the calibration of the various instruments

edited by:

UG Briel, B Aschenbach, G Hasinger, H Hippmann, E Pfeffermann
P Predehl, JHMM Schmitt, W Voges, U Zimmermann

Max-Planck-Institut für extraterrestrische Physik
85740 Garching, FRG

IM George, SL Snowden, TJ Turner

NASA/Goddard Space Flight Center
Greenbelt, MD 20771, USA

L David, FR Harnden Jr, KE Kearns, MV Zombeck

Harvard/Smithsonian Center for Astrophysics
Cambridge, MA 02138, USA

MA Barstow, JP Osborne, JP Pye, M Watson, RG West, R Willingale

Department of Physics & Astronomy
University of Leicester, Leicester, UK

WORKING DRAFT

85740 GARCHING BEI MÜNCHEN, FRG

Log of Changes

Release Date	**Sections Changed**	**Brief Notes**
1992 Nov 17	First Draft	OGIP Internal Distribution
Dec 02	Chpt 3 & Appendices E, F	Special issue for HUG
Dec 06	Chpts 3 & 4	Reviewed discussion of Matrices
1993 Oct 05	Updates throughout	Major restructuring
1994 Feb 22	Updates throughout	Major restructuring at MPE
May 15	Updates throughout	Comments from GSFC
Jun 30	Chpts 5 & 6	inclusion of HRI and WFC chapters
Aug 02	Updates throughout	Comments from GSFC
1996 Feb 15	Chpt 5	Major revision of HRI report

Contents

List of Figures

List of Tables

ROSAT Acronyms & Abbreviations

ADC	Analog-to-Digital Converter
AIT	Astronomisches Institut der Universität Tübingen
AMCE	Attitude Measurement & Control Electronics
AMCS	Attitude Measurement & Control System
AO	Announcement of Opportunity
ASTERIX	UK X-ray data analysis package running within the Starlink ADAM/ICL environment
BMFT	Bundesministerium für Forschung und Technologie
CEM	Channel Electron Multiplier
CSS	Coarse Sun Sensor
CDHS	Command & Data Handling System
EXSAS	Extended Scientific Analysis System
FITS	Flexible Image Transport System
fov	Field-of-view
GOF	Guest Observer Facility
GSFC	Goddard Space Flight Center
GSOC	German Space Operations Center (Weilheim, Germany)
HEW	Half Energy Width
HRI	High Resolution Imager
HV	High Voltage
IUC	International User's Committee
LHEA	Laboratory for High Energy Astrophysics (at NASA/GSFC)
MCP	Microchannel Plate
MDR	Master Data Record (raw data from GSOC)
MJD	Modified Julian Day
MPE	Max-Planck-Institut (für Extraterrestrische Physik)
NASA	National Aeronautics and Space Administration
OBC	On-Board Computer
OGIP	Office of Guest Investigator Programs (at NASA/GSFC)
PI	Principle Investigator, or Pulse Invariant
PROS	Post Reduction Off-line Software
psf	Point-Spread Function
PSPC	Position Sensitive Proportional Counter
PVC	Performance Verification & Calibration (phase)

ROSAT **Acronyms & Abbreviations** (*continued*)

RAL	Rutherford Appleton Laboratory
RDA	*ROSAT* Data Archive
RDF	Rationalized Data File
ROR	*ROSAT* Observation Request
SAA	South Atlantic Anomaly
SAAD1 & SAAD2	South Atlantic Anomaly Detectors 1 & 2
SAO	Smithsonian Astrophysical Observatory
SASS	Standard Analysis Processing System
S/C	Space Craft
SERC	Science and Engineering Research Council (UK)
STC1 & STC2	XRT Star Trackers 1 & 2
S/W	Software
UKRDAC	UK *ROSAT* Data Archive Center
UT	Universal Time
UTC	Universal Time Clock
WFC	Wide-Field Camera
V&V	Verification & Validation (of SASS products)
WFC	Wide Field Camera
XMA	XRT Mirror Assembly
XRT	X-ray Telescope
XUV	Extreme Ultraviolet
ZDE	Zentrale Daten Einheit

Chapter 1

INTRODUCTION

1.1 ROSAT Mission Overview

(*Source:* Primarily Aschenbach *et al.* 1985; NRA 91-OSSA-3)

ROSAT, an acronym for the German word *Röntgensatellit*, resulted from a proposal made by the Max-Planck-Institut für extraterrestrische Physik (MPE) to the Bundesministerium für Forschung und Technologie (BMFT) in 1975. The original version of the project entailed an all-sky X-ray survey to be carried out with a moderate angular resolution ($\lesssim 1'$) imaging telescope. Between 1977 and 1982, extensive studies of the project were carried out by German space companies in Prephase-A and Phase-A studies. Following the regulations of the ESA convention, BMFT offered collaboration on *ROSAT* to the ESA member states in 1979. The University of Leicester proposed a Wide Field XUV Camera (WFC) to be flown alongside the main X-ray telescope (XRT) in order to extend the spectral bandpass to lower energies. The XRT covers the $\sim 6 - 100$Å ($\sim 2.4 - 0.12$ keV) band, and the WFC covers the $\sim 60 - 300$Å ($\sim 0.21 - 0.05$ keV) band. In 1982, an agreement between BMFT and NASA concerning US participation in the *ROSAT* project was reached: in return for 50% of the pointed observing time being made available to US Principle Investigators (PIs), NASA agreed to provide a high resolution imager (HRI) for the focal plane of the XRT as well as to launch the satellite on board the Space Shuttle. Agreement was reached between BMFT and SERC in 1983: in return for 12% of the pointed observing time being made available to UK PIs, SERC would supply the WFC and associated sub-systems. The Challenger accident on 1986 January 28 brought significant changes to the spacecraft design and a delay in the launch. In 1987 December, the decision was made to launch *ROSAT* with an expendable Delta-II launch vehicle, rather than the Space Shuttle. *ROSAT* was finally launched into low Earth orbit (Table 1.1) from Cape Canaveral on 1990 June 1.

Spacecraft operations are controlled from the German Space Operations Center (GSOC) ground station in Oberpfaffenhofen, Germany. Contact occurs for ~ 8 minutes on five or six contiguous orbits out of 15 orbits per day. Thus there are groups of contacts over an ~ 8 hour period followed by a ~ 16 hour period of no contact.

Table 1.1: Orbital Characteristics of *ROSAT*

Launch	1990 June 1
Nominal Lifetime	18 months
Initial Altitude	580 km
Inclination	53°
Period	96 minutes
Precession	66 days

The main aim of the *ROSAT* mission was the first all-sky survey (1990 August to 1991 January) with imaging X-ray and XUV telescopes, possessing an X-ray sensitivity of about a factor of 1000 higher than that of *UHURU* (Voges 1992; Snowden & Schmitt 1990). During that mission phase, the satellite scanned the sky continuously along great circles roughly perpendicular to the earth–sun direction. Thus sky strips of 2 and 5 degrees width (for the XRT/PSPC and the WFC instruments, respectively) and 360 degrees length were observed during each orbit. Due to the applied scan law, these sky strips lay perpendicular to the ecliptic plane and their intersection with the ecliptic plane precessed with a rate of about 1 degree per day (roughly following the solar motion). In this way the ecliptic poles received up to 50 ksec exposure while sky fields near to the ecliptic plane were seen for some hundreds of seconds during the half year survey period. About 60000 sources have been detected in the survey, an order of magnitude greater than were known before the *ROSAT* mission. No further all-sky survey is planned in the foreseeable future, thus the *ROSAT* results will strongly influence the observations of the next generation of large X-ray missions like *XMM*, *AXAF*, and *ASTRO-E*, which will fly near the end of this decade.

The survey was followed by Pointed Observation Phases, where the 3–axis stabilized observatory investigated selected targets over the entire sky. Usually the observation times during these mission phases are appreciably longer than during the survey. In very deep exposures this resulted in point source sensitivities up to a factor 10 higher than achieved by *EINSTEIN* with appreciably better spatial and spectral solution.

On the whole, *ROSAT* has had few significant operational difficulties. By far the most severe problem occurred in early 1991 when there was an almost fatal on-board computer glitch which sent the spacecraft (S/C) tumbling out of control, destroying one of the PSPCs and severely damaging the WFC (see Section 1.2.2). A number of subsystems have also failed: the STC-2 startracker (Section 1.2.5) and the Y- and Z-gyros (Section 1.2.3). For a full mission history see Appendix A.

Further information on the *ROSAT* mission, its history, and payload, can be obtained from Trümper (1983) and in The *ROSAT Mission Description* (NRA 91-OSSA-3).

1.2 Payload Description

(*Source:* Primarily NRA 91-OSSA-3)

1.2.1 Overview

ROSAT is a three-axis stabilized satellite with a total mass of 2.429 tonnes. The telescope assembly is ∼4 m in length. The scientific payload consists of:

- **The X-ray Telescope (XRT)** with its 2.40 m focal-length mirror assembly consisting of 4 nested Wolter-I mirrors. The focal plane instrumentation consists of a carousel on which there are 2 Position Sensitive Proportional Counters (PSPCs), each with a filter wheel carrying a boron filter, and a High Resolution Imager (HRI) (for details see Sections 2 and 3).
- **The Wide Field Camera (WFC)** with its 0.525 m focal-length mirror assembly consisting of 3 nested Wolter-Schwarzschild mirrors (co-aligned with the XRT). The focal plane instrumentation consists of a curved microchannel plate (MCP) a carousel containing 8 filters, of which 6 are science filters (for details see Section 6).

The rest of the payload includes:

- The on-board computer (OBC) and the Command & Data Handling System (CDHS)
- The attitude measuring and control system (AMCS) including:
  - 2 startrackers (STC-1 & STC-2) used for optical position sensing and attitude determination (Section 1.2.5). An additional startracker (WFC STC) provides the WFC with independent attitude determination, however this sensor is not (at present) used for spacecraft control.
  - 4 gyros and 3 reaction wheels used for attitude control (Section 1.2.3)
  - a Sun Sensor (Section 1.2.7)
  - a Magnetometer (Section 1.2.8)
- 2 South Atlantic Anomaly Detectors (SAAD1 & SAAD2) used to safeguard the health of the focal plane instruments during passage through the South Atlantic Anomaly and particle belts (Section 1.2.6)

Power is supplied through 3 solar panels providing 1 kW of power during Sun-lit parts of the orbit, and through a rechargeable battery during the shadow phase (S/C night, up to 40 minutes per orbit).

A schematic view of the *ROSAT* spacecraft is shown in Figure 1.1.

1.2.2 Command & Data Handling System (CDHS)

The *ROSAT* Command & Data Handling System (CDHS) collects on-board data, sends them to ground, receives commands from ground, and decodes the command addresses and distributes then to the appropriate subsystems. The system consists of a redundant Intel 10-bit processor system with 40 Mbyte ROM and 74 Kbyte RAM, two tape recorders which are able to store 700 Mbits of data from *ROSAT* , a redundant transponder system, and an S-band bi-directional antenna system. Since there are only five or six contacts per day of roughly eight-minute duration, the data are initially stored on tape and then dumped to ground with a data rate of 1 Mbit s^{-1}. In addition to this link, housekeeping data are transmitted to ground during contacts via a 8 kbit secondary S-band link. Commands, generated on ground, are sent to the space craft via an S-band command link at a capacity of 1 kbit s^{-1} or 10 commands per second. Command verification further slows this link. The software of all subsystems on board can be updated via the command link in order to react to changing requirements. This feature was used extensively for the reconfiguration of the attitude control system after loss of several hardware components.

1.2.3 The AMCS

(*Source:* Primarily NRA 91-OSSA-3)

The *ROSAT* Attitude Measurement and Control System (AMCS) achieves 3-axes stabilized pointing using up to 3 gyros (out of 4 gyros, denoted as X-, Y- & Z-gyros, plus the cross-coupled S-gyro) and 3 reaction wheels (RW-1, RW-2 & RW-3) in connection with the sun sensor and the magnetometer. The high torque of the momentum wheels allows fast slews (180° in ~15 minutes) such that *ROSAT* can observe 2 targets on opposite hemispheres each orbit. (It is uneconomical to observe more than 2 targets per orbit due to slewing overheads.) The AMCS pointing is accurate to $\sim 1'$, the pointing stability is $\sim 5''$ with a $\sim 10''$ jitter radius. The XRT boresight calibration is discussed in Section 2.2.

PSPC pointed observations are usually carried out in a special "wobble mode" (see Section 1.3.3) whereby the telescope's pointing direction is slowly moved back and forth by $\simeq \pm 3'$ with a period of 400 s. The direction is diagonal to the coarse wire mesh of the PSPC window support structure and is designed to prevent unwanted shadowing of X-ray sources behind this mesh. The on-axis point-response function of the XRT is comparable to the wire diameter of the coarse mesh. HRI observations were also wobbled in order to smooth out quantum-efficiency variations in the microchannel-plate detector.

1.2.4 In-Orbit Performance

(*Sources:* NRA 91-OSSA-3; Hasinger 1992)

The in-orbit performance of *ROSAT* is closely related to the performance of its AMCS, hence the Mission Timeline (see Snowden & Schmitt 1992) is very much influenced by any problems in the attitude control system. Although all of what follows can be found in chronological order in the Appendix A (*ROSAT* Mission History), the relevant events, concerning the in-orbit performance, are described in this section in more detail.

Intermittent attitude problems were experienced both during the All-Sky Survey and (particularly) AO-1 mission phases due to an excessive drift rate of the X-gyro. The X-gyro was therefore taken out of the attitude control loop during the sky-survey, but included again during AO-1 with a compensatory bias introduced into the control software.

On 1991 May 12, the motor current to the Y-gyro glitched to exceed its operational limit. While the gyro was regained for a short time, controlling it became impossible, and the gyro was considered to have failed beyond retrieval. At this point, *ROSAT* had lost a non-redundant component of the AMCS and normal operations became impossible. The satellite remained in "safe-mode" until 1991 May 18, when attitude control was successfully regained in "Reduced-Pointing" mode utilizing the (unreliable) X-gyro. The problem appeared to be electrical in nature and probably unrelated to the drift problems experienced with the X-gyro. However, given the problems with the X-gyro, GSOC planners had to tightly constrain slews and acquisition of targets, allowing them to achieve equilibrium for the gyro drift. Slews were reduced to one direction and constrained to be short, guide stars needed to be available when the satellite was over Weilheim Ground Station (*i.e.,* target declinations were constrained to be $> +20$ degrees), a reduced sun cone angle was enforced (90 ± 5 degrees) and only one target was observed per day. Also during this period, an increased level of solar activity led to high levels of radiation, causing the detector to safe itself several times. These conditions resulted in a yield of $\sim$ 30,000 seconds of *ROSAT* data for each day of observation. After a long slew on 1991 July 5, *ROSAT* became lost due to Earth occultation and a lack of guide stars, resulting in the S/C going into safe-mode until recovery on July 7. The uploading of new AMCS S/W on July 8−9 enabled a slight relaxation in the reduced pointing phase observing constraints, allowing southern hemisphere observations and a large sun cone of 90 ± 12 degrees. Further modifications to the AMCS on-board software enabled a successful resumption of normal pointing operations on 1991 November 4.

The software commanding the startrackers was improved in 1991 October allowing the tracking of six stars in search windows of $2^\circ - 3^\circ$, as compared to the previous limit of 3 stars in a 1° window. Magnetometer information has also been utilized since that time. The combination of Magnetometer and Sun Sensor data allows a 3-axis determination on the day-side of the orbit. The gyros are still needed for slews and velocity damping in the control loop.

A large transient in the *ROSAT* Z-gyro current occurred late on 1992 February 6, reminiscent of that which immediately preceded the loss of the Y-gyro in 1991 May 12. The S/C was put into safe mode and observations suspended. The Z-gyro, although operating continuously with too high a current, was still giving meaningful readings of angular velocities. However, its output signal seemed to be scaled wrongly, indicating a factor of 3-4 slower speeds than the spacecraft was actually performing. Further evaluation indicated the outputs of the gyro were still valid, however the scale factor had increased by a factor of ∼2.8. The most convincing explanation of this is that 1 of 3 phases of the gyro motor failed, and consequently the motor current had increased. To compensate for the decreased Z-gyro output, a change of the on board software was developed (including a factor 2.8 decrease in the scale factor) and successfully up-linked on February 20. This software patch meant that the scale factors of the other gyros can no longer be commanded, *ROSAT* went back on the Mission Timeline on 1992 February 24 and the first three slews were successfully performed. This success indicated that the new Z-gyro scale factor was correctly determined and appeared to be stable.

The RW-3 reaction wheel has demonstrated above nominal static and dynamic friction. This causes the wheel to stop at rotation rates close to zero.

1.2.5 The XRT Startrackers

(*Sources:* NRA 91-OSSA-3; Hasinger 1990,1992)

Two CCD startrackers are provided on the XRT (designated STC-1 and STC-2) for position sensing on guide stars. The optical axes of the startrackers are tilted by 3° with respect to the optical axis of the XRT (*i.e.,* to the S/C Z_R-axis; Section 2.5.3). The field of view of each sensor is a rectangle measuring $\sim 4^\circ \times 5^\circ$ with an overlap of about 2°. The overlap region of the 2 startrackers also overlaps with about half of the PSPC and HRI fields of view (Figure 1.2).

During operation, bright optical sources must be avoided by the startrackers, particularly the Moon and Earth's sunlit limb. These prevent any position determination when in the *fov* .

The startracker alignment matrices (between the startracker and S/C coordinate frames) were corrected for misalignments which occurred during launch and kept constant thereafter. Small thermal motions of the startrackers with respect to the S/C are corrected to an accuracy of $\sim 1''$ within the GSOC attitude solution S/W using the "Fiducial Light Filter" (described in TN-2002-4700 MB/106).

Due to a conventional digital electronics failure, use of STC-2 was lost 1990 September 8 (see also Appendix A). The software commanding of the remaining startracker (STC-1) was improved over several months during the fall of 1991 to allow the tracking of six stars in search windows of $2^\circ - 3^\circ$, as compared to the previous limit of 3 stars in a 1° window. This new software was uplinked in stages culminating in the resumption of normal S/C operations (following the interruption due to the loss of the Y-gyro; Section 1.2.3) on 1991 November 4. Despite occasional hiccups, no significant degradation in the performance on STC-1 has been detected.

1.2.6 The South Atlantic Anomaly Detectors (SAADs)

(*Source:* Pfeffermann *et al.* 1987)

Certain parts of the *ROSAT* orbit are contaminated by the very intense particle background: the belt regions and the South Atlantic Anomaly (SAA). The focal plane detectors are put into a detector specific "safe mode" during passage through these regions. Normally, time tagged commands turn down the HV of the operating detector (to 0 for the PSPC, to a low value for the HRI). As a backup, two charged particle detectors (the SAADs; one redundant) monitor the particle background, and if the rate exceeds an adjustable threshold, delivers a signal to the ZDE to reduce the detector high voltage.

The SAAD is an N-type silicon semi-conductor with an area of 10 cm^2 and a thickness of 700 μm. Its corresponding electronics are partly integrated in the sensor box and one of the main electronic boxes. The sensor box contains the semiconductor, an HV-converter, and the front-end electronics (a charge sensitive pre-amplifier, followed by a pulse-shaping amplifier). For redundancy at high count rates, the detector current is also monitored.

1.2.7 The Coarse Sun Sensor (CSS)

The coarse sun sensor assembly consists of two identical half sphere sensors, providing complete 4 π steradian sun direction information. Each sensor provides angle information of the sun line with respect to two perpendicular axes.

The spacecraft coordinate system is right handed (X_R, Y_R, Z_R). The X_R axis points towards the sun within ± 20^o.

The symmetry axis of the sensors is mounted in-line with the -X_R axis and +X_R axis respectively. The sensor outputs correspond to one angle in the $X_R - Z_R$–plane and one angle in the $X_R - Y_R$–plane with nominal zero output when the sun is in the -X_R or -Y_R direction.

The sensitivity for the inner region (± 0.1 rad) is of the order of 100 mV/rad within either of the symmetry planes ($X_R - Y_R$–plane or $X_R - Z_R$–plane of the sensor). The output is a monotonic characteristic between -83^o and +83^o. Between 83^o and 97^o the characteristic decays linearly to zero.

The measurement performance parameters are given in Table 1.2.

Table 1.2: Performance of the *ROSAT* Coarse Sun Sensor

Range	4 π
Zero Bias Error	± 0.50
Tolerances on 83^o, 97^o points	± 10
Tolerances on output voltage	± 5% when illuminated with 1 solar constant

After the Y-gyro loss, the CSS has been used for coarse target acquisition. A software patch in the AMCE was designed and tested, and has been in operation since the start of 1991 October. After the Z-gyro loss in 1993 October, the CSS has been used together with the magnetometer, the S-gyro, and the degraded X-gyro for attitude control.

Table 1.3: Performance of the *ROSAT* Magnetometer

Range	50 A/m
Scale factor	0.2 V/A/m
Bandwidth	1.0 Hz
Bias error	< 0.5 A/m over the temperature range
Linear error	< 5%
Alignment	± 0.50

1.2.8 Magnetometer

The magnetometer consists of a three-axis sensor. It provides vector-component information as analog signals, suitable to determine magnitude and direction of the environmental magnetic field. Relative to the spacecraft coordinate system (right handed x,y,z), the magnetometer outputs correspond to a right handed perpendicular-axis orientation. The signs of the output voltages correspond to the signs of the magnetic vector components (the signs of the sensor coordinate axes). Three analog outputs with a ±10 Volts range represent the three vector components of the measured magnetic field.

The magnetometer is mounted on the deployable antenna boom to displace it a sufficient distance from sources of stray magnetic fields within the S/C which would otherwise cause interference. The electronics are placed within the spacecraft structure.

The measurement performance parameters are given in Table 1.3.

After the loss of the Y-gyro, the magnetometer has been used for coarse target acquisition. Extensive investigations to test the method were performed at MPE. The method became operational in 1991 October and after the loss of the Z-gyro and the degradation of the X-gyro replaces nearly the complete gyro package.

1.2.9 Data Storage and Transmission

Up to 700 Mbits of data (scientific, attitude, and housekeeping data from both the XRT and WFC) can be stored on the two on board tape recorders, and transmitted to the ground during ground station contacts. All necessary telecommands for S/C operations for one day must be loaded during the five or six consecutive GSOC contact orbits. At any given time, at most ~ 30 pointing positions can be stored by the system. Thus a large number of very short duration observations cannot be performed.

1.3 Planned Mission Phases

The scientific instruments on board *ROSAT* were activated two weeks after launch (1990 June 1). The following six weeks were devoted to the calibration and verification (Performance, Verification, and Calibration, PVC phase) of all hardware components (see Section 1.3.1) and included operational tests of survey and pointed observations. After the PVC phase, the all-sky survey was performed in a continuous 6 month period using the PSPC in the focal plane of the X-ray telescope. After the survey, the pointed-observation (Guest Observer) phase began, starting with two six-month announcements of opportunity (AO), and yearly AOs thereafter.

(See also Appendix A which provides a table of important dates.)

1.3.1 PVC Observations

A series of pointed observations and a five-day "mini-survey" were made over a roughly six-week period prior to the start of the all-sky survey. The purpose of these observations was instrument calibration and performance verification, including checking out S/C systems, turn-on of both XRT and the WFC focal plane detectors, boresighting, spectral and spatial calibration, and background measurements. Whilst many "standard" X-ray calibration sources were observed, this phase also included some targets from the approved AO-1 program selected to provide a range of scientific objectives. A summary list of these PVC observations is contained in Appendix B. The calibration observations are described in more detail in Chapter 7.

1.3.2 The All-Sky Survey

(*Source:* Aschenbach *et al.* 1985; NRA 91-OSSA-3; see also Voges 1992, Snowden & Schmitt 1990)

During the six-month survey phase, nearly the entire sky was scanned in 2° (5° for the WFC) strips centered on great circles running through the ecliptic poles, roughly perpendicular to the Earth-Sun line. The rotation period was synchronized to the orbital period by the scan control law in such a manner that no Earth occultations occurred and the zenith angle was minimized. The nominal scan rate was $\sim 360^\circ$ of ecliptic latitude per satellite orbit, and the nominal progression rate of 0.986° per day, which was increased to $\sim 1.46^\circ$ per day at the end of the survey.

The PSPC (with a 2° field-of-view) was in the focal plane of the XRT during the all-sky survey. The S1 and S2 filters were used alternately by the WFC (5° field-of-view) in order to obtain 2 XUV colours in the 60 – 200 Å band.

The last week of the scheduled survey phase was lost due to the "solar slew" on 1991 January 25 described in Appendix A. However, the unobserved region was surveyed between 1991 February 23−25 and 1991 August 3−13 during breaks in the AO-1 mission phase. Figure 1.3 is an Aitoff projection of the celestial sphere showing the (logarithmic) exposure time of the *ROSAT* all-sky survey.

1.3.3 Pointed Observations

Wobble Mode

(*Source:* Primarily NRA 91-OSSA-3)

During both PSPC and HRI pointed observations, the telescope's pointing direction was in general slowly moved back and forth (by $\simeq \pm 3'$ with a period of 400 seconds) in a diagonal direction to the coarse wire mesh of the PSPC window support structure. This was done for the PSPC in order to prevent unwanted shadowing of X-ray sources behind this mesh. The amplitude of the wobble was not always the same, and was smaller (about half the normal amplitude) during the "Reduced Pointing" mode of 1991 May 18 – November 4.

1.4 Observing Constraints

The Sun
The solar panels of the *ROSAT* spacecraft are fixed with respect to the XRT axis (Figure 1.1). In order to maintain a sufficient power supply, the solar panels must always be pointed within a 15° cone around the Sun. Consequently, the sky accessible to *ROSAT* at any given time is a $30^\circ \times 360^\circ$ band perpendicular to the solar vector (corresponding to $\sim$ 26% of the whole sky). Due to the solar motion, this viewing path covers the whole sky in a period of six months. Targets in the vicinity of the ecliptic plane can be observed twice a year for $\sim$ 30 days, whereas targets within 15° of the ecliptic poles can be observed at all times. During the reduced pointing phase, the Sun Angle constraint was $90^\circ \pm 5^\circ$, as detailed in Section 1.2.3 above.

Earth Occultations *ROSAT* was placed into a circular low Earth orbit with an initial altitude of 580 km. As seen from the satellite, the Earth subtends a core of (half) opening angle $\sim 68^\circ$, most targets are therefore be occulted for part of the orbit and observations are broken into smaller segments which are interleaved with observations of other targets. Hence, the resulting data stream for a particular target will in general show large data gaps, as illustrated in Figure 1.4).

No Earth occultation occurs for targets in directions perpendicular to the instantaneous orbit plane (which changes due to precession), they are located in the so-called continuous viewing zones. Attempts are made to schedule targets in continuous viewing zones whenever feasible since such targets can be observed with essentially no loss in viewing time other than that due to the passage of *ROSAT* through the radiation belts and SAA.

The South Atlantic Anomaly & Radiation Belts
The *ROSAT* orbit includes passages through the South Atlantic Anomaly (SAA) and the northern and southern radiation belts. In these regions a significantly enhanced charged particle density is encountered which precludes turning on the detector high voltage. On average $\sim$ 27% of the time during an orbit is not available for scientific observations.

Atomic Oxygen

The *ROSAT* PSPC detector entrance windows, as well as one of the WFC filters, are made of polycarbonate materials. When exposed to atomic oxygen (the predominate atmospheric species at the orbital altitude of *ROSAT*) such substrates will be ablated quickly. The problem will be most severe when the viewing direction of the spacecraft coincides with the instantaneous spacecraft velocity vector. The angle between the viewing direction and the instantaneous velocity vector is therefore kept $\gtrsim 28^\circ$. The atomic oxygen problem is most severe at those times when the Sun reaches maximum elongation above or below the spacecraft orbital plane.

Atmospheric Drag

Due to the low altitude of the *ROSAT* orbit, the orbit is effected by atmospheric drag. The magnitude of the effect is proportional to atmospheric density, which in turn depends upon solar activity. Due to the intrinsic unpredictability of solar activity, precise predictions of the exact spacecraft position during its orbit are consequently difficult to make on long time scales.

Strong X-ray Sources

The detectors in the XRT focal plane must be protected from exposure to very strong X-ray sources. At present, the only forbidden source is

```
  Sco X-1   at RA(2000) 16H 19M 54.9S,  dec(2000) -15D 38M 27.8S
```

No *ROSAT* pointing will be scheduled with this source in the *fov* .

The occurrence of an increasingly bright hot spot (a localized region of partial detector breakdown) required a reduction in the PSPC HV setting on 1991 October 14 (see also Appendix A). Then, on 1993 March 24, a bright source appeared to cause breakdown (corona) in the detector. Since that time, bright ($>$ 150 counts s^{-1}) sources have been avoided for fear of a recurrence of this problem.

The Moon

The XRT Startrackers should not be exposed to bright optical sources. In particular, with the moon in the field-of-view, a useful aspect solution cannot be derived.

References to Chapter 1

Aschenbach, B. *et al.* 1985, *ROSAT PSPC Scientific Data Processing Requirement Document*, MPE Internal Report 44.

Hasinger, G. 1990, MPE *ROSAT* Memo TN-ROS-ME-ED34/002.

Hasinger, G. 1992, Informal Note dated 1992 April 29.

Pfeffermann, E. *et al.* 1987, *Proc. SPIE* 733, 519.

Snowden, S.L., & Schmitt, J.H.M.M. 1990, *Astrophy. & Space Science*, **171**, 207

Snowden, S.L., & Schmitt, J.H.M.M. 1992, in *Data Analysis in Astronomy IV*, eds. V. Di Gesu *et al.* (New York:Plenum), p. 121.

Trümper, J. 1983, *Adv. Space Sci*, **2**, 241.

Turner, T.J., 1991, *ROSAT Newsl*, **6**, 2.

Turner, T.J., 1992, *ROSAT Newsl*, **7**, 3.

Voges, W. 1992, in Proceedings of the European ISY Symposium Space Science with Particular Emphasis on High Energy Astrophysics, ESA ISY 3, eds. T. D. Guyenne & J. J. Hunt (Noordwijk: ESA Publ.Div.), 9

Figures to Chapter 1

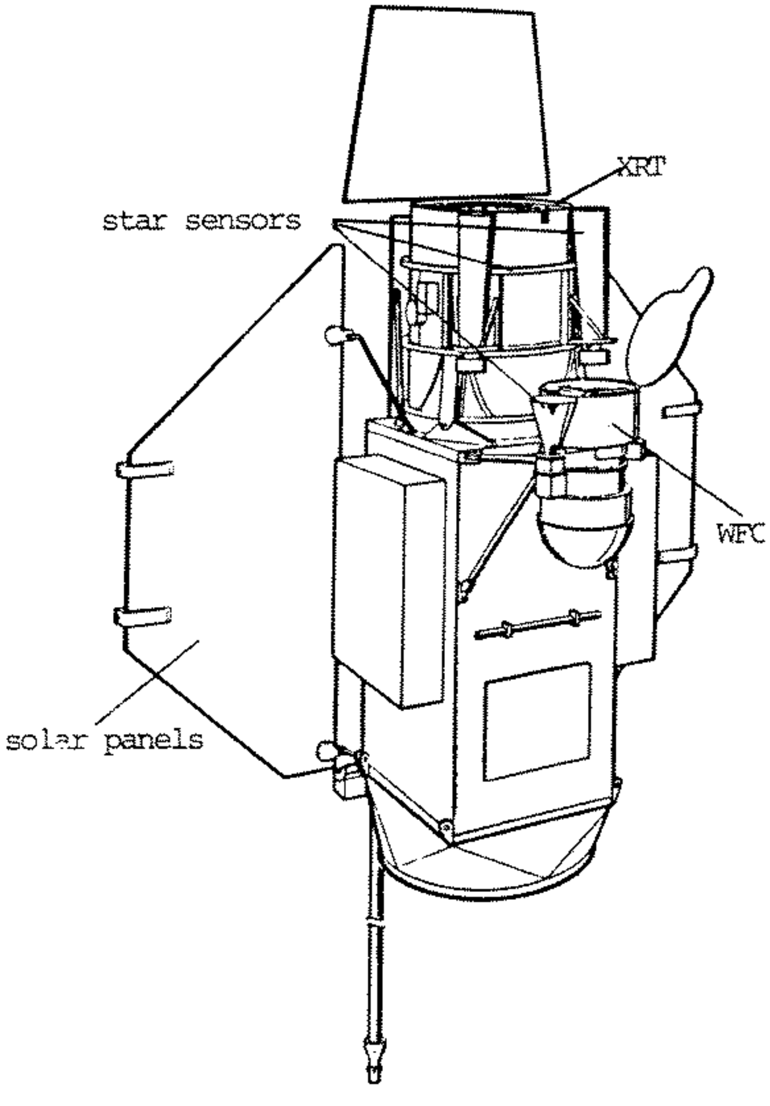

Figure 1.1: Schematic view of the *ROSAT* spacecraft.
(*Source: ROSAT* AO-2 Technical Description).

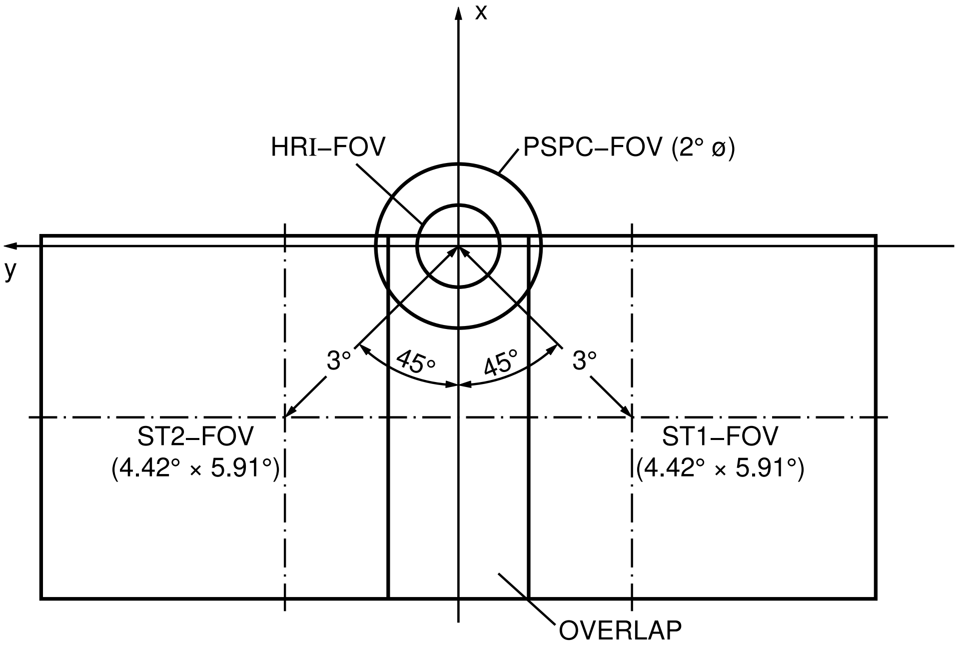

Figure 1.2: The fields of view of the *ROSAT* Positional Sensitive Proportional Counter (PSPC), High Resolution Imager (HRI), and Startrackers.

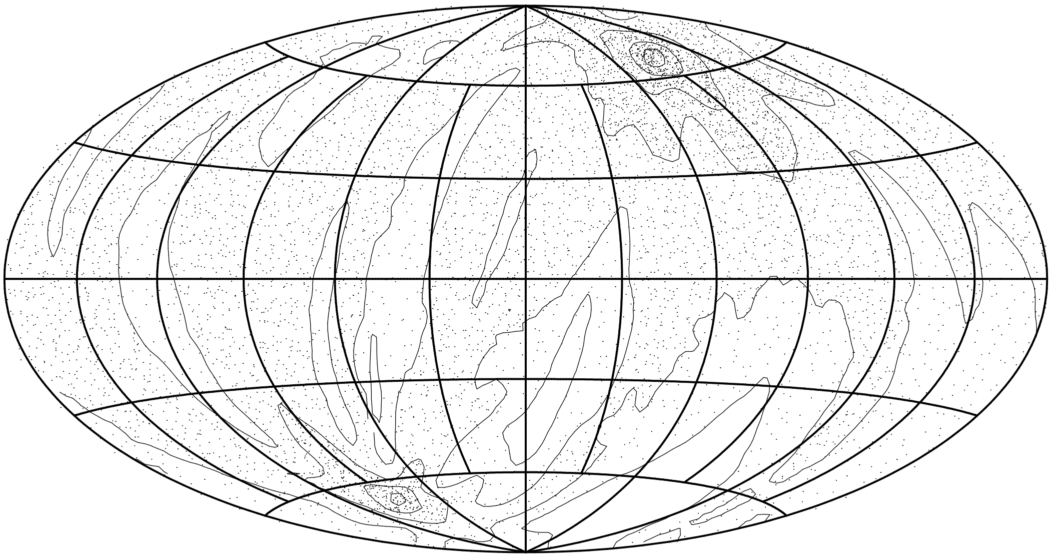

Figure 1.3: An Aitoff projection of the celestial sphere showing the (logarithmic) exposure time of the *ROSAT* all-sky survey. The spring equinox is located at the centre, with increasing RA plotted to the left. The lowest contour indicates a PSPC total exposure of 250 s, with each additional contour representing an increase by a factor 2. The rough WFC exposure time in each survey filter can be obtained by multiplying these values by a factor 3 (due to the larger field-of-view of the WFC).
(*Source:* NRA 91-OSSA-3).

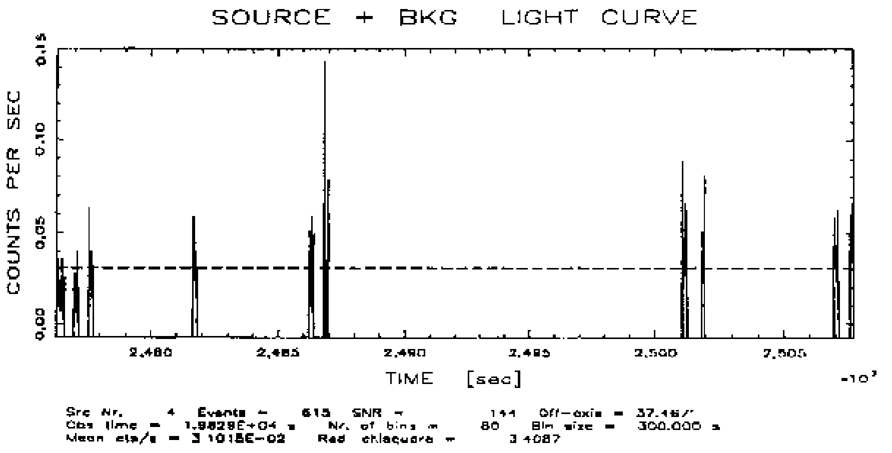

Figure 1.4: Example *ROSAT* PSPC data stream for a target demonstrating Earth Occultations, *etc.* This *ROSAT* PSPC light curve shows a typical *ROSAT* data sampling pattern, in this case the exposure time on the target was ~ 20,000 seconds. The large gaps in the data depend on the observation scheduling. An observation as long as this may be scheduled over a week or two. The small gaps are due to earth occultations and SAA passages. Additional gaps can appear in the accepted Good Time Intervals (GTIs) due to screening on such parameters as aspect error.

Chapter 2

THE XRT

The X-ray telescope (XRT) on *ROSAT* consists of the following subsystems:

- the X-ray Mirror Assembly (XMA)
- a magnetic deflector
- two South Atlantic Anomaly Detectors (SAADs)
- a focal plane turret containing
  - 2 Position Sensitive Proportional Counters (PSPCs) and associated filter wheel
  - 1 High Resolution Imager

A schematic view of the XRT and its various subsystems is shown in Figure 2.1.

2.1 The XRT Mirror Assembly

The XRT X-ray mirror assembly (XMA) consists of 4 nested grazing incidence Wolter-I mirrors with a maximum aperture of 83.5 cm and a focal length of 240 cm. All of the 8 mirror shells (4 paraboloid/hyperboloid pairs) are constructed of Zerodur, a glass ceramic with an almost negligible thermal coefficient, and are coated with a thin layer of gold to enhance the X-ray reflectivity. Typical grazing angles are between 1° and 2° depending upon the sub-shell considered

The focal plane plate scale of the XRT is 11.64 μm arcsec^{-1}

2.1.1 The XMA Support Structure

The mechanical concept for the XMA uses a straightforward cantilever design. The four paraboloidal mirrors are mounted at one end to a central supporting flange, which carries the four hyperboloidal shells on its opposite side. The central flange, which is 78 mm thick Invar steel, actually consists of 5 solid annuli which are interconnected by 16 radial struts. Flanges of similar shape but much thinner stabilize the mirror shells at the entrance and exit planes. The area obstructed by the struts is about 10% of the total. The outermost annulus of the central flange connects the mirror system to the optical bench via a short conically shaped tube which produces the axial stiffness and stability. The mirror shells are made of Zerodur with a wall thickness ranging from 16 to 25 mm increasing with mirror diameter. The supporting plates and flanges are made of Invar. For the optical bench and the stiffening cone, a carbon fibre compound material was chosen. In order to accommodate the slightly different thermal expansion rate of Zerodur, Invar, and carbon fibre, the mirrors are not mounted directly to the Invar support plates but are bonded to thin-walled Invar sleeves, which are bolted to the Invar support flange.

In order to suppress stray-light, which arises primarily from singly reflected rays either off the parabolas or the hyperbolas, a set of stops in the form of circular blades has been incorporated at the front aperture, in the section about midway down the parabolas and hyperbolas and at the exit plane.

2.2 XMA/Detector Boresight Calibration

(*Source:* Hasinger 1990)

The main boresightings were performed separately for the PSPC and HRI during the PVC phases of the mission (see also Appendix C). These comprised of 5–9 successive pointings at a bright X-ray target for which the celestial position is accurately known, and intended to determine the actual alignment matrices between the startrackers (Section 1.2.5) and the XRT. The results were derived at MPE and communicated to GSOC for inclusion in the GSOC attitude solution S/W. The basic (pre-launch) plans for the boresight procedure, residual errors, and accuracy specifications are described in TN-2002-2160 DS/032, TN-2002-2160 DS/047 & TN-2002-2160 DS/044 respectively.

In principle, the boresight parameters should remain stable for the whole mission, however the accuracy of determination of the necessary boresight correction was improved with experience, consequently the boresight correction folded into SASS has changed with time.

2.2.1 Boresight-Calibration Results

(*Source:* Kürster & Hasinger 1992, 1993)

The above MPE *ROSAT* AMCS status reports, give details of the deviations seen between XRT derived positions and those given in catalogues (*e.g.,* Simbad, the Bright Star Catalogue, an internal MPE X-ray catalogue, and PI supplied positions).

Previously, systematic discrepancies have been noted between the optical and X-ray positions of *ROSAT* targets. In an MPE study, the 1σ scatter of the distribution of optical versus X-ray positions was $6.1''$ for the PSPC (B) and $6.4''$ for the HRI. The PSPC data showed a systematic offset of $6.9''$ while the HRI showed a negligible systematic offset (the HRI always had a boresight

Table 2.1: *ROSAT* XRT/detector boresighting results

Detector	Source	$< \Delta x >$	$< \Delta y >$	σ_x	σ_y	σ_{tot}
PSPC	Fig 2.2	-0.13 ± 0.5	3.98 ± 0.52	3.91	4.09	5.66
PSPC	Fig 2.3	2.34 ± 0.11	4.54 ± 0.14	0.57	0.73	0.93
HRI	Fig 2.4	1.29 ± 1.97	1.37 ± 1.64	4.81	4.01	6.27

correction of $10''$ in the Y-direction). For a long time, no correction was made to SASS to account for this systematic effect in the PSPC data. This was because there was noted a large scatter in the offsets (up to $20''$), and the effect was not understood. It was finally decided to correct the SASS for the mean offset of $6''$ in the PSPC data. The correction was implemented in 1992 December at MPE (SASS 6-2), and affects data processed since then (or processed since 1993 January in the USA, which is equivalent to observations made since 1992 September). Also, all reprocessed (Rev2) data will have this (or an updated) boresight correction included.

There were some inaccuracies in the original study, however, notably that the nearest SIMBAD source was always taken as the optical counterpart, when in fact that was not always the ID with the best position. This meant of course that the boresight error was originally underestimated. A new study then showed the deviations from expected (SIMBAD) positions still lay clustered around $3'' - 4''$ on the positive detector y axis. Another $3'' - 4''$ correction was required, in the same sense as the original correction.

These boresight corrections do not get rid of the scatter in the difference between optical and X-ray positions. It is thought that this may be due to residual star-tracker errors. Apparently, the startracker has variations in quantum efficiency between the pixels. This means that the centroiding to get the position of the guide stars can be skewed. It is unlikely that this can be corrected for, as not all of the star tracker pixels are calibrated. This seems like the most likely origin of the large scatter in the discrepancies in X-ray positions mentioned above. (For a further discussion of the boresight problems see Appendix D).

The most recent results are summarized in Fig 2.2, Fig 2.3, Fig 2.4 and Table 2.1, where the boresight offset is given by the mean values $< \Delta x >$ and $< \Delta y >$ and $\sigma_{tot} = \sigma_x^2 + \sigma_y^2$.

Detector specific systematic errors can also occur in derived X-ray positions. For bright sources, these can be as large as $\sim 4''$ for both the PSPC and the HRI.

No temporal variations in the boresight offsets have been found.

2.3 Effective Area of the XMA

(*Source:* Aschenbach 1990a,b)

2.3.1 Overview

The collecting area provided by the XMA is a function of off-axis angle and energy due to combined effects of:

1. the decrease in the reflectivity of the gold coating with energy,
2. vignetting (including obstruction by the XMA support structure)
3. scattering by the XMA.

2.3.2 The Reflectivity of Gold

The reflectivity of the gold-coating on the XRT mirrors is a decreasing function of energy with a number of additional (minor) absorption edges. The energy dependence has been calculated on the basis of theoretical values for the optical constants of gold, and tested by ground calibration measurements in the PANTER facility. By comparing the experimental and theoretical results (taking into account the non-parallel beam testing geometry and the fact that only a few X-ray lines can be used) the final on-axis effective area was derived. A satisfactory agreement was reached by using the optical constants available in the literature.

2.3.3 Vignetting

Off-axis rays strike the mirror surface at a shallower angle such that the projected geometric area decreases. Furthermore (but to a lesser extent), the average reflectivity of the gold surface is reduced. In addition, off-axis rays suffer a higher degree of obstruction due to the radial struts which stabilize the XMA (see Section 2.1.1), and for very large off-axis angles due to the field-stops, which are introduced to reduce stray light. Together, these effects lead to an energy-dependent decrease in the effective area of the XRT as a function of (increasing) off-axis angle (collectively referred to as vignetting).

There is an additional effect due to the magnetic deflector. This was designed such that it does not additionally block X-rays on-axis. However for an offset angle $\gtrsim 5'$, the radial support struts of the deflector are no longer in a projected shadow of the XMA support struts, and therefore an additional loss is encountered (see also Aschenbach 1990a).

To verify the theoretical vignetting function using in-flight data, the radial profiles of the detector maps created from all-sky survey data (Snowden *et al.* 1994) were studied. After masking out the window-support structure ring and ribs and binning the counts in radial annuli, the count-rate ratios then give the vignetting at very high S/N. There is good agreement with the preflight vignetting function (which was parameterized as a double power-law function) out to $\sim 40'$. Above $40'$, there are small discrepancies where the model diverges from the data. The survey data initially dip slightly under the model but then rise up and go above the model, crossing it at about $54'$. The size of this discrepancy and the radius where is starts appears to be a function of energy.

This effect could be due to systematic errors in the PSPC event linearization, in particular due to the "window correction" (see Section 3.5.3).

2.3.4 Mirror Scattering

Small-scale irregularities in the mirror surface give rise to small-angle scattering, the level of which is energy dependent. The scattering level and its energy dependence (*i.e.,* the radial point response function) was measured in the diverging beam of the PANTER facility (see Section 2.4).

2.3.5 Calculated Effective Area

The area of the *ROSAT* XMA as a function of energy is shown in Figure 2.5 for on axis and several off-axis angles. The reduction in the areas due to obstruction by the telescope support structure (Section 2.1.1) have been included. It can be seen that, besides the various edges due to gold, the area of the XMA is fairly constant as a function of energy in the 0.3–1 keV band.

Between 1.0 and 1.7 keV, the telescope has been calibrated on ground and compared with predictions using tabulated optical constants. Up to 1.7 keV, the highest X-ray energy available as X-ray line used in the calibration, the agreement is satisfactory. Beyond that energy, optical constants are not available and a comparison cannot be made.

The fall-off beyond 1 keV is because reflection efficiency is a function of energy and the angle required to focus the photons decreases with increasing X-ray photon energy. The steep rise below 0.2 keV is due to the optical characteristics of gold.

2.4 Angular Resolution of the XMA

(*Source:* CAL/ROS/92-001, Hasinger *et al.* 1992; see also Predehl *et al.* 1993)

The angular resolution of the *ROSAT* XMA (alone) is determined by:

1. the degree of scattering by the mirror shells
2. the off-axis blur of the XMA.

2.4.1 The XMA Scattering Profile

Microroughness of the reflecting mirror surfaces leads to non-specular reflection of X-rays, *i.e.,* scattering. The importance of scattering by the *ROSAT* XMA is small compared to previously available X-ray mirrors, offering the ability to perform high contrast imaging. The form of the scattering is a complex function of energy, grazing angle and the scale size of the mirror surface roughness. Theoretically, assuming the grazing angle remains constant, the scattering fraction should increase as E^2. Due to the laws of diffraction, the shape parameters should be $\propto E^{-1}$.

The detailed *psf* parameters and their associated E dependences have been determined for the XMA and PSPC-A & PSPC-C using 4 monochromatic energies (0.28, 0.93, 1.49 & 1.70 keV) at the PANTER facility in Neuried. The resultant predicted *psf* curves have been compared to a number of PVC and AO-1 datasets in OGIP Calibration Memo CAL/ROS/92-001 (see also Section 4.1).

The analytical form derived for the fraction of photons within the component of the *psf* due to XMA scattering as a function of energy is given by:

$$F_{scatt} = 0.075E^{+1.43} \tag{2.1}$$

Even at high energies F_{scatt} is small compared to the other components of the total *psf* (Hasinger *et al.* 1992). The model and the PANTER data from which Equation 2.1 was derived are also shown in Hasinger *et al.* 1992. The increase in F_{scatt} with E is slower than the E^2 power law expected. This is due to the fact that the effective grazing angle averaged over all mirror shells is not constant.

The PANTER tests confirmed that this component was well approximated by a Lorentzian function, steepening to a power law at large r, *i.e.*,

$$\begin{aligned} PSF_{scatt}(E,r) &= \tfrac{A_{scatt}(E)}{(1+(2r/r_{scatt}(E))^2)} && \text{for } r \le r_b \\ &= PSF(E,r_b)\ (r/r_b)^{-\alpha} && \text{for } r > r_b \end{aligned} \tag{2.2}$$

where

$$r_b(E) = 861.9/60\ E^{-1}\ \text{arcmin} \tag{2.3}$$

and

$$\alpha = 2.119\ +\ 0.212E \tag{2.4}$$

The width of the lorentzian, r_{scatt}, as a function of energy was found to be:

$$r_{scatt}(E) = 79.9/60\ E^{-1}\ \text{arcmin} \tag{2.5}$$

The two parameters governing the shape of PSF_{scatt} (*i.e.*, r_b and r_{scatt}) were constrained to be proportional to E^{-1} (see section 2.4.1) during the analytical fitting to the PANTER data.

The normalization of the lorentzian, A_{scatt},is given by

$$A_{scatt} = F_{scatt}(E)/I^{\infty}_{scatt}\ \text{normalized counts arcmin}^{-2} \tag{2.6}$$

where

$$I^{\infty}_{scatt} = \pi(r_{scatt}/2)^2\ \left[\ln(1 + (2/r_{scatt})^2 r_b^2) + 2r_b^2\left((r_{scatt}/2)^2 + r_b^2\right)^{-1}(\alpha-2)^{-1}\right] \tag{2.7}$$

is the renormalization factor such that[1]

$$\int_0^{\infty} PSF_{scatt}(E,r)\ 2\pi r\ \mathrm{d}r = F_{scatt}(E) \tag{2.8}$$

The mirror scattering has no significant dependance on off-axis angle of the observation. For further details see Hasinger *et al.* 1993.

---

[1] Note that due to a typographical error there was a factor 2 missing from the following equation in all versions of CAL/ROS/92-001 prior to 1992 October 5 (the software used to generate the figures was correct, however)

2.4.2 The Off-Axis Blur of the XMA

An analytic description of the off-axis *psf* of grazing incidence optics is complicated. A convenient measure of the image spread is the so-called RMS blur radius, defined as the radius within which 68% of the photons fall. The expected *ROSAT* XMA rms blur circle radius increases rapidly with off axis angle.

The XMA off-axis point response as a function of energy is shown in Figure 2.6 where the widths of the mirror and PSPC detector components contributing to the *psf* are compared (for four energies). The figure illustrates how the mirror effect dominates over the PSPC effect outside of about 14′.

The change in mirror blur with increasing off-axis angle was parameterized as a Gaussian with

$$m_\sigma(\theta) = 1/60(0.219\theta^{2.848})^{1/2} \text{ arcmin}$$

For a complete parameterization of the XMA+PSPC off-axis *psf* see CAL/ROS/93-015 (Hasinger *et al.* 1993) and Section 4.1.2.

2.5 XRT Coordinate Systems

(*Source:* Hasinger 1986,1990)

In this section we consider the following coordinate systems:

- The Celestial Inertial Reference Frame
- The Cartesian Relative Coordinate System (Sky-Coordinate System)
- The *ROSAT* Coordinate System
- The Image Display Coordinate System

The additional detector-specific coordinate frames will be discussed in the following chapters.

2.5.1 The Celestial Inertial Reference Frame (X_I, Y_I, Z_I)

(*Source:* Hasinger 1990)

All positions on the sky ultimately refer to the equatorial reference system for the mean equinox 2000.0, with cartesian coordinates X_I, Y_I, Z_I, and the equivalent polar coordinate frame under the equatorial system (Right ascension α, declination δ). The ecliptic coordinate system (X_{IE}, Y_{IE}, Z_{IE}) was also used (particularly for the data storage, image, source analysis during the survey phase), with equivalent polar coordinates ecliptic longitude (λ) and latitude (β).

2.5.2 The Cartesian Relative Coordinate System

(*Source:* Hasinger 1990)

The relative coordinate system is a cartesian frame ($X_{REL}, Y_{REL}, Z_{REL}$) which projects the equatorial frame (α, δ) onto the plane *fov*. The Z_{REL}-axis is aligned with the nominal pointing direction (or the centre of the strip during the All-Sky Survey phase), the Y_{REL}-axis parallel to the local meridian in the direction of increasing δ, and the X_{REL}-axis perpendicular to the local meridian in the direction of increasing α (Figure 2.7).

2.5.3 The *ROSAT* Coordinate System

(*Source:* Hasinger 1986,1990)

The aspect solution for a given observation is referenced to the *ROSAT* (S/C) cartesian coordinate system (X_R, Y_R, Z_R). This virtual right-handed frame is fixed to the S/C (Figure 2.8) with the Z_R-axis aligned with the optical axis of the XRT (and parallel to that of the WFC) in the pointing direction, and the X_R-axis perpendicular to the solar panels in the anti-Sun direction. In orbit, the *ROSAT* coordinate system is defined by the GSOC attitude solution derived from the measurement of stars in the startracker *fov* (Section 1.2.5).

2.5.4 The Image Display Coordinate System

(*Source:* Hasinger 1990)

The Image Display, or North/South (NS), system is a cartesian frame (X_{NS}, Y_{NS}, Z_{NS}) optimised for use by image display S/W. By convention, astronomical images are usually displayed in the same sense as one would see from the Earth (*i.e.,* North to the top, East to the left). However, image display devices usually display images from top-to-bottom and from left-to-right. Thus the transformation from the relative coordinate system (X_{REL}, Y_{REL}; Section 2.5.2) to the NS system is (Figure 2.7):

$$\begin{aligned} X_{NS} &= -X_{REL} \\ Y_{NS} &= -Y_{REL} \\ Z_{NS} &= Z_{REL} \qquad (2.9) \end{aligned}$$

(the Z_{NS}-axis is aligned with the nominal pointing direction of the S/C, as is the case for the Z_{REL}-axis).

References to Chapter 2

Aschenbach, B., Bräuninger, H., Kettenring G., 1983, *Adv. Space Research* **2**, No. 4, 251.

Aschenbach, B., 1990a, *ROSAT Notiz* 1990 Jan 19.

Aschenbach, B., 1990b, *ROSAT Notiz* 1990 Jul 25.

Hasinger, G. 1986, Informal Note 1986, Jul 02.

Hasinger, G. 1990, MPE *ROSAT* Memo TN-ROS-ME-ED34/002.

Hasinger, G, Turner, T.J., George, I.M, & Boese, G. 1992, *Legacy*, 2, in press. (CAL/GEN/92-001)

Hasinger, G, Boese, G., Predehl, P., Turner, T.J., Yusaf, R., George, I.M, & Rohrbach, G. 1993, *Legacy*, in press, (CAL/GEN/93-015).

Kürster, M. & Hasinger, G. 1992, MPE *ROSAT* Memo TN-ROS-ME-ZA00/028.

Kürster, M. & Hasinger, G. 1993, AMCS Status Report March 10th.

Predehl, P., Schmitt, J.H.M.M., & Snowden, S.L. 1992, *Science*, **257**, 935.

Snowden, S. L., McCammon, D., Burrows, D.N., & Mendenhall, J.A. 1994, *Astrophys. J.*, **424**, 714.

Figures to Chapter 2

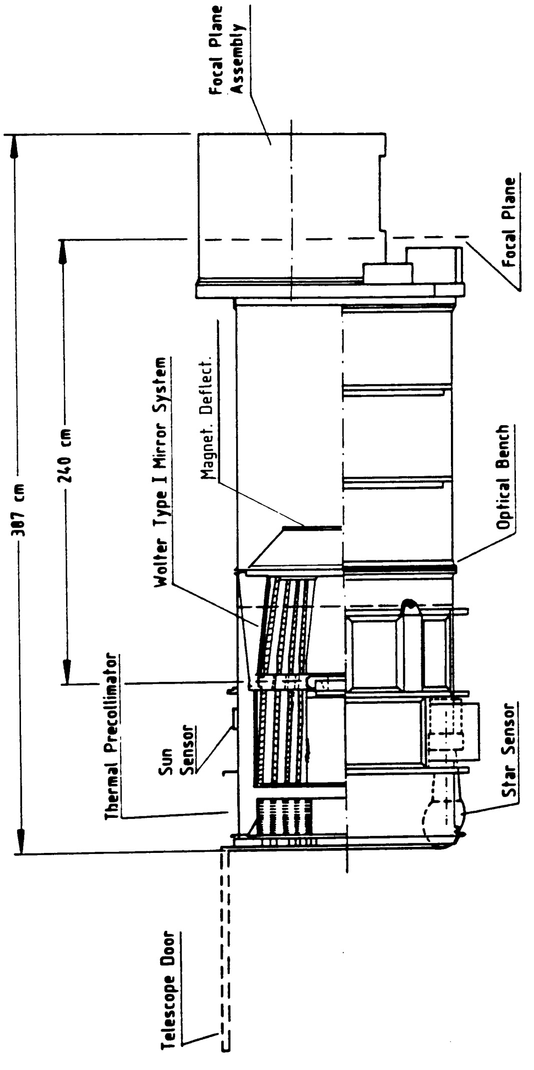

Figure 2.1: Schematic cross-sectional view of the *ROSAT* telescope tube housing the fourfold nested 80 cm Wolter type I mirror system and the focal plane turret containing two PSPCs with filter wheels and one HRI.
(*Source:* Trümper 1983).

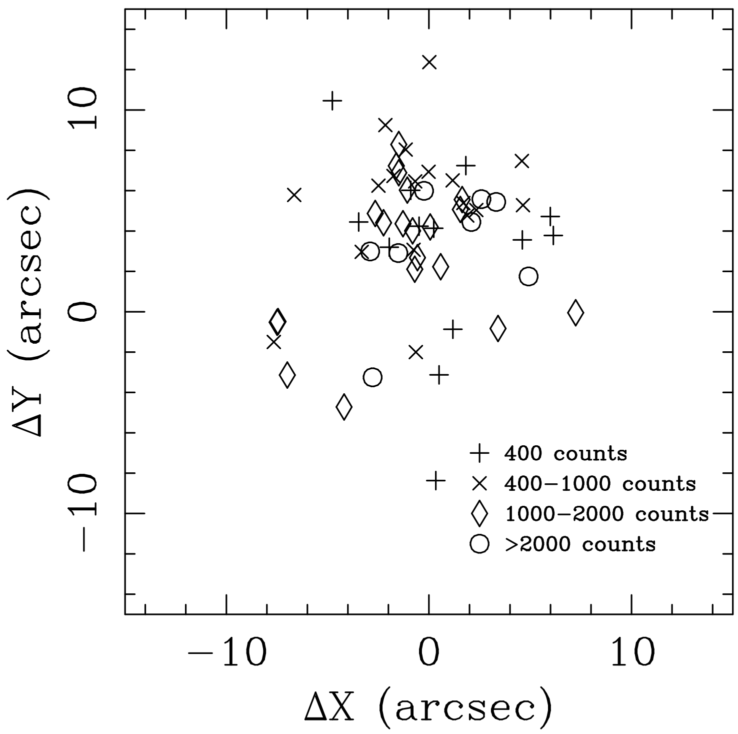

Figure 2.2: The deviations of detector positions of 61 selected point sources (61 different observations) from expected (SIMBAD) positions. Only sources with positional accuracy better than $2''$ in the SIMBAD catalogue have been used. The different symbols refer to sources with: plus signs (+) - less than 400 counts, crosses (X) - less 400−1000 counts, diamonds - 1000−2000 counts, circles - 2000−10000 counts.

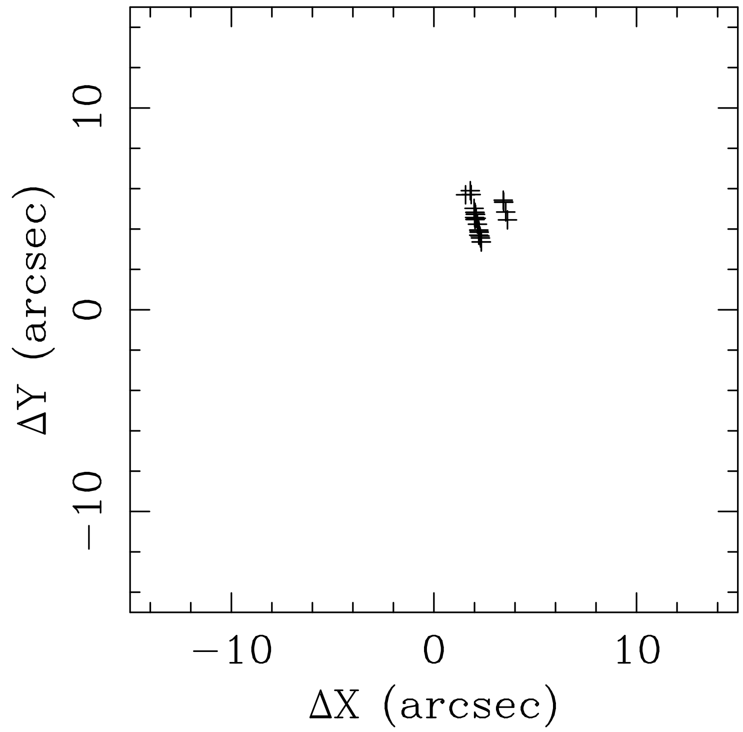

Figure 2.3: The deviations of detector positions for 28 observations of the same source, 3C279 (PIs Madejski & Fink).

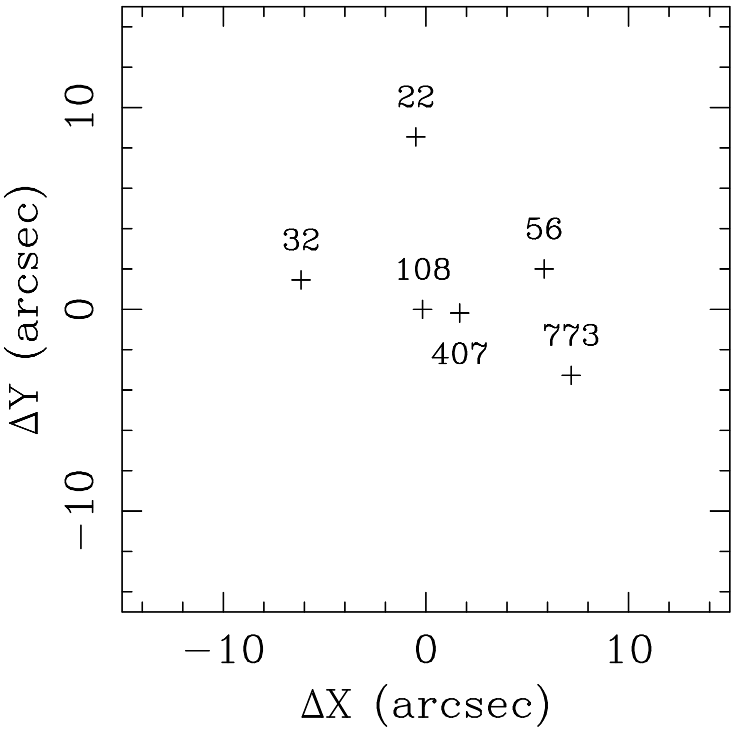

Figure 2.4: The deviations of detector positions from expected (SIMBAD) positions for 6 point sources observed with the HRI. The numbers indicate the number of photons available for the measurement.

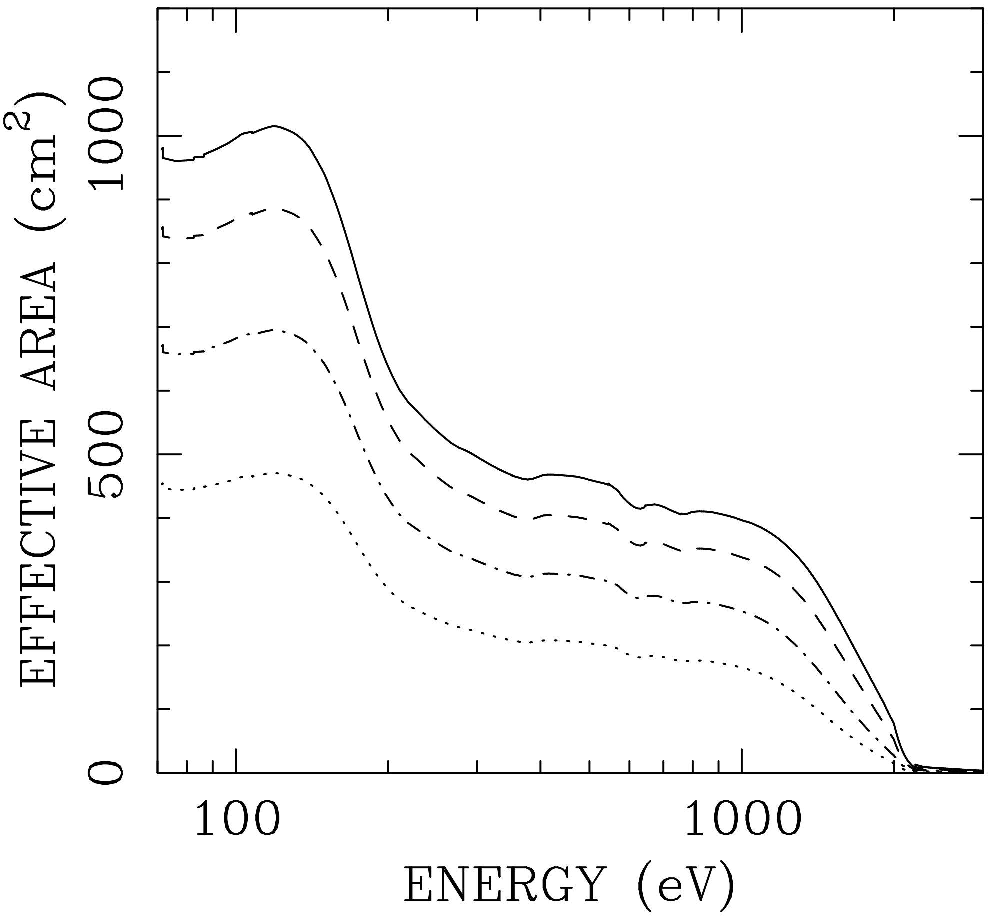

Figure 2.5: The effective area of the *ROSAT* XMA as a function of energy for (from top-to-bottom) off-axis angles 0, 20, 40, & 55′.
(*Source:* Aschenbach 1990,b)

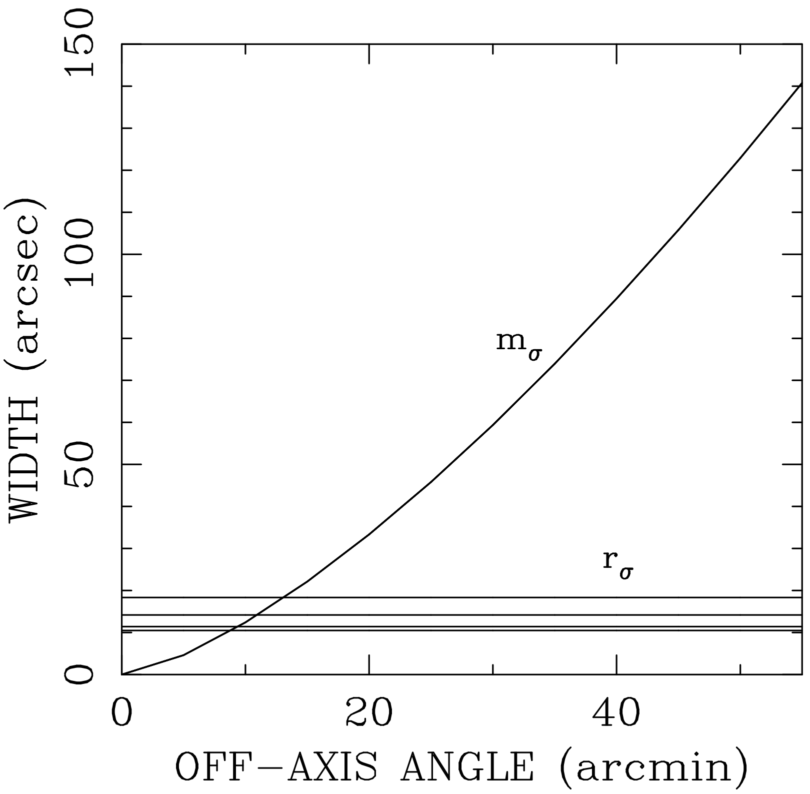

Figure 2.6: The XMA point response as a function of off-axis angle, m_σ, and the PSPC contribution of the *psf* at four different energies, r_σ, are compared. The figure illustrates how the mirror effect dominates over the PSPC effect outside of about 14′. The lines of constant detector component represent (from top to bottom) 0.28, 0.50, 2.0 and 1.0 keV (the detector Gaussian has a minimum between 1 and 2 keV, as detailed in Hasinger *et al.* 1992, thus the inversion).

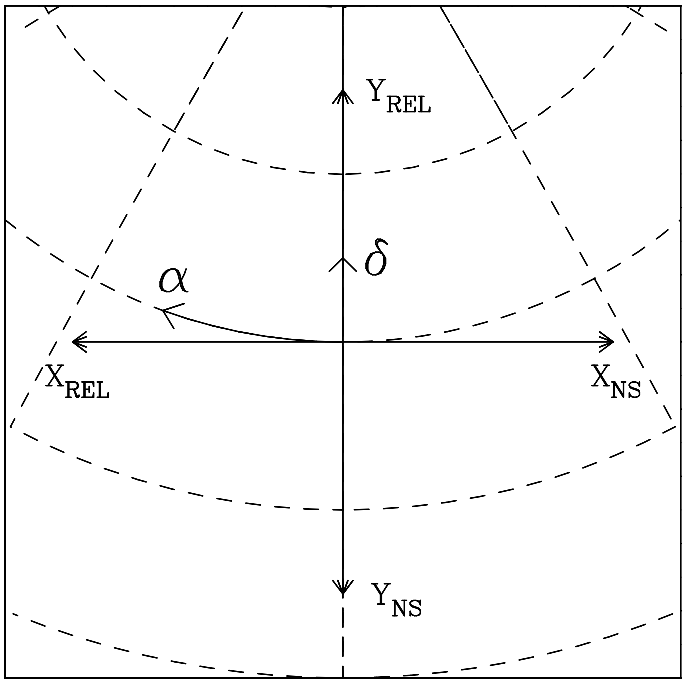

Figure 2.7: The relationships between the celestial inertial reference system, the cartesian relative coordinate system and the image display coordinate system. The Z-axes are directed into the page along the S/C pointing direction. (*Source:* Hasinger 1990).

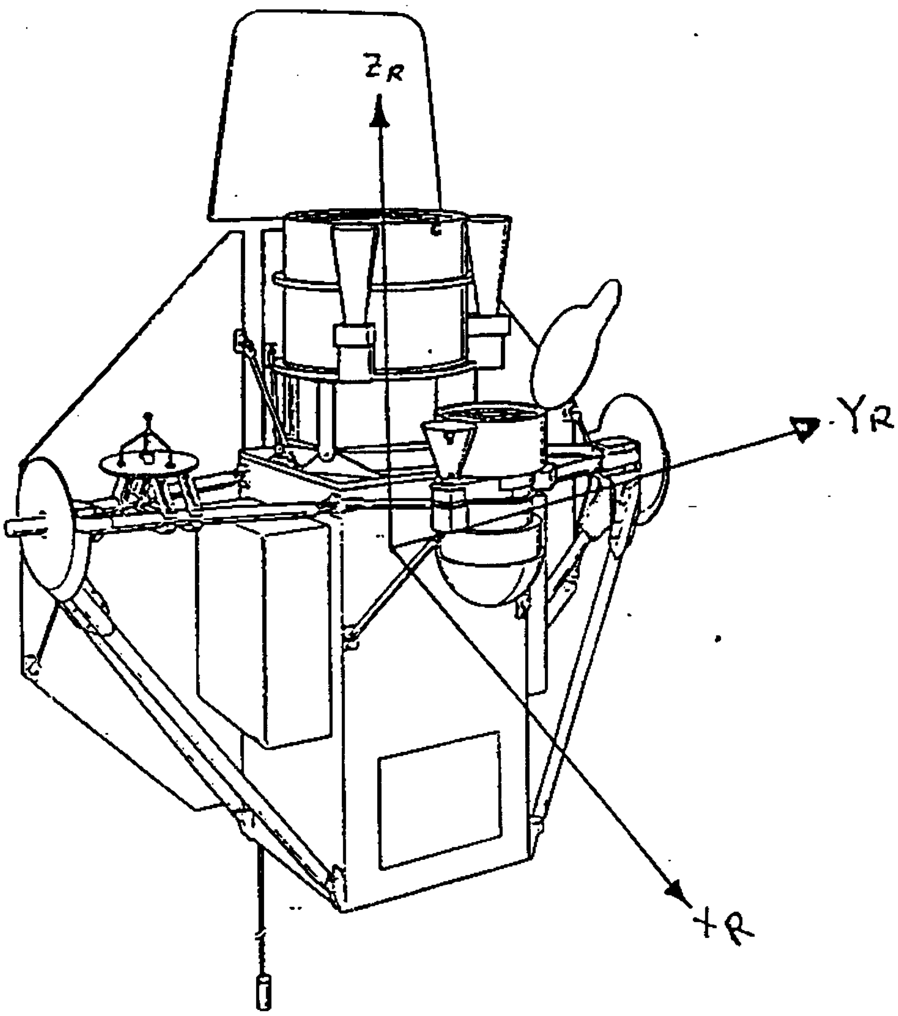

Figure 2.8: The *ROSAT* spacecraft coordinate frame. This virtual right-handed frame is fixed to the spacecraft and the Z_R axis is aligned with the optical axis of the XRT in the pointing direction, while the X_R axis is perpendicular to the solar panels in the anti-sun direction.
(*Source:* Hasinger 1990).

Chapter 3

THE POSITION SENSITIVE PROPORTIONAL COUNTER (PSPC)

3.1 Overview

(*Source:* adaptation from Aschenbach 1985)

Two redundant Position Sensitive Proportional Counters (PSPC-B and PSPC-C) are mounted on a carousel within the focal plane turret of the *ROSAT* XRT (Figure 2.1). Two flight-spare detectors (PSPC-A and PSPC-D) were also constructed and used for some of the ground calibration measurements. PSPC-C was to be the primary detector for the mission and was used for the PVC phase and the bulk of the All-Sky Survey until its destruction during the "Solar slew" following an AMCS glitch on 1991 January 25 (Section 1.2.2). The reserved PSPC-B detector was used thereafter (and hence during all AO pointed observations except those performed during the PVC phase).

The PSPCs (Figure 3.1) are multiwire proportional counters developed by MPE. Each consists of essentially two separate counters: the anode A1 with the cathodes K1 and K2 as the position sensing, X-ray sensitive counter, and the anode A2 as the anticoincidence counter for background rejection. Each electrode is a wire grid, with the wires bonded onto a ceramic support frame. The anode grids have gold-plated tungsten wires, 10 μm in diameter and a spacing of 1.5 mm and 2 mm for A1 and A2, respectively. At the edges of the anode grids are guard wires with increasing diameters to lower the electric field. The cathode grids are made of platinum iridium wires, 50 μm in diameter and with 0.5 mm spacing. The cathodes are grouped by seven or eight for signal processing.

3.2 Operation

(*Source:* Primarily Snowden 1988)

The anode and cathode grids are contained in a gas-filled counter housing containing a mixture of 65% argon, 20% xenon and 15% methane. An X-ray photon, passing through the thin plastic entrance window, will be photo-electrically absorbed by the counter gas producing a photo-electron. The relative contribution of each of the gas components to the absorption cross-section is shown in Figure 3.2, and the resultant mean free path (*i.e.,* absorption depth) in Figure 3.3. The primary electron is thermalized and in the process causes the ionization of other gas atoms forming a secondary electron cloud. The positive ions (including the ion initially ionized) can also add to this cloud by Auger and shake-off processes when energetically allowed. The mean energy required to create a secondary electron is approximately constant over the entire energy range of the PSPC (deviations are most likely to occur just above the gas absorption edges). The probability distribution function for the number of secondary electrons can be described by a Gaussian whose width is given by the modified Fano factor, f', which takes on integer values only (and is obviously truncated at zero). The number of electrons contained within the secondary electron cloud is therefore approximately proportional to the energy of the incident photon (giving rise to the name of the device).

The secondary-electron cloud drifts through the K1 cathode grid toward the A1 anode grid (Figure 3.1). When the electrons of the charge cloud approach closely enough to an anode, the electric field strength becomes sufficiently high for the secondary electrons to ionize additional gas atoms (*i.e.,* the energy that the electron gains from the electric field between collisions is greater than the ionization energy of the gas) causing the charge cloud to be amplified by a (gain) factor of $\sim 5 \times 10^4$. The avalanche of charge onto the anode leads to a charge pulse at the anode and an induced signal at the cathodes, which are all processed by charge-sensitive preamplifiers.

The cathode grids are divided into 25 (K1) and 23 (K2) cathode strips. Each strip consists of seven or eight cathode wires tied together, and is connected to an independent preamplifier. Depending on the energy of the photon, a cathode signal is typically induced on 3 to 5 strips (although, "Ghost Images" can occur for events with pulse heights corresponding to energies $\lesssim 0.15$ keV, – see Section 3.5.4). These signals are digitized by means of pulse shapers, peak detectors, and analog-to-digital converters (ADC). After checking for validity of the event, the position is calculated by adopting a centre-of-gravity calculation. To get the position in both co-ordinates, the two cathode grids are arranged perpendicularly to each other (Figure 3.1).

The wires of the anode grid are connected in parallel to one preamplifier with pulse shaper, peak detector, and ADC. Its signal is used to obtain the energy of the X-ray photon and also as the trigger signal for the cathode read-out electronics. The time required by the electronics for conversion, validity checking, and position calculation is < 1 ms, leading to a maximum average event rate of $> 10^3$ s^{-1}.

In conjunction with the signals of the "veto" anode (A2), the signals of the outer cathode strips of K1 and K2 are combined in an anti-coincidence circuit. The gas depth of these veto counters is such that ionizing particles as well as resonant scattered X-rays (coming from the frames and counter body) are detected (see Section 3.6.1). The achieved background rejection efficiency is around 99.8%.

3.2.1 Low Pulse-Height Tails

If photoabsorption of the incident X-ray occurs too close to the entrance window of the proportional counter, electrons of the secondary electron cloud (generated during the thermalization of the primary electron) can be lost by diffusion to the window. (The ratio of the diffusion coefficient to the drift velocity of electrons in the gas is constant for the entire energy range of the counter.) In addition, secondary electrons can also be lost to the front cathode wire grid (K1; Figure 3.1). In both cases, the detected pulse-height (and therefore associated energy) will be shifter to lower values producing a low pulse-height tail. However, if the size of the secondary electron cloud is large compared to the spacing of the cathode wires, all events will be affected by the grid to roughly the same degree, and the situation can reasonably approximated by a simple increase in the mean energy required to create an electron–ion pair.

The effect of these two processes is most noticeable in the lab for monochromatic lines at low energy. However, for flight data, the effect is most noticeable for hard, absorbed sources (such as the Crab) where there is a nonzero flux (or "tail") in the 1/4 keV band where because of high foreground absorption there are no true source photons.

3.2.2 The Rate-Gain Effect

At very high count rates, such as from the Crab (count rates ∼800 counts s^{-1}), the detector gain saturates due to the reduction in the electric field caused by the pseudo-continuous presence of a substantial electron cloud. However, it is currently thought that this effect was also important for the observation of Mkn421 (∼150 counts s^{-1}). Figure 3.4 shows the effect in the Crab data (top panel). Here the Crab data have been fit with a power-law of photon index $\Gamma = 2.08$ and $N_{\rm H} = 3 \times 10^{21}$ H I $\rm cm^{-2}$ using a detector response matrix with the nominal gain and a gain lowered by 5%. Measurements in the PANTER test facility showed a gain drop of 1% for a 1.5 keV X-ray count rate of 500 counts s^{-1}, and a drop of 2% for a 3.0 keV X-ray count rate of 500 counts s^{-1}. This effect will be further investigated using the PANTER measurements.

3.2.3 The Gas Control System

For a stable operation of the PSPC, the detector gas must be replenished at a flow rate of several $\rm cm^3\ min^{-1}$. There are several reasons for this constant flow. The first is to maintain the relative composition of the detector gas mixture (65% Ar, 20% Xe, 15% CH4), which would otherwise be changed by the differential gas diffusion through the thin polypropylene/lexan window. The second reason is to prevent gas poisoning by polymerization products of the quench gas as well as outgasing from glue and plastic. In order to maintain a temperature-independent gas gain, the detector gas is density rather than pressure controlled. Otherwise, a one degree temperature change would result in a 5% gain shift.

The basic components of the gas supply system are the gas tanks (three tanks of 12 l each with an initial pressure of 200 bar) with pressure regulators, two redundant solenoid valves for the detector pressure regulation, and two artificial leaks (2.5 $\mathrm{cm}^3\ \mathrm{min}^{-1}$ and 3.8 $\mathrm{cm}^3\ \mathrm{min}^{-1}$) at the outlet of each detector. Sealed reference volumes are integrated in the detector housings to guarantee a good thermal coupling between detector and reference gas. They are filled with detector gas at the nominal operating pressure (1465 mbar at 22^o C). The gas control unit maintains the detector pressure at the pressure of the reference volume, yielding a density control (*i.e.,* when the temperature goes up, the regulating pressure goes up accordingly, and vice-versa). The control unit is a bistable regulator with a selectable duty cycle (1 s - 60 s).

3.2.4 PSPC Gas Flow

(*Sources:* Plucinsky *et al.* 1993, and MPE status Bulletin no. 19)

In 1991 June it became apparent that the behaviour of the PSPC background had changed. The background count rate in the lowest channels started to increase and grew to more than ten times the previously observed values by 1991 October. A hot spot also developed at the rim of the detector which was easily observable in the real-time data. Flushing the PSPC from a different gas supply and reducing the gain by reducing the high voltage eliminated the hot spot and reduced, but did not eliminate, the contamination in the low pulse-height channels. During this period, the flow rate was increased to about 6 $\mathrm{cm}^{-3}\ \mathrm{min}^{-1}$ as part of the attempt to decontaminate the detector.

Unfortunately, the low pulse-height contamination started to increase again after 1991 October and continued to increase until 1992 February, when the PSPC gas supply was changed to the third tank (three tanks were flown).

In 1992 January, problems were encountered with the regulating valve. It apparently stuck a number of times during HRI observations (during which the PSPC was routinely flushed). As a measure to extend the valve's lifetime (it began working again for unknown reasons), it was decided to lower the valve "click-rate" by a factor of two (which does not change the flow rate). At the end of 1992 February, Tank A was empty and the gas supply was switched to Tank C was started. Since PSPC-B appeared to well-behaved, the flow rate was switched back during 1992 mid-March to 4 $\mathrm{cm}^{-3}\ \mathrm{min}^{-1}$, where it remained until the flow rate reduction made at the start of AO-4.

The PSPC gas flow rate was reduced on 1992 June 10, the same day that the HRI was moved into the focal position. This allowed the PSPC until June 15 (the beginning of AO-4) to reach equilibrium at the new flow rate. The flow rate was reduced from 3.8 to 2.5 $\mathrm{cm}^{-3}\ \mathrm{min}^{-1}$, *i.e.,* by about 35%, on 1993 June 10.

3.2.5 The PSPC Electronics

The PSPC electronics were developed, tested, and calibrated at MPE. They are described by Metzner 1986 (see Appendix C: SUMMARY OF *ROSAT* MEMOS).

3.3 The Quantum Efficiency of the PSPCs

The Quantum Efficiency of PSPC-B (the curve for PSPC-C would be nearly identical) as a function of energy is shown in Figure 3.5. The curve includes the window transmission, average transmission of the window support mesh (79%), and the absorption of the counter gas. The window becomes almost completely transparent by 2 keV, where the counter gas becomes no longer optically thick. The X-ray absorption of the counter gas is close to 100% in the 0.1–2.0 keV band. The fall-off at $\sim$ 2 keV occurs where the effective area of the X-ray mirrors also cuts off (see Figure 2.5).

3.3.1 PSPC Entrance Windows

Window Support Structure

The thin plastic entrance window of the PSPC requires additional support to withstand pressure of the counter gas against vacuum. A schematic view of the support structure is shown in Figure 3.6. It consists of a rigid circle (28 mm diameter) with eight equally spaced radial struts. On a smaller scale than this "wagon wheel" structure are two mesh systems: the coarse mesh of 100 μm tungsten wires with 2 mm (171.8$''$) spacing, and a fine mesh with 25 μm tungsten with 0.4 mm (34.4$''$) spacing.

The ribs and both meshes are completely opaque to X-rays in the *ROSAT* energy band. Excluding those areas within the shadow of the ribs, the average energy independent transmission of the window support structure (*i.e.,* the mesh) is 79%. It should be noted that this average transmission is obtained only over a sufficiently large area ($\sim 3' \times 3'$) to average over the mesh spacing; over smaller areas, the transmission due to the window support structure may be different depending on how much of the area of the X-ray beam is actually occulted by the mesh grid wires.

In the vicinity of the centre of the *fov*, the point response for a point source is so sharp (and hence the illuminated area on the PSPC entrance window so small) that significant shadowing behind the coarse mesh can occur. Therefore, a slow spacecraft "wobble" is performed in pointed observations in a direction diagonal to the mesh structure (see Section 1.3.3). In this fashion, the coarse mesh grid will be smoothed out when projected into sky coordinates and the permanent occultation of X-ray sources behind the coarse wire mesh is not possible. As the average transmission loss caused by the wires is known, this wobble prevents significant uncertainties in source flux. However, the periodic obscuration of sources by the wires will create artificial temporal variations in

Table 3.1: Derived composition of the PSPC windows (from Schmitt & Snowden 1990)

PSPC	PPL μg cm^{-2}	Lexan μg cm^{-2}	Carbon μg cm^{-2}	Oxygen μg cm^{-2}	χ^2
A	90.94	34.03	52.50	5.07	34.2
B	91.70	35.67	54.17	5.25	9.9
C	94.36	32.42	51.74	5.60	10.4
D	94.77	38.58	57.14	4.38	2.9

source light curves of order tens of seconds to minutes.

The X-ray Transmission of the Entrance Windows

The PSPC entrance window consists of a $\simeq 1\mu$m foil of polypropylene ($[C_3H_6]n$) coated with $\simeq$ 50 μg cm^{-2} graphite (for electrical conductivity to prevent charge buildup on the window which would affect the electron drift velocity; the graphite has impurities of ~8% oxygen) and $\simeq$ 40 μg cm^{-2} lexan ($[C_{16}H_{14}O_3]n$, to decrease UV transmission).

The ground calibration results from measurements of the X-ray transmission of each of the 4 PSPCs is given in Schmitt & Snowden (1990). Note, the only detectors actually flown were: PSPC-C (which was in use prior its destruction during the accidental *ROSAT* Sun-slew on 1991 January 25), and PSPC-B. The available (PANTER) ground calibration measurements consist of window-average transmission values at 0.183, 0.277, 0.525, and 0.93 keV for each detector (corresponding to boron, carbon, oxygen, and copper fluorescent X-ray sources, respectively). In addition there are measurements of the total surface mass density, and that of polypropylene & lexan, and lexan only. The difficulties and analysis method used to disentangle the contributions from the various components (especially in view of the large carbon content in each) are described in detail in Schmitt & Snowden (1990).

In Figure 3.7, the calculated best-fit transmission curves are shown for each window (assuming the atomic cross-sections of Henke *et al.* 1982) along with the measured data points. ¿From the results summarized in Table 3.1, it can be seen that the fits are formally acceptable for all but the window of PSPC-A. The bad fit for the PSPC-A window, the apparently systematically low 0.183 keV data (see Figure 3.7), and the oxygen contamination of the graphite are all further discussed in Schmitt & Snowden (1990). For convenience, the calculated transmissions at each energy for which there are PANTER data are listed in Table 3.2. It should be noted that these values do **NOT** include any corrections for shadowing by the window support grid or gas absorption-efficiency.

The modelled window transmission for PSPC-B (the window transmission for

Table 3.2: Calculated transmissions of the PSPC windows (from Schmitt & Snowden 1990)

Energy keV	PSPC-A	PSPC-B	PSPC-C	PSPC-D
0.183	0.300	0.290	0.296	0.278
0.277	0.642	0.636	0.640	0.624
0.525	0.143	0.137	0.141	0.124
0.930	0.613	0.606	0.611	0.594
1.487	0.878	0.875	0.877	0.870

PSPC-C in nearly identical) is shown again in Figure 3.8. It can be seen that the transmission is essentially zero at energies just above the carbon edge at 0.284 keV, and approximately 50% at energies just below the edge.

The UV Transmission of the PSPC Window and the UV Quantum Efficiency of the PSPC

Thin foils such as the PSPC entrance window can be UV transmitting despite a lexan coating; the UV transmission is concentrated in a relatively small spectral range around 1700 Å (~7 eV) where the mass absorption coefficient of polypropylene has a local minimum. During the *ROSAT* calibration phase, the A-type stars β Leo and β Car were observed for approx. 2000 s each and not detected.

3.3.2 The PSPC Filter Wheel

The Four Positions

A filter wheel with four positions is mounted in front of the detector. The open and closed filter wheel positions are used for "standard" observations and for monitoring the particle background. The third position contains a Boron filter, the insertion of which allows an increase of spectral resolution at low energies. The PSPC filter wheel carries three calibration sources in the fourth position, which produce aluminium (1.49 keV) fluorescent K-shell photons by X-ray excitation from Fe-55. These X-rays are used to illuminate the PSPCs in order to measure in-orbit temporal variations in the PSPC gain (see Section 3.4.1).

The Boron Filter

(see Stephan *et al.* 1991)

The spectral resolution of the PSPC in the carbon window below 0.28 keV is ~80% (FWHM). A further subdivision of the carbon band into two bands is possible since the boron filter has little transmission between 0.188 keV and 0.28 keV. The boron filter itself consists of a carbon film with a coating of boron carbide. The whole structure is supported by a tungsten wire mesh with a thickness of 20 μm and spacing of 4 mm. The filter itself has a diameter of 28 mm ($40'$), hence only the central portion of the PSPC f.o.v is covered. The rest of the PSPC *fov* is open. The transmission of the boron filter as a function of energy is shown in Figure 3.9.

3.4 The Spectral Capability of the PSPC

The energy resolution of the PSPC approaches that of a single wire proportional counter, *i.e.,* $\Delta E/E = 0.43(E/0.93)^{-0.5}$ (FWHM) over the entire sensitive area of the detector. The spectral resolution measured with the on-board calibration source is 27% FWHM at 1.5 keV.

3.4.1 PSPC Gain

The gain of the PSPC describes the relationship between the energy of the detected X-ray photon and the pulse height produced in the electronics (pulse-shaping, peak-detector, ADC, *etc.*) connected to the anode (Figure 3.1). For a perfect PSPC, the relationship is determined only by the electrical potential between the cathode and the anode and by the counter gas composition and density. In reality, there are spatial variations across the face of the detector as well as temporal variations.

The *ROSAT* PSPC gain has had two significant changes. First, the gain was lowered by $\sim$ 30% on 1991 October 11, when the high voltage was changed from 3060 to 3000 volts (one of several measures taken to reduce some detector hotspot problems and low pulse-height contamination). Second, the gas flow rate was changed on 1993 June 10, at which point the mean of the Al K_α line dropped from channel 103 to 100.

Method of Determination

Illuminating the PSPC with a monochromatic X-ray source, the resultant pulse height distribution can in general be described by a polya function (although there are systematic differences at lower energies, Jahoda and McCammon 1988). Measurements in the lab, covering the energy band 0.1–2.0 keV result in a specific relationship between the pulse height channel K and the X-ray energy E at a certain position and given detector parameters. ¿From this information, the photon redistribution matrix is derived.

Spatial Variations

The two main sources of spatial variations in the gain of PSPCs are:

- mechanical inaccuracies of the grid system leading to different electrical field strengths and hence different gains
- the anode wire grid causing a "binning", with a period of the wire distance.

(Both effects also give rise to a nonlinearity in the position measurement, see also Chapter 3.5.3).

During ground calibrations, the spatial gain variations were measured by illuminating a slit mask which replaced the PSPC entrance window. Two slit-mask geometries were used: perpendicular and parallel to the anode wires. It was found that perpendicular to the direction of anode A1, the variation is about ±5%, whereas parallel to A1, there is virtually no spatial gain variation ($< \pm 2\%$). The magnitude of this effect is a function of the depth within the counter where the photon is absorbed, and therefore of energy (Figure 3.10). These measurements were used to construct correction tables to be used for each individual event. (A description of these measurements can be found in Briel *et al.* 1988). After correction, tests with an illuminated pinhole mask across the surface of the PSPC revealed a residual gas gain variation of less than 1%, which was consistent with the statistical uncertainty in the mean of the pinhole pulse-height spectra. After correction, the pulse-height distribution of a cosmic X-ray source is therefore essentially independent of where within the detector the X-rays were absorbed.

In SASS, this correction is performed by the subroutine DCORG. This correction removes the above described gain variations. Since the nonlinearities are perpendicular to the anode wire direction, this correction depends on the X coordinate. The correction is parameterized in terms of X_1, the electronically corrected coordinate system.

$$A_4 = A_3/(LF(X_1) + HA(A_3) \times HF(X_1)) \tag{3.1}$$

where A_3 are intermediate-processing channels where PHA channels have been corrected for ADC nonlinearities, gain-saturation, and temporal variations and A_4 are the PI channels which appear in the events file, and the spatial corrections LF and HF are read from an 800 element vector under (SASS)
`P$MANPAR:gain_kor3_c.dat` and `gain_kor3_b.dat`
while HA is a 256 vector read from
`P$MANPAR:gnampl_new.dat`.
The 800 element spatial correction is averaged every 10 detector bins (rounding down) and the spectral vector correction for channels > 256, is set to that for channel 256.

ADC nonlinearities

The analog-to-digital converter (ADC) shows nonlinearities in bin width of $< 3\%$ per channel (although on average they are linear). The effective channel width has been calibrated by performing a spline fit to a cumulative spectrum of all ground calibration data accumulated by $\sim$ 1990 March ($\sim 10^6$ events,

Figure 3.11) and subtracting a smooth spline function (see Figure 3.12). The nonlinearity is corrected by drawing a random real number, RAN (between 0 and 1.0), within the non-equidistant channel

$$A_1 = BE(A_i) + RAN \times BW(A_i) \tag{3.2}$$

where A_i & A_1 are the measured (integer) & corrected (real) pulse height bins, and BE & BW arrays containing the (lower) edge and width of the 256 non-equidistant channels respectively (see also Chapter 8).

Gain Saturation

At large charge input, the PSPC shows some saturation of the gain (*i.e.,* a fall-off in the signal amplification). This is a reasonably minor effect ($\sim 0\%$ below 1 keV, $\sim 10\%$ at 2 keV) and has been modelled using the spectral calibration data. The gain saturation correction was determined using the same data used to create the detector response matrix. An analytic relationship was determined between the mean of the fits to the calibration data and the true gain. (Since the Al $K\alpha$ calibration line is at 1487 eV, it too is affected by the gain saturation.) In the SASS processing, first the channel at which gain saturation becomes significant is estimated based on the mean channel of the Al K_α line. Then, the gain correction is calculated based on the empirical relationship between gain and calibration line channel. This gain correction is later used to make the temporal correction for the entire PSPC channel range. For details of the algorithm and SASS calibration files used see Chapter 8. The nominal gain is assumed to bring the Al K_α line into channel ~ 151. The gain saturation correction is shown in Figure 3.13 for a range in nominal gains.

Temporal Gain Correction

(*Source:* Hasinger & Snowden 1990)

The detector gain (*i.e.,* pulse height as a function of energy) changes slowly due to variations in the gas density, composition, high voltage, pressure, and temperature. The temporal gain variation is corrected by normalizing the event pulse height by a function of the temporal gain $G(t)$ (see Chapter 8).

In-orbit, temporal variations in the PSPC gain are monitored using the an X-ray calibration line (at 1.49 keV) provided by the Al K_α source on the PSPC filter wheel (Section 3.3.2).

The actual frequency of the gain calibration measurements, (each taking $\sim$ 5 minutes) depends on the mission phase but calibrations are performed at least once per weak. There are small temporal gain variations of less than 1% within each orbit. Investigations of these variations are under way, the results will be added to the hand-book when they are available.

The effect of the temporal gain correction (applied on top of the gain saturation correction) is demonstrated in Figure 3.14 for a range of nominal gains. The channel offset is the rough number (position gain corrections are not considered here) of channels added to the PHA channel to produce the PI channel.

3.4.2 Detector Response Matrices

(*Source:* Jane Turner, 1992 November 16, update 1993 August)

What follows are some notes on the PSPC-related aspects of the two most recent (and the only commonly used) post-launch matrices, those released on 1992 March 11 and 1993 January 12.

92mar11 Matrix

For this post-launch matrix, a number of sources showed residual carbon absorption features which probably are an artifact of the calibration available at that time (see Figure 3.16). After attempts at recalibration and after some alterations in detector operational parameters, it was decided that this matrix is currently the most appropriate to use for data taken before 1991 October 11 (S/C clock 42910000).

This corresponds to the following matrices:

In PROS: `xspectraldata$dtmat_6.ieee` combined with either `offar2_5.ieee` for `PSPC-B`, or `offar1_5.ieee` for `PSPC-C`.

In EXSAS: `exsas_cal:drmpspc_ao1` combined with either `exsas_cal:effarea_pspcb` or `exsas_cal:effarea_pspcc`

IN ASTERIX: `/star/asterix/data/rosat/drmpspc.sdf` combined with `/star/asterix/data/rosat/pspcc_eff.sdf`

93jan12 Matrix

This matrix was the result of a recalibration based strongly on the bright source Mkn421. This source was chosen because of the belief that its spectrum is, to a first approximation, featureless. While this choice can justifiably be criticised, there are no perfect soft X-ray spectral calibration targets, and very few that can be considered good. Subsequent to the analysis done to produce this matrix, it was found that there might be an additional source of error in using the Mkn421 data. There is a suggestion that the data were possibly affected by the rate-gain effect (see Section 3.2.2), even though the count rate was only ~ 150 counts s^{-1} and the source is relatively soft. The production of this matrix was made as a temporary solution until the engineering model PSPC could undergo additional ground calibration tests in the PANTER facility. This matrix is thought to be the best available for data taken after 1991 October 11.

This corresponds to the following matrices:

In PROS: `xspectraldata$dtmat_36.ieee`, combined with `offar2_6.ieee` for `PSPC-B` (no longer relevant for PSPC-C data).

In EXSAS: `exsas_cal:drmpspc` combined with `exsas_cal:effarea_pspcb`

IN ASTERIX: `/star/asterix/data/rosat/drmpspc.sdf` combined with `/star/asterix/data/rosat/pspcb_eff.sdf`

Notes on the Spectral Response Matrices

PROS stores the photon redistribution files and effective area files (and filter information) separately, while XSPEC uses a file which is a convolution of these. PROS uses a 34 channel matrix. XSPEC uses a 256 channel matrix but it should be noted that 256 PI channels were not originally intended for use during scientific analysis, rather it was always intended that these raw channels be binned so that known remaining digitization effects could be reduced. There appear to be two subtly different philosophies regarding the correct procedure for this rebinning:

After excluding "bad" channels, the 256 channel data should be either:

1. binned such that each new bin contains the same oversampling of the spectral resolution. This is to prevent dramatically different oversampling factors at various energies skewing the spectral fit. The SASS channels were selected to provide this, but a number of people suggest 19 channels are (statistically) the most appropriate number. Thus rebinning the SASS channels by a factor of two is close.

   The advantage of using the 256 channel spectra and not the 34 SASS channels is the ability to ignore only the raw bad channels without loosing any good data, the 34 channel spectrum is pre-binned such that some good data can be within a channel also containing bad data.

2. binned such that there are sufficient counts in each new bin so that χ^2 analysis can be used (if desired), *i.e.,* group to a minimum of 20 counts per channel.

It should be noted that the skewing of the spectral analysis is only likely to be significant for high S/N data from very steep (or absorbed, flat) sources. The best recipe may therefore be to use a combination of both methods.

While the PROS xspectraldata area contains other matrices, these are not recommended for use. Dtmat.ieee was an early (pre-launch) matrix and `dtmat_5.ieee` was the first post-launch matrix, both are non-detector specific and use `offar.ieee` as the effective area file.

As of 1993 July, it is recommended that a 2% systematic error per channel be used for spectral analysis (until the calibration can be improved). Alternatively, use both matrices to see what the effect on the spectral fitting is.

For PROS users:

The correspondence between the PROS 34-channel spectra and PI bins is listed in Table 3.3. The PI bins, 256 channels, are 10 eV wide, with the low energy given by $E_{low} \sim N_{chan} \times 10.0$ eV (by the inherent nature of proportional counters, this is not an exact relation and should only be considered in a statistical sense). The lower level discriminator is set in ADC channel 7, for the observations before 1991 October, and ADC channel 10-11 for those thereafter. To be conservative, in the 256 channel scheme, for data taken before 1991 October 14 channels 1-8 and channels above $\sim$ 200 should be ignored. For data taken since 1991 October 14 channels 1-10 and channels above $\sim$ 200 should be ignored.

The upper limit is a loose one, as the effective area calibration gets gradually worse between 2 -2.5 keV. We do not recommend using data above $\sim$ 2.2 keV at this time. The counts detected in channels 260-370 are due almost entirely to the particle background. PROS will display these events, by specifying the desired range in PI channels.

MPE Notes on the Creation of the 1993 January Matrix

(*Source:* Hasinger & Snowden Note placed in MPE public area on 1992 November 25)

Every event is transformed through a long chain of correction procedures from the raw telemetry to calibrated time, position, and amplitude. In particular, the data are corrected for: 1) ADC nonlinearity, 2) gain saturation, 3) temporal gain variations, 4) small-scale electronic position variations, 5) spatial gain variations, and 6) large scale window-position variations (see Chapter 8). The detector response matrix contains our best current knowledge of the mirror effective areas, the composition of the PSPC entrance window, and a physical model of the characteristics of the counter gas and the proportional counter energy resolution properties.

Nevertheless, there are residual systematic uncertainties at the few percent level in almost every element of the above chain. It is also possible that other (unknown) systematic effects have not been included at all. Most of the detailed information originates from extended ground calibrations with monochromatic lines at nominal gain; important elements were also derived or verified in orbit. Small systematic features in the residuals of PSPC spectral fits have been a well-known problem for some time now, in particular for high signal-to-noise ratio sources. Due in part to the relatively poor energy resolution of proportional counters, the various possible reasons for such effects are exceedingly difficult to disentangle. One of the major problems in determining a final in-flight calibration is that there exists no bona fide continuum calibration source that has a well defined spectrum in the 0.1–2 keV range, and is suitable for the PSPC (similar to the Crab Nebula for higher energy X-rays). A sample of bright source spectra of various types has therefore been collected for a better diagnosis.

To date, the pointed observation of the bright BL Lac object MKN421 (SEQ Nr. WP700513, PI Thomas, exposure time 33000 s, taken in low-gain mode in 1992 May 4−7) comes the closest to the ideal of an in-orbit calibration source. MKN421 has a relatively small galactic $N_{\rm H}$ value of 1.61×10^{20} H I cm^{-2}, as re-measured recently by J. Lockman (1992, private communication), which turned out to be slightly higher than the value of 1.45×10^{20} H I cm^{-2} published by Elvis, Lockman, & Wilkes (1989). In the *ROSAT* all-sky survey, MKN421 was variable and had a count rate of 18–28 counts s^{-1}, but with an apparently constant spectral shape (Fink *et al.* 1991). *Ginga* data were taken simultaneously with the *ROSAT* all-sky survey. A combined spectral fit to the *ROSAT* /Ginga data shows very good agreement between the two instruments in the overlapping energy range (1.5–2.4 keV), albeit with relatively poor statistical

Table 3.3: Relationship between the 34 SASS and PI spectral channels

SASS channel	Low Energy (keV)	High Energy (keV)	PI Channels (inclusive)	Channels Recommended For Spectral Fitting
1	0.07	0.09	7+8	not to be used in any fit
2	0.09	0.11	9+10	
3	0.11	0.14	11–13	start here after 1991 October 11
4	0.14	0.17	14–16	
5	0.17	0.20	17–19	
6	0.20	0.24	20–23	
7	0.24	0.28	24–27	
8	0.28	0.32	28–31	
9	0.32	0.37	32–36	
10	0.37	0.42	37–41	
11	0.42	0.47	42–46	
12	0.47	0.52	47–51	
13	0.52	0.58	52–57	
14	0.58	0.64	58–63	
15	0.64	0.70	64–69	
16	0.70	0.77	70–76	
17	0.77	0.84	77–83	
18	0.84	0.91	84–90	
19	0.91	0.99	91–98	
20	0.99	1.07	99–106	
21	1.07	1.15	107–114	
22	1.15	1.23	115–122	
23	1.23	1.32	123–131	
24	1.32	1.41	132–140	
25	1.41	1.50	141–149	
26	1.50	1.60	150–159	
27	1.60	1.70	160–169	
28	1.70	1.80	170–179	
29	1.80	1.91	180–190	
30	1.91	2.02	191–201	
31	2.02	2.13	202–212	Insufficient calibration of eff. area and energy response at energies above 2 keV
32	2.13	2.24	213–223	
33	2.24	2.36	224–235	
34	2.36	2.48	236–247	

quality (Fink 1992). The 0.1–10 keV spectrum can be well fit with a slowly curving power law spectrum with a photon index of about 2.45 at low energies and an index of 2.82 at high energies. Such a convex spectral shape is predicted by inhomogeneous synchrotron models which are fashionable for BL Lac jets. The oxygen absorption trough feature which was reported from Einstein OGS data of PKS 2155-304, another bright BL Lac object, would have too small an equivalent width to be observed with the PSPC, if it were present in MKN421 at the same strength. During the pointed observation, the source was almost a factor of 10 brighter so that a total of 5 million photons were accumulated for a very high statistical significance spectrum in the 0.1–3 keV range.

We first used this spectrum to better define the residual systematic features in the 92mar11 response matrix We fixed the $N_{\rm H}$ at the above value and fit a broken power law (BPL) in the energy range 0.2–1.8 keV (power-law indices and break point were allowed to vary). Table 3.4 gives the fractional residuals over the full energy range (0.1–3 keV) defined as: Res = (Data-Model)/Data, Channel 151 = 1.49 keV.

There are three major obvious deviations:

1. a model deficiency in the range 0.1–0.2 keV. At 0.1 keV this amounts to about 30%, above 0.2 keV this effect has gone away.
2. a systematic model excess in the window absorption trough above the carbon edge, reaching a maximum of -11% at about (ca. 0.4 keV).
3. a model deficiency above 1.8 keV. At the nominally highest PSPC photon energy of 2.5 keV, this amounts to 25%. However, with the low-gain data it is possible to reach energies of 3 keV, where the excess is about 40%.

In addition, there is a small (±4%) ripple in the energy channels 69 and 70. This effect, only apparent in extremely high signal to noise spectra, is due to a sharp feature in the PSPC position dependent gain correction at the Xe-M edge at 672 eV. A similar feature is expected at the Ar-L edge at 245 eV, but is not easily visible due to the steep falloff of pulse-height spectra in this energy range. A change has been made to the PSPC correction procedure which avoids these artifacts for SASS Rev1 processing. The MKN421 data were reprocessed using this improvement.

The next step was an iterative procedure to minimize these residuals with various trials to change the physical parameters of the proportional counter model (*i.e.,* width parameters, the energy width of the discontinuities at the edges of the counter gas, the amount of electrons lost by drifting back to the window, *etc.*) within reasonable limits allowed by the ground calibration results and in-flight data. These changes gave a substantial improvement of effect (2) around 0.4 keV, from -11% to -4.5%, suggesting that the previously relatively large residuals in this energy range may be due to systematic errors in the ground calibration of the physical counter model parameters. However, the details of the carbon absorption edge in the PSPC window transmission may also have some effect.

This didn't change the shape and magnitude of the residuals at low and high energies. For each of the effects (1) and (3), there are at least two different physical explanations for which we lack calibration data to address at this point. Naturally, combinations each of the effects below could be, and probably are, responsible for the residuals:

1. a) The excess at low energies could be due to a few % smaller value for the window thickness compared to the preflight calibration. In this case the net effective area at lower energies would be larger than expected. Indeed, some of the detailed studies done on calibration data of the white dwarf HZ 43 point in this direction (Fleming, private communication). The window thickness calibration is based on measurements averaged over the entire window at only four energies, the lowest of which was 0.18 keV. The transmission of the window at 0.1 keV is therefore not well constrained.
   b) A similar effect could be produced by an offset of 3-5 eV (less than half a channel) in the pulse height versus energy relation at low energies, which could be produced by the on-board electronics (ADC, pulse shaper, peak detector, etc.). There is no information about this offset from the flight-model calibration. The fact that most pulse height spectra rise very steeply in the energy range 0.1-0.15 keV exaggerates any such uncertainty by a large factor.

2. a) The excess at high energies could be due to a larger mirror reflectivity above the Au-M edge at 2 keV compared to the theoretical predictions. Indeed there are at least two incompatible models for the optical constants of gold in the energy range 2-3 keV.
   b) A similar effect could be again due to an uncertainty in the gain (channel versus energy) curve. The effect of gain saturation has only been reasonably measured at the nominal gain and above, and then only reliably up to 1.7 keV. A gain saturation effect which is less severe than extrapolated (by about 2-3% in absolute channels, or about 10% of the predicted gain saturation effect) could easily explain the findings. Again, because of the steep decrease of all spectra in this energy range, the effect in the residuals is amplified by a large factor.

Since we have no further calibration information at this time which would allow us to distinguish between these different possibilities and to refine our physical understanding of the situation, we took the brutal and somewhat distasteful approach of simply fudging the response matrix values with the residuals to the Mkn421 fit, *i.e.,* multiply every entry in the matrix with the factor (Figure 3.16):

$$FUDGE = Model/Data. \tag{3.3}$$

The response matrix created this way, 93jan12, has been tested on our sample of bright sources. In general the fits achieved were better (note: later tests showed the 92mar11 matric to be better for data collected during high-gain-state observations). For more details see Table 3.5.

The improvement in the fit to the low-gain spectrum of HZ 43 was particularly spectacular. While the fit with the previous matrix had very severe discrepancies at low energies, an acceptable Chi-square was obtained by fixing all shape parameters (temperature, gravity) to the best currently available multiwavelength model (Fleming, private communication) and only allowing the normalization to vary. Such a good fit could unfortunately not be achieved for the high-gain spectrum of HZ 43, indicating a residual gain-dependent shape of the response curve. (See also Mapiwotzki *et al.* 1993, who require a factor 1.77 to fit the amplitude of the HZ 43 spectrum.)

Using the 93jan12 matrix, the Crab Nebula data appear to be systematically shifted to a lower energy, compared to the model (also true using the 92mar11 matrix). Indeed, after reprocessing the Crab data with a 5% lower gain, we achieved an almost perfect fit to the Crab data in the energy range 0.4-2 keV. The most straightforward explanation for the discrepancy is a rate-dependent gain effect in the PSPC. While for most observations this should have no effect, it is unfortunately significant for bright and hard calibration targets (like the Crab). Ground re-calibrations showed that the rate-gain saturation effect is to small to account for the observed gain shift in the Crab spectrum (see also Section 3.2.2).

In the course of our matrix optimization attempts we have identified a number of uncertainties or lack of knowledge about the following calibration items:

- (a) ADC offset
- (b) window thickness
- (c) shape of the window transmission near the carbon edge
- (d) actual energy of the window carbon edge
- (e) Gold reflectivity above 2 keV
- (f) gain saturation at high energies and low gain
- (g) shape of the low-energy response function at low gain
- (h) rate-gain effect

While for (a) and (b) we cannot obtain further calibration data for the flight models, the effects (c)-(h) are relatively independent of the specific counter and therefore can be re-calibrated on ground using the engineering model PSPC. (a) can also be studied using the engineering model in order to obtain information about the possible magnitude of this effect. We have therefore planned a number of additional ground calibration tests with the engineering model of the PSPC, partially at the PANTER facility and partially in a synchrotron laboratory. Data were collected at the PANTER facility in early 1994 but have not yet been collected at synchrotron facility. We do not anticipate a new response matrix for some time.

While we have always attempted to improve our knowledge of the PSPC performance and to push down the uncertainties as far as possible, we advise *ROSAT*

Table 3.4: Spline fit to the fractional residuals of MKN421

Channel	Matrix		Channel	Matrix	
	92mar11	93jan12		92mar11	93jan12
10	0.245	0.306	100	-0.000	0.000
12	0.164	0.187	110	-0.011	-0.013
14	0.107	0.103	120	-0.000	-0.043
16	0.071	0.049	130	0.007	0.004
18	0.052	0.019	140	0.003	0.005
20	0.043	0.006	150	-0.002	0.003
25	0.038	0.014	160	-0.002	0.004
30	-0.002	0.007	170	0.002	0.006
35	-0.078	-0.034	180	0.011	0.014
40	-0.111	-0.045	190	0.033	0.034
45	-0.071	-0.016	200	0.060	0.059
50	-0.014	0.008	210	0.089	0.088
55	-0.002	-0.005	220	0.123	0.120
60	0.018	0.003	230	0.161	0.155
65	0.033	0.017	240	0.203	0.192
70	0.028	0.013	250	0.246	0.228
75	0.019	0.007	260	0.288	0.261
80	0.009	0.001	270	0.328	0.289
85	0.002	-0.002	280	0.362	0.311
90	0.002	0.000	290	0.390	0.323
95	0.003	0.003	300	0.410	0.324

Using a broken power law with N_{H} fixed to 1.61×10^{20} cm^{-2}
final fit: Slope_1: 2.06 Break 0.77 keV Slope_2: 2.61

observers to include systematic errors of about 2 percent (in quadrature) in their PSPC spectral fits and to be cautious about the interpretation of narrow spectral features, particularly those of small equivalent width as well as possible high-energy excesses. It is also strongly recommended to rebin the spectra into no more than the 34 energy bins defined by SASS (see the *ROSAT* data products guide).

Caveat Emptor: While we freely admit that the fudged matrix being released is not the best solution to the problem of the residual systematics in spectral fits, it is the only possibility available to us at this time. The present release is intended only as an intermediate update until more calibration data have been collected and analyzed. We have certainly noted the overwhelming desire for a "better" calibration of the XRT/PSPC, we ourselves certainly share this concern.

Table 3.5: Tests of 93jan12 on a variety of different sources

Source Name	Type	Courtesy	Type of Fit, Remarks
MKN421	BL Lac	Thomas	BPL, gal.NH, used to fudge DRM_31
PKS 2155-304	BL Lac	Brinkmann,Comastri	BPL, gal.NH, good fit, no features
H1426+42	BL Lac	George	BPL, gal.NH, good fit, no features
Sum of RMSS	QSOs	Hasinger, Comastri	PL, no features >0.2 (NH ambiguous)
MKN766	Sy1	Molendi, Comastri	PL+BB, no features, gal. NH
Chi Per	Be-HMXB	Haberl	PL, highly absorbed, good fit
?	OB bin	Haberl	RS+RS, good fit
HZ 43	WD	Fleming	WD-model, 1 parameter, good fit
Crab	SNR		PL, 1 parameter, 5% lower gain

3.4.3 Afterpulses

Due to contamination of the gas supply, a number of observational data sets are effected by "After Pulses" (APs). These are low pulse-height events (PHA channels less than ~ 15) associated with both X-ray photons or particle background events, and occur within approximately 0.35 ms of the primary event (the nominal deadtime for a PSPC event is ~ 0.25 ms). The most likely cause of APs is negative ion formation in the vicinity of the anodes. They have a soft, steep spectrum effecting only PHA channels 15 and below, in which they can contribute up to a few % of the total count rate. The spectrum changes slightly as a function of time, but is similar to a single electron spectrum. The number of AP events also changes as a function of time and this along with its correlation to the PSPC gas tank swaps and other variables is currently under investigation.

Figure 3.4 shows (bottom panel) the effect of the afterpulses on spectra. In this case the crab data have been corrected manually for the rate-gain effect before fitting with a power-law spectrum.

While AP events associated with photons can be rejected (eliminate all events occurring within 0.35 ms of the preceeding event; note that this produces an additional deadtime component which must be included), those associated with particle background events cannot, since the precursor event is almost always vetoed by the on-board S/W and hence not included in the telemetry stream. The number of APs appears to be: - worse for high gain datasets, and - worse for harder spectra

AP events are not always adequately taken into account using standard background subtraction techniques, and the effect can be quite significant for extended sources (see Snowden *et al.* 1994a).

3.4.4 Spectral Recalibration Plans

MPE has used the PANTER facility to perform a number of recalibration experiments of the PSPC using the engineering model. Data have been collected to examine both the rate-gain effect and the residual systematics in the spectral calibration, *i.e.,* at/over:

1. high count rates to examine the rate-gain effect,
2. four gain states in order to investigate the amplitude and systematics of all gain-dependent effects,
3. an energy range extended from the original pre-launch calibrations to better determine energy dependent effects.

3.5 The Positional Capability of the PSPC

3.5.1 Method of Position Determination

The position of an event in the PSPC is determined from the amplitudes of signals on the two mutually perpendicular cathode grids, K1 and K2 (Figure 3.1). The cathode grids are divided into 25 (for cathode K1) and 23 (for cathode K2) cathode strips. Each strip consists of seven or eight individual cathode wires linked together and connected to a charge-sensitive preamplifier. Typically an event will induce a signal on 3 to 5 strips, although this is not the case for events with pulse heights corresponding to $\lesssim 0.15$ keV (see Section 3.5.4). The signals from each preamplifier processed and have their signals digitized by means of pulse shapers, peak detectors, and analog-to-digital converters (ADCs). After verifying the validity of an event, the position is calculated by a centre-of-gravity calculation and assigned an $X_{DET}^{raw}, Y_{DET}^{raw}$ position. (A detailed description of the method of position determination and its ground calibration measurements can be found in Briel *et al.* 1988).

3.5.2 PSPC Spatial Resolution

(*Source:* Günter Hasinger, 1991 December 16)

The *psf* of the *ROSAT* PSPC (alone) can be divided into 3 components:

1. The effect of the finite penetration of photons into the counter
2. The intrinsic spatial resolution of the counter
3. The existence of "Ghost Images" (see Section 3.5.4).

The detailed *psf* parameters and their associated dependences on energy have been determined for the XMA, PSPC-B, and PSPC-C using 4 monochromatic energies (0.28, 0.93, 1.49 & 1.70 keV) at the PANTER facility in Garching. Specifically, the components of the *psf* due to the intrinsic spatial resolution of the PSPC, and the effects due to the finite penetration of photons into the counter were treated independently. The resultant predicted *psf* curves have been compared to a number of PVC and AO-1 datasets in Hasinger *et al.* 1992 (see also Section 4.1).

Focus and Penetration Effects

The design distance between the XMA and PSPC is such that ~ 1 keV photons of an on-axis source are brought to a focus (along a surface of a cone of half-angle 8.5°) at an optimum depth within the PSPC drift region, such that the Gaussian spatial distribution of pulses on the cathode wires is minimized. Consequently the image of a point source is sharpest at 1 keV.

The combined contribution of focussing and the finite penetration of photons into the counter on the *psf* can be modelled as an exponential function where r is the radial distance from the centroid position of the radial profile, in arc minutes.

The e-folding angle, r_τ, was found to be

$$r_\tau(E) = \frac{1}{60}\ (50.61E^{-1.472} + 6.80E^{+5.62})^{1/2}\ \text{arcmin.} \tag{3.4}$$

The Intrinsic Resolution of the PSPC

Preflight PANTER calibration tests confirmed that this component is well approximated by a Gaussian, as expected from the statistics of the primary electron generation process, *i.e.,*

$$PSF_{int}(E,r) = A_{int}(E)\ \exp\left(-\frac{1}{2}(\frac{r}{r_\sigma(E)})^2\right)\ \text{normalized counts arcmin}^{-2} \tag{3.5}$$

The derived analytical form for the width of the gaussian, $r_\sigma(E)$, as a function of energy is given by:

$$r_\sigma(E) = 1/60\ \left(108.7E^{-0.888} + 1.121E^{+6}\right)^{1/2}\ \text{arcmin} \tag{3.6}$$

3.5.3 The Linearization of the Event Positions

(*Source:* Hasinger 1986,1990)

The (raw) PSPC readout system ($X^{raw}_{DET}, Y^{raw}_{DET}$)

(*Source:* Hasinger 1986,1990)

As described in Section 3.5.1, a valid event is assigned to the position $X^{raw}_{DET}, Y^{raw}_{DET}$. The following corrections are performed on the raw detector coordinates ($X^{raw}_{DET}, Y^{raw}_{DET}$) of individual events to produce linearized detector coordinates (X_{DET}, Y_{DET}):

1. The electronic position correction
2. The window correction

Small Scale Non-Linearity (Electronic Position Correction)

(*Source:* Hasinger & Snowden 1990)

The electronic correction removes the small-scale nonlinearities induced by the PSPC wires. This correction is independent of $X_{DET}^{raw}, Y_{DET}^{raw}$, but is a function of pulse height. For every X_{DET}^{raw} or Y_{DET}^{raw} position, a correction value is calculated from the temporal-gain-corrected pulse height, A_3 (Section 3.4.1), using a parabola. The correction vector is added to the original position of the event. For equations and calibration file names see Chapter 8.

Large Scale Non-Linearity (Window Correction)

(*Source:* Hasinger & Snowden 1990)

The window correction removes the large-scale distortions due to the bulging detector window. The PSPC counter gas, at a pressure of 1.5 bar, causes a bulging in the support grids between the aluminum struts to a scale height of ~ 1.2 mm. Since the electric field lines run perpendicular to the equipotential plane (the window), and since the primary electron cloud drifts along these field lines, the position of an X-ray event can be slightly shifted towards the centre of the detector for events within the central ring of the window-support structure. For events outside of the central ring, the direction of the shift is dependent on the event location. This shifting of positions obviously introduces spatial nonlinearities. The correction (termed "golden disk") is a function of detector coordinates and energy. The amplitude of the energy dependent term is assumed to be a smooth function of penetration depth (Figure 3.15), and is normalized to 1.0 at 0.93 keV (since the shape of the golden disk was determined from measurements at this energy). For calibration file names and the equations for the coordinate correction, see Chapter 8

3.5.4 The Positional Response for Events with Small Pulse-Heights ("Ghost Images")

As described in Section 3.5.3, the position of an event in the PSPC is determined from the amplitudes of signals on the two cathode grids. The specific algorithm uses the signals from each cathode grid. For events with large pulse-height amplitudes, this works very well since the strength of the signals on the cathode segments is related to the strength of the signal on the anode. However, for events with small pulse-height amplitudes, occasionally only one cathode segment of a grid will have a signal above the lower discriminator. This still gives a well specified, but unfortunately incorrect, position. If two segments of one grid have signals but only one of the segments from the other grid has a signal, then the determined position will lie along a line. If only one segment from each grid has a signal, then the determined position will lie at a point. This structure is very apparent when looking at an image of events in detector coordinates with pulse heights less than channel 15 (~ 0.15 keV). There is a cross-work pattern of lines with bright spots at the intersections. There are secondary bright spots in the centers between the lines since the probability is greater there to get signals on four cathodes (see Section B.1.1).

3.6 The PSPC Background

(*Source:* Snowden *et al.* 1994a)

Four different components have been identified in the non-cosmic background of PSPC observations. The two best understood components are the particle background and the background caused by solar X-rays scattered into the field of view by Earth's residual atmosphere along the line of sight. The other components have been identified through their temporal variations, as observed in the *ROSAT* sky survey (Snowden & Schmitt 1990; Voges 1992; Snowden *et al.* 1994b). One consists of short term enhancements (STEs) which include auroral X-rays, the other of long term enhancements (LTEs) which are of unknown origin. STEs have a variation time scale between much less than 1 orbit (1 orbit $\sim$ 95 minutes), and $\sim$ 2 orbits. LTEs have durations of $1 - 2$ days or more but were probably present at some level during more than 80% of the sky survey (and so probably affect most pointed observations, at least in the early part of the mission, as well).

Of these various contributors to the non-cosmic background, only the particle background is completely intrinsic to the PSPC and satellite structure. The scattered solar X-ray background and in all probability the LTEs originate externally to *ROSAT* as a diffuse X-ray flux and are impossible to discriminate against in event processing. STEs are likely to have a variety of sources from auroral X-rays to enhanced particle precipitation producing X-rays from the mirror surfaces. Discrimination against these X-rays in event processing is also impossible.

3.6.1 Particle Background Reduction Method and Ground Measurements

(*Source:* Pfeffermann)

To discriminate between real X-ray events and charged particle events $-$ or charged particle induced events $-$ the following anticoincidence conditions are implemented in the PSPC and in the experiment electronics.

1. Minimum ionizing particles entering the detector deposit an energy signal $\geq$ 6 keV in the proportional counter. Since this energy is well above that of any expected X-ray, these events are vetoed by the upper energy level discriminator.

2. Spurious X-ray events, originating from the detector housing or the frames of the wire grids by particle interaction, are typically absorbed by the counter gas near the edge of the detector in a five sided anticoincidence counter system. Anode A2 is the back veto counter and senses background events originating from the central mounting plate of the PSPC, as well

as charged particles passing the whole detector system. The cathode strips on the edges of cathode 1 and 2 are broader (12.5 mm K1 and 10 mm K2) compared to the position sensing strips. Using the signals of these broader strips in anticoincidence provides side vetos in the x- and y-directions. The gas depth of the veto counters is sufficiently optically thick to stop spurious X-rays of $E \leq 2.5$ keV with an efficiency of $\geq$ 95%. For geometric reasons, the detection efficiency of the side veto in K1 is somewhat lower, resulting in a higher background at the lowest and highest Y-coordinates.

3. Events passing these veto conditions are additionally checked by the experiment electronics, using the signal pattern of the event on the cathode strips of K1 and K2. Events with more than 5 triggered cathode strips in one cathode or events showing signals in cathode strips which are not contiguous are excluded from further evaluation.

Ground tests carried out with a Co-60 source measured the background rejection efficiency of γ rays (1.17 and 1.3 MeV) to be 99.5%.

3.6.2 The Particle Background

(*Source:* Plucinsky *et al.* 1993, Snowden *et al.* 1992)

The PSPC rejection efficiency for particle events is very high, and leaves a residual count rate of only ~ 0.15 counts s^{-1}, 1×10^{-3} counts s^{-1} cm^{-2} keV^{-1} or 5×10^{-6} counts s^{-1} arcmin^{-2} keV^{-1}. About 77% of events originate in the detector while the remainder enter through the counter window. During typical conditions, the count rate of residual events is well correlated with the master veto rate. The master veto is the anticoincidence counter for the selection of accepted events.

The PSPC rejection efficiency for particle background events in the pulse-height channel range 18-249 is well described by a power-law, a flat component, and an Al K_α line at 1.5 keV. Typically, the ratio between the power-law and the flat components remains constant to ±4%, while the relative Al K_α contribution increases with increasing master veto rate. The spatial distribution of counts with pulse heights > 18 is uniform over the field of view except for a small radial gradient for the internally-produced component and shadowing of the externally-produced components (Al K_α line and flat continuum) by the window support structure. During observations in low gain mode the particle background can also be monitored by the count rate in channels 260-370, since essentially all of these events are produced by particles.

3.6.3 The Scattered Solar X-ray Background

(*Source:* Snowden & Freyberg 1993)

At the altitude of *ROSAT* (~ 550 km), and with the zenith-angle observation constraint (observations are made at $< 97^\circ$), the scattering is dominated by atomic oxygen with Thomson scattered X-rays in the 1/4 keV band and oxygen

K_α fluorescent scattered X-rays at 0.53 keV. Field-of-view-integrated minimum count rates of ~ 0.25 counts s^{-1} (4×10^{-5} counts s^{-1} arcmin^{-2}, on axis) during day-side observations with excursions to $\sim$ 40 counts s^{-1} (6×10^{-3} counts s^{-1} arcmin^{-2}) or more in particularly bad geometries in the 0.1-1.0 keV band are found. Typical cosmic background count rates in the same band range from $3 - 12$ counts s^{-1} (5×10^{-4} to 2×10^{-3} counts s^{-1} arcmin^{-2}, on axis), demonstrating the possible severity of the contamination.

The temporal variation of the solar scattered X-ray background is dominated by the observation-geometry induced variations of the sunlit column density of Earth's atmosphere along the observation line of sight. This variation can be adequately modeled allowing a reasonable subtraction of the background counts.

The severity of the contamination by scattered solar X-rays has been much reduced as the mission has progressed, due to the reduced solar flux as solar maximum is left behind (*ROSAT* was launched close to solar maximum). The reduction comes both from the lower atmosphere (which also adds to the longevity of the mission because of reduced atmospheric drag) and from a lower solar X-ray luminosity.

3.6.4 Auroral Induced X-Ray Background

While auroral X-rays are a specific example of STEs, they deserve a special note. They can completely dominate a pointed observation, with count rates exceeding 200 counts s^{-1} in particularly bad geometries. Not surprisingly, the most sensitive geometries for auroral X-ray contamination are where the satellite is passing near the northern or southern particle belts and the observation is of a far northerly or southerly target, which requires a large zenith angle. In this geometry, the line of sight can pass through the particle belts at relatively low altitudes where the atmospheric density (and therefore number of scatterers) is large.

3.6.5 Cosmic X-Ray Background

Whether the cosmic X-ray background is a source of contamination or an interesting signal is obviously dependent on one's scientific point of view. In most observations and for all energies less than $\sim$ 2 keV it is typically the dominant background component. The cosmic X-ray background is both spatially and spectrally anisotropic with independent variations of greater than a factor of five in surface brightness in the hard and soft bands. The structure is due to both variations in emission and foreground absorption. The angular scale of the structure varies from the coarse all-sky negative correlation between galactic N_H and the 1/4 keV background to few arc-minute scale emission by clusters of galaxies (most obvious at higher energies). Thus, there is no "typical" cosmic background flux or spectrum.

3.6.6 Other possible Contributions to the Background

A background component, variable in magnitude and related primarily to the particle background, became apparent in the summer of 1991. This component consists of very low pulse-height afterpulses which follow very shortly after a "precursor" event. Some of these afterpulses can be removed by rejecting all events occurring within 0.35 ms after another event, which eliminates all such events associated with telemetered X-ray events. Unfortunately, except near a bright source, most of the precursor events are particle background events which have been vetoed by the on-board electronics and are therefore not telemetered to the ground, which makes selecting against their afterpulses impossible.

3.7 The Deadtime of the PSPC

(*Source:* Hasinger 1990a)

Following the collection of an event, a proportional counter will be "dead" for a certain time interval during which no other event can trigger the electronics and therefore be detected. Nominally, the event deadtime for the *ROSAT* PSPCs was estimated to be $\simeq 170$ μs (the gate trigger time of a single event). However analysis of ground calibration data have revealed that the PSPC deadtime is a function of both the event pulse height (*i.e.,* incident photon energy) and the incident count rate. There are also significant differences between the individual PSPCs (with the deadtimes for PSPC-A & -D systematically higher by 5–10% than those for PSPC-B & -C). The actual PSPC deadtimes are therefore in the range 180–280μs. The deadtime properties are not a strong function of position across the counters.

Most of the time, the PSPC deadtime in orbit will be dominated by vetoed particle background events

3.7.1 Dependence on Count Rate

For an individual detector and a single photon energy, the event deadtime is well approximated by a linear function of count rate. Only at count rates > 600 counts s^{-1} are deviations sometimes found.

3.7.2 Dependence on Pulse Height (Photon Energy)

There is a 10–20% increase in the deadtime between 0.28 keV and 1.47 keV. This is most likely due to an increase in the fraction of "double-triggers" (*i.e.,* events that cause a second trigger due to wiggles in the decay of the initial pulse) with increasing pulse height.

3.7.3 Deadtime of Background Events

Section incomplete (see Hasinger 1990a)

3.8 The Timing of the PSPC Events

(*Source:* Predehl 1993)

The standard correlation between S/C clock and UTC does not permit the timing of events down to millisecond accuracy. Therefore, a special method has been implemented:

The central data processing unit of the focal instrumentation ("ZDE") runs in a software cycle which is started every second by a pulse provided by the S/C-clock. This cycle can be paused by other sources of interrupts, *e.g.,* on the reception of telecommands or the warmstart of the computer performed on reception of the on/off-command "RESET". Upon the reception of the RESET-interrupt, the ZDE needs 532.8 ms to perform a couple of tasks necessary for resetting some registers etc., then it enters an idle-loop which is stopped on the next one-second interrupt. The time difference between the RESET- and the SECOND-interrupt is measured by a software counter, one count corresponds to 0.0113774 ms.

Whenever the RESET on/off-command is sent (typically once per week during the first ground contact on monday), the time when the command "leaves" the antenna is recorded at the ground station. As a source for an additional time delay, the distance between ground station and the satellite has to be taken into account. This information is delivered by GSOC together with the time when the command has been sent. The value of the idle-loop counter is sent to ground by a special telemetry frame. The information from both channels is combined for generating the clock correlation.

The S/C-clock exhibits a slight drift which has been specified to be smaller than 10^{-7}. The S/C-clock is reset about once per year in order to prevent an overflow of the 32-bit counter. Occasionally, this has also happened accidentally.

SASS adds an offset to the S/C clock in order to create homogeneously increasing event-times. These event times (not the S/C-clock!) are the relevant times for the users and are, for instance, contained in the PETs.

For most applications, it is sufficient to perform a linear regression to the correlation data within a period between two consecutive clock resets. The transformation from event-time (EVT) to UTC for an interval i is

$$UTC[d] = \frac{(EVT[s] - OFS_i[s]) \times (1 + DRF_i)}{86400} + RES_i[d] \qquad (3.7)$$

with DRF is the clock-drift, OFS is the offset added by SASS, and RES is the time of a clock-reset. All the relevant numbers can be found in Table 3.6. Clock-period 3 has been split into two sub-intervals at July 1, when a leap second was inserted. Differences between values calculated by this method and the true S/C-clock conversion are always less than 10 ms. The residuals can be obtained from the Figures 3.17 a) through e).

Table 3.6: S/C clock resets

period	date	RES [d]	DRF	OFS [s]
1	01.06.90	151.879749069	-8.863748E-8	0
2	26.01.91	25.386330848	-8.934155E-8	20606971.33
3a	12.02.92	42.353305347	-8.401761E-8	53608920.63
3b	01.07.92	42.353293327	-7.956741E-8	53608920.63
4	19.01.93	18.705978489	-7.181173E-8	100663296.50

References to Chapter 3

Aschenbach, B. *et al.* 1985, *ROSAT PSPC Scientific Data Processing Requirement Document*, MPE Internal Report 44.

Briel, U.G., Pfeffermann, E., Hartner, G. & Hasinger, G. 1988, Proceedings of SPIE, V. **982**, 401.

Briel, U.G., Burkert, W., & Pfeffermann, E. 1989, Proceedings of SPIE, V. **1159**, 263.

Elvis, M., Lockman, F.J., & Wilkes, B. 1989, *Astr. J.*, **97**, 777.

Fink, H.H., *et al.* 1991, *Astr. Astrophys.*, **246**, L6.

Fink, H.H. 1992, Proc. ISY, 77.

Hasinger, G. 1986, Note 1986 July 2.

Hasinger, G. 1990, MPE *ROSAT* Memo TN-ROS-ME-ED34/002.

Hasinger, G. 1990a, MPE *ROSAT* Memo TN-ROS-ME-ZA00/026.

Hasinger, G., Boese, G., Predehl, P., Turner, T.J., Yusaf, R., George, I., & Rohrbach, G., 1993, *Legacy*, **4** (CAL/ROS/93-015).

Hasinger, G., & Snowden, S. 1990, Note 1990 March 17.

Hasinger, G., Turner, T.J., George, I., & Boese, G. 1992, *Legacy*, **2**, 77 (CAL/ROS/92-001).

Henke, B.L., Lee, P., Tanaka, T.J., Shimbabukuaro, R.L., & Fujikawa, B.K. 1982, Atomic Data and Nuclear Data Tables, **27**, 1.

Jahoda, K., & McCammon, D. 1988, *Nuc. Inst. and Methods*, **A272**, 800.

Metzner, G., 1986, *Nuc. Inst. and Methods*, **A242**, 493.

Plucinsky, P.P., Snowden, S., Briel, U.G., Hasinger, G., & Pfeffermann, E., 1993, *Astrophys. J.*, **418**, 519.

Predehl. P. 1993, ?

Schmitt, J., & Snowden, S.L. 1990, MPE *ROSAT* Memo TN-ROS-ME-ZA10/038.

Snowden, S.L., & Schmitt, J.H.M.M. 1990, *Astr. Sp. Sci.*, **171**, 207.

Snowden, S. 1988, MPE *ROSAT* Memo TN-ROS-ME-ED52/31.

Snowden, S., Plucinsky, P.P., Briel, U., Hasinger, G., & Pfeffermann, E. 1992, *Astrophys. J.*, **393**, 819.

Snowden, S.L., & Freyberg, M.J. 1993, *Astrophys. J.*, **404**, 403.

Snowden, S. L., McCammon, D., Burrows, D.N., & Mendenhall, J.A. 1994a, *Astrophys. J.*, **424**, 714.

Snowden, S. L., *et al.* 1994b, in preparation.

Stephan, K.-H., Schmitt, J.H.M.M., Snowden, S.L., Maier, H.J., & Friscke, D. 1991, *Nuc. Inst. and Methods*, **A303**, 196.

Voges, W., 1992, in *Proc. of Satellite Symp. 3*, eds. T.D.Guyenne & J.J. Hunt (Noordwijk:ESA Pub. Div), 9.

Figures to Chapter 3

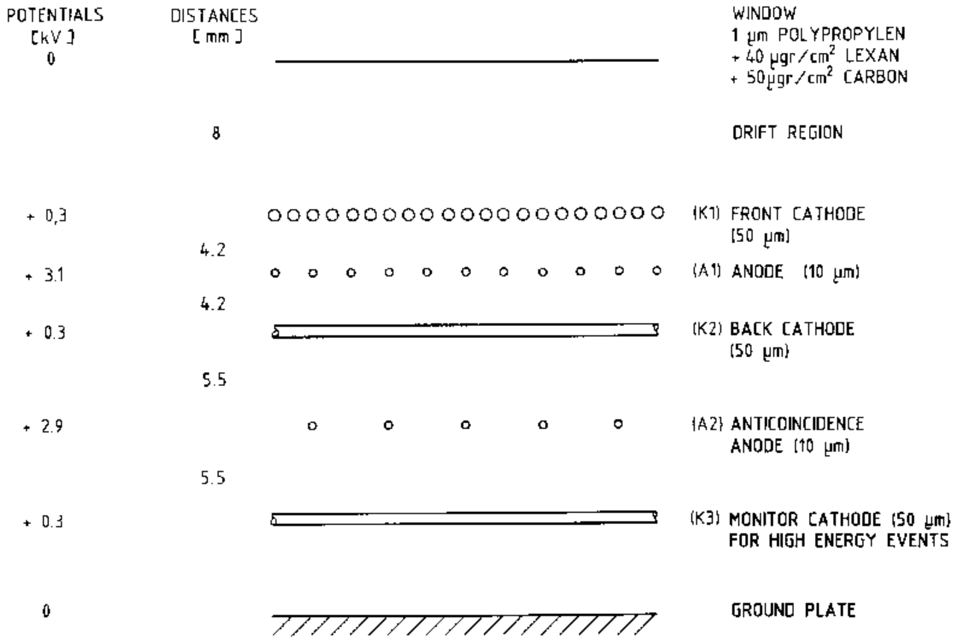

Figure 3.1: Schematic cross-sectional view of a *ROSAT* PSPC. The mutually perpendicular cathode grids (K1 & K2) are gold-plated molybdenum wires with a 0.5 mm spacing used to determine the position of events (Section 3.5.3). The A1 anode grid consists of gold-plated tungsten wires of 1 mm separation used to determine the energy of events (Section 3.5.3). The A2 anode is of identical construction as A1 (except with a 2 mm wire separation) and used as an anti-coincidence counter. The filling gas is a mixture of 65% argon, 20% xenon and 15% methane.
(*Source:* Aschenbach 1985)

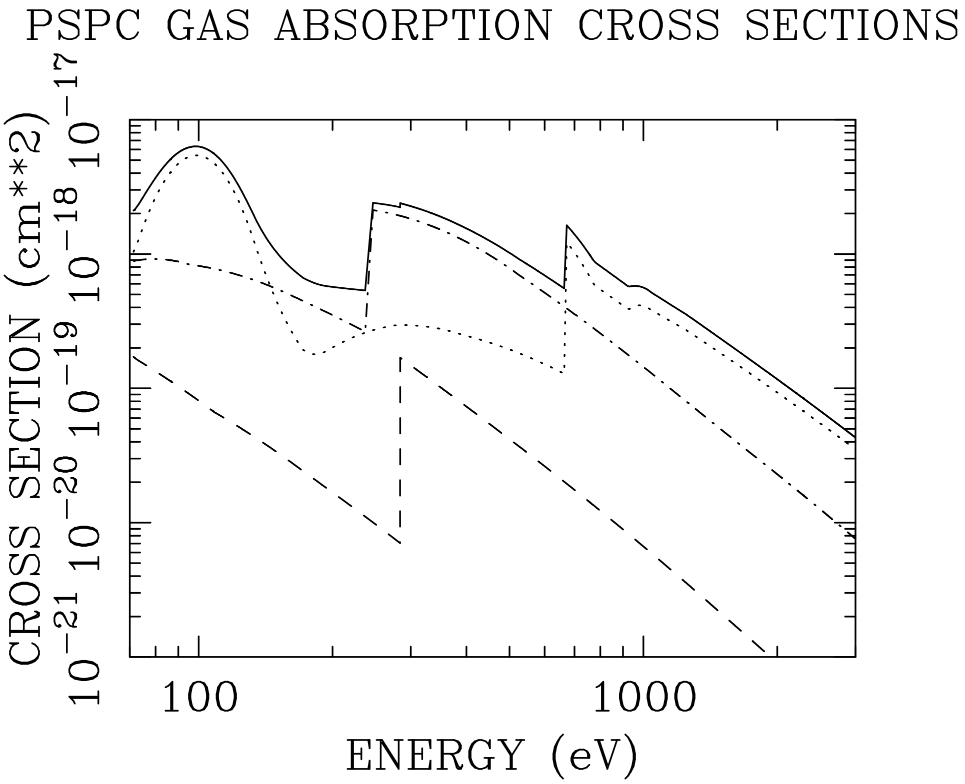

Figure 3.2: The absorption cross-sections of the various components which comprise the *ROSAT* PSPC counter gas. The curves are as follows at the far right from the top of the plot: the total cross section, the cross section from xenon, the cross section from argon, and the cross section from methane. It can be seen that for $E > 245$ eV (the Ar L-edge) one gas alone (Ar for 245 eV $<$ $E <$ 672 eV, Xe for $E >$ 672 eV) dominates the absorption. For $E <$ 245 eV the component dominating the absorption switches smoothly between Ar and Xe.
(*Source:* Snowden 1988)

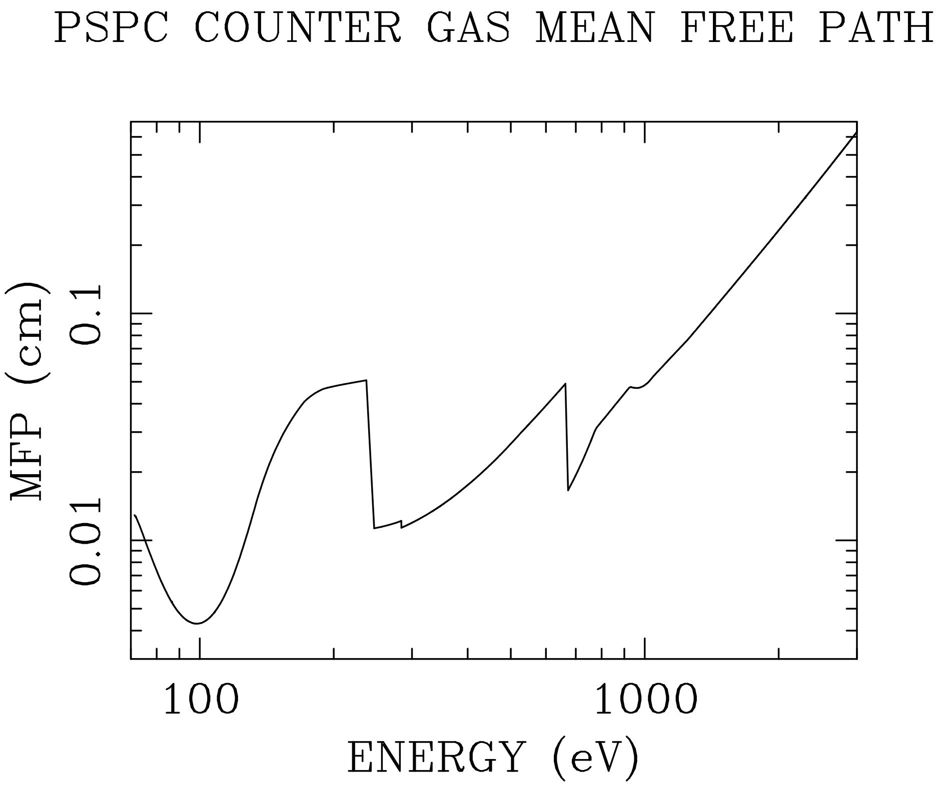

Figure 3.3: The mean free path of the *ROSAT* PSPC assuming a mixture of 65% argon, 20% xenon and 15% methane. Photons of energy $\lesssim$ 150 eV (and just above the absorption edges) are absorbed at a depth less than the characteristic size of the resulting secondary electron cloud. At these energies a fraction of the secondary electrons are therefore lost to the window, and thus giving rise to a low pulse height tail to the PSPC pulse height distribution response to a monoenergetic X-ray input (see Section 3.2.1). The drift region, *i.e.*, separation between the window and the K1 cathode, is $\simeq$ 8 mm (Figure 3.1).
(*Source:* Snowden 1988)

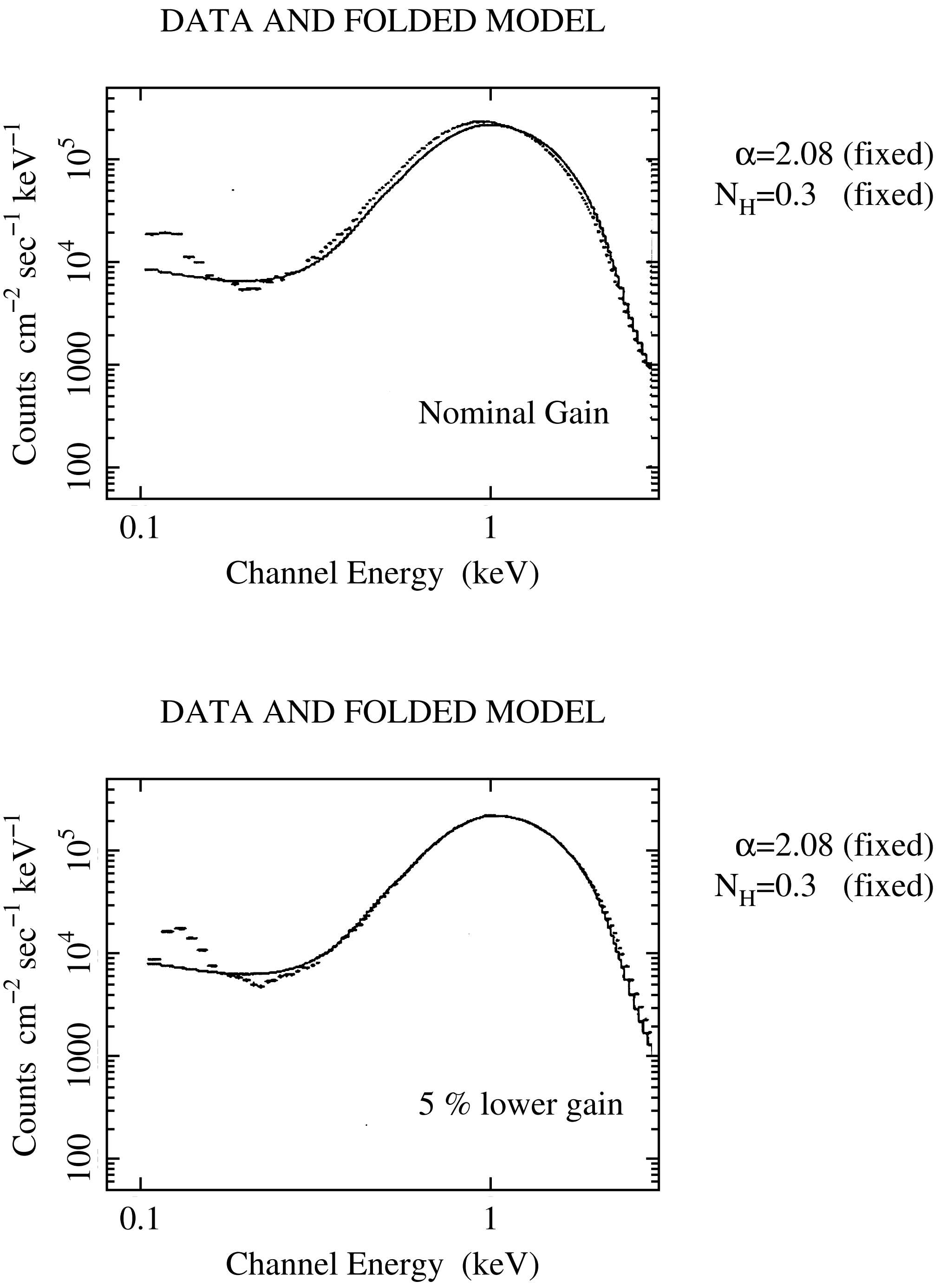

Figure 3.4: Rate-Gain and afterpulse effects in the Crab data. The top panel shows the power-law fit to the crab data, with nominal gain. The high count rate of the crab saturates the PSPC gain. The lower panel shows the fit after the gain assumed in the response matrix has been manually lowered by 5%. The very soft residual in the lower panel is afterpulse contamination.
(*Source:* G. Hasinger p. comm 1993)

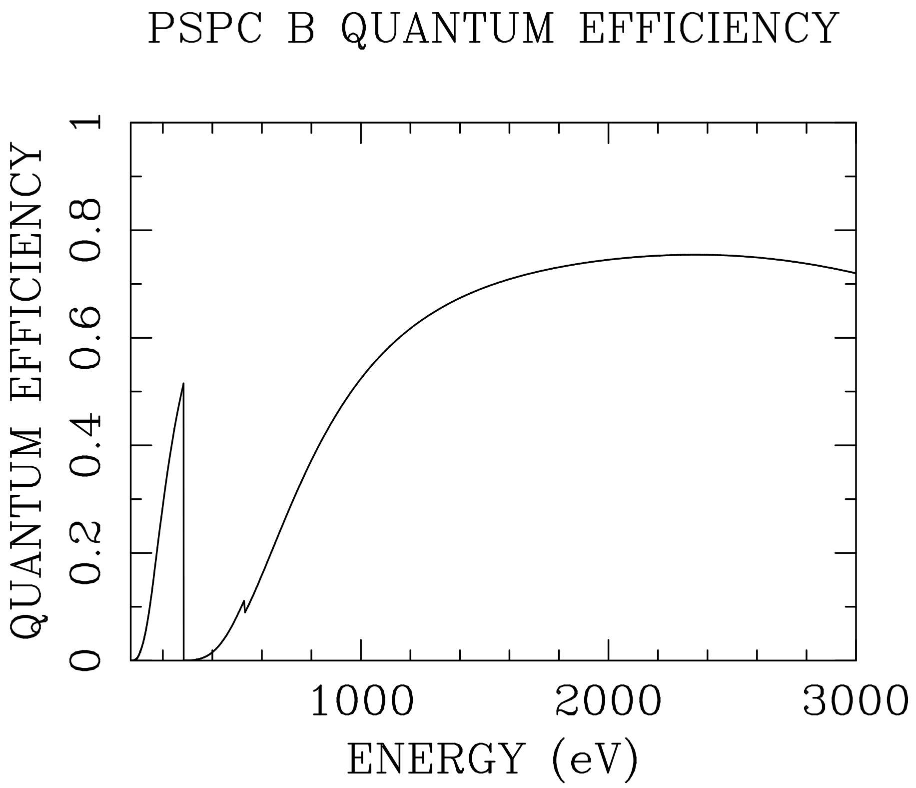

Figure 3.5: The Quantum Efficiency of the *ROSAT* PSPC as a function of energy. Included are the window transmission, the average transmission of the window support mesh, and the gas stopping efficiency.
(*Source:* NRA 91-OSSA-3)

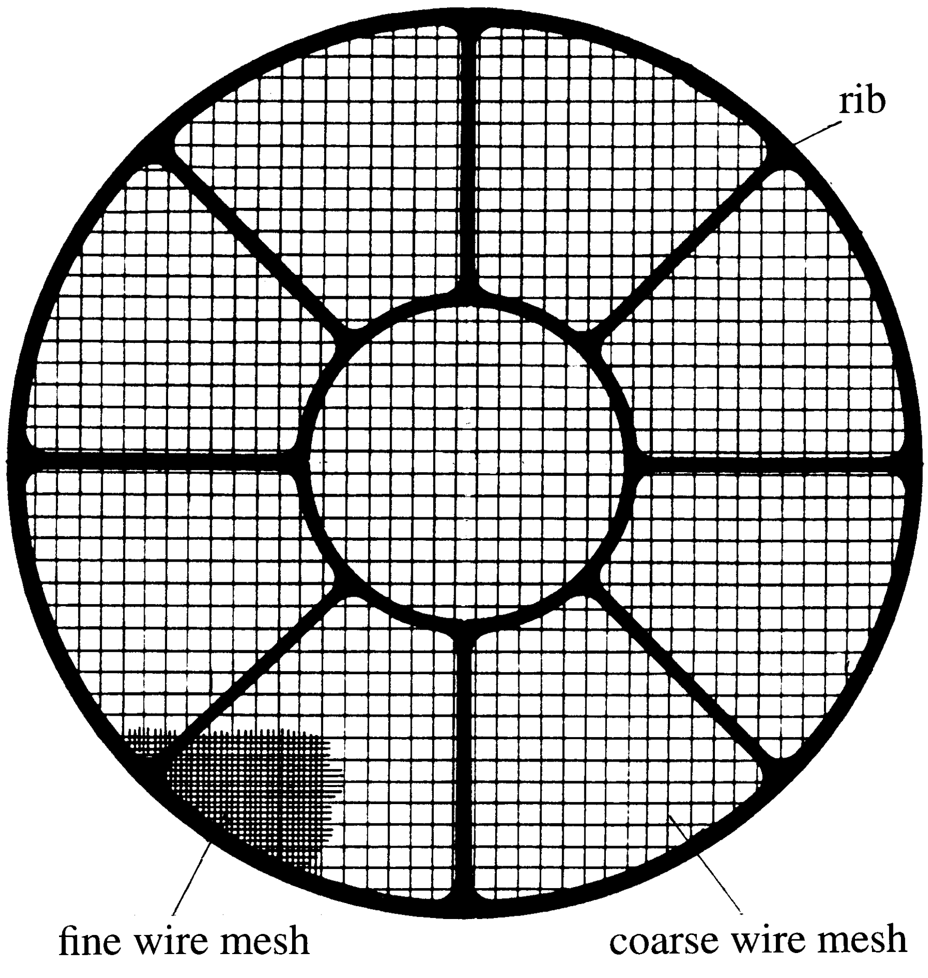

Figure 3.6: A schematic diagram of the *ROSAT* PSPC window support structure showing the ribs, ring and wire meshes.

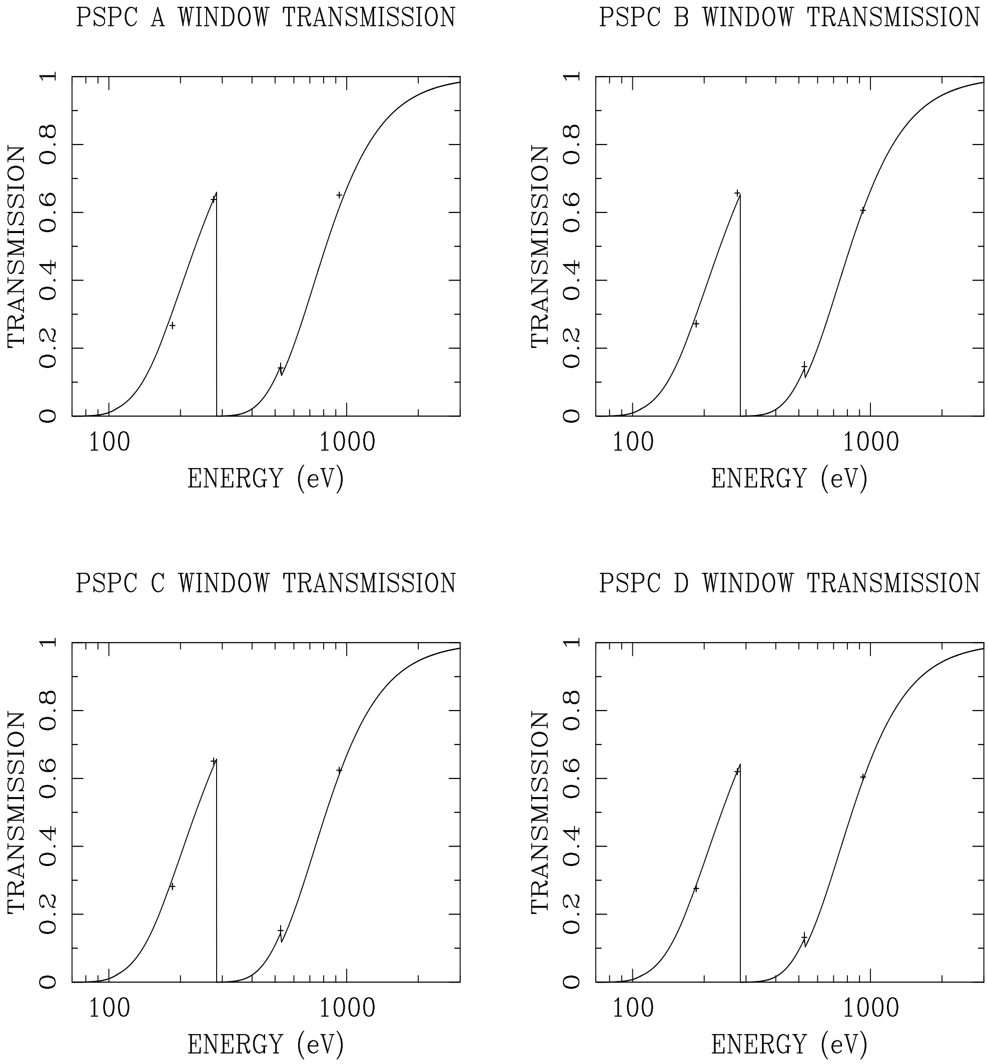

Figure 3.7: The ground calibration results for the transmission of each *ROSAT* PSPC entrance window as a function of energy. Note that the transmission here *does not* include the average transmission of the window support mesh. (*Source:* Schmitt & Snowden 1990)

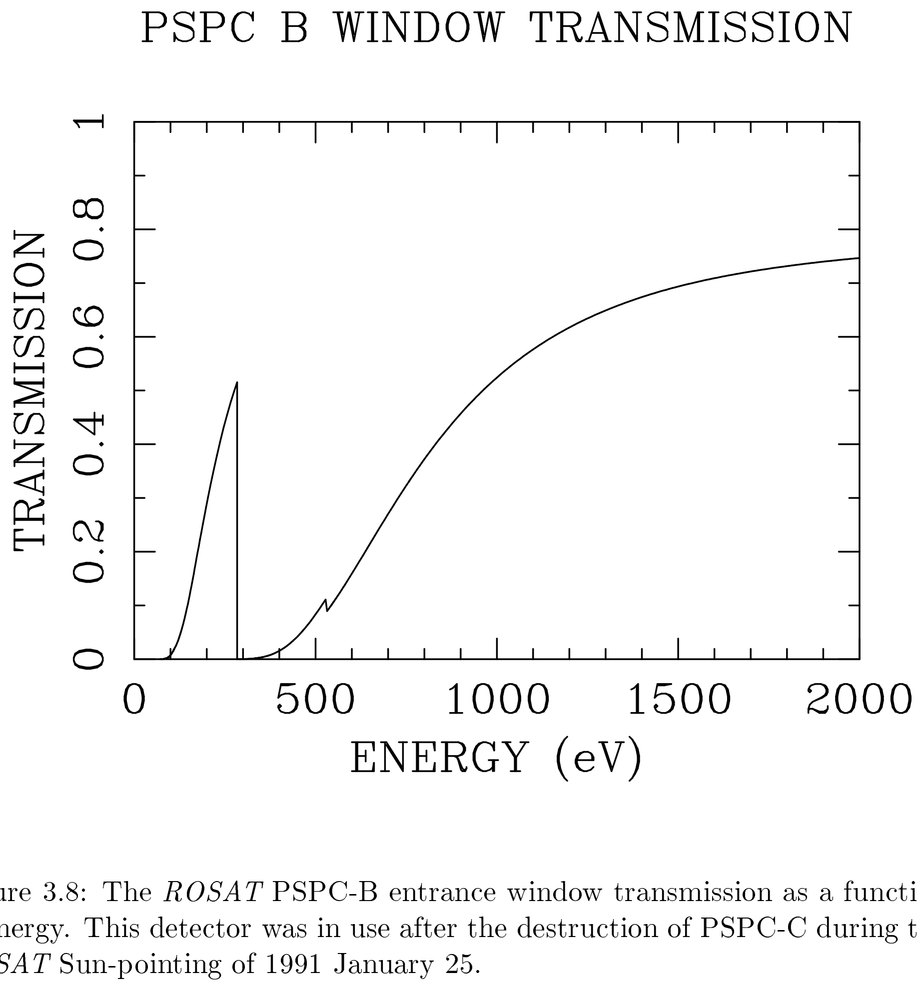

Figure 3.8: The *ROSAT* PSPC-B entrance window transmission as a function of energy. This detector was in use after the destruction of PSPC-C during the *ROSAT* Sun-pointing of 1991 January 25.

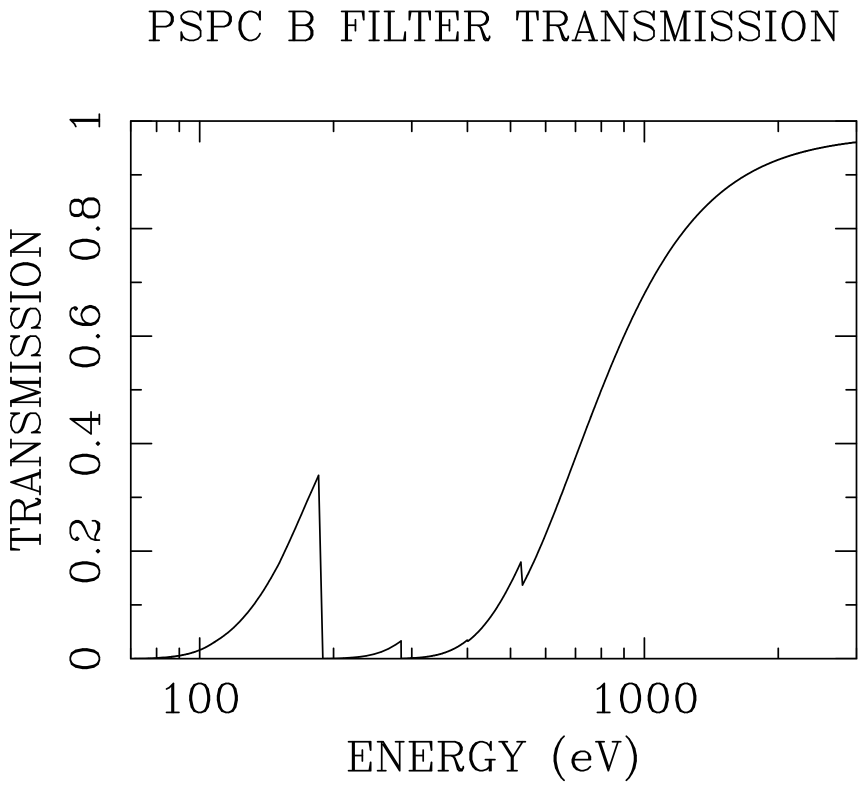

Figure 3.9: The transmission of the boron filter of the *ROSAT* PSPC as a function of energy. Note that this filter only covers the centre of the PSPC field of view.

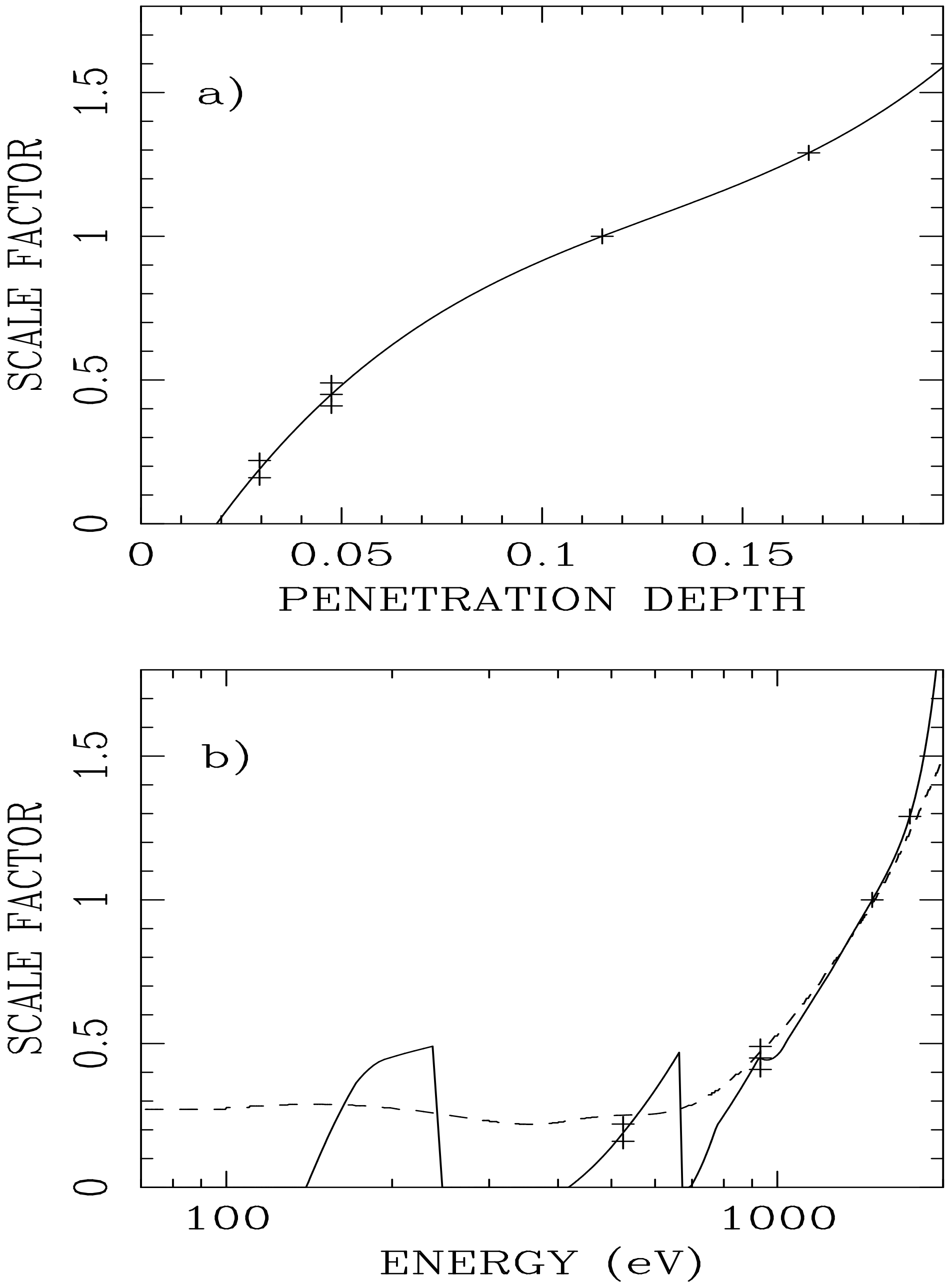

Figure 3.10: Amplitude of the high frequency term in the spatial gain correction as a function of penetration depth (a) and energy (b). The plus signs show the data of PSPC-A through D, the solid curve is a third-order polynomial fit to the data. The dashed line in b) shows the curve weighted by effective area, which is used by SASS. The curve is truncated at 1.8.
(*Source:* Hasinger & Snowden 1990)

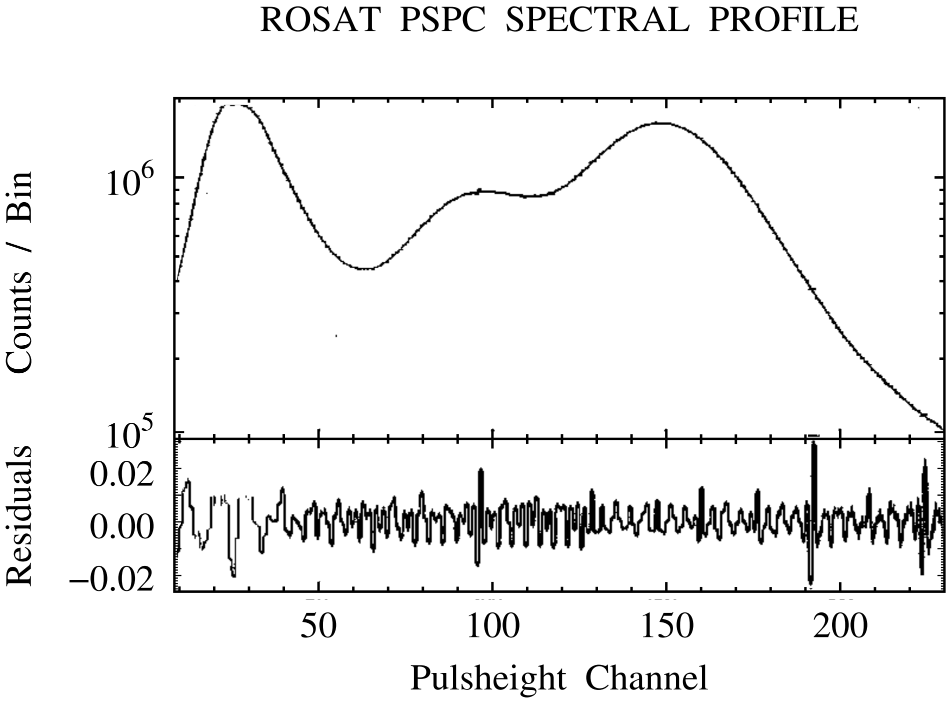

Figure 3.11: Upper panel: The cumulative spectrum from all PSPC ground calibration data (processed up to ∼ 1990 March 17) fitting with a smooth spline function (upper panel) assuming no ADC nonlinearities. The corresponding residuals (lower panel) demonstrate the ADC (pulse height) bins do not have equal widths though on average they are linear to within ∼ 3%. The residuals are used to determine the true channel boundaries, and thus enable individual events to be corrected for the ADC nonlinearities.
(*Source:* Hasinger & Snowden 1990)

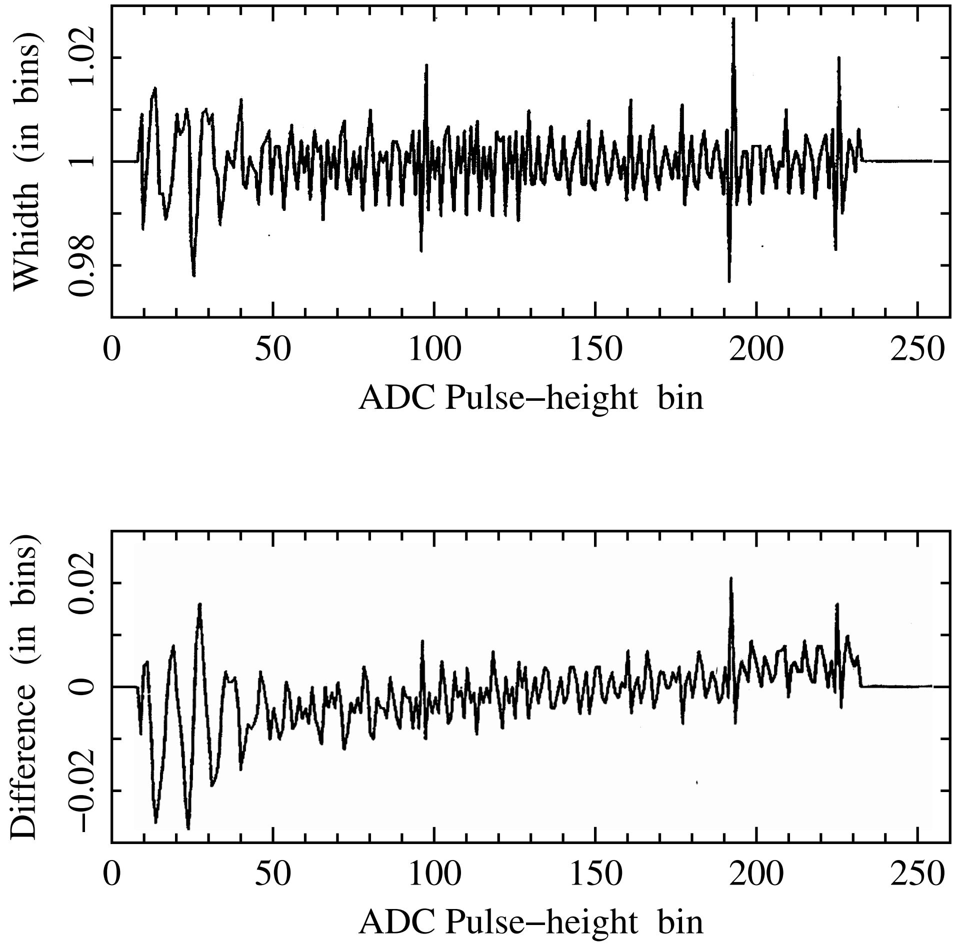

Figure 3.12: Upper panel: The width (in channels) of each ADC pulse height bin (*cf.* the lower panel of Figure 3.11).
Lower panel: The difference between the upper bound of each pulse height channel assuming a linear ADC relationship and that derived from the smooth spline fit to ground calibration data. Both plots are derived from the data file used by SASS5_0 to correct for the nonlinearities in the ADC (*cf.* the lower panel of Figure 3.11).

.

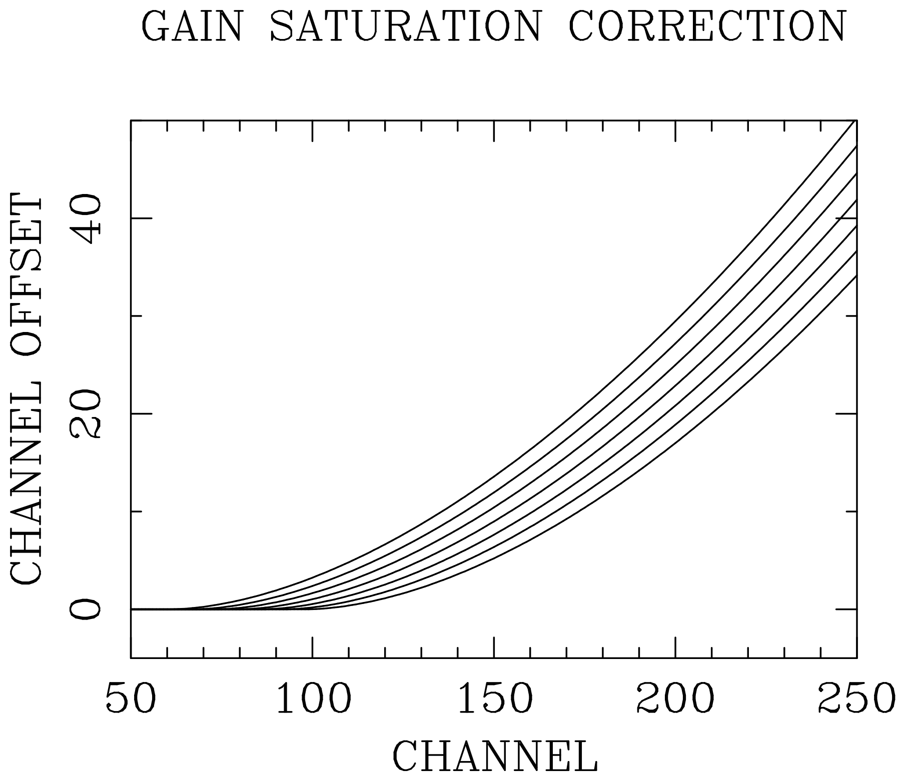

Figure 3.13: The difference between the true and measured pulse height channel due to gain saturation. The curves are for nominal gains of 90 (top), 100, 110, 120, 130, 140, and 150 (bottom).
(*Source:* Hasinger & Snowden 1990)

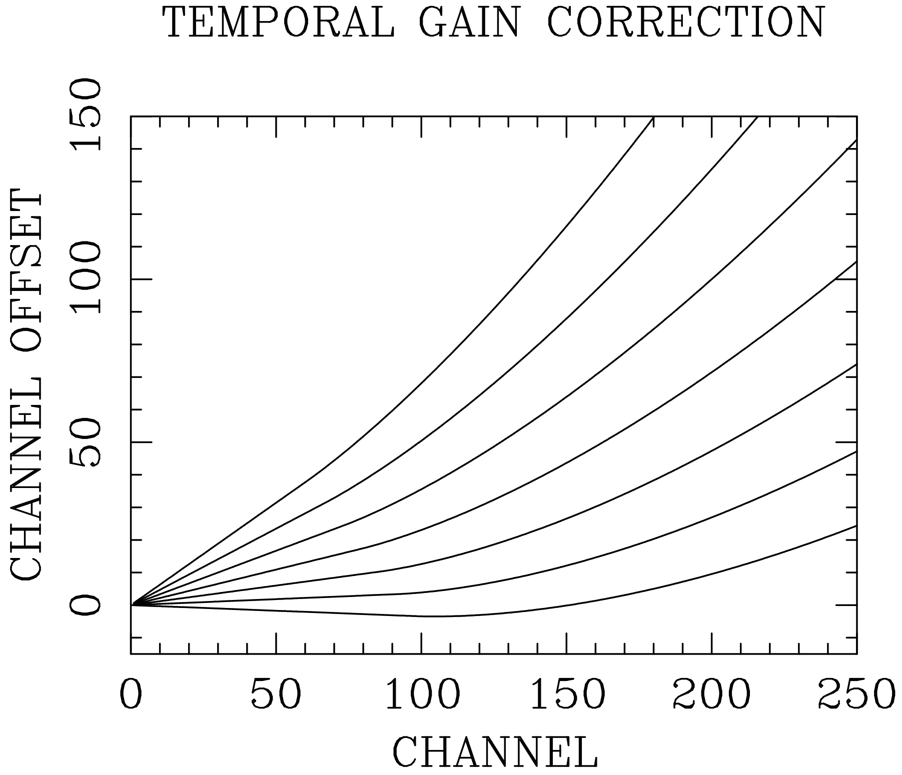

Figure 3.14: The difference between the true and measured pulse height channel. The curves of Figure 3.13 are now corrected for the variations in absolute gain. The curves are for nominal gains of 90 (top), 100, 110, 120, 130, 140, and 150 (bottom). The deviations from straight lines are caused by corrections for the gain saturation effect.
(*Source:* Hasinger & Snowden 1990)

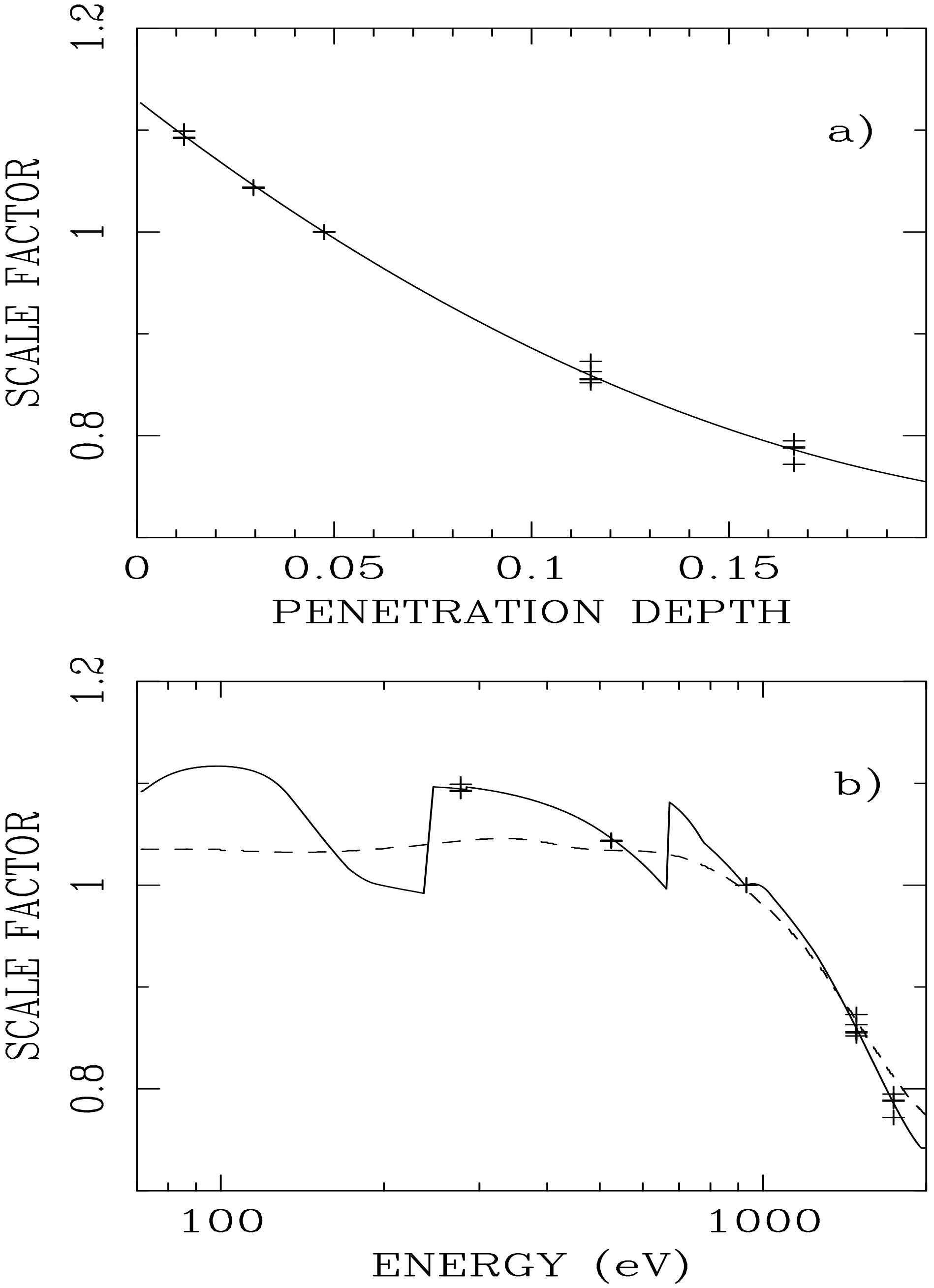

Figure 3.15: Scale factor of the "Golden Disk" as a function of penetration depth (a) and energy (b). The plus signs show the data of PSPC-A through D, the solid curve is a parabolic fit to the data. The dashed line in b) shows the curve weighted by effective area, which is used by SASS.
(*Source:* Hasinger & Snowden 1990)

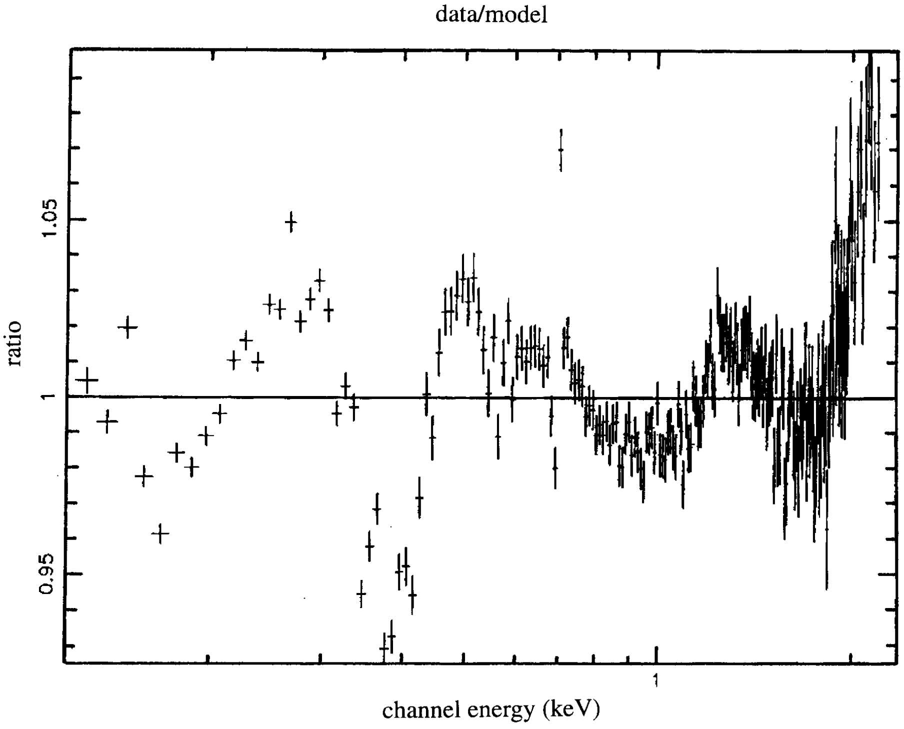

Figure 3.16: The ratio plot of data minus model residuals from a broken power-law fit to the PHA spectrum from Mkn421. The absorbing column was allowed to be a free parameter (but the best-fit was close to the line-of-sight value). The plot illustrates the systematic deficit between ~ 0.3-0.4 keV observed in many spectra. The sharp rise above 2 keV reflects the uncertainty in our knowledge of the optical constants used to calculate the effective area of the mirror.

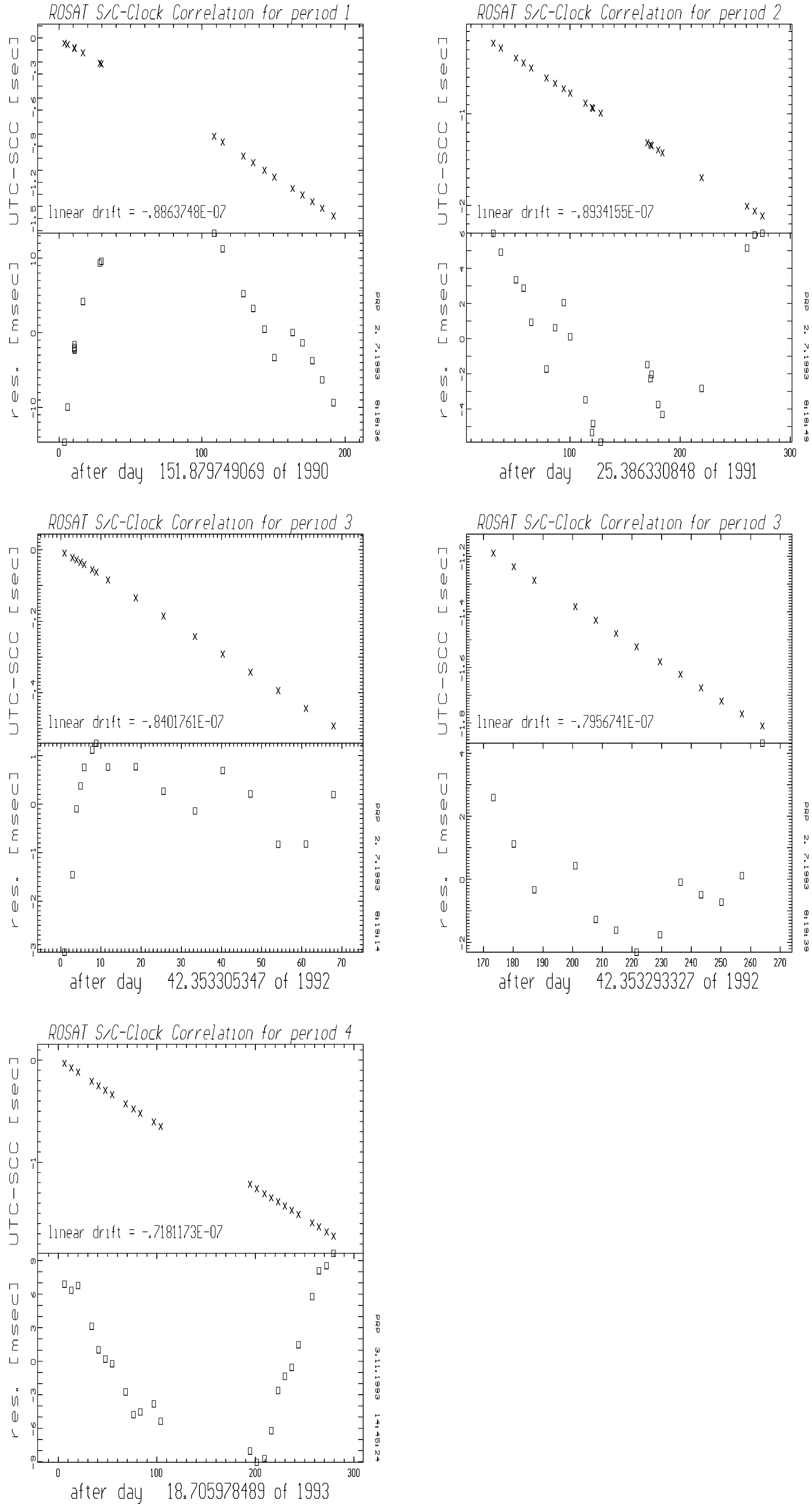

Figure 3.17: *ROSAT* S/C-clock correlation for different periods: a) Period 1, b) Period 2, c) Period 3, d) Period 4, and e) Period 5

Chapter 4

CHARACTERISTICS OF THE ROSAT PSPC + XMA INSTRUMENT

4.1 Spatial Resolution

As detailed in CAL/ROS/92-001 and 001a (Hasinger *et al.* 1992 (H92) and 1992a) and CAL/ROS/93-015 (Hasinger *et al.* 1993), the point spread function (*psf*) of the *ROSAT* X-ray mirror assembly (XMA) + PSPC is a convolution of 5 components:

1. The XMA scattering profile
2. The off-axis blur of the XMA
3. The intrinsic spatial resolution of the PSPC
4. Focus and detector penetration effects
5. A widening of the PSPC resolution due to the existence of "Ghost images" (for PHA channels < 15 only)

There is also some residual ellipsoidal blur due to uncorrected attitude motion, but for the PSPC, this component is usually negligible compared to the other effects (see H92 for more details). The XMA scattering profile, the intrinsic spatial resolution of the PSPC, and focus and detector penetration effects have already been described in H92 and Hasinger *et al.* (1993). The *psf* was parameterized for on-axis observations from PANTER ground calibration measurements. In H92 it was shown that the derived analytical functions satisfactorily described 5 moderate signal-to-noise datasets in all but the softest band where "Ghost Imaging" was already known to be a problem. Hasinger *et al.* (1993) extend the treatment to include a parameterization of the change in shape of the *psf* with off-axis angle.

Examination of a bright point source observed off-axis reveals asymmetry in the distribution of source counts which becomes easily noticeable once the source is observed outside of the central ring of the PSPC (*i.e.,* $> 20'$ off-axis). The asymmetry is produced because for off-axis irradiation, half of the mirror sees a different grazing angle compared to the other. The two relatively sharp outer boundaries of the blur area, which have different radii of curvature, are produced by the front and rear aperture planes of the mirrors, respectively. The hole in the *psf* is due to the central hole in the mirror aperture (the mirror consists of four shells). The imaged is defocussed at large angles as the detector is flat (actually bowed out slightly by counter gas pressure) but the focal plane is curved (in the sense opposite to the bowing of the detector). The radial struts also interfere with the photon distribution as they shadow part of the detector. This combination produces the diffraction-like radial pattern seen on bright sources observed at large offset angles.

While early attempts to parameterize the change in shape of the *psf* concentrated on the ground calibration data taken at the PANTER facility, a comparison of those data with in-flight data showed significant differences. These differences are due to the finite source distance in the PANTER facility, which results in a beam divergence of about $10'$. The consequence of this divergence is that the PANTER data have the hole on the inner side of the peak of counts for off-axis sources, while the in-flight data show the hole on the opposite side. In addition, the PANTER image shows greater interference between the *psf* and the PSPC wire grid (effects which are reduced by the wobble of in-flight observations). As a consequence of these differences, in flight data, collected from a variety of bright serendipitous sources detected in pointed observations, were finally used to parameterize the off-axis dependence of the *psf*, while the components which are independent of off-axis angle were carried over from the higher-quality on-axis data.

The off-axis blur of the telescope, although highly structured and asymmetric, has been modeled by a simple Gaussian for comparison to a radially integrated profile. This Gaussian term for the off-axis blur is added in quadrature to the Gaussian term describing the intrinsic PSPC resolution. Since the model approximates the behaviour of the detector by the addition of Gaussian, exponential, and Lorentzian terms, instead of a mathematically correct convolution of terms, the contribution of the other terms must be adjusted relative to the on-axis case, to allow for the off-axis behaviour of the Gaussian term. The new term for the exponential fraction describes the relative diminishing of this term with increasing offset angle, due to the increase of the Gaussian term.

The mirror scattering term remains as noted in Section 2.4

4.1.1 Focus and Penetration Effects

The design distance between the XMA and PSPC (the window of which is bowed slightly out due the internal pressure of the counter gas) is such that photons of ~ 1 keV on-axis source are brought to a focus (along a surface of a cone of half-angle 8.5°) at an optimum depth within the PSPC drift region such that the Gaussian spatial distribution of pulses on the cathode wires is minimized. Consequently the image of a point source is sharpest at 1 keV.

The analytical form derived for the fraction of photons within this component as a function of energy is given by whichever is the smaller of the following two terms:

$$F_{exp}(E,\theta) = 10^{-1.635\ +\ 0.639E\ +\ 0.052E^2} e^{-0.5(\theta/12)^2} \tag{4.1}$$

OR

$$F_{exp}(E,\theta) = 1.0 - F_{scatt} \tag{4.2}$$

Equation 4.2 is necessary to avoid the "exponential artifact" of H92 which made the *psf* parameterization invalid above 2 keV.

The combined contribution of focussing and the finite penetration of photons into the counter on the *psf* can be modelled as an exponential function where r is the radial distance from the centroid position of the radial profile, in arc minutes.

$$PSF_{exp}(E,r) = A_{exp}(E)\ \exp\left(-\frac{r}{r_\tau(E)}\right) \text{ normalized counts arcmin}^{-2} \tag{4.3}$$

The e-folding angle, r_τ, was found to be the same as for the on-axis case

$$r_\tau(E) = \frac{1}{60}\ (50.61E^{-1.472} + 6.80E^{+5.62})^{1/2} \text{ arcmin} \tag{4.4}$$

The normalization, $A_{exp}(E)$, is given by

$$A_{exp}(E) = F_{exp}(E)/\left(2\pi(r_\tau(E))^2\right) \text{ normalized counts arcmin}^{-2} \tag{4.5}$$

and as for the other components, has been normalized such that the integral of $PSF_{exp}(E,r)2\pi r\mathrm{d}r$ over the range $0 \le r \le \infty$ equals $F_{exp}(E)$.

4.1.2 The Gaussian Intrinsic Resolution and Mirror Blur Term

Due to the inherent statistics of the primary electron generation, the intrinsic spatial resolution of the *ROSAT* PSPC is expected to be a Gaussian. Theoretically its width is $\propto E^{-1/2}$ and independent of θ. All photons not in the other two components are assumed to be in this component. Thus the fraction of photons within this component as a function of energy is given by:

$$F_{int} = 1\ -\ F_{scatt}\ -\ F_{exp} \tag{4.6}$$

Note that this becomes zero above 2 keV from equation 10.

$$PSF_{int}(E,r) = A_{int}(E)\ \exp\left(-\frac{1}{2}(\frac{r}{G_\sigma(E)})^2\right) \text{ normalized counts arcmin}^{-2} \tag{4.7}$$

The derived analytical form for the width of the detector gaussian, $G_{\sigma}(E,\theta)$, as a function of energy is given by:

$$r_{\sigma}(E) = 1/60\ \left(108.7E^{-0.888} + 1.121E^{+6}\right)^{1/2}\ \text{arcmin} \qquad (4.8)$$

The analytical form for the Gaussian mirror blur is

$$m_{\sigma}(\theta) = 1/60\ \left(0.219\theta^{2.848}\right)^{1/2}\ \text{arcmin} \qquad (4.9)$$

These two Gaussian widths are combined as follows:

$$G_{\sigma}(E,\theta) = (r_{\sigma}^2 + m_{\sigma}^2)^{1/2} \qquad (4.10)$$

The normalization, $A_{int}(E)$, is given by

$$A_{int}(E) = F_{int}(E)/\left(2\pi(G_{\sigma}(E))^2\right)\ \text{normalized counts arcmin}^{-2} \qquad (4.11)$$

where the denominator is the renormalization factor such that the integral of $PSF_{int}(E,r)2\pi r\mathrm{d}r$ over the range $0 \leq r \leq \infty$ equals $F_{int}(E)$.

This model has been tested against in-flight data and the model and test results are written up in Hasinger *et al.* (1993).

4.2 Mirror Plus PSPC Response Matrices

PSPC + mirror response matrices are now available as part of the multi-mission legacy /caldb (calibration database) area. The caldb area is accessible via anonymous ftp to legacy.gsfc.nasa.gov under /caldb/data/rosat/pspc/cpf (cpf stands for calibration product file). The matrices are available as FITS format (with .rmf extensions) as:

`pspcb_92mar11.rmf`

`pspcc_92mar11.rmf`

`pspcb_93jan12.rmf`

`pspcc_93jan12.rmf`

The "matrix" is a convolution of the detector effective area vector, photon redistribution matrix, and PSPC window vector (which includes the window-support wire mesh transmission). GSFC has software to convolve the boron filter response and vignetting functions with the matrices, as required. The FITS matrices are compatible with old style SF PHA files, or new FITS PHA files for XSPEC versions 8.2 and later. The difference should not be noticeable once inside XSPEC. The advantage of the FITS formats is that they remove the need to transport the files as ascii (and hence remove the need for rdrsp and mkrsp).

`pspcb(c)_92mar11.rmf` corresponds to PROS matrix `xspectraldata$dtmat_6.ieee` combined with either `offar2_5.ieee` for `PSPC-B`, or `offar1_5.ieee` for `PSPC-C`.

`pspcb(c)_93jan12.rmf` corresponds to PROS matrix `xspectraldata$dtmat_36.ieee`, combined with either `offar2_6.ieee` for `PSPC-B`, or `offar1_6.ieee` for `PSPC-C`.

4.2.1 Total Spectral Response-Effective Area

There are now three sets of official TOTAL effective areas which have been distributed by SASS. Just to be clear, the total effective area files contain:

1. the on-axis mirror effective area
2. the mirror vignetting function
3. the window transmission (including the average transmission of the wire mesh)
4. the gas absorption function

with only the window transmission changing between the 3 datasets. However, it is planned to update the gas absorption function to include effects (different path lengths in the active regions) due to the bulge in the PSPC window due to gas pressure (which is likely to amount to few percent changes in the total effective area above 2 keV).

It should be noted that up until the latest datasets (`SASS_AREA_B_NEW2` and `*._C_NEW2`), rigorous checks were not made that all components were included correctly. The 1st datasets (`SASS_AREA_B` *etc.*) are likely to have a errors at low energies. Based on high gain HZ43 observations, the polypropylene thickness (within the window) was reduced by 1σ to produce `SASS_AREA_C_NEW1`. Unfortunately there was a low energy problem in these data. The `SASS_AREA_B_NEW2` and `*._C_NEW2` files were adjusted for PI < 10 to reduce this low energy problem. There is also a few percent change at the C edge, *cf.* `SASS_AREA_B_NEW1` *etc.* (which had gone unnoticed); see Chapter G.

It should be noted that the detector maps do show variations at the few percent level on scales of tens of arc minutes. This is consistent with window thickness variations at fabrication. The 0.25 keV map may also have a top-bottom (in detector coordinates) gradient at a similar level. Furthermore, some ablation is possible within the central, most-used region of the detector. Currently however, it is not intended to fold these effects into the effective area datasets, although the effects are under confirmation/investigation.

4.2.2 Absolute Flux Calibration

Simultaneous PSPC (survey) + Ginga data are in reasonably good agreement at 1 keV, indicating a good absolute flux calibration of the PSPC. AGN datasets have been analysed and written-up (proceedings of the the Garching AGN meeting of 91 November). These agree to within 10% in the overlap regime. While many of those sources have complex spectra and cannot be used for this study, there are some good calibration sources such as 3C272 (where the break to a soft excess is well below the overlap region). The background flux in the 1/4 keV band was compared to the Wisconsin, *SAS-3*, and *HEAO-1* A-2 all-sky survey data and the agreement is again good to within about $\sim 10\%$.

The overlap of Galactic sources are disappointing in the sense that many are weak hard X-ray sources and in many cases the analysis of the ROSAT/Ginga data is incomplete.

One unresolved discrepancy is that the PSPC data from N132D show a flux ~30% higher than that indicated by the BBXRT and *Einstein* SSS data for the same source (the latter two agree well). The IPC flux of N132D, however, agrees well with the PSPC.

References to Chapter 4

Hasinger, G, Turner, T.J., George, I. & Boese, G. 1992 *Legacy*, **2**, 77 (CAL/ROS/92-001).

Hasinger, G, Turner, T.J., George, I. & Boese, G. 1992 *Legacy*, **3**, 46 (CAL/ROS/92-001a).

Hasinger, G, Boese, G., Predehl, P., Turner, T.J., Yusaf, R., George, I. & Rohrbach, G. 1993, *Legacy*, 4 (CAL/ROS/93-015).

Chapter 5

THE ROSAT HIGH RESOLUTION IMAGER (HRI)

(*Source* L.P. David, F.R. Harnden Jr., K.E. Kearns, and M.V. Zombeck
U.S. *ROSAT* Science Data Center/SAO
April 1993
Revised 1996 February: J.D. Silverman, D.E. Harris, S.L. Snowden, and F.A. Primini

5.1 Overview

For purposes of planning HRI observations (and of analyzing data as well), the performance of the combined HRI and *ROSAT* XRT (X-Ray Telescope) is described in this report, which is based upon laboratory, ground-based, and in-flight data.

The HRI information in this document supersedes that in previously issued versions of the "*ROSAT* Mission Description" (e.g., APPENDIX F of the U.S. announcement NRA 91-OSSA-3; references below to "Appendix F" refer to the version dated "January 1991"). It has been reorganized to some extent in order to improve the clarity of presentation. To assist those familiar with Appendix F, the following concordance is provided for finding updated material corresponding to sections of that appendix:

	This document	Appendix F section
5.1	OVERVIEW	4.3.1
5.2	Performance	4.3.2
5.2.1	Detector Geometry	4.3.2.1
5.2.2	Spatial Response	4.3.2.4
5.2.3	Effective Area	4.3.2.2, 11.1
5.2.4	Background	4.3.2.6, 7.8.3
5.2.5	Spectral Response	none (i.e., new)
5.2.6	UV Response	4.3.2.3
5.2.7	Event Timing	4.3.2.5
5.3	Feasibility of observations	11.
5.3.1	General Assumptions	11.1
5.3.2	Point Source Sensitivity	11.2, 11.5
5.3.3	Expected Count Rates	11.3
5.3.3	Examples	11.3.1
5.3.4	Time Variability Studies	11.6
5.3.5	Comparison to the *Einstein* HRI	11.7

5.2 Performance

The *ROSAT* High Resolution Imager (HRI) is very similar to the *Einstein* Observatory HRI and is comprised of two cascaded microchannel plates (MCPs) with a crossed grid position readout system. The detector performance can be characterized by such parameters as those listed in Table5.1. Two significant changes from the *Einstein* instrument that have affected the performance of the detector are: the substitution of CsI for MgF_2 as the detector photocathode, and the introduction of a thin aluminum-coated plastic membrane (the "electrostatic shield") near the front MCP (in addition to the UV/Ion shield which is situated farther in front of the detector).

5.2.1 Detector Geometry

Field of View

The 36mm-diameter HRI MCPs have a holding-fixture open aperture diameter of 30mm, and the readout system has a working area of 27mm x 27mm. Hence the net useful field of view is given by the intersection of the circular MCP and square readout, as shown in Figure 4.9 of Appendix F. The CsI photocathode used in the HRI is evaporated in the pattern shown in Figure 4.9, so that there are four small "tabs" of uncoated MCP area which are used to monitor the stability of the photocathode.

Table 5.1: *ROSAT* HRI Performance Summary

Field of View	38 arc minutes (square)
Spatial Resolution	1.7 arc seconds (FWHM)
Quantum Efficiency	30 percent at 1 keV
Window Transmission	75 percent at 1 keV
Background (counts arcmin^{-2} s^{-1})	1.0 10^{-3} internal 2.1(1.7 – 8.3) 10^{-3} external* 6.9(3.5 – 13.8) 10^{-4} XRB† 3.8 10^{-3} Typical Total
Temporal Resolution	61 μsec
Dead Time	0.36 to 1.35 msec

*Depending upon orbital location. †Depending upon viewing direction.

Plate Scale

The Andromeda galaxy (M31) was observed for 50 ksec, with numerous point sources detected. With 12 identified sources distributed over the HRI field from this observation (data courtesy of F. Primini), the mean plate scale determined with a standard astrometric plate reduction method was found to be:

$$0.499 \pm 0.001 \text{ arc seconds per pixel}$$

(Note that there are 8192 such "pixels" in the "sky-coordinate" event lists distributed to *ROSAT* HRI observers.)

The relationship between *Einstein* and *ROSAT* pixels was also measured (using 23 M31 sources that were matched to Einstein HRI detections) and found to be:

$$1\ \textit{ROSAT}\ \text{pixel} = 1.0050 \pm 0.0007\ \textit{Einstein}\ \text{pixel}$$

5.2.2 Spatial Response

Absolute Positions

The process of determining boresight offsets (systematic zero-point shifts found by comparing measured and known positions of catalogued objects) for the HRI has led to the conclusion that there are time-varying errors in the attitude solutions used to correct event positions. Although most known objects are detected at positions within $10''$ of their catalog positions, residual discrepancies can be present even after application of the boresight corrections. This can be particularly evident in a comparison of observations of the same object taken six months apart (and hence at spacecraft roll angles differing by 180 degrees).

Compensation for such effects is possible whenever X rays are detected from previously known objects whose positions have been accurately catalogued.

Table 5.2: Energy Dependence of the Mirror Scattering

E (keV)	% photons outside a 10″ radius
0.18	0.7
0.28	1.3
0.93	6.0
1.49	11.0
1.70	13.3

Preflight measurements

The pre-launch HRI positional resolution was measured in the lab using a shadow mask with a test pattern consisting of alternating bars of open and closed area of various widths, as shown in Figures 4.13 and 4.14 of Appendix F. Mean values from such measurements gives $\sigma = 8.4\mu$m, which at the *ROSAT* X-ray telescope focal length of 2.4 m, yields an intrinsic FWHM resolution of 1.7″ for the HRI.

Large scale geometrical distortions of the HRI were measured by projecting a mesh pattern on the face of the detector (cf. Appendix F and its Figure 4.15 for details) and found to be less than 1″ over its field of view. Note, however, that the image resolution varies over the field due to the off-axis response of the X-ray telescope. Small-scale differential non-linearity was also determined to have an RMS deviation from the mean of less than $\approx 0.1''$.

In-flight Point Spread Functions (PSF)

The PSF describes the surface brightness distribution of imaged point sources. There are three significant components: the XRT PSF, the HRI PSF, and a residual blurring attributable to the aspect correction (often discernible as a small ellipsoidal component).

On-Axis PSF

Although the XRT PSF has a central core with a FWHM of 3″ (as determined by ground test), microroughness in the mirror surfaces leads to a slight but measurable scattering of X rays and produces a small energy-dependent tail or wing in the PSF. As determined by ground test measurements, the fraction of imaged photons in the tail (beyond 10″) of the image of a point source is given in Table 5.2.

The HRI PSF has a central core with a FWHM of 1.7″ (as determined in the laboratory). In the absence of the electrostatic shield, the PSF has a near-Gaussian shape, but the electrostatic shield (introduced to reduce the background count rate) has broadened the PSF, creating a so-called "halo". X-rays interacting in the interchannel web in front of the MCPs produce electrons that are "captured" in microchannel pores a considerable distance from the initial event site, initiating an electron avalanche leading to a false position. Although the region between the shield and the MCP is, to first order, field free, fringe electrostatic fields deflect the web electrons back into the MCP. The magnitude of the effect is predicted to decrease with increasing energy, whereas mirror scattering increases with energy.

The in-flight, on-axis PSF, which includes aspect solution effects, has been determined from a 9.1 ksec exposure of HZ43 which yielded 109,000 net counts. Figure 5.1 shows the azimuthally averaged surface brightness profile of this observation. The HRI halo is obvious in Figure 5.1 and dominates the PSF beyond approximately 15″. The solid curve is a parametric representation of the in-flight, on-axis, PSF and consists of the sum of two Gaussians and an exponential. This functional form for the azimuthally averaged PSF, provides a good description of the PSF out to a radius of 2′, and is given by:

$$PSF(R) = A_1 e^{-0.5(\frac{R}{S_1})^2} + A_2 e^{-0.5(\frac{R}{S_2})^2} + A_3 e^{\frac{-R}{S_3}}$$

where the radial distance, R, is in arc seconds, and:

$A_1 = 0.9638$ $S_1 = 2.1858$ arcsec
$A_2 = 0.1798$ $S_2 = 4.0419$ arcsec
$A_3 = 0.00090$ $S_3 = 31.69$ arcsec

Note the arbitrary normalization of the above expression for the azimuthally-averaged surface brightness. Figure 5.1 shows that there is an additional component in the PSF beyond 2′, but this component will be well below the background in most observations. We have not fit this additional component, since we do not know at present how strongly it depends on energy.

The azimuthally averaged surface brightness for on-axis observation of HZ43, AR Lac and LMC X-1 is shown in Figure 5.2. Since these sources represent a wide range of mean X-ray energies, this figure demonstrates that the combined PSF (HRI/XRT) is largely energy independent within 2′.

The integrated surface brightness (encircled energy function) for the long HZ43 observation is shown in Figure 5.3. The extended HRI halo is evident in this figure and shows that approximately 15% of the total power is scattered beyond 10″, 7% beyond 1′, and less than 1% beyond 5′. Figure 5.4 shows the encircled energy function for HZ43, Ar Lac, and LMC X-1. This figure shows that the encircled energy function is consistent within the statistical errors for these three sources, and is not strongly dependent on the photon energy.

The on-axis PSF given above is based on a single long observation of HZ43 with excellent photon statistics. Such an observation is required in order to accurately parameterize the HRI halo. We have also looked at a number of shorter (nearly on-axis) observations of HZ43, AR Lac, LMC X-1, and the meaty source taken throughout the mission in order to determine the reproducibility of the on-axis PSF. In general, there is no difference (within the statistics) beyond 10″. This indicates that the HRI halo is stable and approximately energy independent. However, due to random errors in the aspect solution, the width of the core of the HRI images can vary. Fitting the above functional form

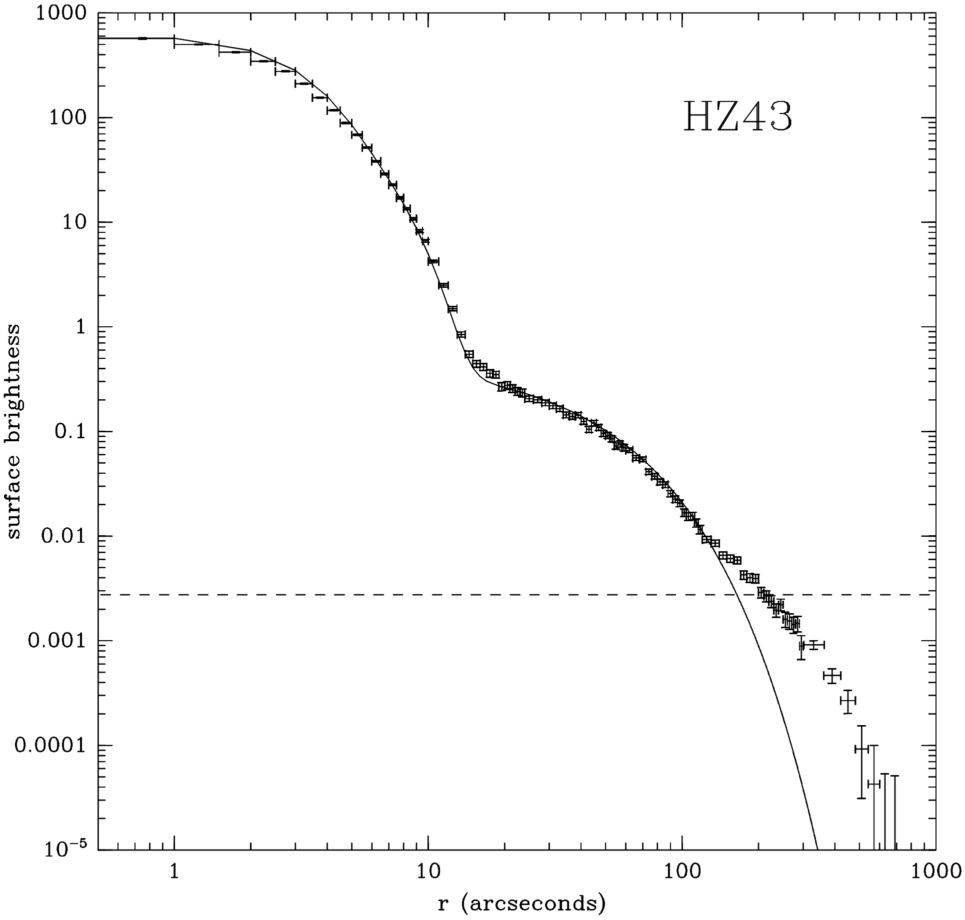

Figure 5.1: The point spread function from a long exposure of HZ43. The surface brightness is in units of counts per pixel. To improve the statistics, the data were binned in increasingly larger annuli (0.5, 1, 2, 4, 10, and 60 arc seconds). The dashed line is the background rate in this observation determined between $8'$ and $12'$ off-axis. Also shown is the parametric form for the PSF.

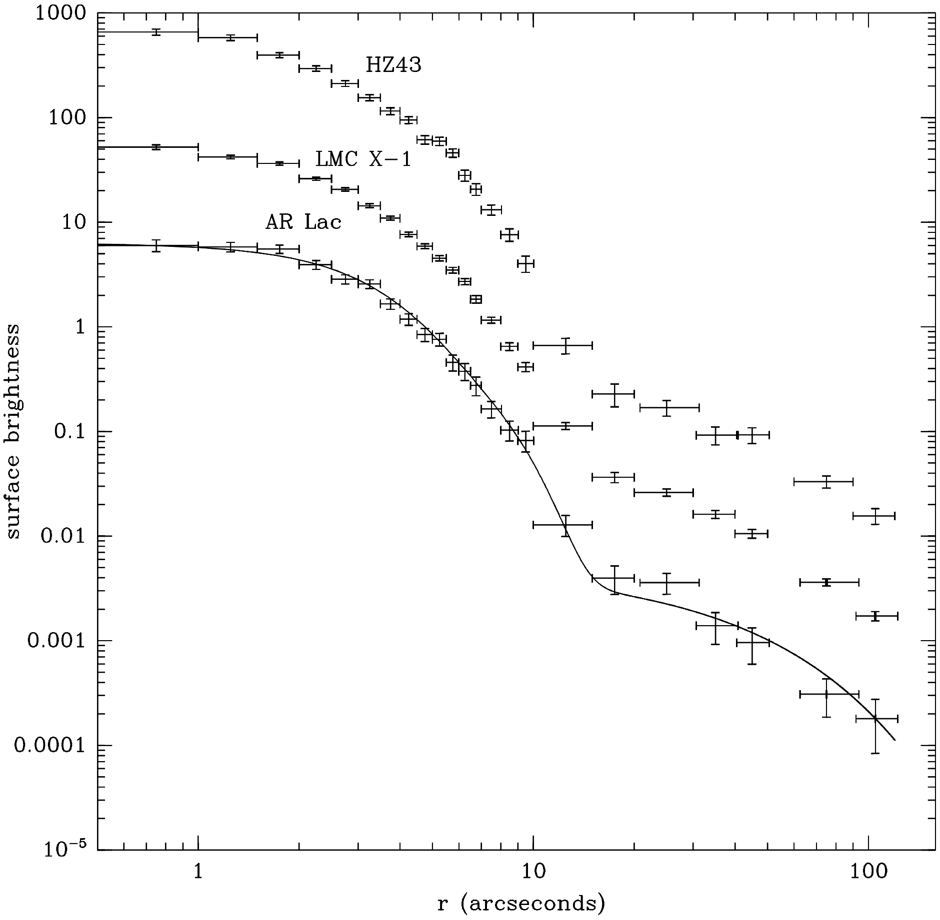

Figure 5.2: A comparison of the point spread functions of HZ43, LMC X-1, and AR Lac with arbitrary normalization. To improve the statistics, the data were binned in increasingly larger annuli (0.5, 1, 2, 5, 10, and 30 arc seconds). Also shown is the parametric form for the PSF normalized to the AR Lac observation.

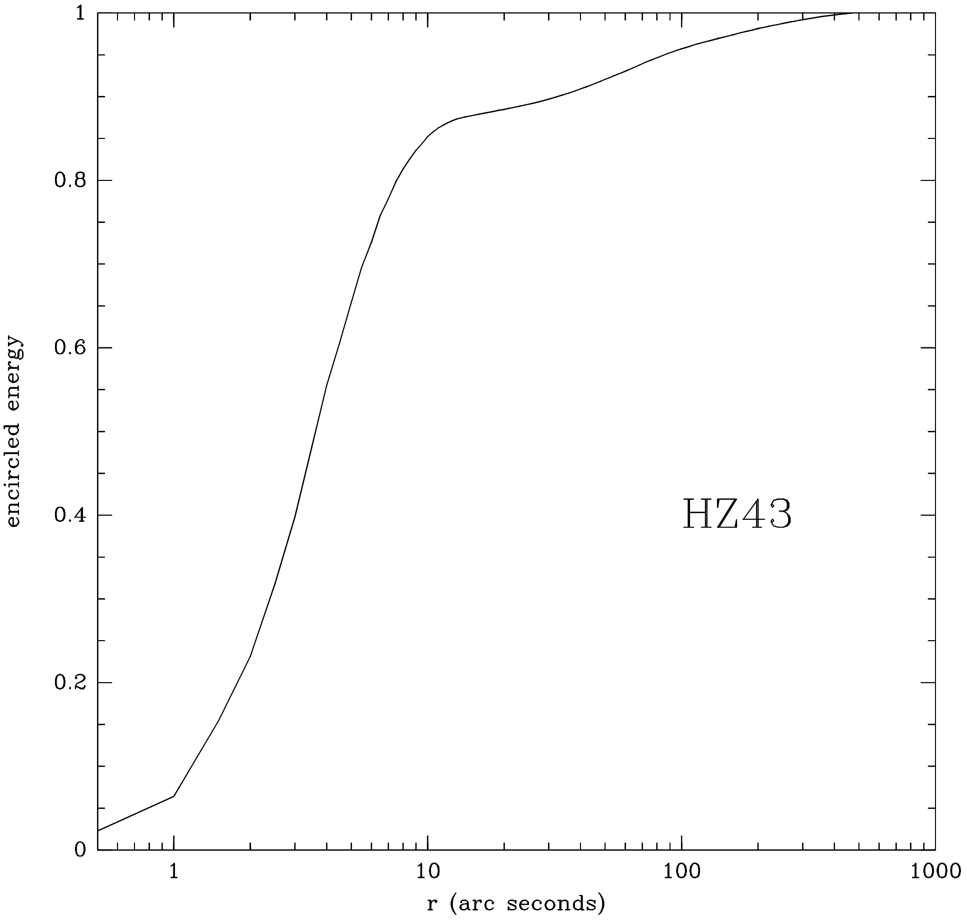

Figure 5.3: The on-axis encircled energy function from a long exposure of HZ43. The profile has been normalized to unity at $8'$. This figure shows that approximately 15% of the power is scattered beyond $10''$, 7% is scattered beyond $1'$, and less than 1% is scattered beyond $5'$.

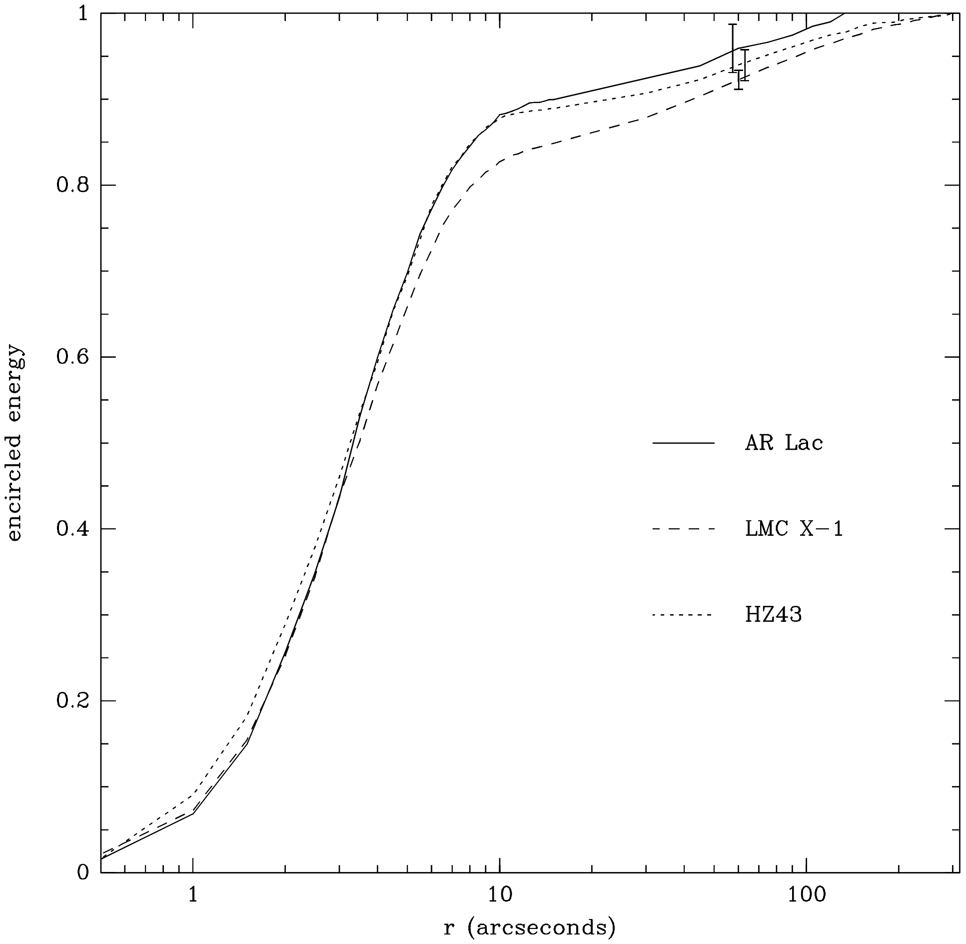

Figure 5.4: A comparison of the on-axis encircled energy functions for observations of HZ43, LMC X-1, and AR Lac. Some extended emission is evident in the profile of LMC X-1. The error bars shown in the figure were all evaluated at $1'$, but were offset slightly on the graph for clarity.

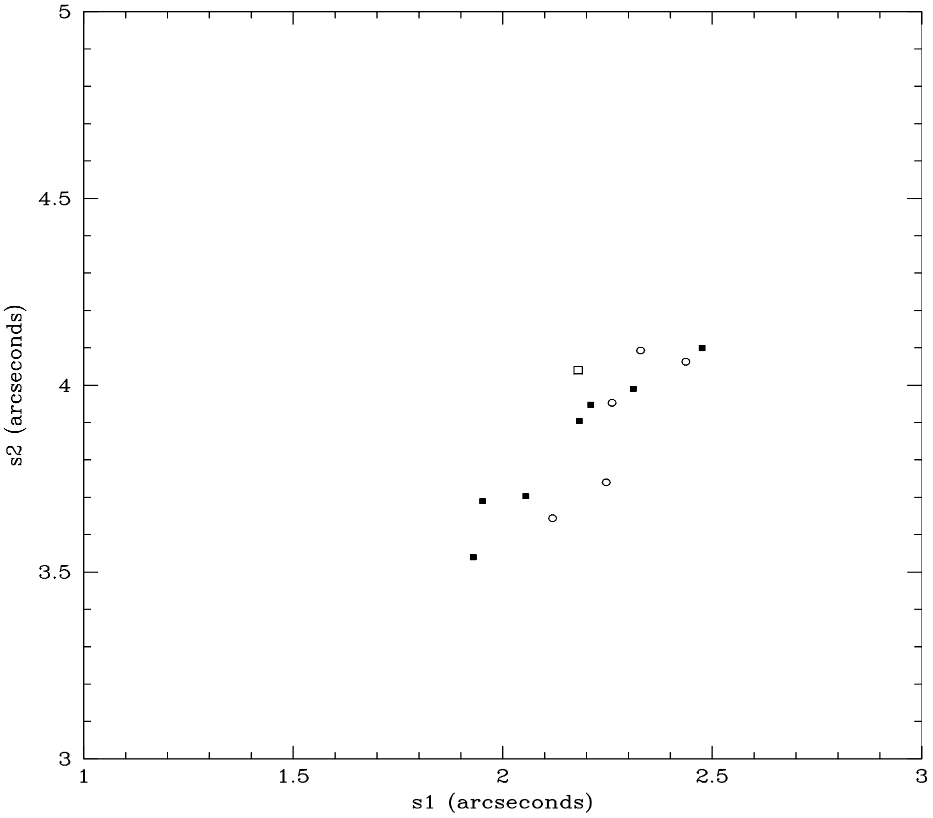

Figure 5.5: The best fit values of S1 and S2 to a sample of point sources observed nearly on-axis (within 3′). The pair of values in the on-axis PSF given above is shown as an open square. Observations of the meaty source are indicated by open circles.

of the PSF to this sample (treating the width and normalizations of the two gaussians as free parameters) shows that the best fit value of S1 varies from 1.9″ to 2.5″, and the best fit value S2 of varies from 3.5″ to 4.1″ (see Figure 5.5). Variations in S1 and S2 between observations of the same source (eg. the meaty source) span almost the entire range of values shown in Figure 5.5.

Residual errors in the aspect solution also occasionally produce asymmetrical features in the PSF. Figure 5.6 displays images of the so-called "meaty source" (a white dwarf star newly discovered with the WFC) illustrating the inner core's appearance when the aspect solution is correct and when there are errors leading to an ellipsoidal image. The major axis of the ellipsoidal images are not aligned with the wobble direction. The asymmetry is the strongest between 5″ and 10″ from the centroid of the image and can have amplitudes up to 30%. When possible, the user should use the image of a known point source within 5′ of their target as a template for the HRI PSF.

The actual two-dimensional PSF has a 16-fold-symmetrical pattern ("radial

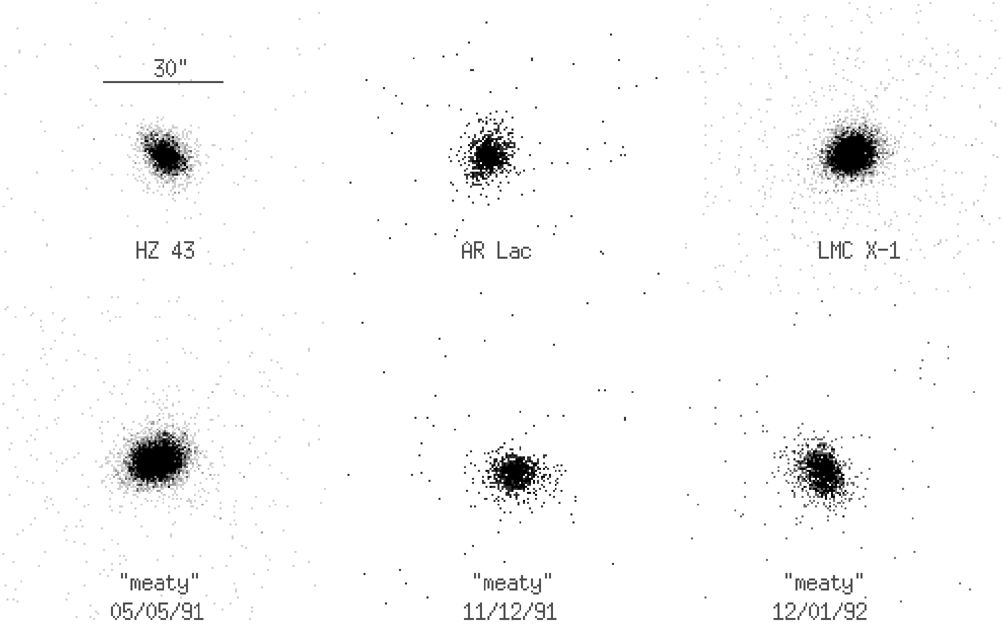

Figure 5.6: Comparison of several nearly on-axis (within a few arc minutes) HRI images of point sources. While the core of the images are symmetrical, the surface brightness between $5'' - 8''$ can exhibit some asymmetry. This feature is randomly oriented (i.e., it is not in the direction of the wobble) and depends on the date of the observation. The three images at the bottom of the figure show the WFC "meaty" source observed at three different times. Notice that the asymmetry is present in the first and last observation, but not in the intermediate observation.

spokes") caused by the shadowing of mirror-scattered X rays by the mirror-support structure, as well as an ellipsoidal component due to an imperfect aspect solution. The radial spokes should only appear in images with large numbers of detected photons in observations which are not "wobbled".

Off-Axis PSF

The spatial resolution of the HRI off-axis is dominated by the XRT PSF which degrades rapidly with increasing off-axis angle. Figures 5.7 and 5.8 display several off-axis pointings of HZ43 and LMC X-1 and illustrate how the images change with off-axis angle. Figure 5.9 shows contours of the HZ43 images. The images were first smoothed with a gaussian filter with $\sigma = 1''$ ($\theta \leq 6.0'$), $\sigma = 2''$ ($8.6' \leq \theta \leq 12.0'$), and $\sigma = 4''$ ($13.5' \leq \theta$). These images show that the PSF starts to degrade beyond $5'$ off-axis. Beyond $12'$ off-axis, the images become very asymmetrical. A central "bar" in the images well off-axis is perpendicular to a line connecting the optical axis and the image centroid.

The 50% power radius was determined for a series of off-axis pointings of HZ43, AR Lac, and LMC X-1. The asymmetry at large angles has been ignored and the 50% power radius has been computed from radial binning about the image

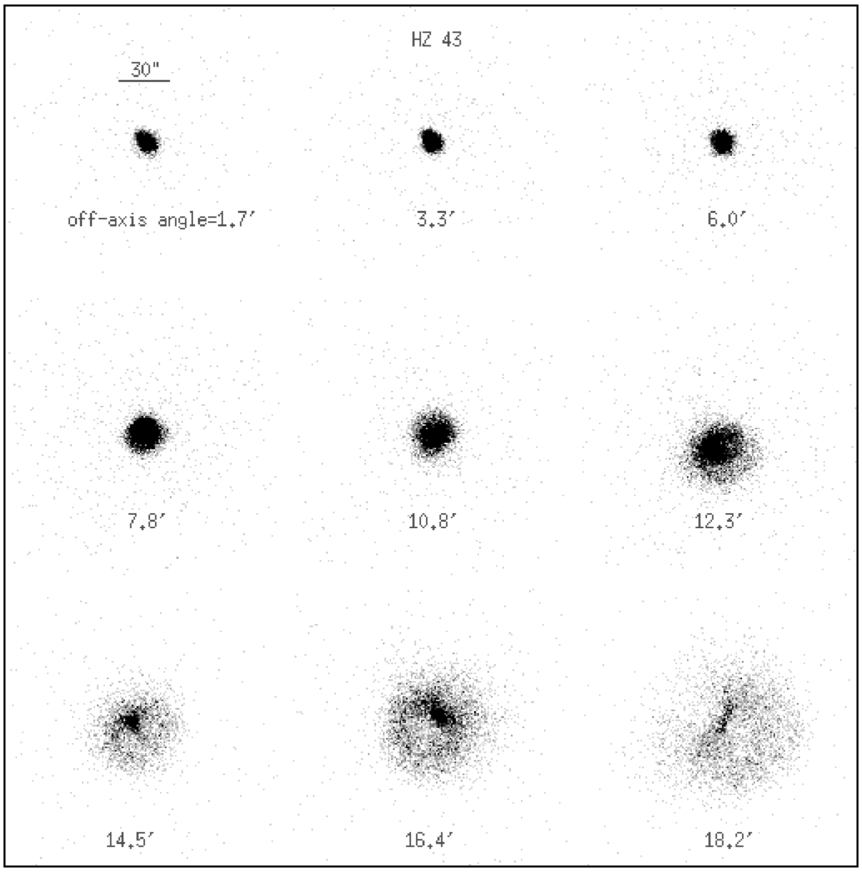

Figure 5.7: HRI images of HZ43 at nine different angles off-axis.

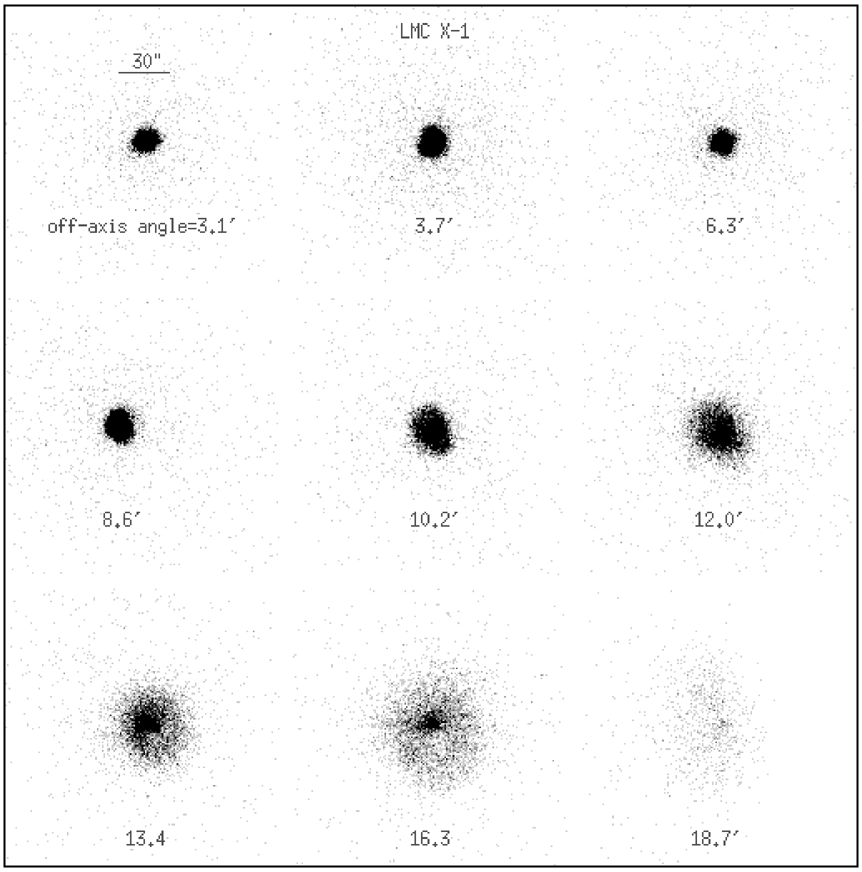

Figure 5.8: HRI images of LMC X-1 at nine different angles off-axis.

centroids. Figure 5.10 is a plot of the 50% power radius as a function of off-axis angle for these sources. The solid curve is the best-fit to the following parametric representation of the 50% power radius.

$$r_{50} = \frac{2.35}{2}[\sigma^2_{HRI} + \sigma^2_{aspect} + (\sigma_{mirror} + a\theta^b)^2]^{0.5} \text{ arcsec}$$

where θ is given in arc minutes, with the following values for the parameters:

$$\begin{aligned} \sigma_{HRI} &= 0.74 \text{ arcsec} \\ \sigma_{aspect} &= 1.0 \text{ arcsec} \\ \sigma_{mirror} &= 1.3 \text{ arcsec} \\ \text{a} &= 0.0205 \\ \text{b} &= 2.349 \end{aligned}$$

It is best to use a circle of radius r_{50} when extracting counts of a source detected off-axis. The total net count rate (corrected for scattering) is then simply twice the net count rate within r_{50}.

A parametric representation of the azimuthally averaged off-axis HRI PSF has also been derived which is a simple extension of the on-axis expression. To

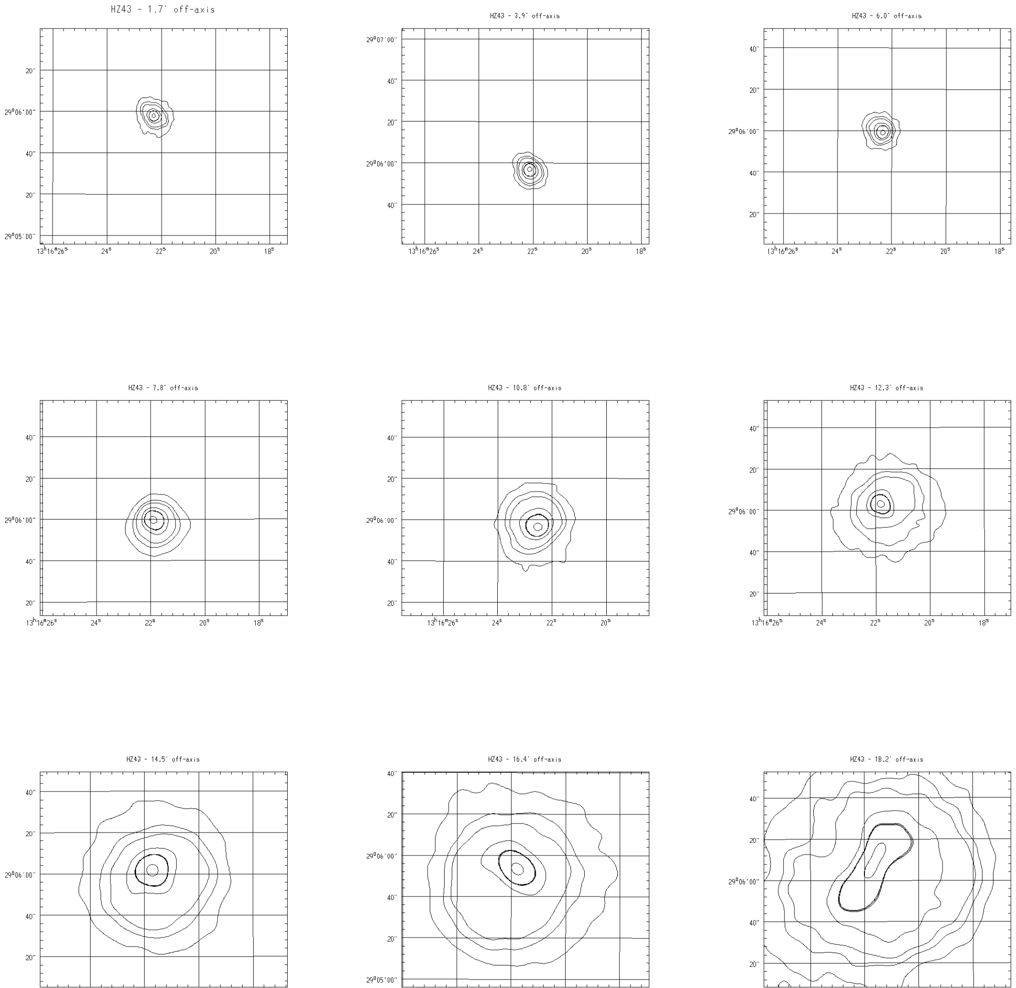

Figure 5.9: Contour plots of the HZ43 images. The contours are at 1, 5, 10, 30, 50, and 90% of the peak value, with the 50% contour level shown in bold.

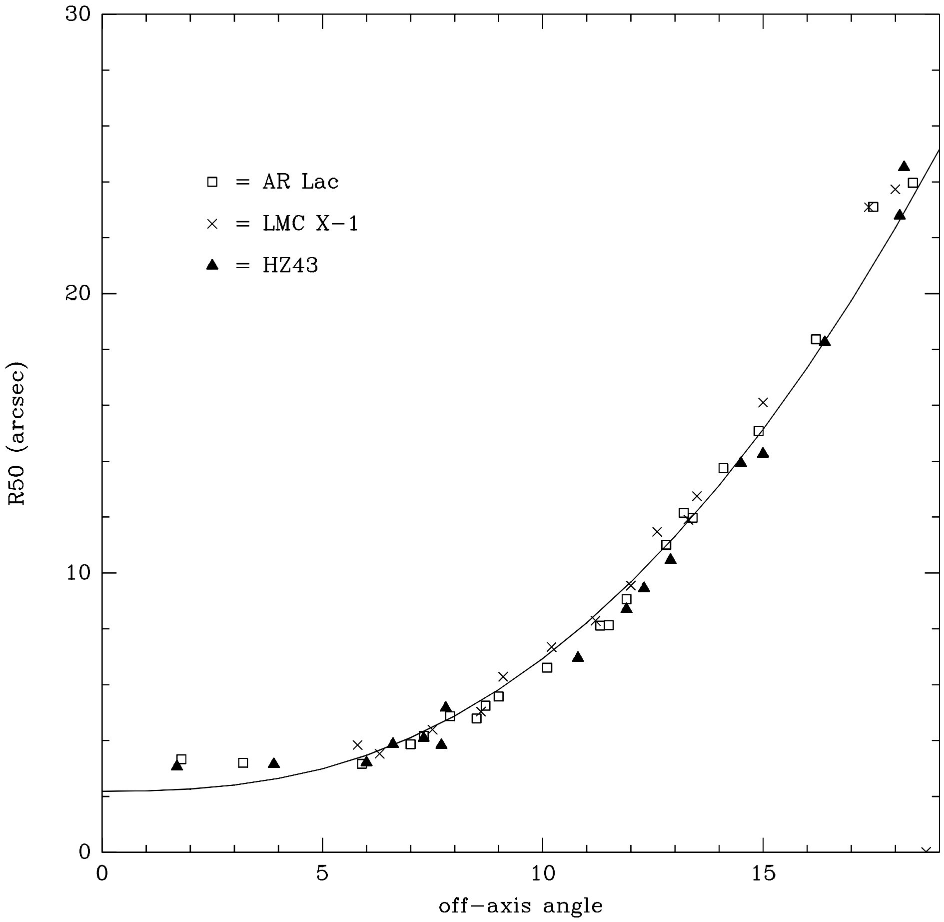

Figure 5.10: The 50% power radius in images of HZ43, LMC X-1, and AR Lac as a function of angle off-axis. The parametric expression given in the text is also shown for comparison.

determine the off-axis PSF we generated surface brightness profiles for 8 observations of HZ43, spanning a range from $2'$ to $16'$ off-axis. The peak surface brightness was used as the origin, since this generates a monotonically decreasing profile. The set of 8 HZ43 surface brightness profiles were first fit to the on-axis PSF, treating the normalization and width of the two gaussians as free parameters (the photon statistics in these data were insufficient to fit the exponential term). We found that the best fit values of the smaller gaussian were essentially independent of the angle off-axis. We then refit the set of 8 profiles treating only the width of the broader gaussian as a free parameter. The best fit values of s2 are well parameterized by a cubic polynomial in the off-axis angle, and are given by

$$S2 = 3.3 + 0.019\theta - 0.016\theta^2 + 0.0044\theta^3$$

where theta is the angle off-axis in arc minutes. Substituting this expression into the on-axis HRI PSF gives the general off-axis representation.

NB: We do not force this expression to reproduce the on-axis value given above. The fact that this expression gives S2 = 3.3 for $\theta = 0$, compared to the on-axis value of 4.0 given above, reflects the variation in aspect quality from observation to observation.

Users should note that point sources observed off-axis exhibit significant amounts of nonazimuthal symmetry. The above expression is useful for determining scattering corrections and for use in detect algorithms, but should not be used for image deconvolution. There are a large number of sequences in the PROS calibration directory xrcal containing several objects observed at different angles off-axis. The actual HRI data should be used for any two-dimensional image deconvolution.

5.2.3 Effective Area

The effective area of the HRI/XRT is the product of the HRI quantum efficiency and the XRT collecting area. The XRT collecting area has been determined from ground tests with the PSPC. The HRI quantum efficiency was also determined in ground tests.

On-axis Effective Area

Figure 5.11 (which appeared as Figure 11.1 of Appendix F) is a plot of the on-axis effective area of the HRI/XRT as a function of incident energy; this function is tabulated in Table 5.3 (Table 11.1 of Appendix F).

Off-axis Effective Area

The XRT effective area varies smoothly with off-axis angle and energy. Figure 5.12 shows the XRT vignetting function (normalized to unity on-axis) for a range of photon energies. Vignetting is less than a 10% effect within $10'$ at

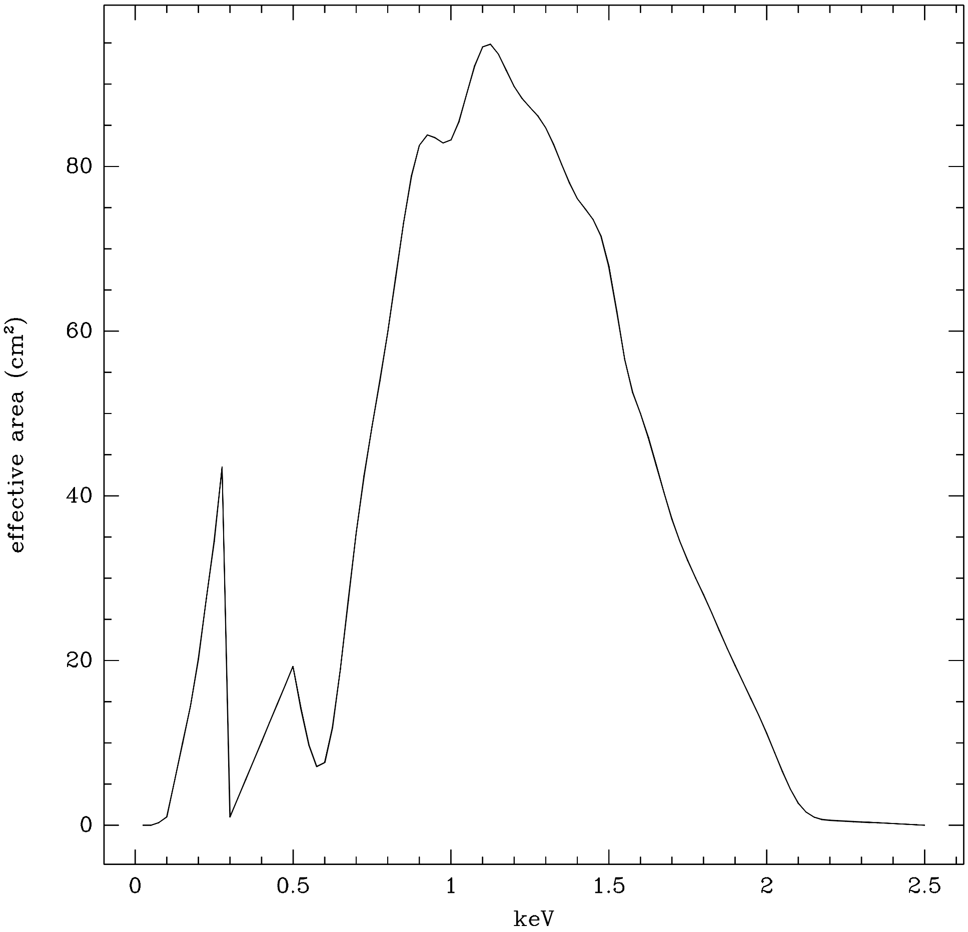

Figure 5.11: The on-axis effective area of the XRT/HRI vs photon energy

Table 5.3: *ROSAT* XRT+HRI Effective Area

Energy (keV)	Lambda (Å)	Effective Area (cm^2)	Energy (keV)	Lambda (Å)	Effective Area (cm^2)
0.10	124.0	1.0	1.10	11.3	94.5
0.20	62.0	20.2	1.20	10.3	89.7
0.28	44.3	43.5	1.30	9.5	84.7
0.28	44.1	0.0	1.40	8.9	76.1
0.30	41.3	1.0	1.50	8.3	56.5
0.40	31.0	10.6	1.60	7.8	50.0
0.50	24.8	19.3	1.70	7.3	37.2
0.60	20.7	7.6	1.80	6.9	28.0
0.63	19.7	11.9	1.90	6.5	19.4
0.70	17.7	35.5	2.00	6.2	11.2
0.80	15.5	59.9	2.10	5.9	2.7
0.90	13.8	82.6	2.20	5.6	0.6
1.00	12.4	83.2	2.30	5.4	0.4
			3.40	5.2	0.2

all energies of interest. The vignetting function at 1.0 keV is well fit with the following parametric representation:

$$V(\Theta) = 1.00 - 1.49 \times 10^{-3}\Theta - 3.07 \times 10^{-4}\Theta^2$$

where Θ is in units of arc minutes.

The spatial uniformity of the HRI quantum efficiency was measured six months before launch in a series of flat field tests at three energies: 0.28, 0.93, and 1.49 keV. The quantum efficiency of the HRI varies by less than 10% over the detector and is nearly energy independent. Figure 5.13 is a representative contour plot of the spatial variation in the quantum efficiency of the HRI.

Long-term stability

It appears that the effective area has not varied significantly since launch. Observations of the sources HZ43, Vega, A2256, and N132D at several epochs yield non-varying count rates:

Source Count Rates

Table 5.5 shows measured HRI count rates for a sample of sources and compares these rates to that of the PSPC and the *Einstein* Observatory HRI and IPC.

5.2.4 Background

The HRI in-orbit background is composed of several components:

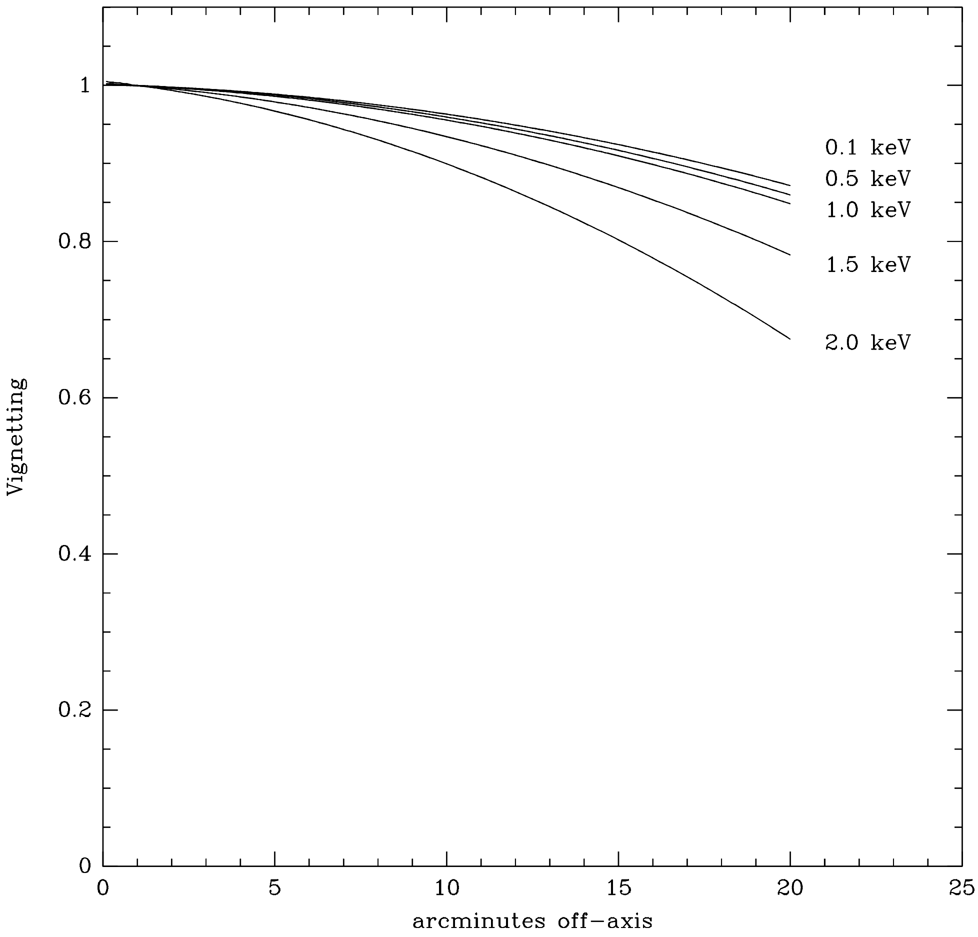

Figure 5.12: The vignetting function of the XRT at 5 photon energies in the HRI field of view. The vignetting function is normalized to unity on-axis.

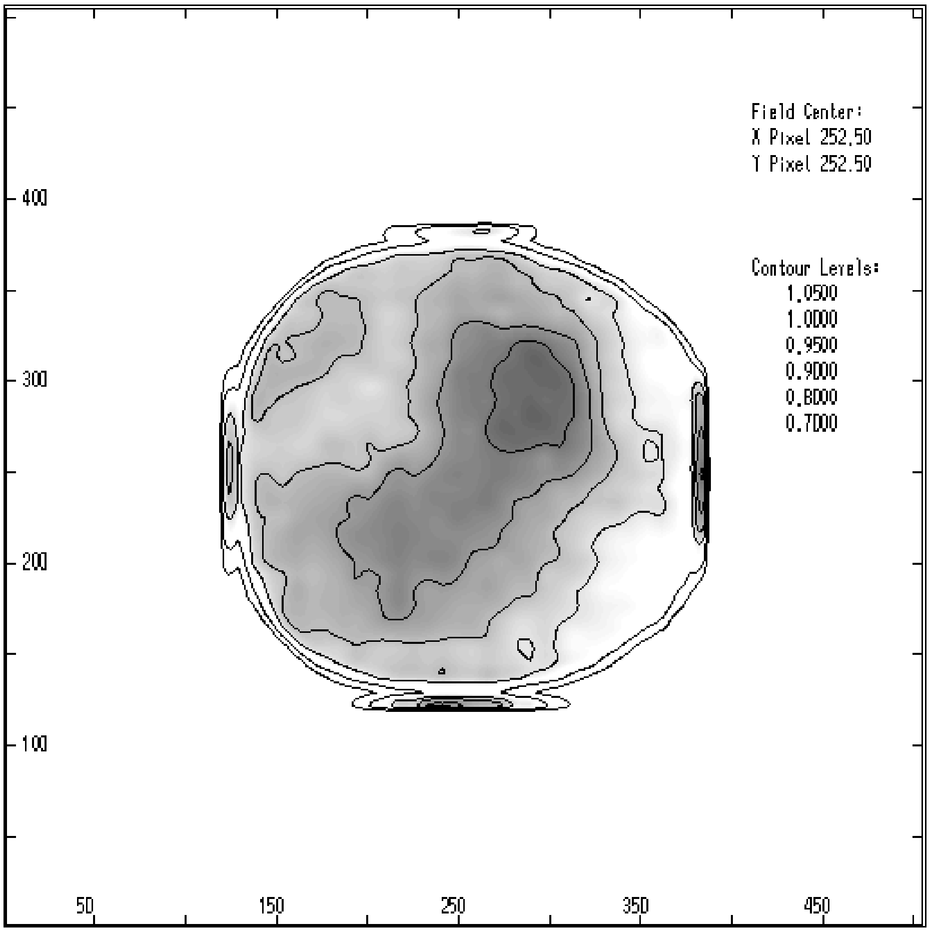

Figure 5.13: Contours of the HRI QE map used by the on-line processing (SASS). The image has been blocked by a factor of 16 yielding 8″ pixels. The QE map shown in this figure was generated by combining ground based flat field measurements at C(0.28 keV), Cu(0.93 keV), and Al(1.49 keV) in the correct proportions for a power law spectrum with an energy index of -1. The composite image was then smoothed with a 32″ gaussian producing statistical errors of 1%. The QE is normalized to unity on-axis and the contours are at 0.7, 0.8, 0.9, 0.95, 1.0, 1.05 and decrease outward. Note that the QE of the HRI varies by less than 10% over most of the field of view.

Table 5.4: HRI QE Stability

Source	Date of Observation	Count Rate (counts s^{-1})
A2256	1990 July 1	0.61 ± 0.01
	August 3, 1992	0.62 ± 0.01
HZ43	1990 July 2	12.3 ± 0.2
	1991 December 11	12.0 ± 0.2
	1992 June 9	11.91 ± 0.04
Vega	1991 March 20	0.10 ± 0.01
	1992 March 21	0.11 ± 0.01
	1992 September 18	0.10 ± 0.01
N132D	1990 July 3	4.41 ± 0.13
	1991 February 9	4.77 ± 0.02
	1992 September 18	4.89 ± 0.06
	1993 April 17	4.61 ± 0.04
	1994 January 10	4.51 ± 0.04
	1994 July 15	4.65 ± 0.05
	1995 February 11	4.54 ± 0.04
	1995 March 11	4.68 ± 0.04

Note: The count rate for A2256 is determined from the net emission within a $6'$ radius.

Table 5.5: X-ray Count Rates (counts s^{-1}) for Different Instruments

	Object	*ROSAT* HRI	*Einstein* HRI	*ROSAT* PSPC	*Einstein* IPC
	HZ43	12.0	3.6	100	3.8
v	AR Lac	0.65	0.69	7.4	1.3
v	Cyg X-2	72	27.8	180	NA
v	LMC X-1	3.8	1.3	10	10.55
v	LMC X-3	2.6	2.7	NA	NA
	Cas A	17	6.3	57	61
	Tycho	10.2	3.4	NA	22.3
	Kepler	5.4	1.7	NA	7.3
	E0102.2-72.2 (SMC SNR)	0.96	0.25	NA	0.79
	N132D	3.6	1.1	10.6	4.0
a	A2256	0.62	NA	1.7	0.34

Notes: v - variable source; a - the count rate for A2256 is determined from the net emission within a $6'$ radius.

Table 5.6: HRI Background Rates

Internal	1.5 (1.0-2.0)	counts s^{-1}
External	3.0 (1.0-10)	counts s^{-1}
XRB	1.0 (0.5-2.0)	counts s^{-1}
Total	5.5 (2.5-14)	counts s^{-1}
	7.8×10^{-1}	counts s^{-1} cm^{-2}
	3.8×10^{-3}	counts s^{-1} $arcmin^{-2}$
	1.1×10^{-6}	counts s^{-1} $arcsec^{-2}$

a) The internal background is believed to come mainly from residual radioactivity in the MCP glass and the surrounding detector structure. This was measured on the ground with a rate of $\sim$ 1.5 counts s^{-1} over the entire device. This appears to be a stable component of the background and is uniform over the detector.

b) The X-ray background (XRB) contribution (comprised of both galactic and extragalactic components) varies across the sky, with a typical value in the *ROSAT* energy band of 1.0 count s^{-1}, over the detector.

c) The externally induced background from charged particles, earth scattered solar radiation, and auroral photons. On average, the externally induced background rates are higher for *ROSAT* than for *Einstein* due to the higher inclination and altitude of the orbit. The external background rates vary considerably during an orbit and also from orbit to orbit, with a minimum of 1 count s^{-1} up to about 10 counts s^{-1}, at which point the HRI high voltage is reduced to protect the detector from overload.

Figure 5.14 shows the variation in the background rate during an HRI observation of the North Ecliptic Pole (NEP). The lowest rates occur when the satellite is crossing the equator and the highest rates occur at the northern and southern extremities of the orbit. In many cases the HRI high voltage needs to be reduced in these regions to protect the detector from overload. Table 5.6 summarizes the average in-orbit values (and ranges) of all the background components.

Figure 5.15 compares the pulse height analyzer (PHA) distribution of the background in the NEP observation during low background intervals (count rate $<$ 5.0 counts s^{-1}; dominated by detector noise and the XRB) and high background intervals (count rate $>$ 5.0 counts s^{-1}; dominated by externally induced background events). Even though the background is dominated by different particles during these intervals, the spectra are consistent given the very modest energy resolution of the HRI. The background rate is the greatest in the lowest PHA channels since radioactive decay in the MCP glass and charged particles can produce electrons anywhere within the MCPs. These electrons are accelerated through through a smaller potential difference than electrons produced near the entrance of the MCPs. The background in PHA channels $<$ 10 is very uniform across the detector. The background in PHA channels $>$ 10 is enhanced beyond $15'$ off-axis due to the greater gain in the detector (see §3.5).

Also shown in Figure 5.15 is the PHA distribution in an HRI observation of AR Lac. Notice that the AR Lac spectrum is much more strongly peaked than the background spectrum. Most of the AR Lac source photons fall between PHA channels 3 and 7. In general, to obtain maximum sensitivity for detecting point sources or for analyzing low-surface brightness extended objects, the user is advised to screen out the highest background intervals and only examine PHA channels between approximately 3 and 8, inclusive. The optimum range of PHA channels depends on the source, the source position on the detector, and the date of observation. The user is advised to compare the source and background spectra for each observation to determine which channels should be screened out.

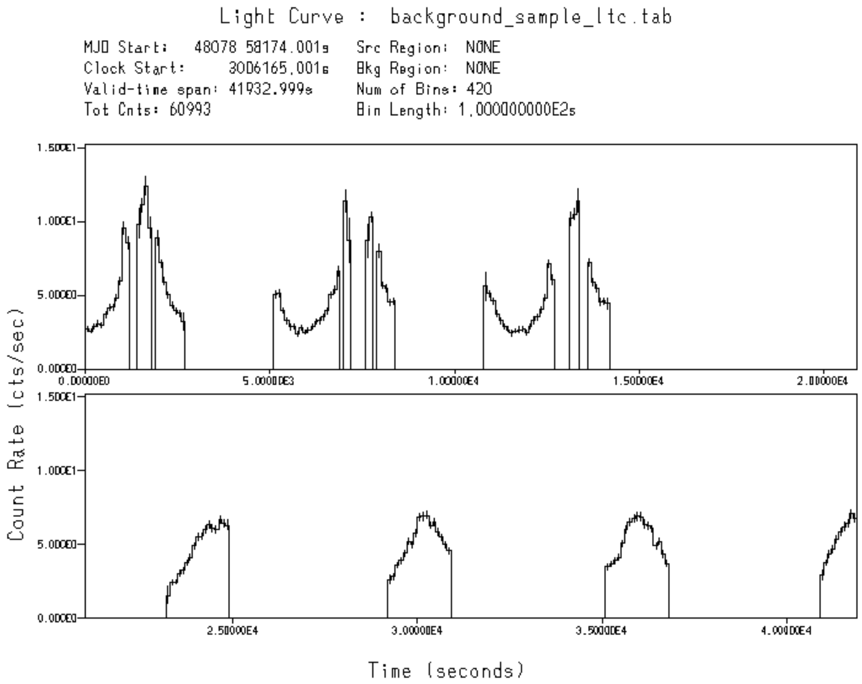

```
Light Curve :  background_sample_ltc.tab
MJD Start:   48078 58174.001s   Src Region:  NONE
Clock Start:      3006165.001s   Bkg Region:  NONE
Valid-time span: 41932.999s     Num of Bins: 420
Tot Cnts: 60993                 Bin Length: 1.000000000E2s
```

Figure 5.14: The background rate over the entire HRI field in a portion of the 40 ksec observation of the NEP

5.2.5 Spectral Response

The HRI, with its CsI-coated MCPs, was found during ground testing to possess a crude spectral sensitivity which has been verified with in-flight data. Because such a capability lies beyond the baseline HRI requirements, however, resources to permit the quantitative exploitation of this potential were never part of the RSDC budget. Consequently, although we have acquired the necessary data to make this possible, the actual task of fully understanding and calibrating the HRI spectral response has not been completed. Any efforts to derive quantitative spectral results from HRI data must therefore entail extensive, careful analysis on the part of individual investigators.

Figure 5.16 shows the PHA distribution from ground-based measurements at 7 energies, and Table 5.7 lists the mean PHA channel at each energy. Note that there is a systematic increase in the mean pulse height channel with increasing photon energy except for the Si line (the Si measurement may have been affected by the presence of Si in the glass in the microchannel plates). Table 5.7 shows that the mean PHA varies by approximately 2 channels over the energy range of the *ROSAT* mirror.

Spatial Gain Variations

It was also found from the ground based flat-field measurements that the gain of the HRI varies spatially across the detector. Figure 5.17 is a contour map of

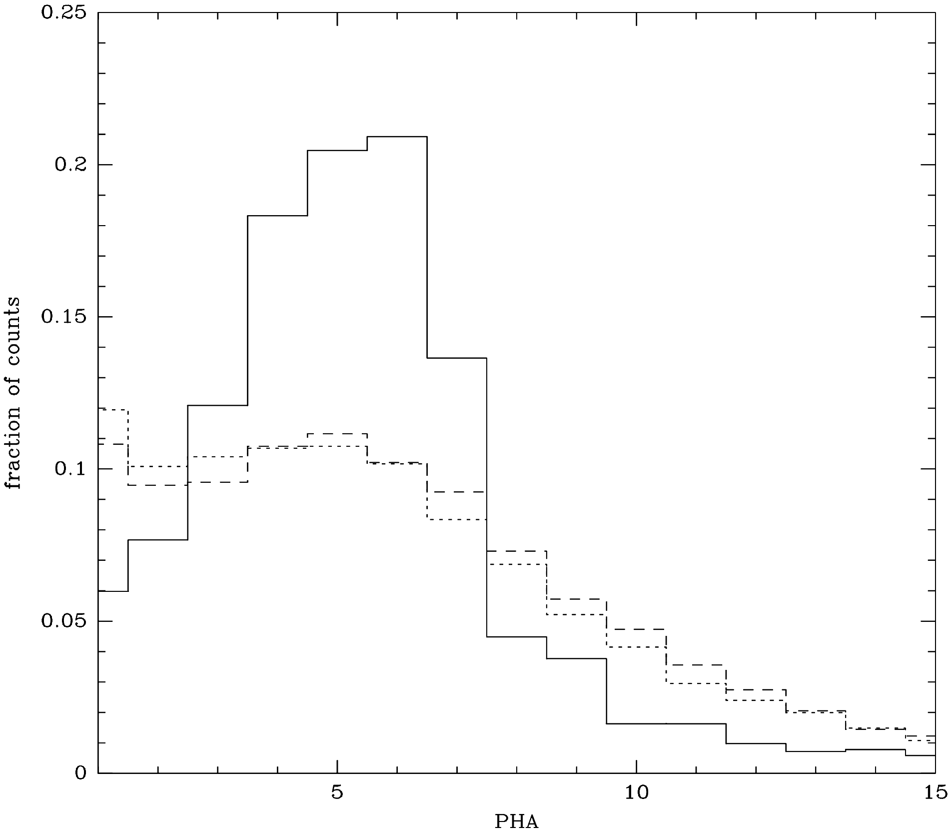

Figure 5.15: The PHA distribution of the HRI background during high background intervals (dashed curve), low background intervals (dotted curve), and AR Lac (solid curve)

Table 5.7: Mean PHA from Ground-Based Measurements

X-ray target	mean PHA
B (0.18 keV)	3.30
C (0.28 keV)	3.96
O (0.53 keV)	3.99
Fe (0.71 keV)	4.15
Cu (0.93 keV)	4.58
Al (1.49 keV)	5.44
Si (1.74 keV)	4.82

the mean pulse height channel for the Cu-K (0.93 keV) flat field data averaged over a spatial scale of about $1'$. The mean pulse height channel increases from 4 near the center of the detector to approximately 7 near the edge. However, within $5'$ of the optical axis, the gain only varies by 10%. The spatial variation in the gain is also similar at all photon energies. In Figure 5.18 we show the computed average channel for HZ43 and N132D plotted against the expected value at that position on the detector from the Cu gain map.

The RSDC at SAO has produced fits versions of the gain maps such as that shown in Figure 5.17 (available via anonymous ftp: sao-ftp.harvard.edu and on legacy). These maps have a scale of $8''$/pix and are thus useful (when rolled to match an observation) for determining the relative gains of features. Users should be mindful that (a) The gain maps were made from ground calibrations before launch, and therefore do not represent accurate values for any given date during the mission (see the next section); (b) the normal satellite's wobble will mean that any X-ray feature will actually experience the gains from somewhat different areas of the detector; and (c) observations taken over intervals of more than a few days will have a range of roll angles.

Temporal Gain Variations

The pulse height distribution for celestial sources and the UV calibration lamp have displayed a systematic change during the first 4 years of the mission: The peak and mean pulse height channel have shifted to lower values. Figure 5.19 shows the pulse height distribution of three HRI observations of N132D. Notice that the peak (and mean) in the pulse height distribution had decreased by 2 channels before the high voltage increase, a change comparable to the difference between the response of the HRI to the Al-K line (1.49 keV) and B-K line (0.18 keV) measured during the ground based tests.

We have used the in-orbit bright earth data to monitor the gain map, and determine whether the spatial structure observed during ground-based tests has varied during the mission. By composing gain maps of the bright earth data we find that the decrease in the HRI gain evident in Figure 5.19 is uniform across the detector.

Spectral Response Matrix

G. Fraser (1992, file "spec_resp_zero.tex", available on GSFC anonymous ftp node legacy.gsfc.nasa.gov, in sub-directory "/rosat/doc/hri") has analyzed the on-axis ground based data by fitting Pearson functions to the 7 pulse height distributions shown in Figure 5.16. A detailed analysis of his results are given in his report. The relative FWHM of the fitted pulse height distributions vary from 66% (for the Al-K and Fe-K lines) to 107% (for the B-K line). Fraser concludes that "the average pulse height per pixel has very little dynamic range and is a very poor indicator of photon energy". However, he also notes that "the softness ratio, (counts in channels 1-5)/(counts in channels 6-11), used by (Wilson *et al.* 1992, Ap.J. Lett., 391, L75) does seem the most sensitive energy indicator that can be constructed." (As noted below, the actual channels fulfilling this purpose will change as a function of the temporally-dependent gain.)

Using the ground-based data (see Figure 5.16) we constructed a spectral redistribution matrix for the HRI. We then fit the pulse height distributions of several observations of HZ43 and one observation of 3C273. PSPC spectra of HZ43 are well fit with an unabsorbed black body spectrum with a temperature of 0.02 keV ($\chi^2 = 27$ for 24 degrees of freedom). Table 5.8 lists the χ^2 values obtained by fitting the HRI observations of HZ43 with the same unabsorbed black body spectrum, with only the normalization treated as a free parameter. The minimum χ^2 values are extremely high no matter what PHA channels are included in the fit. The best fit absorbed power-law model to the PSPC spectrum of 3C273 is obtained with $N_{\rm H} = 1.6 \times 10^{20}$ cm^{-2} and an energy index of $\alpha = 0.9$. Since the HRI observation of 3C273 has 30,000 net counts we fit the HRI spectra with 0, 2, and 5% systematic errors, added in quadrature with the statistical errors. Table 5.9 lists the minimum χ^2 values obtained by fitting the HRI observation of 3C273 with $N_{\rm H}$ and α fixed. We also fit the HRI pulse height distribution treating α as a free parameter. The best fit energy index so obtained for 3C273 is significantly steeper than that obtained from the PSPC observation.

Hardness Ratios

While it is very difficult to obtain quantitative spectral information from the HRI (i.e., temperatures or power-law indices), it is still possible to obtain qualitative information on a scale of a few arc minutes using hardness (or softness) ratios. Wilson *et al.* (1992, Ap.J. Lett., 391, L75) showed that the extended emission in NGC1068 is harder than the nuclear component using a softness ratio defined by the channels [1:5]/[6:11]. Since the HRI gain varies temporally and spatially, the user may want to define the PHA boundaries on a case by case basis. For example, in the two observations of N132D shown in Figure 5.19, the fraction of the total counts in PHA channels $6 - 11$ decreased from 40% to 10%.

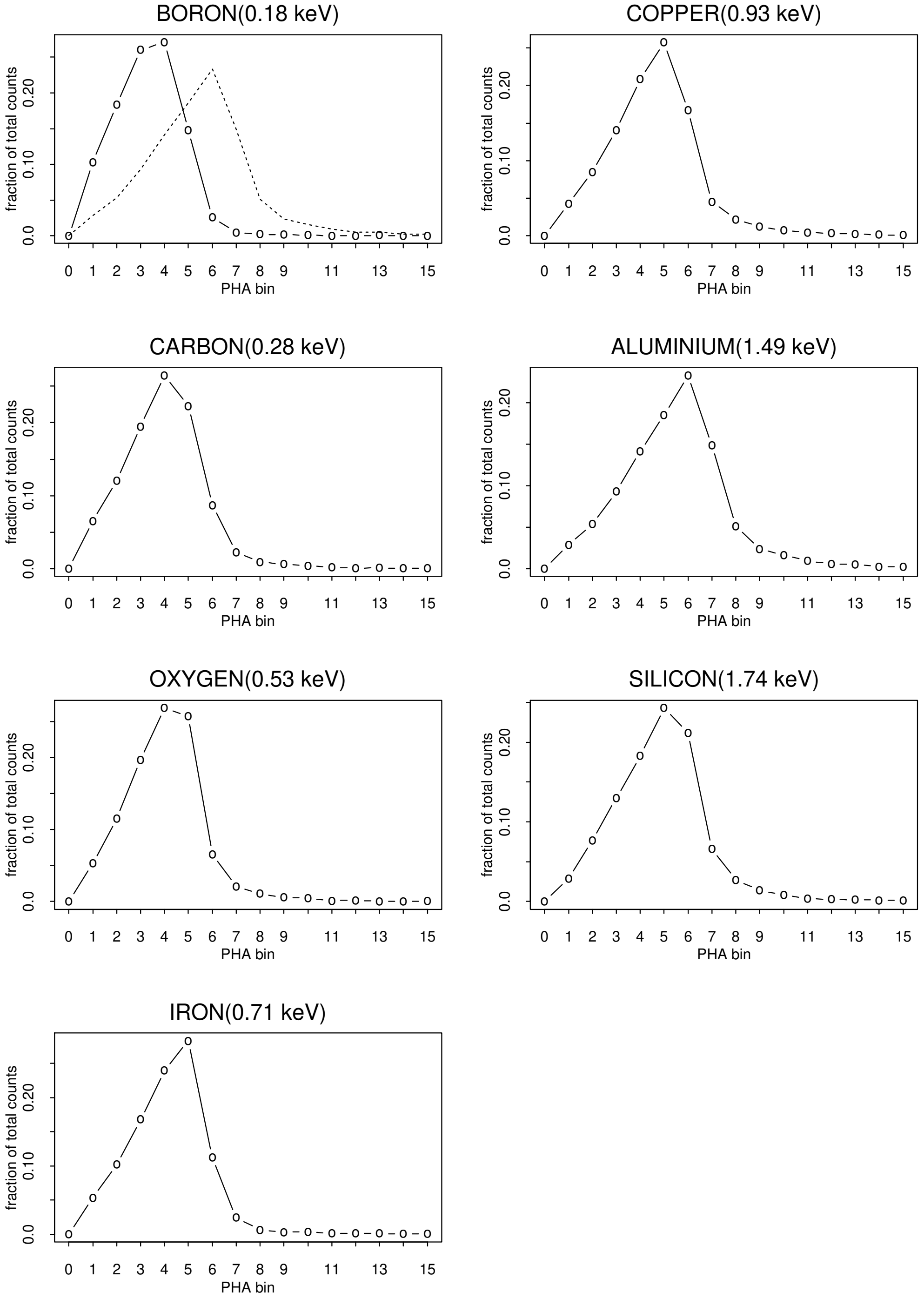

Figure 5.16: The pulse height distribution from ground-based measurements at 7 energies within a $1' \times 5'$ strip centered on the detector The dashed curve in the Boron panel is the PHA distribution of the Al data, and is included to show the full spectral range.

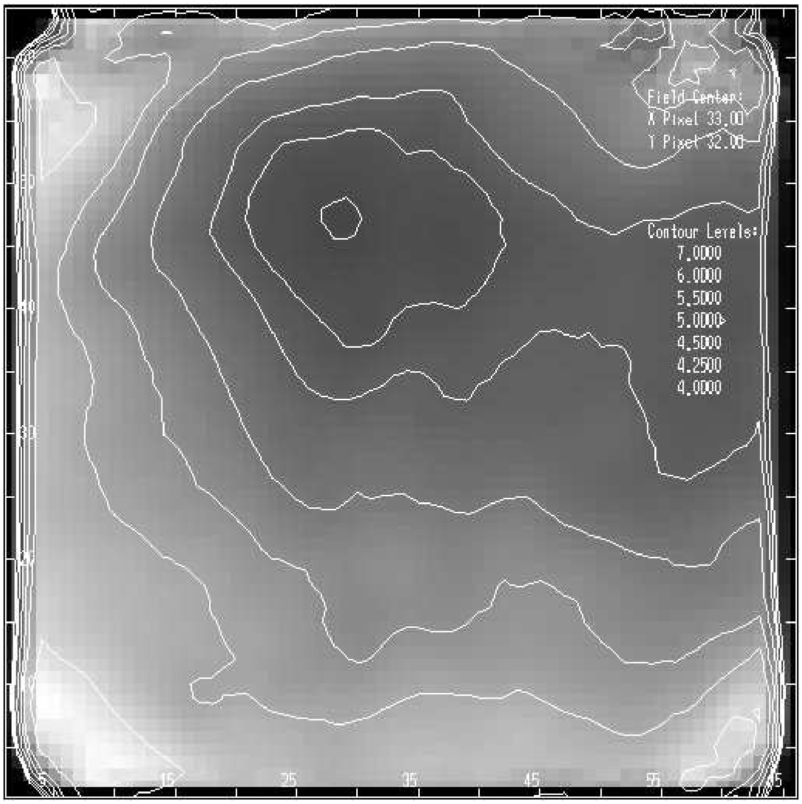

Figure 5.17: The spatial variation in the centroid of the pulse height distribution in the ground based Cu(0.93 keV) flat field image. The image was first blocked by a factor of 64, producing 32″ pixels with 1% statistical errors. The contours are at PHA values of 4.0, 4.25, 4.5, 5.0, 5.5, 6.0, 7.0 and increase outward.

Table 5.8: Spectral Fitting Results for HZ43

sequence	date	off-axis angle (arcmin)	χ^2 [1:6]	χ^2 [2:6]	χ^2 [3:6]
110196	7/2/90	1.7	373	354	332
110198	7/2/90	3.9	457	-	-
110197	7/2/90	7.8	1685	-	-
141809	12/11/91	1.3	60	-	-

Note: This table lists the results of fitting HRI observations of HZ43 with a redistribution matrix derived from the ground based flat field tests. The extracted pulse height distributions are fit to an unabsorbed black body model with kT=0.02 keV, which gives an acceptable fit to the PSPC observations of HZ43. The pulse height channels included in the fit are given in in the brackets.

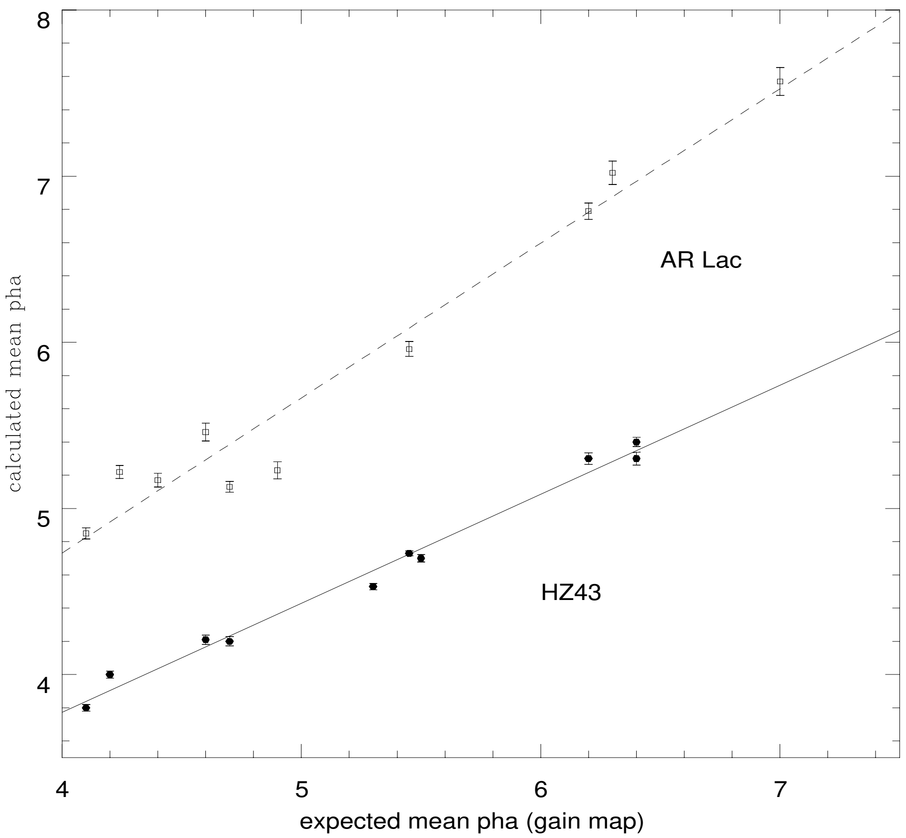

Figure 5.18: PCV phase observations of HZ43 and AR Lac were taken at many positions on the detector surface. The observed mean PHA of the calibration source measurements are plotted with errors against the expected mean PHA from the ground based measurements of copper (0.93 keV). The line represents the best least squares fit of the data points.

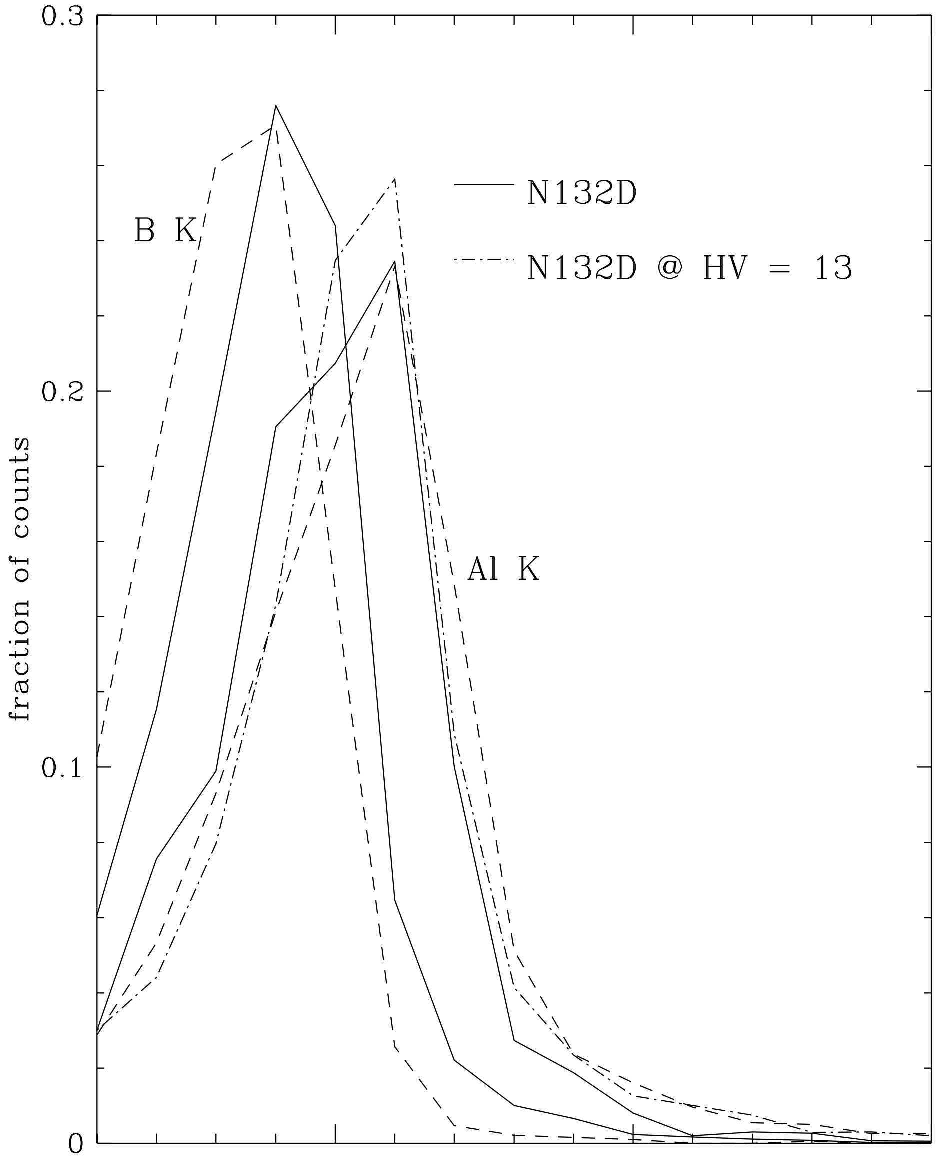

Figure 5.19: The pulse height distribution in 3 HRI observations of N132D. The highest gain observation (solid line) was taken during the PCV phase, the lowest gain observation was taken in 1993 April, and the observation shown in the dot-dash line was taken in 1994 July, just after the HV increase. Also shown (dashed lines) are the pulse height distributions of the Al-K (1.49 keV) and B-K (0.18 keV) lines obtained during the ground based tests. Although the total count rate (in all PHA channels) has remained nearly constant (see Table 5.4), the earlier observations show a downward trend in the peak of the distribution. The latest observation shows that the HV increase has restored the peak to within 0.5 channels of the original.

Table 5.9: Spectral Fitting Results for 3C273

systematic error	χ^2 $N_{\rm H}$ and α fixed	χ^2 $N_{\rm H}$ fixed, α free	α
0%	2634	1547	2.5 ± 0.1
2%	1198	55	2.6 ± 0.1
5%	318	13	2.6 ± 0.2

Note: This table lists the results of fitting an HRI observation of 3C273 with a redistribution matrix derived from the ground based flat field tests. The second column gives the value of χ^2 obtained by fitting PHA channels 1 through 6 to the best fit absorbed power-law model from the PSPC observation of 3C273 ($N_{\rm H} = 1.6 \times 10^{20}$ cm^{-2} and $\alpha = 0.9$). The third column lists the minimum χ^2 obtained with $N_{\rm H} = 1.6 \times 10^{20}$ cm^{-2}, and α treated as a free parameter. The fourth column gives the best fit value of α with the 90% confidence limits for one interesting free parameter.

5.2.6 UV Response

The preflight prediction of the detector UV response was underestimated. Vega (V = 0.03, A0 V, distance= 8.1 pc), a star relatively bright in the UV, gives a count rate of 0.10 counts s^{-1} (7 times that of the *Einstein* HRI), and beta Car (V = 1.68, A0 III, distance=26 pc) gives a count rate of 0.006 counts s^{-1}. While it is believed that the offending radiation occurs primarily in the 1500–1700 Angstrom band, there is no explanation as to why the PHA distribution for Vega is "softer" than that from the UV Calibration lamp (1800 Angstrom); compare Figures 5.20 and 5.22 (see also Silverman et al. 1996). If the above band is responsible for the Vega count rate, the effective area of the HRI in the 1500 - 1700 Angstrom band is 1×10^{-6} cm^2.

A report in the literature (Arp 1995) interpreted some low level features in maps constructed in only the lowest pulse height channels as "leaked" UV radiation from celestial emission. Subsequently, it has been shown that the observed features are caused by the known properties of the spatial gain map (Silverman et al. 1996).

5.2.7 Event Timing

Each event detected with the HRI is time tagged with a precision of 61 μsec relative to the *ROSAT* spacecraft clock. The processing time for determining the position of an event is dependent upon the event location between the readout taps in the crossed grid charge detector and varies from 0.36 to 1.35 msec. For an event rate of 100 counts s^{-1}, the dead time losses will vary from 4 to 15 percent. The standard dead time correction formula can be used: $n_t = n(1+n\rho)$ where n_t is the true rate, n is the observed rate, and ρ is the dead time per event. The dead time varies linearly with position, but since source

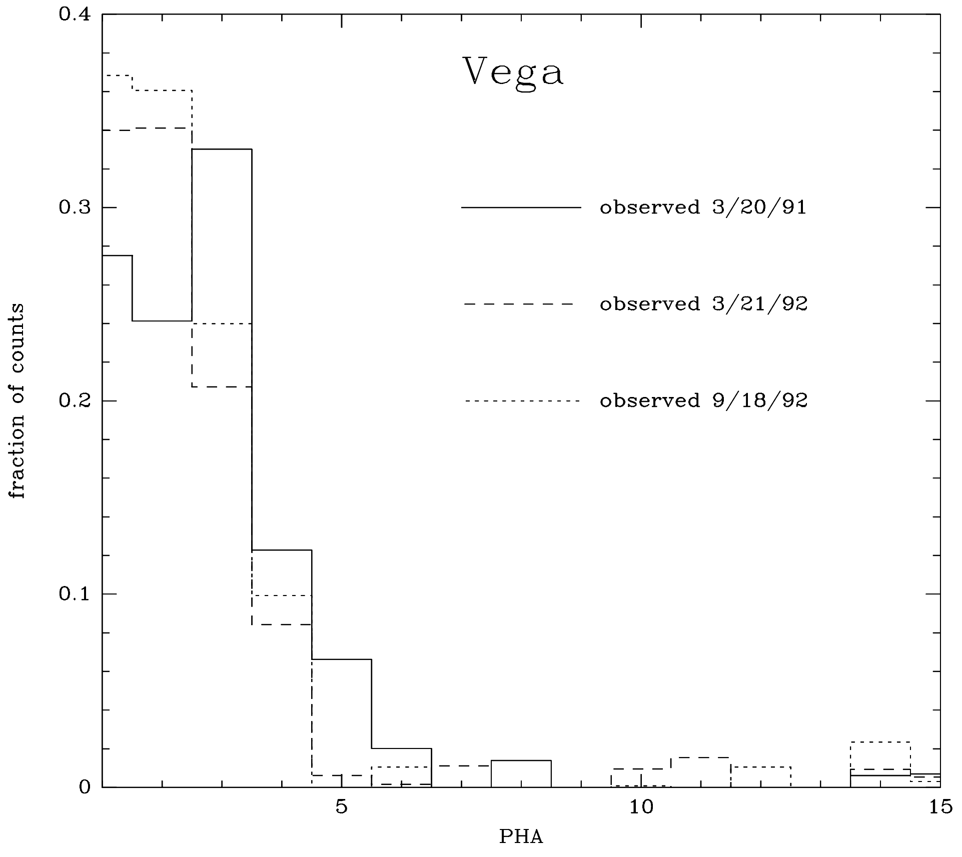

Figure 5.20: The pulse height distribution in several HRI observations of Vega. While the peak in the pulse height distribution has continuously shifted downward during the mission, the total count rate (in all PHA channels) has remained nearly constant (see Table 5.4).

photons will be recorded over a distribution of fine positions due to spacecraft motion and the point spread function of the telescope, there is no single value of dead time for a particular source observation. As a first approximation, it is possible to use a typical value of $\rho = 0.85$ msec.

A separate scalar on the HRI counts preprocessed events with a dead time of only 30 μsec. The contents of this scalar are entered into the telemetry once each second as secondary science. Thus if the HRI is observing a bright source, the intensity as derived from the processed events in the image can be corrected for the dead time using the data rates determined from the secondary science scalar.

5.2.8 High Voltage Increase

On 1994 June 21 at 8:59 GMT, the HRI high voltage was increased from level 12 to 13 in order to approximately recover the detector's original PHA distribution. Figure 5.21 shows an observation of the on-board UV calibration lamp taken during the HV increase. It exhibits an increase of 4% in the calibration lamp count rate, indicating the HV level change has approximately recovered the original UV sensitivity. In Figure 5.22 the PHA distributions before and after the increase are compared with an observation taken shortly after launch, showing that the mean PHA has recovered to within 0.5 channels of the original. See also Table 5.4 and Figure 5.19

5.2.9 Hotspot appearance

General

At the end of the Würzburg conference (circa 1995 September 29) Thomas Preibisch alerted MPE about a feature near the edge of the HRI field. Approximately two weeks later, many datasets were examined at MPE and 3 sequences which showed this effect were identified. SAO was notified on 16 October. and subsequently examined this sporadic feature. Many people at MPE, GSFC, and at SAO have contributed to this report.

During the course of the *ROSAT* Results Archive visual inspection, J. Silverman discovered a second hotspot in a different corner of the detector.

Although the precise cause of HRI hotspots are not known, they are thought to be a defect in a single pore of the micro channel plate. Some of the hotspots discovered before launch were subsequently incorporated into the HRI "hotspot map" which is used in the SASS processing to reject all events happening at given locations.

The original hotspot (aka #1) and the second are similar in several respects but differ in their PHA distribution, their variability characteristics, and the length of time they have been active. Because of their respective locations, HS#1 appears as a radial streak (in a normally wobbled observation), often appearing to extend into the region where there are few or no background counts. HS#2 being in an adjacent corner, appears as a tangential streak.

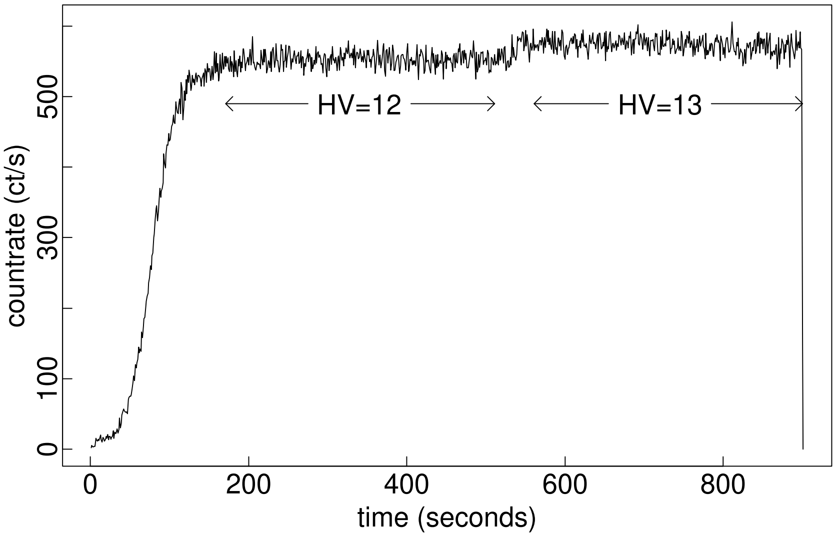

Figure 5.21: UV calibration observation taken during the HV change, showing a 4% increase in count rate. The marked regions are those used in the following figure.

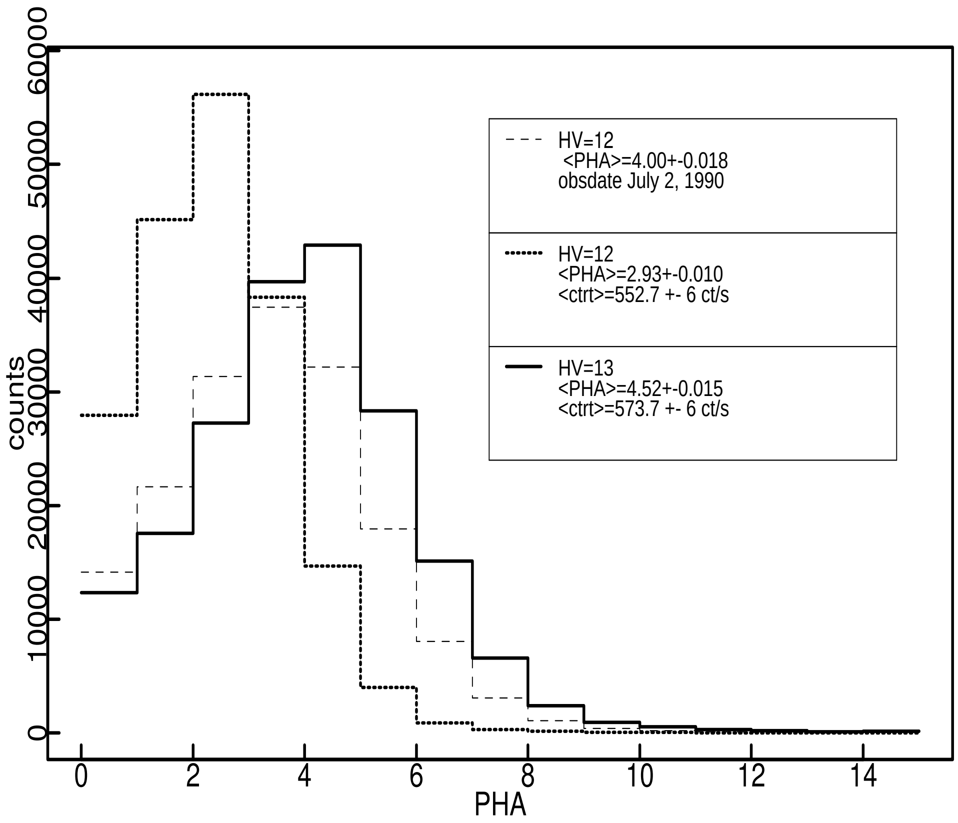

Figure 5.22: Comparison of PHA distributions of UV calibration data taken shortly after launch (dashed line) with data taken immediately before and after the HV change, 1994 June 21. (Counts are normalized to equal observation times.)

While it is somewhat surprising that both hotspots appeared within a few months of each other after years of no occurrences, they seem to be isolated events; no additional hotspots have been found. Since they are both at the very edge of the detector and their intensity is small enough that they do not encroach on the telemetry limit, they have essentially no impact on the quality of the scientific returns of the HRI. Monitoring of both hotspots has been incorporated into the verification software running at SAO; MPE continues to watch current activity on quick look data from the satellite; and the *ROSAT* Results Archive quality checking serves as a backup monitor for any new occurrences.

Spatial

Both hotspots have quasi power law distributions (sigma = 1.4″), with most of the photons falling within a circle of r=6 pixels. This size circle does not appear to be a function of time; even for short bursts, the spatial distribution is maintained.

	HOTSPOT #1	HOTSPOT #2
detector coordinates:	rawx = 440.5	rawx = 3636
	rawy = 484.5	rawy = 552

Temporal

For #1, an examination of light curves and plots of the KS test show that there are many intervals and obis when no activity is seen. #2 is quite different, being more steady (less "sparking" or "flickering"). For both, the average count rate drops quickly as the length of the time bin is increased.

	HOTSPOT #1	HOTSPOT #2
First known occurrence	8Jul95/rh800694	mid-Mar95
Last known occurrence	continues (Jan96)	19Jun95
Largest known counts s^{-1} (1 sec bins)	57(rh300399)	much less than #1
Largest known <counts s^{-1} > for a seq:	0.76 (17.2ksec)	0.0177(28 ksec)
Incidence of Detection (Jul-Sep 1995)	120 out of 240 seqs;	7/240

PHA

The PHA distribution differs for the two hotspots.

HOTSPOT #1	HOTSPOT #2
85% in channel 1 15% in channel 2 <1% in channel 3	peaks in channel 1; then decreases with about 1/2 counts in channels 4-10.

Viewing and Deleting

To view the hotspot in PROS;

```
> xdisplay "rh123456n00.qp[key=(rawx,rawy][186:697,230:741]"
(change coordinates for HS#2)
OR > xexamine rh...qp[key=(rawx,rawy)]
```

To make a KS plot, in the xtiming package of PROS,

```
> timsort rh....qp[key=(rawx,rawy)]
region: box 441 485 20 20
> vartst

> ksplot
```

To obliterate the hotspot, use qpcopy with the same [key=...] as above and specify a region (box or circle) to be excluded.

To view the hotspot in MIDAS/EXSAS:

in EXSAS the following commands will produce ”detector images (200x200)” with hotspot No.1 and No. 2 in the center with the maximum resolution:

```
bin/image XDET,YDET 1 pixel ,340,384,540,584   *events *hs1-area
bin/image XDET,YDET 1 pixel ,3536,452,3736,652 *events *hs2-area
```

5.3 Feasibility of observations

All guest investigators are asked to quantitatively discuss the feasibility of their proposed *ROSAT* observations. This section provides guidelines as to how to proceed with HRI observations.

5.3.1 General Assumptions

In order to estimate the HRI response to a cosmic X-ray source, several performance characteristics of the combined HRI and *ROSAT* telescope are needed.

In the sections that follow we provide estimates of minimum source count rate detection and expected count rates from sources. The assumptions that were used in providing these estimates are:

- The effective area shown in Figure 5.11 (Figure 11.1 of Appendix F) and listed in Table 5.4 (Table 11.1 of Appendix F) is the product of the XRT area and the HRI quantum efficiency.
- The HRI point source detection cell size is chosen so that 50 percent of the source photons fall within the detection cell. Hence the cell size must be matched to the XRT point spread function, the HRI detector resolution, and the aspect uncertainty (the latter currently being the largest factor in this choice).
- The HRI background rate is discussed above in section 3.4. For the present purposes, the X-ray background was computed from the spectrum shown in Figure 11.2 of Appendix F, which is a compilation of Wisconsin and LLL measurements (Ap.J. 193, L133; Ap.J., 172, L67) of the diffuse galactic background, and an extrapolation of a power law fit to the extragalactic background. In estimating the HRI count rate we integrate this spectrum over the total effective area of the XRT/HRI. Note that the UV/Ion Filter and electrostatic shield greatly reduce the HRI sensitivity at low energies and that there is a major dip in effective area at the carbon edge. It should also be noted that the galactic component of the X-ray background varies with the viewing direction. We have taken a conservative estimate of the galactic background in the sense that we use the high emission estimates in calculating the HRI count rates. In some cases the HRI background count rates due to galactic emission may be up to a factor of 5 lower than the value of 1.0 count s^{-1} used here and section 11 of Appendix F.

None of these assumptions is absolutely correct, but they provide a typical description of the XRT+HRI performance which may be useful in preparing *ROSAT* observation proposals.

5.3.2 Point Source Sensitivity

The point source sensitivity for an observation, and therefore the required observation time, can be approached in several different ways depending upon what specific question is being asked. In all cases, the required point-source sensitivity is determined by the minimum number of source counts needed to satisfy particular statistical criteria. For example, if the scientific goal is to measure the X-ray flux from a specific object, then the appropriate signal to noise requirement might be 3. On the other hand, the determination of source existence might require a signal to noise ratio of 5 in order to avoid spurious detections due to statistical fluctuations. Three different perspectives for the determination of the required exposure for an observation are considered:

- It is desired to know the flux of a given source. In this context, Gaussian statistics are appropriate as quantitative information about the source is required, rather than a simple detection.
- It is desired to know whether a given source emits X-rays. In this context, Poisson statistics are appropriate as existence, not flux, is at issue.
- It is desired to search a field of an observation for X-ray sources. In this context either Poisson or Gaussian statistics can be used depending on the scientific goals of the observer. However, an additional aspect must be considered: the number of false detections to be expected over the search region.

Flux of a Source – Gaussian Statistics Case

This is the most useful case as in general not just a detection, but a measurement of the flux (or upper limit on the flux) of a source is required.

On-axis, the signal to noise ratio is given by:

$$K_{snr} = N_{src} / \left(var(N_{tot}) \right)^{1/2}$$

where N_{src} is the number of source counts, and $var(N_{tot})$ is the variance in the total counts (source + background) and is typically given by $var(N_{tot}) = N_{src} + N_b$, which assumes no uncertainty in the background.

The minimum detectable source count rate corresponding to a particular signal to noise ratio is given by the relationship

$$R_{min} t = K_{snr}^2/2 + \left(\left(K_{snr}^2/2 \right)^2 + K_{snr}^2 R_b t \right)^{1/2}$$

where R_{min} denotes the minimum detectable source count rate, R_b the total background rate in the detection cell (about 2.7×10^{-5} counts s^{-1}), t the observation time, and K_{snr} the signal to noise ratio (snr) threshold for detection.

This is derived by combining the equations defining the snr and variance, and using the additional relation, counts = rate x time.

As an illustrative example, we show in Figure 11.3 in Appendix F, the point source sensitivity for $K_{snr} = 5$ versus observing time for a source with a power law spectrum. That is, we assume a point source with a power law spectrum of energy index 0.5 similar to the extragalactic X-ray background. A hydrogen column density of 5×10^{20} cm^{-2} is used. Notice that the sensitivity increases linearly with observing time for short observations where there are virtually no background counts in the detection cell. For observations that are long enough for background to be significant, longer than about 10^5 s, the sensitivity increases only as the square root of the observation time.

In general, the conversion from HRI counts to energy flux depends on the spectrum of the X-ray source. For the power law spectrum characterized by the parameters given above, this conversion is given by: 1 count $\mathrm{s}^{-1} = 1.06 \times 10^{-10}$ erg cm^{-2} s^{-1} in the energy band 0.1 to 2.4 keV. The following section discusses the conversion from energy flux to count rate in more detail.

Off-axis, sensitivity estimates must take into account the cell size from the off-axis PSF (cf. Section 3.2). The cell size can be taken as the 50% power radius, i.e., a square region where 50% of the source counts will fall. The background rates must also be scaled to the new cell size.

The vignetting correction in Figure 5.12 can be used to scale down the number of counts detected from off-axis sources due to the decrease in telescope area; since the HRI field of view is limited, the slight energy dependence of the vignetting correction can usually be neglected for feasibility purposes.

Existence of a Source – Poissonian Statistics Case

The typical HRI background in on-axis detection cells ($\sim 5'' \times 5''$) is of order unity or lower for most HRI observations ($\lesssim 100$ ks), and therefore in the range where Poisson statistics are appropriate for source-detection analysis. For example, the number of background counts expected in a detection cell for a 20 ks observation is 0.55. A 5σ detection of a source using Poissonian statistics would then require 7 counts, for a count rate of 3.5×10^{-4} counts s^{-1} in the detection cell, a total count rate of 7.0×10^{-4} counts s^{-1}. The count rate of the source, however, is known to less than 3σ. In lieu of an analytic function (of which none exists), Figure 5.23a displays a contour plot of limiting (total) count rate for a source detection on a grid of significance (sigma) and exposure. The plot was generated for the on-axis detection cell and assumes the nominal background rate. Figure 5.23b shows the same information for a region of interest $10'$ off axis where the detection cell is $\sim 12'' \times 12''$ and the background count rate $\sim 1.6 \times 10^{-4}$ counts s^{-1}. Off axis, the same considerations of vignetting correction and larger detection cells as for the Gaussian case must be taken. The conversion between count rate and flux is the same as above.

Detection of Previously Unknown Sources Over a Field

If one wishes to survey a field for X-ray sources, one should consider the number of false sources expected in the region. If one is interested primarily in source detection (Poisson statistics case), one can obtain a rough estimate of the number of false sources by considering the number of independent detect cells in the region of interest. For example, in the inner $10'$ diameter region, there are approximately 10000 $5'' \times 5''$ detect cells. Setting the detection significance level at 10^{-4} would therefore produce, on average, one false source in the region. One must be careful, however, in applying this analysis to source detection algorithms which use sliding detect cells, since adjacent cells are not independent. In such cases, the false source rate may best be determined by simulations. The PROS task QPSIM may be used to simulate QPOE files containing blank HRI fields with given background rates.

In the Gaussian statistics case, there is no simple way, a priori, to estimate the number of false sources from the count rate significance threshold. In this case, simulations are necessary, and were, in fact, performed to set detection thresholds for the *ROSAT* HRI Level 1 software in the SASS system. It was determined there that for typical HRI exposures, detection thresholds of $2-3\sigma$ resulted in approximately 1 false source per field in each cell size used. Based on experience with the *Einstein* Observatory, a more conservative limit, say $3-4\sigma$ might be appropriate. Again, observers may wish to perform their own simulations if this point is crucial to their feasibility analysis.

5.3.3 Expected Count Rates (in detect cell = 50% of total)

The expected HRI count rates depend sensitively on the assumed incident spectrum, which is not well known for many sources. In general, the convolution of the effective area and incident spectrum needs to be calculated to predict the HRI counting rate. Since the effective area is not a simple analytic function, the convolution is not straight-forward. In order to facilitate count rate calculations we provide a series of tables and graphs which give the energy-to-counts conversion factor (ECF) for several spectral models and various spectral parameters. These are based upon the counts collected in a $5'' \times 5''$ detect cell which is assumed to contain 50% of the total source counts that fall on the HRI detector. (Note that other estimation techniques may use the total counts and hence may differ by a factor of two from the results obtained by following the procedures described here.)

Tables for computing the expected count rates in the *ROSAT* HRI were generated for four spectral models. These are:

1. Thermal Bremsstrahlung (Exponential plus Gaunt Factor) Spectrum (Table 11.2, Figure 11.4 of Appendix F), where kT is in keV.
2. Power Law Spectrum (Table 11.3, Figure 11.5 of Appendix F), where α is the energy index.
3. Raymond-Smith Plasma Spectrum (Table 11.4, Figure 11.6 of Appendix F), where kT is in keV.
4. Blackbody Spectrum (Table 11.5, Figure 11.7 of Appendix F), where kT is in keV

For each spectral model we calculate the factor by which the unabsorbed source flux (in units of 10^{-11} erg cm^{-2} s^{-1}) has to be multiplied in order to obtain the expected HRI on-axis count rate within the $5'' \times 5''$ detect cell. The conversion factor is as a function of the intrinsic source spectrum (characterized by α or kT),and the interstellar absorption column density $N_{\rm H}$.

The curves shown in Appendix F Figures 11.4 - 11.7 (or Tables 11.2 - 11.5 reproduced here for convenience) should be used as follows:

1. Estimate the **un** absorbed source flux $F_{S,0}$ (in units of 10^{-11} ergs cm^{-2} s^{-1}) in the *ROSAT* pass band 0.1 - 2.4 keV. This is the flux which would have been incident on the Earth in the absence of any absorption.
2. Estimate the interstellar absorption column density.
3. With the assumed values of $N_{\rm H}$ and spectral parameter (α or kT) read from the figures or tables the resulting energy-to-counts conversion factor ECF.
4. Multiply $F_{S,0}$ and ECF to obtain the expected *ROSAT* HRI count rate.

Table 11.2 Thermal Bremsstrahlung

ROSAT HRI Energy to Count Conversion Factors (50% of counts)

log($\mathbf{N_H}$)

kT	**0.0**	**18.0**	**18.7**	**19.0**	**19.7**	**20.0**	**20.7**	**21.0**	**21.7**	**22.0**
0.01	3.91e-2	3.76e-2	3.21e-2	2.64e-2	5.94e-3	1.13e-3	2.53e-5	1.00e-9	1.0 0e-9	1.00e-9
0.03	1.18e-1	1.15e-1	1.04e-1	9.21e-2	3.94e-2	1.77e-2	6.83e-4	6.07e-5	1.0 0e-9	1.00e-9
0.05	1.69e-1	1.66e-1	1.53e-1	1.40e-1	7.57e-2	4.28e-2	3.42e-3	4.67e-4	2.1 0e-6	1.00e-8
0.10	2.12e-1	2.09e-1	1.98e-1	1.86e-1	1.21e-1	8.05e-2	1.22e-2	3.50e-3	1.5 0e-4	1.82e-5
0.30	2.05e-1	2.03e-1	1.96e-1	1.88e-1	1.42e-1	1.10e-1	4.16e-2	2.62e-2	6.0 2e-3	1.93e-3
0.50	1.98e-1	1.96e-1	1.91e-1	1.85e-1	1.50e-1	1.24e-1	6.51e-2	4.78e-2	1.4 8e-2	5.73e-3
1.00	1.86e-1	1.85e-1	1.82e-1	1.78e-1	1.53e-1	1.35e-1	8.81e-2	7.06e-2	2.6 7e-2	1.17e-2
3.00	1.68e-1	1.68e-1	1.65e-1	1.63e-1	1.47e-1	1.35e-1	9.95e-2	8.36e-2	3.5 9e-2	1.72e-2
5.00	1.63e-1	1.63e-1	1.60e-1	1.58e-1	1.44e-1	1.33e-1	1.01e-1	8.55e-2	3.7 7e-2	1.83e-2

Table 11.3 Power Law

ROSAT HRI Energy to Count Conversion Factors (50% of counts)

log($\mathbf{N_H}$)

α	**0.0**	**18.0**	**18.7**	**19.0**	**19.7**	**20.0**	**20.7**	**21.0**	**21.7**	**22.0**
0.0	1.44e-1	1.43e-1	1.42e-1	1.41e-1	1.32e-1	1.25e-1	1.03e-1	8.93e-2	4.25 e-2	2.17e-2
0.5	1.64e-1	1.63e-1	1.61e-1	1.58e-1	1.41e-1	1.29e-1	9.45e-2	7.96e-2	3.50 e-2	1.71e-2
1.0	1.81e-1	1.80e-1	1.75e-1	1.70e-1	1.41e-1	1.21e-1	7.52e-2	6.02e-2	2.42 e-2	1.12e-2
1.5	1.90e-1	1.90e-1	1.81e-1	1.73e-1	1.32e-1	1.05e-1	5.09e-2	3.79e-2	1.36 e-2	5.97e-3
2.0	1.88e-1	1.86e-1	1.77e-1	1.67e-1	1.16e-1	8.50e-2	3.06e-2	2.05e-2	6.41 e-3	2.65e-3
2.5	1.78e-1	1.76e-1	1.66e-1	1.54e-1	9.85e-2	6.68e-2	1.75e-2	1.01e-2	2.67 e-3	1.04e-3
3.0	1.64e-1	1.61e-1	1.51e-1	1.39e-1	8.20e-2	5.19e-2	9.92e-3	4.76e-3	1.04 e-3	3.74e-4

Table 11.4 Raymond-Smith

ROSAT HRI Energy to Count Conversion Factors (50% of counts)

log($\mathbf{N_H}$)

kT	**0.0**	**18.0**	**18.7**	**19.0**	**19.7**	**20.0**	**20.7**	**21.0**	**21.7**	**22.0**
0.01	5.17e-1	4.98e-1	4.29e-1	3.56e-1	8.75e-2	1.86e-2	1.59e-5	2.00e-7	1.0 0e-9	1.00e-9
0.03	3.39e-1	3.28e-1	2.90e-1	2.50e-1	8.41e-2	2.80e-2	4.09e-4	3.20e-5	1.0 0e-9	1.00e-9
0.05	2.97e-1	2.92e-1	2.73e-1	2.51e-1	1.43e-1	8.16e-2	5.50e-3	6.24e-4	2.7 0e-6	1.00e-7
0.10	2.74e-1	2.72e-1	2.63e-1	2.52e-1	1.88e-1	1.38e-1	2.54e-2	7.27e-3	2.6 9e-4	2.91e-5
0.30	1.92e-1	1.92e-1	1.89e-1	1.86e-1	1.68e-1	1.52e-1	1.02e-1	7.82e-2	1.7 5e-2	3.95e-3
0.50	2.41e-1	2.40e-1	2.38e-1	2.35e-1	2.22e-1	2.12e-1	1.75e-1	1.47e-1	4.2 9e-2	1.14e-2
1.00	2.27e-1	2.26e-1	2.22e-1	2.17e-1	1.95e-1	1.83e-1	1.51e-1	1.31e-1	5.3 3e-2	2.08e-2
3.00	1.75e-1	1.74e-1	1.72e-1	1.69e-1	1.54e-1	1.44e-1	1.11e-1	9.50e-2	4.2 7e-2	2.05e-2
5.00	1.66e-1	1.66e-1	1.64e-1	1.61e-1	1.48e-1	1.38e-1	1.06e-1	9.07e-2	4.0 8e-2	1.99e-2

Table 11.5 Blackbody

ROSAT HRI Energy to Count Conversion Factors (50% of counts)

logN$_\mathrm{H}$)

kT	**0.0**	**18.0**	**18.7**	**19.0**	**19.7**	**20.0**	**20.7**	**21.0**	**21.7**	**22.0**
0.01	5.59e-2	5.38e-2	4.65e-2	3.88e-2	9.98e-3	2.35e-3	4.80e-6	1.00e-7	1.0 0e-9	1.00e-9
0.03	2.02e-1	1.98e-1	1.85e-1	1.71e-1	9.85e-2	5.79e-2	4.62e-3	5.61e-4	9.0 0e-7	1.00e-9
0.05	2.48e-1	2.45e-1	2.35e-1	2.23e-1	1.55e-1	1.08e-1	1.66e-2	4.00e-3	7.0 7e-5	3.50e-6
0.10	1.89e-1	1.87e-1	1.83e-1	1.78e-1	1.47e-1	1.21e-1	5.07e-2	3.05e-2	4.4 0e-3	9.29e-4
0.30	1.77e-1	1.77e-1	1.76e-1	1.76e-1	1.71e-1	1.66e-1	1.44e-1	1.25e-1	5.4 5e-2	2.52e-2
0.50	1.39e-1	1.39e-1	1.39e-1	1.38e-1	1.36e-1	1.34e-1	1.21e-1	1.09e-1	5.5 2e-2	2.88e-2
1.00	1.04e-1	1.04e-1	1.03e-1	1.03e-1	1.02e-1	1.01e-1	9.29e-2	8.49e-2	4.7 2e-2	2.65e-2
3.00	8.48e-2	8.48e-2	8.47e-2	8.46e-2	8.38e-2	8.29e-2	7.71e-2	7.11e-2	4.1 3e-2	2.41e-2
5.00	8.18e-2	8.17e-2	8.17e-2	8.16e-2	8.09e-2	8.00e-2	7.45e-2	6.88e-2	4.0 3e-2	2.37e-2

Blackbody spectrum example

The expected (50% in detect cell) count rate from a source with a blackbody spectrum (perhaps a neutron star) needs to be estimated. The source has L$_x$ = 10^{33} ergs s^{-1} in the *ROSAT* energy band (0.1 to 2.4 keV), and is at a distance of 2 kpc with N$_\mathrm{H}$ = 1×10^{21} cm^{-2} (log(N$_\mathrm{H}$) = 21). The assumed temperature is equivalent to 0.1 keV. The unabsorbed flux for this source is $F_{S,0} = 2.09 \times 10^{-12}$ ergs cm^{-2} s^{-1}, or in units of 10^{-11} the flux is $F_{S,0} = 0.209$. From the Table 11.5 or Figure 11.7 the appropriate ECF is 3.05×10^{-2}, and the expected count rate is 6.37×10^{-3} counts s^{-1}. We estimate that a detection of this source at the 5σ level will require an observation time of about 4,000 seconds.

Power-law spectrum example

Consider a distant AGN with a power law spectrum of energy slope 0.5 which is at a luminosity distance of 1000 Mpc and is viewed through an absorption column of 5×10^{20} cm^{-2} (log(N$_\mathrm{H}$) = 20.7). The AGN luminosity in the *ROSAT* band is L$_x$ = 10^{44} ergs s^{-1}. We want to determine how long an observation is required for a 10σ detection. The unabsorbed flux is $F_{S,0} = 8.37 \times 10^{-13}$ ergs cm^{-2} s^{-1}. The ECF for this spectral model is taken from Table 11.3 or Figure 11.5, it is 9.445×10^{-2}, which gives a count rate 7.91×10^{-3} counts s^{-1}. Using the sensitivity formula from section 11.2, we calculate that the observation time needed to detect this source at the 10σ level (50% in detect cell) is about 12,600 seconds.

Raymond-thermal spectrum example

What is the conversion factor from counts (50% in detect cell) per second to energy flux for a particular spectrum? For example, a Raymond-Smith Plasma with a temperature corresponding to 1 keV and a column of 5×10^{21} cm^2 (log(N$_\mathrm{H}$) = 21.7). The ECF for this spectral model is taken from Table 11.4 of Figure 11.6, it is 5.33×10^{-2}. That is, a flux of 1×10^{-11} ergs cm^{-2} s^{-1}

in the *ROSAT* energy band (0.1 to 2.4 keV) will give a count rate of 5.33×10^{-2} counts s^{-1} in the HRI. Inverting this relationship gives the result that 1 count $s^{-1} = 1.88 \times 10^{-10}$ ergs cm^{-2} s^{-1}. In general the conversion factor from counts per second (50% in detect cell) to energy flux is given by: 1 count $s^{-1} = 1 \times 10^{-11}$/ECF ergs cm^{-2} s^{-1}.

5.3.4 Time Variability Studies

The time variability of X-ray emission can be studied with the HRI since each detected photon has its time of arrival recorded by the detector. The accuracy of this time is limited by the electronic resolution of the HRI processor which is 61 μsec relative to the *ROSAT* spacecraft clock. The relative arrival times of photons during a single observation is accurate to this value. The absolute accuracy of the *ROSAT* spacecraft clock, and its conversion to UT, is expected to be a few milliseconds.

The HRI has a processing dead time during which events may not be counted which varies between 0.36 and 1.35 msec per event. The variation is discussed in section 4.3.2.5 and depends on the fine position of the event. Thus there is a dead time correction that needs to be made for calculating the true event rate from a source. A mean dead time of $\rho = 0.81$ msec can be used for this purpose, and the true rate is then given by: $n_t = n(1 + n\rho)$, where n is the observed rate.

Due to the telescope wobble and the small variations in the QE of the HRI on spatial scales of a few arc minutes (see Figure 5.13), the count rate of a source can vary by 5% between the extremities of a wobble. This can produce a low amplitude source variability on a time scale of approximately 100-400 seconds in some sources.

As for the PSPC, the HRI observations are typically interrupted once per orbit, and sometimes as much a three times per orbit. Typical continuous viewing times for a source will be about 2000 seconds, with some cases lasting up to 4000 seconds. Long term monitoring of sources on time scales of weeks of more will be limited by the solar view constraints of the satellite. This limits source accessibility to about one month every six months for a source in the elliptic plane, with greater access time for sources closer to the ecliptic poles.

5.3.5 Comparison to the *Einstein* HRI

Comparisons between the *Einstein* and *ROSAT* HRI's must account for the different detector photocathodes and band passes of the two telescopes. As shown by the effective area comparison given in Figure 11.8 of Appendix F, the HRI effective area of *ROSAT* exceeds that of *Einstein* over most of the *ROSAT* energy band (because of the increased area of the *ROSAT* mirrors and the greater sensitivity of its CsI photocathode). As can be seen from Table 5.5, observed *ROSAT* count rates are typically a factor of 3 to 4 times those measured with the *Einstein* HRI (the values of this ratio, of course, depending upon interstellar absorption and the intrinsic source spectra).

The better scattering performance and a smaller point spread function of the *ROSAT* XRT, vis a vis the *Einstein* telescope, should ultimately permit the use of a 5″ detect cell, as assumed above for feasibility calculations, provided the aspect contribution to the PSF can be reduced.

5.4 References

Arp, H.C. 1995, Astron. Astrophys., 294, L45.

Silverman, J.D., Kearns, K.E., and Harris. D.E. 1996, ADASS V Proceedings Astron. Soc. Pacific (in press).

Zombeck, M.V., David, L.P., Harnden, Jr., F.R., and Kearns, K., Proc. SPIE, Vol. 2518, pp. 304-321, 1995.

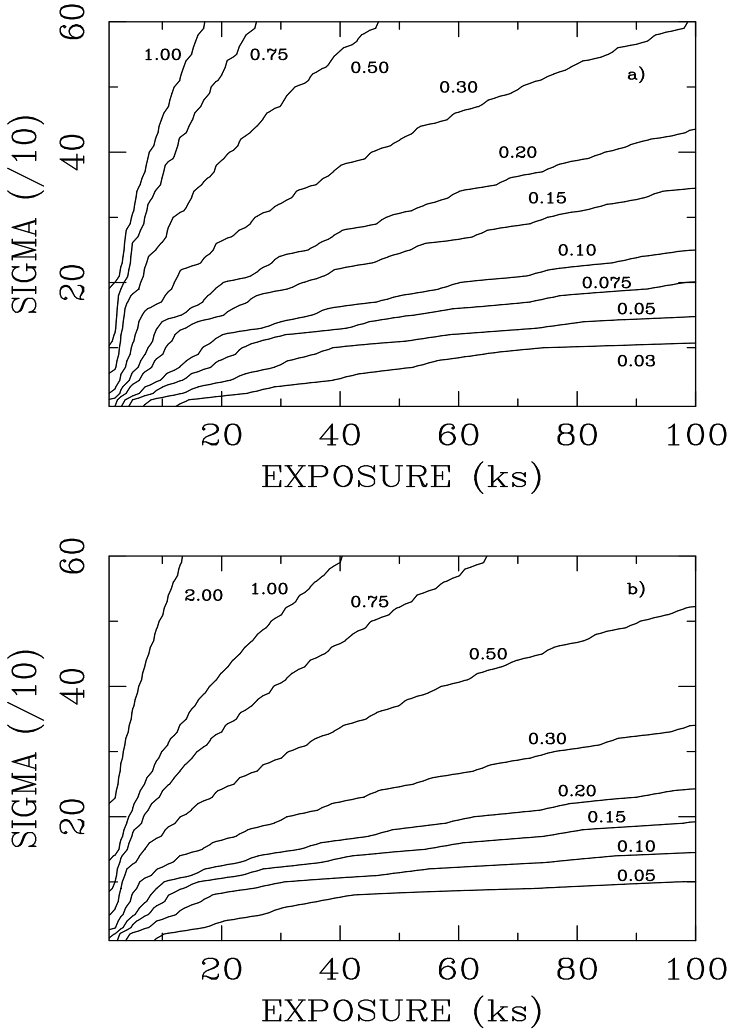

Figure 5.23: The relation between source count rate, statistical significance, and exposure for an HRI observation using Poisson statistics is shown. The contour plots show the source count rate in units of 10^{-3} counts s^{-1} versus exposure in ks and sigma (a value for σ of 50 refers to 5σ). Plot a) is for the on-axis case, plot b) is for $10'$ off axis.

Chapter 6

The Wide Field Camera

(*Source* M.A. Barstow, J.P. Osborne, J.P. Pye, M. Watson, R.G. West, R. Willingale
University of Leicester, Leicester, UK)

This section describes the Wide Field Camera and its scientific performance based on in-flight measurements and calibration. The WFC is an autonomous instrument having its own star tracker (to provide aspect information), thermal control system and Command & Data Handling System (CDHS). The WFC relies upon the ROSAT spacecraft for power, on-board data storage and telemetry. Data are queued into the spacecraft data handling system by the WFC CDHS.

6.1 Description

A schematic diagram of the Wide Field Camera (WFC) showing the main components – grazing incidence mirrors, filters and microchannel plate (MCP) detectors – is shown in Figure 6.1.

6.1.1 Mirrors

The WFC optics consist of a nested set of 3 Wolter-Schwarzschild Type I mirrors, fabricated from aluminium and coated with gold for maximum reflectance. The mirrors provide a geometrical collecting area of $456\,\mathrm{cm}^2$ with a common focal length of 525 mm. The grazing incidence angles chosen (typically $\approx 7.5^\circ$) allow the collecting area to be optimised whilst retaining a wide (2.5° radius) circular field of view and a high-energy reflectivity cut-off at 0.21 keV (60 Å). The on-axis resolution is $2.3'$ HEW, degrading to $\approx 4.4'$ HEW at 2.5° off-axis due to inherent optical aberrations. The average resolution for the all-sky survey is $\approx 3.5'$ HEW. The mirror parameters are summarised in Table 6.1.

6.1.2 Detectors

In order to take full advantage of the telescope resolution, both the pair of MCPs in the detector and the resistive anode readout system are curved, like a watchglass, to match the optimum focal surface. A CsI photocathode is deposited directly onto the front face of the front MCP to enhance the EUV quantum efficiency. The detector spatial resolution is substantially (a factor > 2) better than that of the mirror nest and consequently does not contribute significantly to the net performance of the WFC. A focal plane turntable can be used to select one of two identical detector assemblies in flight. Table 6.2 gives details of the detectors.

6.1.3 Filters

The filter wheel assembly contains eight filters, these are listed in Table 6.3. There are six science filters, any of these can be selected to define the wavelength passbands and suppress geocoronal background radiation which would otherwise saturate the detector count rate. (Another function of the filters is to prevent the detection of UV radiation from hot O/B0 stars which would otherwise be imaged indistinguishably from EUV sources.) The six science filters comprise two redundant pairs of 'survey' filters (S1a/S1b and S2a/S2b), together with two 'pointed' phase filters (P1 and P2) which cover somewhat different energy ranges. There are two sizes of filter, large diameter (5° field of view, "S") for the survey and pointed phases, and small diameter (2.5° field of view, "P") for pointed observations only. The S2a filter was damaged in 1991 January and has not been used for the remainder of the mission.

Of the remaining 2 filters, one is a narrow-band UV interference filter ("UV" in the table) used only in conjunction with the UV calibration system which permits in-flight monitoring of detector gain drifts and thermally-induced misalignment of the telescope axis. The other is an "Opaque" filter ("OPQ" in the table) which is opaque to photons, but has a sensitivity to particle background which is very similar to the scientific filters. Originally it was intended that this filter be used in to determine the particle component of the WFC background. In-orbit experience has demonstrated that the opaque filter suffers from an unexpected stray-light leak, seriously reducing its usefulness.

6.1.4 Operational modes

There are 3 software "switches" in the WFC which have a direct influence on the scientific data received from the focal plane detector.

Zoom: The 512×512 pixel output of the WFC can correspond to the full 5° diameter field of view (ZOOM off), or can be 'zoomed' so as to correspond to only the central $\sim 2.5^\circ \times 2.5^\circ$ region of the field (ZOOM on). The angular size of each pixel is therefore halved when the ZOOM is on. This facility is not normally needed, and has only been used for a small percentage of observations, mainly during the earlier phases of the mission.

Data rate: The on-board storage rate for detected events (i.e. photons or background particles) is normally restricted to 200 counts per second. This corresponds to filling the entire WFC allocation of the on-board tape-recorder in 24 hours. There is a high data rate of 400 counts per second which can be used for limited periods, for example to take advantage of the storage allocation not used during intervals when the detector is switched off (e.g. during radiation belt transits). The data rate is normally optimised automatically by on-board software. During the pointed phase of the mission the detector count rate has rarely exceeded the 200 count per second threshold during observations. The dead-time in the WFC, due primarily to losses in the queueing of events by the on-board software, depends on the count rate and which of the two data rates is selected (Figure 6.8).

Electronic windowing: This allows the events stored by the WFC to be restricted to those which are detected within, or outside of, a restricted spatial window within the field of view of the WFC. The window can be any rectangular region specified with a resolution of 32 pixels (i.e. the smallest window possible corresponds to a region $\approx 20' \times 20'$ in extent with ZOOM off). The main use for electronic windowing would be in situations where the total count rate expected from the whole field of view exceeds the normal maximum data rate of 200 counts per second (and would thus lead to large dead times). Electronic windowing can also be used to 'mask out' detector hot-spots or other defects which would otherwise saturate the data rate; windowing of such features, which are expected to be essentially fixed, is achieved within the WFC CDHS using a similar but independent mechanism. To date, neither of the windowing facilities has been used.

6.2 Performance

This section describes the in-orbit performance of the complete WFC telescope (mirrors, detector and filters for the full aperture). Values for the point response function and vignetting were obtained from in-orbit calibration measurements during the mission, and from a full aperture test at MPE's Panter X-ray beam line facility.

6.2.1 Effective area

Figure 6.2 shows the on-axis effective area of the complete WFC for each filter at the time of launch. These curves have been derived from calibration data acquired both on the ground and in-orbit. The systematic uncertainties are probably of order 10% for the S1 and S2 filters and 30% for the P1 and P2. Note that some of the available WFC filters have a secondary transmission band in the far-ultraviolet. Although the far-UV transmission is much weaker than that in the primary EUV bands, problems may potentially arise when observing objects that have a particularly strong far-UV component in their spectrum.

During a period of attitude control failure and uncontrolled pointing on 1991 January 25-26 the ROSAT WFC suffered a severe loss in sensitivity. This is thought to be due to contamination of the detector photocathodes, although the source of the contamination is not known. For some time after this event the efficiency of the instrument continued to drop reaching a minimum around June 1991. It then started to improve slowly but reached a plateau in July 1992 and now seems to have stabilised. Efficiency history curves have been constructed for all the WFC filters from periodic calibration observations of DA white dwarfs; these curves can be used to compare WFC observations at different epochs (Figure 6.6)

6.2.2 Spatial variations in effective area

The reflectivity of the mirror assembly decreases with increasing off-axis angle, dropping linearly to 67% of its on-axis value at 2.5° off-axis. Beyond this the vignetting function is dominated by geometric baffling. Rejection of scattered flux from bright sources outside the field of view is good. Less than 0.5% and 0.01% of the source flux is detected for sources 3° off-axis and 5° off-axis respectively.

In addition to the vignetting intrinsic to the mirror assembly, the quantum efficiency of the WFC microchannel plate detectors vary as a function of position of a source within the field-of-view, probably due to variations in the quantum efficiency of the CsI coating deposited on the face of the MCP. This effect has been calibrated using the survey observation of the bright white dwarf HZ43 by binning the source photons into detector coordinates. Figure 6.7 shows the combined effects of the spatial variations in the detector efficiency and the mirror vignetting.

6.2.3 Point-spread function

The point response function of the WFC is dominated by the performance of the mirrors. Figuring errors determine the on-axis response but aberrations inherent in the optical design dominate at the edge of the field of view. As the energy of the incident photons increases the scattering wings becomes more pronounced (Figure 6.4). At 124 eV and 20 eV the on-axis half energy widths (HEW) are $2.47'$ and $1.93'$ respectively. However, at the edge of the field-of-view the HEW is $4.6'$ and independent of photon energy. The encircled energy fraction for a range of off-axis angles is shown in Figure 6.3. The average HEW over the field of view is $3.5'$. Figure 6.3 shows the in-orbit PSF measured from a 0.9 ksec observation of the bright white dwarf HZ43 in the S2B filter.

6.2.4 Timing

The individual events detected by the WFC are time-tagged to a resolution of approximately 40 ms by the CDHS, which allows the scanning motion of the sky survey to be removed without image degradation due to smearing effects. There are no EUV sources which are bright enough for this timing restriction to be a limitation.

6.2.5 Positional accuracy

The uncertainties intrinsic in reconstructing the true sky position of an event detected by the WFC come from two main sources. Firstly, the resistive anode image readout system of the MCP detectors has a small but significant intrinsic distortion. This is determined largely by the physical parameters of the system (ie. anode resistance and capacitance) but asymmetries are introduced by variations in the resistivity of the anode as a result of the manufacturing process. Consequently, the distortion needs to be removed during the data processing. This task, termed 'linearisation', is performed by means of a look-up table that gives the relationship between the detector coordinate system and that of the telescope. Positional errors introduced by this process are approximately $12'$. In-orbit experience demonstrates that the linearisation parameters have remained stable over the operational life of the detector.

A second source of uncertainty is the reconstruction of the WFC aspect from the startracker data, which is subject to an error of around $12'$. Combined with the linearisation errors the limiting positional accuracy of the WFC is around $30'$, however this limit is achievable only for bright sources close to the optical axis. For other cases the positional uncertainty is dominated by the PSF and by source statistics.

6.2.6 Background

In-orbit experience has shown that the background in the short-wavelength filter ("S1") is dominated by cosmic rays and by a spacecraft related spacecraft glow phenomenon. In the shorter wavelength filters additional components are present due to resonantly scattered photons from the strong emission lines in the solar spectrum (most notably the 304 Å line of He II). Table 6.4 gives the approximate ranges and orbit-averaged count rates for each of the background components, Table 6.5 gives the typical overall background rate in each filter. It should be stressed however that all of the components (with the exception of the MCP intrinsic noise) are time variable with periods ranging from minutes to months, dependant on the component concerned.

6.2.7 UV sensitivity

Some of the available WFC filters have a secondary transmission band in the far-ultraviolet. Although these are much weaker than the primary XUV bands, problems may arise when observing objects that have a particularly strong far-UV component in their spectrum. The count rate detected by the WFC will then be an unresolved mixture of XUV and far-UV photons. In severe cases the scientific return of the observation may be compromised. Observers should ensure that their selected targets do not fall into this category. For any target the severity of the potential problem can be assessed by referring to Table 6.6. This lists predicted count rates for each filter from an $m_V = 0$ blackbody source at temperatures of 10000, 20000 and 30000 K. The expected far-UV count rate from a target can then be estimated by scaling the $m_V = 0$ count rate for the appropriate temperature to the actual m_V value (i.e. by multiplying the value given in Table 6.6 by $10^{-0.4 m_V}$). Note that the UV leak is largest for the S2 filter; for the other filters the UV leak is unlikely to be a problem except for the brightest stars.

6.3 Analysis of WFC data

Background subtraction. Exposure correction. Detailed contents to be decided.

Table 6.1: WFC Mirror parameters

Mirror type	Wolter-Schwarzschild Type I
Mirror material	Ni plated Aluminium
Reflective coating	Au
Number of shells	3
Field of view	5° diameter
Geometric area	456 cm^2
Aperture diameter	576 mm
Focal length	525 mm
Focal plane scale factor	160 μm $= 1'$
High energy cutoff (10% of peak)	0.21 keV
Half energy width (on-axis)	$1.7'$ at 0.04 keV

Table 6.2: WFC Detector characteristics

Diameter	55 mm
Active diameter	45 mm
Radius of curvature	165 mm
Channel diameter	12.5 μm
Channel pitch	15.0 μm
Open area	63%
Length-to-diameter ratio	120:1
Front MCP bias angle	0°
Rear MCP bias angle	13°
Photocathode (front MCP only)	14000 Å CsI

Table 6.3: WFC filters

Filter name/type	FOV diameter (degrees)	Mean energy (eV)	Bandpass (eV) (at 10% of peak)
S1a (C/Lexan/B)	5	124	90–210
S1b (C/Lexan/B)	5	124	90–210
S2a (Be/Lexan)	5	90	62–111
S2b (Be/Lexan)	5	90	62–111
P1 (Al/Lexan)	2.5	69	56–83
P2 (Sn/Al)	2.5	20	17–24
OPQ (Opaque)	2.5	–	–
UV (UV interference)	2.5	–	–

Table 6.4: Field-of-view averaged contributions from the various background components in the WFC. Typical ranges of the background contribution from each component are shown (in units of counts per second per field-of-view), along with a typical orbit-averaged value

Component	Typical range	Averaged
Auroral electrons	0–1000	1
Cosmic rays	4–25	10
He II 304Å	S1: < 1	< 1
	S2: 0–40	10
Other airglow emissions	< 1	< 1
Spacecraft glow	0–300	20
Diffuse XUV background	~ 0	~ 0
MCP intrinsic noise	2	2

Table 6.5: Typical background rates in the various WFC filters

Filter	Counts/sec/FOV	10^{-4} Count/sec/arcmin^2
S1	25	3.5
S2	40	5.6
P1	110	22
P2	320	45

Table 6.6: Predicted far-UV count rate for a blackbody source with $m_V = 0$

Temp (K)	Count rate in each filter (counts s^{-1})			
	S1	S2	P1	P2
10000	5.9×10^{-4}	5.2×10^{-3}	1.0×1^{-9}	$< 1.7 \times 10^{-5}$
20000	4.2×10^{-3}	0.74	5.0×10^{-8}	$< 5.7 \times 10^{-3}$
30000	9.8×10^{-3}	2.1	2.2×10^{-7}	$< 3.9 \times 10^{-2}$

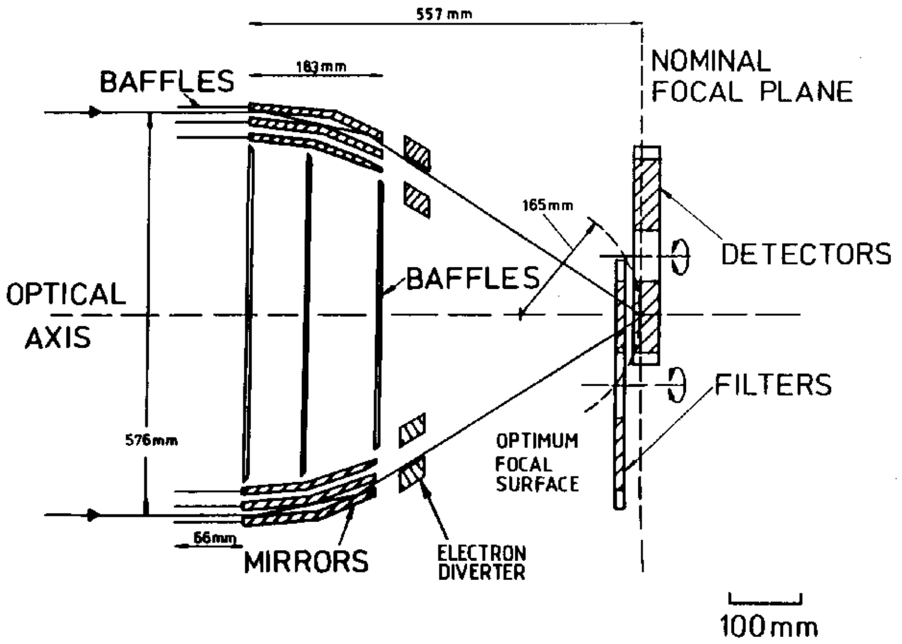

Figure 6.1: Schematic diagram of the WFC showing its principal optical components.

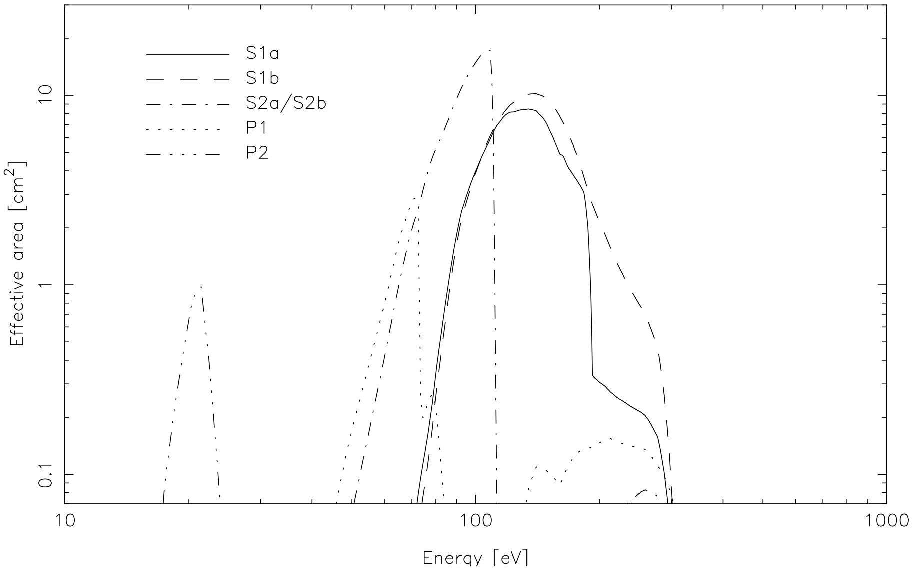

Figure 6.2: The effective area of the WFC for the six science filters (at the time of launch).

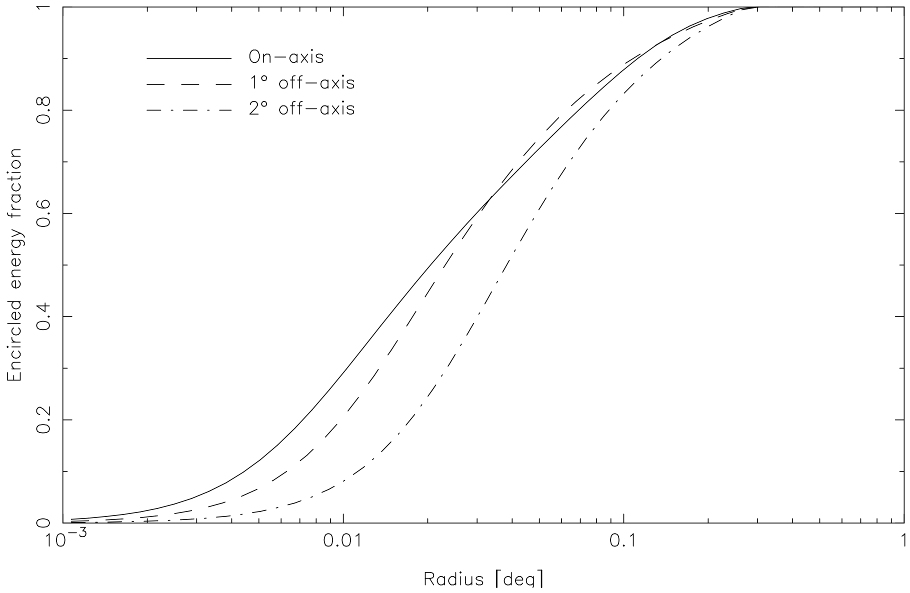

Figure 6.3: In-orbit WFC encircled energy function as measured on-axis and at 1° and 2° off-axis ($E = 124\,\mathrm{eV}$).

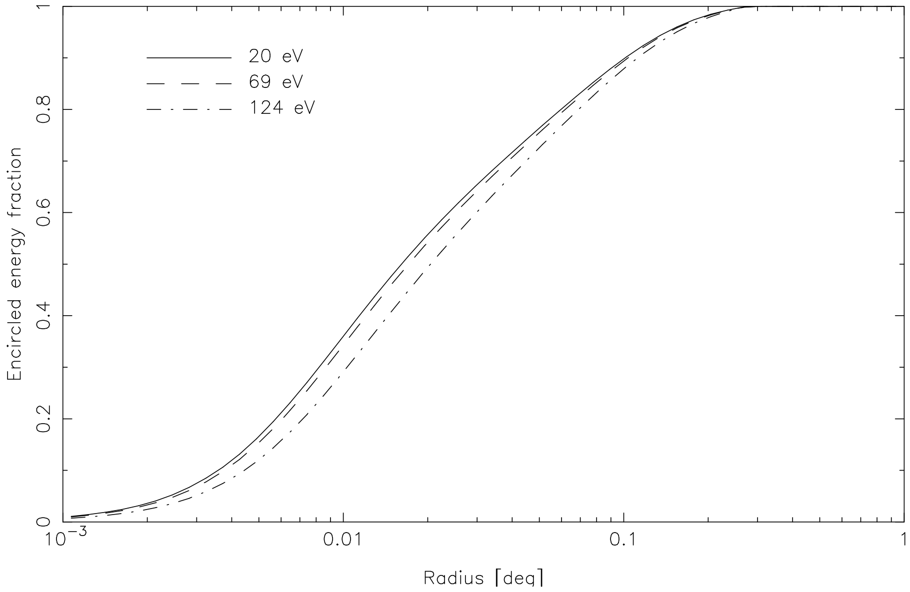

Figure 6.4: On-axis encircled energy function as measured at energies of 20, 69 and 124 eV.

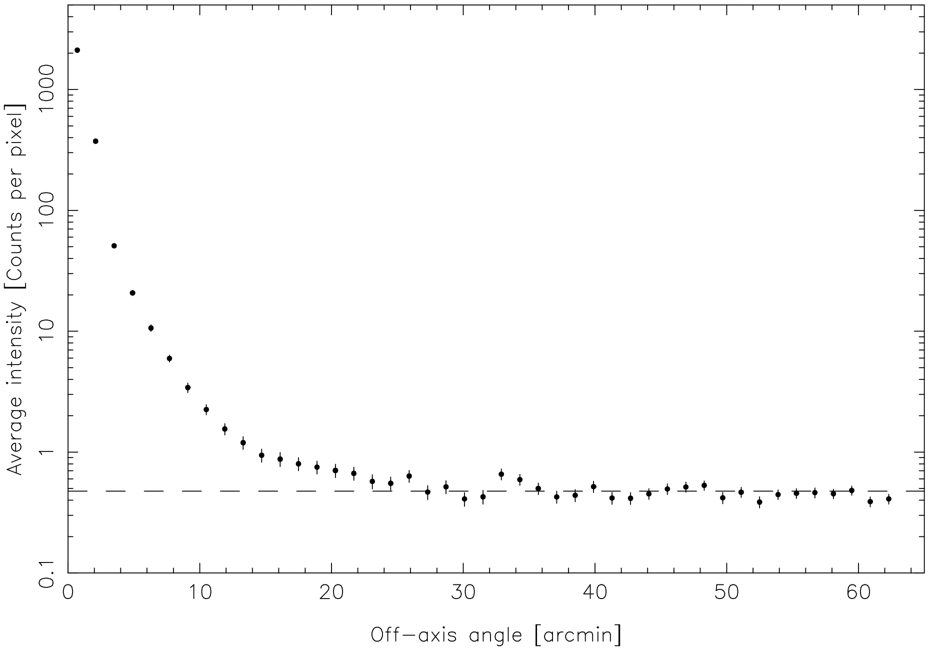

Figure 6.5: Radial response profile derived from an on-axis observation of the bright white dwarf HZ43 during the Performance Verification phase of the mission. The exposure time is 0.9 ksec, and the S2B filter was used for the observation. The dashed line shows the level of the background in the observation.

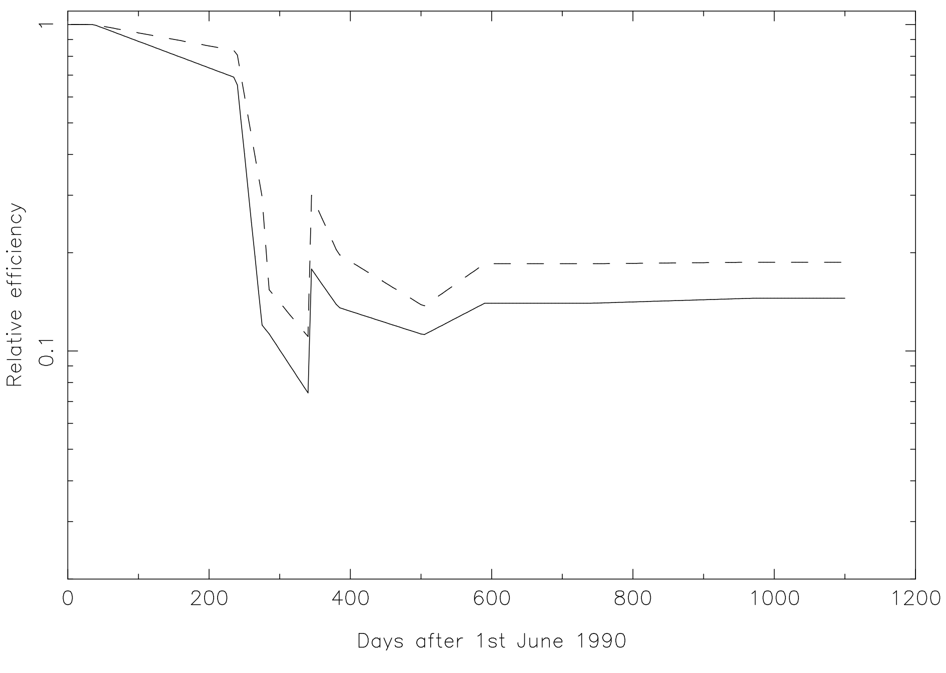

Figure 6.6: The long-term efficiency history of the WFC in the S1 (solid line) and S2 (dashed line) filters. The P1 and P2 filters follow the same trend as the S1 filter.

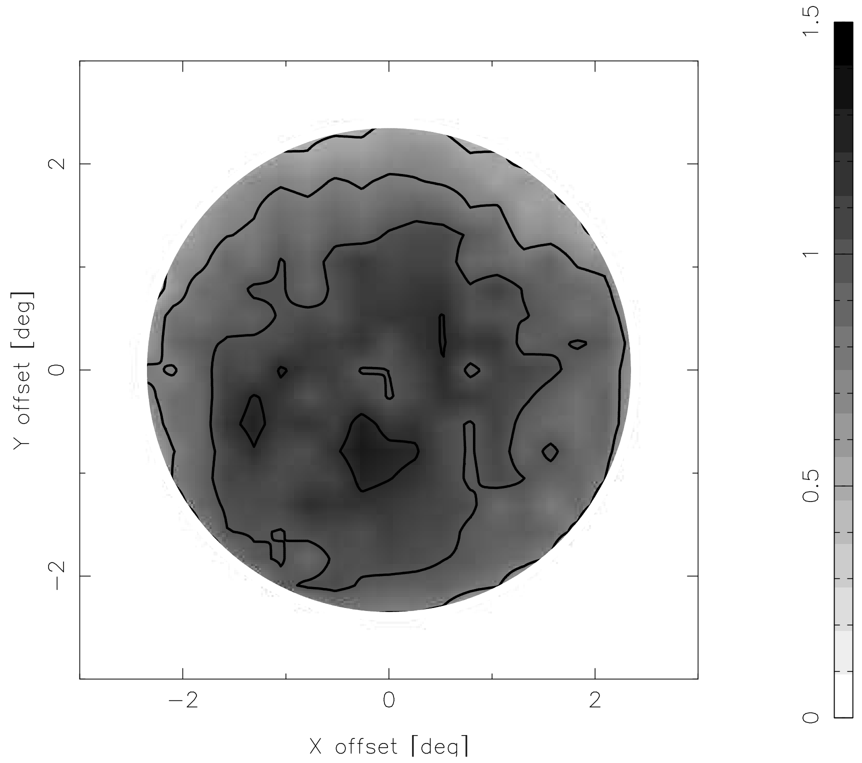

Figure 6.7: The spatial variation in WFC sensitivity, produced from the survey observations of the bright white dwarf HZ43. The sensitivity variations are a combination of the mirror vignetting and the spatial variations in the MCP detector quantum efficiency. Note that the WFC sensitivity peaks off-axis.

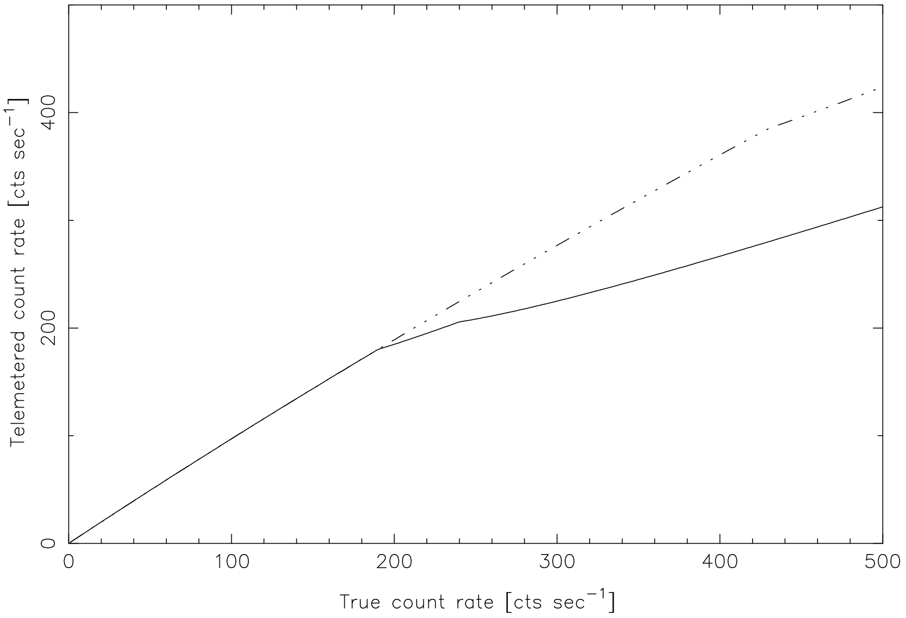

Figure 6.8: Curves showing the telemetered count rate against the true count rate for the WFC in low speed (solid line) and high speed telemetry modes (dashed line). The background count rate in the WFC rarely exceeds 300 counts per second for extended periods of time.

Chapter 7

A GUIDE TO ROSAT PSPC CALIBRATION OBSERVATIONS

7.1 PSPC Calibration Tasks

7.1.1 Spatial Response

Point Spread Function

The primary in-flight calibration datasets related to the *psf* are the AR Lac pointings. AR Lac was chosen for this as it has no discernable extended emission, yet it is a bright X-ray source. The early AR Lac pointings were taken at various positions across the detector, these observations are contained in ROR sequences 110586−110602. Details of these sequences are listed in Appendix B. There was no successful early calibration observation with this source centered in the PSPC, thus in the Hasinger *et al.* *psf* memo (CAL/ROS 92-001), many proprietary sequences belonging to the authors were used as a test of the *psf* model.

Other bright Galactic sources were similarly observed across the face of the PSPC, but most of these had some extended component to their X-ray emission. For example Cyg X-2 was observed over sequences 110001-110012, but is thought to have an extended X-ray emission component due to a dust-scattering halo.

Ghost Images

(*Source:* Article by Nousek and Lesser, *ROSAT* Newsletter #8)

As this effect is related to the softest X-ray photons detectable by the PSPC, very soft X-ray sources were used to quantify the effect. HZ43 was observed at various positions with no wobble, over ROR sequences 110014−110066, in the same way as the *psf* observations were carried out (above). The primary use of these sequences is to illustrate the severe ghost imaging effect.

The electronics processing the signals from the PSPC cathode wires have a lower level discriminator setting which allows distinction between electronic noise and soft X-ray events. For soft X-rays the number of photoelectrons and ions created is small. This means that there is a substantial probability that the sum of the cathode induced signal plus electronic noise may never produce a trigger large enough to pass the lower level discriminator. If all cathode signals in one direction except one are lost, the processing unit assumes that the event occurred directly over the remaining cathode wire (in that direction). If the other direction has a good (more than one contributing signal) position, this results in the formation of a line of events not at the true X-ray location. If both directions only have one cathode contributing to the position determination, the distribution of events will be at four places corresponding to the projection of the source position to the nearest crossing of the cathode wires.

7.1.2 Spectral Response

The earliest Crab spectral data are PI data (Trümper). These now reside in the *ROSAT* archive (sequence 500065F is a boron filter observation of the Crab). Boron filter observations of HZ43 (100113F); N132D (100130F); AR Lac (100588F), and other sources are important to spectral studies are in the archive as well. Observations of constant X-ray sources such as white dwarves (HZ43 and Meaty) and SNR (N132D) allow the project to monitor variations in the response of the detector. calibration observations such as these are combined with calibration line data from the on-board Al K_α calibration source are used in the spectral calibration. For details of the pulse height channel to pulse invariant channel conversion, see chapter 8.

7.1.3 Temporal Response

Timing studies have proved particularly challenging on time scales of a few tens of seconds to minutes. This is due to the modulations produced in the light curves of a constant source as the detector wobble periodically causes source occultations by the window-support wire grid. It has not been possible to date to effectively remove the effect of the wobble from the source light curve. In part, the problem is that the wobble is not strictly along a single vector, and it varies slightly in amplitude and time scale. The accuracy to which the PSPC grid is mapped is also a limiting factor in removing the effect.

7.1.4 Boresight

7.1.5 UV Leak

7.2 Calibration Target Notes

N132D

Brightest X-ray SNR in the LMC. Emission-line dominated X-ray spectrum with strong O lines at 573 and 652 eV. Constant spectrum. Source has an extent of a few arc minutes in the PSPC bandpass.

HZ43

Bright DA white dwarf with $T_e \sim 55,000$ K, nearly pure H atmosphere and very low N_H. Commonly used for calibration the soft X-ray response.

Crab

Power-law emission spectrum due to synchrotron radiation. Size is approximately $1.25' \times 1.75'$. Embedded 33 ms pulsar produces ∼ 10% of X-ray flux. Source is bright enough to use as a rate-gain calibration for the PSPC.

Vela X

10,000 year old remnant of size approximately 6 degrees diameter. Several hundred counts/sec in PSPC and KT$\sim$ 0.13 keV. Contains an X-ray pulsar embedded in an extended synchrotron nebula. X-ray pulsations are found only in the lowest PSPC channels (below 0.85 keV). The spectrum of the pulsar is complex, with an underlying power-law of $\Gamma \sim 2$, a black body from the pulsar, and thermal emission from the SNR.The synchrotron nebula has a power-law of $\Gamma \sim 2$ also. The column density to the pulsar is very low ($\sim 10^{19}$ cm^{-2}).

Pulsar is ∼ 2 UFU with a power-law spectrum. There is a $1'$ nebula surrounding the pulsar.

Meaty

White dwarf discovered by WFC team and thereafter used a soft calibration source.

AR Lac

Eclipsing RS CVn. Two temperature spectrum with very low $N_{\rm H}$ value. Bright, unabsorbed point source used for detector point spread function calibrations.

CYG X-2

LMXB, shallow X-ray dips seen at optical period (9.8 days). Shows oxygen edge at 0.533 keV. Dust halo makes this an extended X-ray source at soft X-ray energies.

CYG X-3

LMXB with high and low states. Partial eclipses observed. Heavily obscured at low energies. Smooth, quasi-sinusoidal modulation suggests the observed X-rays are scattered from an accretion disk corona.

A2256

Nearby (z=0.060) cluster of galaxies. X-ray luminosity (2-10 keV) $\sim 3 \times 10^{44}$ erg cm^{-2} s^{-1}. Core radius is 0.5 MPC ($5'$) and the distribution is smooth. No cooling flow.

LMC X-1

Black hole candidate, soft X-ray spectrum. Embedded in optical nebula. Soft X-ray halo.

LMC X-3

BV3 star and black hole candidate. 1.7 day optical period but no X-ray eclipses seen. Soft X-ray spectrum. Boresight target.

Cas A

Diameter $4'$ SNR. Spectral variations seen across the remnant. SSS found a complex spectrum dominated by strong lines from He-like ions.

Mkn421

BL Lac used a spectral calibration source during its bright state. The assumption of a featureless spectrum, and the 150 counts s^{-1} brightness were the reasons it was used for recalibration of the matrix. Unfortunately this source was affected by the rate-gain and this was not known at the time of recalibration.

Also used to test the tail of the PSPC point spread function to high S/N, after these tests the Lorentzian tail of the *psf* was eventually rescaled (CAL/ROS/92-001a and CAL/ROS/93-015).

β **CAR,** β **LEO, and Vega**

UV leak tests. These stars are A type which are strong UV emitters, but emit no X-rays.

GD695, BPM97895, and EG 187

Bright hot DA white dwarfs. Bright UV point sources, flux and spectral calibration for WFC

δ **Dor,** β **Aur, EPS Lyr**

HRI UV leak cal sources.

Chapter 8

SASS S/W SUMMARY

The chapter SASS S/W SUMMARY will be written by W.Voges and included in the near future.

Chapter 9

STANDARD DATA PRODUCTS AVAILABLE WITHIN THE ROSAT ARCHIVE

(*Source* M. F. Corcoran, U.S. *ROSAT* Science Data Center/GSFC
August 1994)

9.1 Overview

The purpose of the *ROSAT* Data Archive (RDA) is to make *ROSAT* data products available to all users for further detailed analyses. These data products are identical to the FITS products which were distributed to the principle investigator who proposed the observation. In order to divide the workload between the data centers at MPE and GSFC, it was decided that the responsibility for release of data to the archive falls to the *ROSAT* Data Center which distributed the data set to the PI - that is, data sets obtained by German or UK PIs are released to the archive by MPE, while data sets obtained by US PIs are released to the archive by GSFC. In addition, the data are archived in the same format in which it was distributed to the PI.

The RDA provides access to data which resulted from the initial (REV0) processing by SASS, as well as access to data which were processed (or re-processed) by updated versions of the processing system (REV1, REV2). Below we discuss the data products which are archived as a result of REV0, REV1, and REV2 processings. Users should also note that the REV2 archive constitutes the “official” *ROSAT* Data Archive.

Table 9.1: REV0 Data Products in the RDA

Instrument	Archived Data Product
PSPC	lists of accepted photon events
	lists of rejected photon events
	lists of standard accepted times (*i.e.*, "good times")
	total, hard, and soft band images
	a merged exposure map
	attitude information
	spacecraft orbit information
	housekeeping and engineering information
	energy-coded map (German/UK data only)
	lists of catalogued SIMBAD sources in the field
	detector response matrix
	on- and off-axis effective-area file
	point-spread function file
	broad-band instrument map
	postscript plots (US data only)
HRI	lists of accepted photon events
	lists of rejected photon events
	lists of standard accepted times (*i.e.*, "good times")
	total band image
	a merged exposure map
	attitude information
	spacecraft orbit information
	housekeeping and engineering information
	quantum efficiency map (US only)
	bright earth map (US only)

9.2 REV0 Data in the RDA

Data which were processed by SASS versions earlier than version 6.0 (which was available after 1993 TBD at MPE and after 1993 TBD in the US) constitute the REV0 archive. Because of problems with the initial release of SASS (such as the timing problem and often large aspect uncertainties) it was decided by international agreement that the REV0 data products would constitute only an intermediate data archive, and further that some derived products like source lists and background maps produced by the REV0 processing system were too unreliable to constitute an archived data product. As a result only a subset of the REV0 data products distributed to the Principal Investigator were released to the RDA. Thus, for each observation, the REV0 data products in the RDA include only the following data products listed in Table 9.1.

The number of data files archived with each data set depends on the instrument in use. In addition the number and format of the data files depends on where the data were processed. REV0 data processed and released by MPE use a FITS format designed to be used in the EXSAS analysis environment, while data processed and released by GSFC use a FITS format which was designed to be used with the PROS analysis package. Thus, while the data products conform to the FITS standard, there are many differences between the "EXSAS" and "PROS" versions. These differences include the grouping of information in files, differences in labelling of information, and the formats (binary or ascii) of the files themselves. While these differences are for the most part cosmetic, they can prove vexing to the casual archive user who wants to simultaneously analyze a German and a US observation of the same field. Software "translators" are available in EXSAS and PROS to enable correct interpretation of REV0 data in either the EXSAS or PROS formats.

Tables 9.2, 9.3, 9.4, and 9.5 list the data products for typical US and German/UK data sets archived in the RDA for a PSPC and an HRI observation, and the name of the corresponding file in the USRDA.

9.3 REV1 Data in the RDA

REV1 data are those data sets processed by SASS 6.0 or higher and distributed in the same FITS format used for REV0 data (*i.e.*, not the Rationalized Data File format used for REV2 data, see Section 9.4 below). When REV1 data are released to the archive, all the data products listed in Tables 9.1, 9.2, 9.3, 9.4, and 9.5 are archived with each data set as appropriate. However, some problems afflicting the REV0 data products (such as the PSPC timing error) have been corrected in the REV1 data.

9.4 REV2 Data in the RDA

Starting in 1994 April, processing centers in the US and Germany began distributing data in the so-called "Rationalized Data File" (RDF) format. The RDF format was designed by joint effort between the US and German RSDCs. RDF utilizes standard FITS constructs with file extension structures, header keywords, table columns standardized in a generic, multi-mission manner. The adoption of the RDF format by both data centers means that the format of data processed after 1994 April will be site-independent. In addition, since the RDF format is also being utilized by other high-energy astronomy missions such as *Einstein* and *ASCA*, joint analysis of data from these missions and *ROSAT* is made easier. For more information about the RDF format, consult the *ROSAT* Data Products Guide.

REV2 data are those data processed by SASS 6.0 or higher and distributed in RDF format. It is planned that all REV0 data will be reprocessed into REV2 data and released to the archive. In addition, REV1 data will be converted to RDF (although not reprocessed through SASS) and archived. As the RDF versions of the REV0 and REV1 data are archived they will replace the earlier archived versions. This means that eventually the RDA will solely consist of data processed with SASS 6.0 or higher in RDF format.

Table 9.2: Data type description for US-format filtered and non-filtered PSPC data

File description	Sample file in USRDA
photon list	rp110590.fits
broad-band image	rp110590_im1.fits
hard-band image	rp110590_im2.fits
exposure map	rp110590_mex.fits
soft-band image	rp110590_im3.fits
SIMBAD source list	rp110590_sky.fits
public contents file	rp110590.public_contents
photon list	rp110590.fits
master data stor	rp110590.mds
processing parameters	rp110590.par
response matrix	rp110590.dmp
instrument map	rp110590.moi
Off-axis area	rp110590.oar
radiation cal results	rp110590.rcr
exposure map	rp110590_mex.fits
Aspect quality	rp110590.asp
corrected aspect	rp110590.cas
event rates	rp110590.evr
binned housekeeping	rp110590.hkb
split aspect	rp110590.sa
smoothed aspect	rp110590.sas
split orbit	rp110590.so
housekeeping status	rp110590.sta
Extracted SIMBAD list	rp110590_smx.asc
V&V report	rp110590_vv2924.report
aspect plots (1/obi)	rp110590_aaq001_16.plt
event rate plot(1/obi)	rp110590_evr001_16.plt
cover page	rp110590_fps.plt
housekeep. plot(1/obi)	rp110590_hks001_16.plt
broad-band image	rp110590_im1.plt
hard-band image	rp110590_im2.plt
soft-band image	rp110590_im3.plt
SIMBAD source plot	rp110590_smx.plt

Table 9.3: Data type description for US-format HRI data

File description	Sample file in USRDA
photon event list	rh110267.fits
HRI image	rh110267_img.fits
SIMBAD sky list	rh110267_sky.fits
public contents file	rh110267.public_contents
complete photon store	rh110267.cps
merged status history	rh110267.mob
split status history	rh110267.ots
standard good intervals	rh110267.sgi
standard screen results	rh110267.ssc
temporal status history	rh110267.tsh
Processing parameters	rh110267.anp
bright earth intervals	rh110267.obi
bright earth event list	rh110267.obt
Processing parameters	rh110267.par
charged particle bkg	rh110267.cpb
detector background	rh110267.dbm
quantum efficiency map	rh110267.qeg
aspect histogram	rh110267.ah
aspect offsets	rh110267.ao
count rate histogram	rh110267.dms
Science frame quality	rh110267.htl
live-time factors	rh110267.ltf
Observation angles	rh110267.oan
HRI sampling histogram	rh110267.s1d
HRI SAA rates	rh110267.saa
split orbit	rh110267.so
science rates	rh110267.sps
SIMBAD sky plot	rh110267_sky.plt
rates plot (1/obi)	rh110267_str.plt
SIMBAD source list	rh110267_sky.asc
V&V report	rh110267_vv2925.report

Table 9.4: Data type description for MPE-format filtered and non-filtered PSPC data

File description	Sample file in USRDA
photon list	wp110130_events.tfits
broad-band image	wp110130_image1.ifits
hard-band image	wp110130_image2.ifits
soft-band image	wp110130_image3.ifits
energy-coded image	wp110130_imageec.ifits
Exposure map	wp110130_mexmap.ifits
public contents file	wp110130.public_contents
mpe public contents	wp110130.public_contents_mpe
rejected events	wp110130_difevents.tfits
response matrix	wp110130_drmpspc.ifits
instrument map	wp110130_moimp.ifits
Off-axis area, PSPC B	wp110130_effarea_pspcb.tfits
Off-axis area, PSPC C	wp110130_effarea_pspcc.tfits
Quality file	wp110130_quality.tfits
attitude file	wp110130_attitude.tfits
event rates	wp110130_eventrates.tfits
orbit	wp110130_orbit.tfits

Table 9.5: Data type description for MPE-format HRI data

File description	Sample file in USRDA
photon event list	wh110131_events.mt
public contents file	wh110131.public_contents
mpe public contents	wh110131.public_contents_mpe
rejected events	wh110131_difevents.mt
effective area	wh110131_effarea_hri.mt
hot spot map	wh110131_hotmat.mt
quantum efficiency map	wh110131_qefficiency.mt
aspect	wh110131_attitude.mt
event rates	wh110131_eventrates.mt
orbit	wh110131_orbit.mt
data quality	wh110131_qualitylimits.mt
data quality limits	wh110131_quality.mt

Table 9.6: RDF data products

RDF File	Description	Sample PSPC file	Sample HRI file
BASIC	photon events and good times	rp123456_bas.fits	rh234567_bas.fits
	uncorrected events list	rp123456_raw.fits	NA
ANCILLARY	orbit, aspect and housekeeping data	rp123456_anc.fits	rh234567_anc.fits
DERIVED	total band image	rp123456_im1.fits	rh234567_im1.fits
	hard band image	rp123456_im2.fits	NA
	soft band image	rp123456_im3.fits	NA
	exposure map	rp123456_mex.fits	NA
	processing history	rp123456_his.fits	rh234567_his.fits
	total background image	rp123456_bk1.fits	rh234567_bk1.fits
	hard background image	rp123456_bk2.fits	NA
	soft background image	rp123456_bk3.fits	NA
	exposure map	rp123456_mex.fits	NA
	source analysis results	rp123456_src.fits	rh234567_src.fits
	source light curves	rp123456_ltc.fits	NA
	postscript info	rp123456_prt.fits	rh234567_prt.fits

Table 9.6 lists the RDF data products generated for both PSPC and HRI.

Appendix A

ROSAT Mission History

A.1 General Spacecraft & Instrument Status

There are four sources (official & semi-official) of status information concerning the *ROSAT* mission:

- Electronic *ROSAT* Status Reports, produced (semi-independently) by MPE, the NASA *ROSAT* GOF, and the UK *ROSAT* GOF.
- The World Wide Web at MPE, the NASA *ROSAT* GOF, and the UK *ROSAT* GOF.
- Hardcopy newsletters, produced (semi-independently) by MPE, the NASA *ROSAT* GOF, and the UK *ROSAT* GOF.
- Hardcopy memos, produced (semi-independently) by MPE, the NASA *ROSAT* GOF & the HEASARC, and the UK *ROSAT* GOF.

A.1.1 *ROSAT* Status Reports

Electronic Status Reports related to the *ROSAT* mission are issued semi-independently:

- By MPE
- On behalf of the NASA *ROSAT* GOFs by the USRSDC at NASA/GSFC (nominally bi-weekly)
- By the UK *ROSAT* GOF at the University of Leicester

In all cases these are intended to rapidly provide the user community with up-to-date information regarding the status of the satellite and payload, and related topics such as the observing program, AOs, meetings, *etc.* Table A.2 lists all NASA *ROSAT* GOF Status Reports which have been issued to date. For inclusion on the e-mail distribution please, contact LHEAVX::KSMALE. Copies of all earlier reports are available via ANONYMOUS ftp on the legacy.gsfc.nasa.gov machine.

Table A.1: Summary of USRSDC *ROSAT* Newsletters

Number	Date	Highlights
1	1989 Feb	Introduction to MIPS/PROS
Special Ed.	1990 Jan	AO1 summary
4	1990 Jul	PVC info
5	1991 Jun	GOF info
6	1991 Nov	Observation Log, blacklist, IDL
7	1992 Sep	PSPC *psf*, *ROSAT* archive, FTP info
8	1993 Jun	Ghost Image article, IDL & PROS updates
9	1993 Nov	PSPC off-axis *psf*, FTP info
10	1994 May	RDF, archive update

A.1.2 The World Wide Web

The MPE *ROSAT* page URL is
`http://rosat_svc.mpe-garching.mpg.de/`
The GSFC *ROSAT* Mission and GOF page URLs are
`http://heasarc.gsfc.nasa.gov/0/docs/rosat/rosat3.html`
and
`http://heasarc.gsfc.nasa.gov/0/docs/rosat/rosgof.html`
respectively. The UKRDAC can be reached through the Leicester University, Department of Physics and Astromony home page:
`http://www.star.le.ac.uk/`

A.1.3 *ROSAT* Newsletters

Hardcopy *ROSAT* newsletters are issued semi-independently by:

- MPE – *ROSAT Forum*
- The US *ROSAT* Science Data Center (USRSDC) – *ROSAT Newsletter*
- The UK *ROSAT* GOF at the University of Leicester

Table A.1.3 lists all the USRSDC Newsletters have been issued to date. Copies of all these reports are available on request from Karen M Smale, Code 668, NASA/GSFC, Greenbelt MD 20771 (15735::KSMALE; ksmale@heasrc.gsfc.nasa.gov).

A.1.4 Memos

Hardcopy technical memos related to the *ROSAT* mission, data analysis techniques, *etc.*, are issued by:

- MPE

- OGIP
- The UK *ROSAT* GOF at the University of Leicester

Appendix C lists all OGIP Calibration Memos produced related to *ROSAT* . These are available on request from Pat Tyler, Code 668, NASA/GSFC, Greenbelt, MD 20771.

A.2 Important Dates

Below we list the more important dates associated with *ROSAT* operations. As is true for all missions, *ROSAT* has also experienced a number of additional (minor) operational difficulties since launch. A summary of all the periods lost due to satellite problems (the so-called "black-list") can be found in the *ROSAT Newsletter.*

1990 June 1
Launch of *ROSAT* spacecraft on a Delta II from Cape Canaveral, USA, and in-orbit deployment. Initial switch-on and on-board engineering tests performed without any indications of hardware or software problems.

1990 June 16
Start of scientific observations with the First Light Observation of the XRT/PSPC-C pointing at the LMC.

1990 June 17
WFC First Light Observation of the "meaty" source RE1629+780, a serendipitous discovery during the PSPC calibration observation of Abell 2256 on 17 June 1990.

1990 July 1
XRT/HRI First Light Observation of Cyg X-2.

1990 July 1 TBR
One of the two WFC background monitoring instruments (GM tubes) malfunctions, giving WFC operational difficulties.

1990 July 11–15
As part of the PVC phase, the *ROSAT* "mini-survey" was performed.

1990 July 16–29
PVC phase pointed observations using the PSPC (July 16–23) and HRI (July 24–29).

1990 July 30
ROSAT all-sky survey begins (using PSPC-C in the XRT focal plane)

1990 August 17–19
Valve which regulates the flow of gas into the PSPC-C failed on August 17. The gas pressure dropped to point where the high voltage was automatically switched off. No PSPC data were taken between 1990 August 17 14:00 UT and August 19 00:00 UT when a backup value was switched on. Since no area of the sky went totally unobserved, the decision was made not to alter the offset angle and to proceed with the survey timeline as planned. WFC survey observations

continued as planned during this period.

1990 September 8

The *ROSAT* AMCS star tracker STC-2 (Section 1.2.5) stopped working continuously during the scan mode and has since failed completely. STC-1 remains fully operational, and there is only a minor decrease in expected attitude accuracy.

1990 December 22–26

Gyro malfunction and subsequent loss of telescope attitude

1991 January 5–6

Loss of attitude.

1991 January 15–18

At 07:10 UT, the survey rate was increased to 1.2678° per day.

1991 January 25

With all but the last week of the six month all-sky survey completed, an almost fatal OBC glitch on 1991 January 25 at 20:18 UT caused the S/C to start spinning in an uncontrolled manner for $\sim$ 15 hours, with all instruments still operational. The failure is not fully understood, however, its origin may lie in a build-up of radiation-induced events, inhibiting the switchover to the redundant OBC CPU, as should automatically occur after a halt in AMCS telemetry. Housekeeping data taken during the tumbling showed that the satellite scanned across the sun, burning a hole in the window of PSPC-C (and hence destroying the detector) and damaging the S2a filter in use on the WFC. This event was probably the origin of the degradation in WFC efficiency (although not recognized until 1991 May). Three hours after the loss of attitude, the S/C power dropped and non-essential loads (including the scientific payload) were automatically turned off, in which state it remained until January 26 when GSOC successfully managed to revive it during a ground contact period. The (final) "$\sim$1-week" strip of the sky which went unobserved during this time was surveyed later between 1991 August 3–13, thus completing the All-Sky Survey.

1991 February 8

AO-1 pointed observations begun using (the reserve) PSPC-B.

1991 February 16–18

Survey observations to make up lost exposure from July 1990.

1991 March 25–27

Solar flare activity in 1991 much enlarged the radiation belts and increased the PSPC-B background, causing a loss of observations due to the PSPC-B count rate exceeded the danger threshold. Adjustments to the tolerances led to resumed operations, with 80% of the pre-flare efficiency

1991 April 6–10 & April 21

ROSAT suffered a loss of attitude on April 6, and subsequently ended up in safe mode as a result of the extra safety procedures implemented after the loss of PSPC-C. Observations scheduled for April 6–10 were lost. A further attitude loss occurred on April 21 resulting in the loss of an additional day of data before normal operations were restored.

1991 April 26–30
Difficulties were encountered with the uplinking of new software patches developed to address the problems of maintaining known attitude, resulting in the satellite switching to safe mode. By April 30, the problems were resolved.

1991 May 12–18
It became clear that WFC count rates were systematically less than expected based on the WFC survey. A calibration observation of RE1629+781 confirmed the gain loss, and showed that a new operating voltage was required. The WFC count rates were determined to be $\sim 20\%$ of the expected values and the backup detector degradation was even more severe than that suffered by the primary.

The Y-axis gyro on *ROSAT* failed sending the satellite into safe mode. The Z- and S-gyros (Section 1.2.3) functioned normally, but the X-gyro was problematic (and was removed from the control loop during the All-Sky Survey after its drift rate exceeded specifications). Attitude control was successfully regained on May 18. There appears to be no hope of retrieving use of the Y-gyro.

1991 May 18 – November 4
"Reduced-Pointing" mode whereby slews and target acquisition were tightly constrained due to the use of the X-gyro in the control loop. Slews were reduced to one direction and constrained to be short, guide stars needed to be available when the satellite was over Weilheim (*i.e.,* target declinations were constrained to be $> +20$ degrees), a reduced sun cone angle was enforced (90 ± 5 degrees), only one target was observed per day and only PSPC observations were allowed.

Also, during this period, an increased level of solar activity led to high levels of radiation, causing the detector to safe itself several times. These conditions resulted in a yield of $\sim$ 30,000 seconds of *ROSAT* data for each day of observation. New AMCS on-board software enabled a successful resumption of normal pointing operations on 1991 November 4.

1991 July 5–8
After a long slew on July 5, *ROSAT* became lost due to Earth-block and lack of guide stars. Consequently the S/C went into safe mode due to operating too long without reference stars. Successful recovery procedures were carried out over the weekend of July 6–7.

1991 August 3–13
Survey completion observations of the stripe of the sky unsurveyed during the scheduled All-Sky Survey phase due to the "Solar Slew" on 1991 January 25.

1991 October 11 (S/C clock 42910000)
During the preceeding months, PSPC-B had developed a slightly higher background rate extending over the whole sensitive area of the detector but confined to the lowest pulse height channels. A hot spot near the edge of the field of view was also observed. Investigations revealed that the hot spot count rate had increased from about 0.001 to about 0.01 counts s^{-1} over the preceeding $\sim$ 6 month period. Purging of the detector gas and switching the gas supply from tank B to tank A (to exclude the possibility of different gas composition) reduced the hot spot count rate and the count rate in the lowest pulse height channels by approximately a factor of 2. Although no immediate danger for

the detector operation could be identified, the high voltage of the detector was lowered from 3060 to 3000 volts on October 11. As a consequence, the PSPC-B gas gain dropped by approximately 30% and thus the lower PI channel limit of the detector was raised from about 8 to 11. Calibrations at the reduced voltage have shown that there is no change in the spectral resolution of the detector

1991 November 4
The new AMCS onboard software allowed a successful resumption of normal pointing operations, marking the end of the "reduced pointing phase" (which followed the loss of the Y-gyro on 1991 May 12) and the start of AO-2. More than two hundred pointings were carried out in the reduced pointing phase, most of them lasted one day (and were selected from AO-1 targets with approved times $\gtrsim 10^4$ s). The scheduling constraints varied quite frequently and required rapid adjustments by both MPE and GSOC mission planning staff.

1992 February 6–24
A large transient in the *ROSAT* Z-gyro current occurred on February 6, reminiscent of that which immediately preceded the loss of the Y-gyro in 1991 May 12. The S/C was put into safe mode at that time and observations were suspended. The Z-gyro, although operating continuously with too high a current, was still giving meaningful readings of angular velocities. However, its output signal seemed to be scaled wrongly, indicating a factor of 3-4 slower speeds than the spacecraft was actually performing. Evaluation of the Z-gyro malfunction proved that the measurement outputs of the Z-gyro were still valid, however the scale factor had changed by a constant factor of 2.8. The most convincing explanation of the available data implied that 1 of 3 phases of the gyro motor failed, and consequently the motor current had increased. To compensate for the decreased Z-gyro output, a new change of the onboard software was developed and tested on the GSOC simulator over February 18–19. This software patch contained the change of the Z-gyro scale factor by 280%. This software update meant that the scale factors of the other gyros cannot be commanded anymore, which fortunately has little impact on mission operations. The software patch was successfully up-linked on February 20 and passed a first test in the form of a slew to the north ecliptic pole on the same day. After the slew, the attitude was correct and reference stars were identified. *ROSAT* went back on the Mission Timeline on 1992 February 24 and the first three slews were successfully performed. This success indicated that the new gyro scale factor was correctly determined and appeared to be quite stable.

1992 March
The MPE/GSFC/SAO *ROSAT* calibration team found that the HRI point-spread function had an unexpected component which redistributes roughly 10 percent of point-source photons beyond a central core (radius $\sim 10''$) and into a region that extends out to about $5'$, an effect which is relatively independent of energy.

1992 November 1
The US *ROSAT* Public Data Archive (USRPDA), located at the Goddard Space Flight Center in Greenbelt, MD, officially opened.

1993 January 10

Problems with STC-1. In about 30% of the slews to a new target position, the mapping period of the startracker at the end of the slew takes more time (from 1 up to 20 minutes) until the tracker enters the pointing mode. This lead to a minor shortening of some of the observations, while a few targets were lost.

German and UK data entered the US archive later the same month.

1993 January 12

New PSPC response matrix released.

1993 February 24

1000 days in orbit celebration, production of T-shirts, "Tausand und Eine Nacht mit *ROSAT*".

1993 May

The malfunction of STC-1 was traced to a failure in the conventional RAM area. This failure was similar to the cause of the complete loss of STC 2 in autumn 1990, where a much more vital memory cell was lost, which rendered STC-2 unusable. The STC-1 anomaly has stabilized at a rather lower failure rate than observed in January/February, corresponding on average to a 5-10 % loss of observing time.

1993 June

The HRI was moved into the focus on June 10 for the last time in AO-3. The PSPC gas flow rate was reduced the same day. The PSPC had time until June 15 (the beginning of AO-4) to settle down at the new equilibrium. Immediately after the switch-on on June 15, an extended radioactive source calibration was started which was followed by 1 orbit of filter-wheel-closed background measurements. This procedure was repeated the next day. For the first week after the switch-on, the radioactive calibrations were repeated once per day. Background measurements are taken once per week for one orbit.

The PSPC performance at reduced flow rate looked good. The gain dropped slightly, from channel 103 before to 100 after the switchover.

Two cases were found where, due to the reduced accuracy of the onboard gyro system, the AMCS after a slew locked on to an incorrect star pattern. In both cases, only two stars were available in the startracker field of view and the commanded star pattern (essentially star separation and the magnitudes) were fulfilled also by a nearby star pattern, about 2 degrees off from the commanded position. Both the onboard and the ground system attitude software system therefore assumed a correct pointing and could not recognize the error.

1993 August 1

MPE and GSFC (in consultation with SAO) have concluded, through independent analysis of calibration and other data, that there is some temporal variation of the PSPC gain which is not included in the gain correction process currently applied to data in SASS.

This effect showed up primarily as inconsistencies between calibration spectra of N132D taken at different epochs across the *ROSAT* mission. Another artifact of the problem is highly significant residuals in number of spectra compared to the expected model, these appear as large negative residuals below about 0.20 keV and large positive residuals between about 0.20 to 0.4 keV.

1993 August 10

The Off-Axis Point Spread Function algorithm was released.

1993 September 22

Survey Data made available for background estimations.

1993 September

A roll angle error was found. The effect of this roll error is not included in the current SASS processing. (It will be included in the "Rev 1" reprocessing of the entire dataset planned for the near future.)

The error is small, being 0.185 degrees for the PSPC. This corresponds to a position error of 6 arcseconds at the radius of the support ring.

1993 November 26

Timeline operations were resumed with a modified observing program, constructed under the boundary conditions that slews occur only on the day side and no observations be carried out with a sun cone angle between 85 and 95 degrees.

1993 December TBD

End of six-month block of PSPC observations in AO-4.

1993 December 18

ROSAT entered safemode again.

After Christmas and in early January there were a number of occasions during which problems in *ROSAT*'s attitude measurement and control system (AMCS) caused the satellite to drift away from its nominal pointing direction. This ended up with the safe mode being triggered. *ROSAT* remained in safe-mode while the problem was investigated. It soon became clear that the problem was related to the new attitude control strategy which became active after the Z-gyro failure that occurred in 1993 November.

1993 December 22

The wobble was disabled to reduce attitude control problems.

1994 February 2

A temporary observing program began to test some solutions to the pointing problem.

1994 February 26

The observing program restarted at midnight of February 26/27 (UT), beginning with five days of PSPC observations.

1994 March 4

HRI observations began.

1994 June 30

The PSPC was moved into focus for a last seven-day period lasting from 1994 June 30 to July 6. This ended the regular *ROSAT* PSPC guest observer program.

Table A.2: List of NASA/GSFC *ROSAT* GOF Status Reports

Number	**Date**	**Major Content**
1	1991 Mar 21	Overview of project software
2	Apr 03	Satellite & processing status
3	Apr 25	AO2 notes and blacklist
4	May 15	Gyro problems
5	Jun 10	Reduced Pointing Timeline
6	Jul 05	AO2 IUC meeting report
7	Jul 17	Satellite safed
8	Aug 05	SASS status
9	Aug 19	Timeline
10	Sep 06	SASS status
11	Sep 12	Timeline update
12	Oct 04	Attitude software update
13	Oct 21	SASS & satellite status
14	Nov 14	AO3 announcement
15	Nov 20	Guidelines for AO3
16	13 Dec	Databases
17	1992 Jan 7	Mission Planning Status
18	Feb 11	Z-gyro problem
19	Feb 25	general status
20	Feb 28	February 5–28 lost AO-2 sequences
21	Mar 24	April – June AO-2 timeline
22	Mar 31	HRI Spatial Response
23	Apr 8	Proc. problems, WFC bright source catalogue
24	May 11	AO3 results
25	May 22	Science bulletin: Geminga
26	Jun 11	AO1 & AO2 holdovers
27	Jun 11	AO3 timeline
28	Jul 9	rosserv ftp account announced
29	Aug 7	MPE report # 10, calibration
30	Aug 18	IDL routines
31	Sep 8	US workshop announcement
32	Sep 24	Workshop reminder
33	Oct 1	MPE report #11
34	Oct 6	Workshop update
35	Oct 27	Meeting agenda

Table A.2: List of NASA/GSFC *ROSAT* GOF Status Reports (cont.)

Number	**Date**	**Major Content**
36	Nov 16	Public Archive Opens
37	Nov 17	AO4 announcement
38	Nov 25	AO3 timeline
39	Dec 1	New matrix
40	Dec 9	Master Observation List available
41	Dec 14	UK bulletin, matrix bug
42	Dec 17	Archive access
43	Dec 23	HRI performance update
44	Dec 24	PROS hints & pointers
45	1993 Jan 13	New matrix
46	Jan 15	UK & German data released to archive
47		Never Existed
48	Jan 26	Archive note
49	Jan 29	RPS warning
50	Feb 3	MPE bulletin # 15
51	Feb 3	Archive note
52	Mar 1	MPE report # 16
53	Mar 26	Hints & Pointers
54	Mar 30	Report from calibration workshop
55	Apr 19	ftp moves to legacy
56	May 6	UK & German data release
57	May 6	MPE Report # 17
58	May 10	AO4 targets
59	May 12	More UK & German data in archive
60	May 20	1993 workshop
61	Jun 2	AO4 timeline
62	Jul 13	MPE Report # 19: Reduced PSPC gas flow
63	Jul 14	Hints & Pointers # 9
64	Aug 1	PSPC gain problem
65	Aug 10	Off-Axis PSPC *psf*
66	Sep 22	Survey Data available for bgd estimation
67	Oct 13	Error in roll angle
68	Oct 25	The OGIP *ROSAT* PSPC Calibration Guide
69	Oct 26	US *ROSAT* Public Data Archive questionnaire
70	Oct 28	*ROSAT* Science Symposium schedule

Table A.2: List of NASA/GSFC *ROSAT* GOF Status Reports (cont.)

Number	**Date**	**Major Content**
71	Nov 13	*ROSAT* Z-axis gyro fails
72		
73	Nov 30	*ROSAT* operations
74	Dec 9	new Ftools release
75	Dec 13	Caution to check coordinates
76	Dec 15	*ROSAT* sequence-naming conventions
77	Dec 16	New time lines on FTP
78	Dec 22	PSPC PI channels and bands
79	Dec 23	MPE Report # 24
80	Dec 29	Hints & pointers for PROS users
81	1994 Jan 1	AO5 announcement
82	Jan 28	*ROSAT* in safe-hold mode
83	Feb 2	MPE Report # 25
84	Feb 7	RPS5 Note
85	Feb 16	Off-axis point spread function for the *ROSAT* HRI
86	Mar 1	*ROSAT* satellite status, naming conventions, PROSCON
87		MPE Report # 26
88	Mar 14	Short-term timelines
89	Apr 1	MPE Report # 27
90		
91	Apr 22	*ROSAT* archive enhancements
92	Apr 25	Correction to the PSPC Off-Axis *psf* memo
93	May 04	MPE Report # 28
94	May 19	Data set naming conventions
95	Jun 21	New information available
96	Jun 27	Hints and pointers for PROS users #11
97	Jul 05	MPE Report # 29
98	Jul 15	Archive Note
99	Jul 27	Hints & pointers for PROS #12 (PROS 2.3.1 patch)
100	Aug 01	MPE Report # 30

Table A.3: List of OGIP Calibration Memos concerning the *ROSAT* PSPC

Memo code Number	**Date (last update)**	**Title (authors)**
CAL/ROS/92-001	1992 October 5	The On-Axis Point Spread Function: In-flight comparison with the PANTER results. (Hasinger, Turner, George & Boese)
CAL/ROS/92-001a	1992 October 30	Addendum: High Signal-to-Noise In-flight Data (Hasinger, Turner, George & Boese)
CAL/ROS/93-007	1993 July 26	Stability of the PSPC Spectral calibration (Turner)
CAL/ROS/93-015	1993 September 18	The *ROSAT* PSPC Off-Axis Point Spread Function (Hasinger, Boese, Predehl, Turner, Yusaf *et al.*)
CAL/ROS/94-005	1994 April 13	Region Selection Based on Detector Co-ordinates: a cautionary note (Turner)

Appendix B

KNOWN PROBLEMS AND BUGS

B.1 Spatial

B.1.1 Ghost Images

The *ROSAT* PSPC cannot always properly position X-ray events with very low energy. This results in an extension to the image caused by the detector response to very soft X-ray photons, but one which will not fit any *psf* model. The effect is very pronounced below channel 15 (~ 0.15 keV) but is not evident above channel 20 (~ 0.2 keV). For a detailed description see Section 3.5.4 and Nousek & Lesser (1993)

B.1.2 Aspect reconstruction and Attitude Errors

(*Source:* Hasinger, archive users notes)

It has been found that in the Standard Processing, some of the data delivered to the observers may still contain time intervals during which the applied attitude solution shows unacceptably large errors. The aspect error in the attitude file, which is screened against, has been lowered successively from $120''$ to $2''$ (SASS5_4_8, 1992 December 20) and $1''$ (SASS5_6, 1992 March 17) for the PSPC and to $1''$ (SASS5_5_2, 1992 March 10) for the HRI. As long as the formal aspect error is below $1''$ the GSOC attitude solution is reliable within about $10''$. For aspect errors the range $1'' - 10''$, the situation is not unique because the star sensor is usually tracking only one star, which cannot be identified unambiguously. We urge the user to assure himself of the integrity of the data by inspecting the attitude error entries in the attitude file.

Users analyzing data summed over from observations taken several months apart should be aware that the boresighting and irreproducible errors may produce position differences of up to $20''$ between the observations. These can be corrected for by first analysing the datasets separately and then shifting them to a common reference frame using the detected X-ray sources.

Exposure Map

There are a few number of pointed observations with aspect errors less than $1''$ but with the aspect solution drifting away from the nominal position by an appreciable amount. This has the consequence that an unfavourable mean aspect is calculated and not all aspect entries are projected into the aspect histogram and thus these times will not be counted in the exposure map. The situation has been remedied by implementing a new screening technique, accepting only aspects that are within limits from the nominal position (SASS5_9, 1992 August 20). Before 1992 April 22 (SASS5_7), the exposure maps have been produced using an instrument map derived from ground calibration data. In the meantime a set of energy-dependent instrument maps exists in the calibration file, derived from survey data with both PSPC-C and PSPC-B. We therefore urge users to reconstruct their own exposure maps from the attitude file.

Roll Angle

It has recently been realised that there is a systematic error in the roll angle with respect to the astronomical coordinate frame of the PSPC and HRI. The effect of this roll error is not included in the current SASS processing. (It will be included in the Rev2 reprocessing of the entire dataset planned for the near future.)

The error is small, being 0.185° for the PSPC. This corresponds to a position error of $6''$ at the radius of the support ring.

In principle, users can correct for the roll angle error by rotating an image about the centre of the field of view. However, there is also a known attitude solution error which causes X-ray position offsets of order $6''$. The origin of this attitude solution error is not known. Before rotating an image to correct for the roll angle error, the image should be shifted to correct for the attitude solution error. As this cannot be done without accurate positions for a number of the X-ray sources in the field of view, users will make the roll correction only rarely.

B.1.3 High Voltage

High Voltage (HV) checks are done by checking the HV ON/OFF flag, and checking whether the HV value itself is nominal. These pieces of information are stored in housekeeping frames in a rather obscure way.

Due to some misinformation, SASS was checking the wrong HV field. Consequently the HV value indeed remained unchecked and data intervals appeared in the accepted time intervals where the HV was turned on, but the HV had not yet reached its nominal value, as the gain of the PSPC is a strong function of HV, this lead to wrong pulse height information for the affected times. Typically the time between HV getting turned ON and the HV reaching its nominal value is about 18 s. This effect thus will be of no great impact for most observations, but it will affect observations with HV ON and OFF occurrences and short observation intervals. This effect may be seen in the quality file and in the housekeeping plots. Every time when HV is switched ON a time span of 20 s should be cut out of the accepted times.

This bug has been fixed from SASS release SASS5_7_7 onwards (1992 June 15). From this date on the HV value shows a behaviour synchronized with the "HV ok/not ok." status flag. Note that due to some peculiarity in the housekeeping frame notation the HV OFF value appears at slightly more than 2800 volts.

Also note that in some SASS hardcopy the HV monitor strip plot shows considerable jitter. This is the product of the HV monitor, and not an indication of true variation in HV across the observation. The monitor is only good as a crude indicator of HV.

B.2 Spectral

There is some temporal variation of the PSPC gain which is not included in the gain correction process currently applied to data in SASS.

This effect showed up primarily as inconsistencies between calibration spectra of N132D taken at different epochs across the *ROSAT* mission. Another artifact of the problem is highly significant residuals in number of spectra compared to the expected model, these appear as large negative residuals below about 0.20 keV and large positive residuals between about 0.20 to 0.40 keV.

An example of this effect is in

rosat/problems/temporal_gain/spectral_problem.ps

for more detail see /caldb/docs/rosat/cal_ros_93_007

Initial analysis suggests the gain shift is energy dependent. Findings to date are summarized in Prieto, Hasinger, & Snowden (TN TBD).

B.3 PSPC Timing Problems

A bug was found in the timing of individual events and was due to the preprocessing software. The origin of the problem was the spacecraft clock reset which followed the spacecraft tumbling incident of 1991 January 25. All PSPC data after that time will be affected (this problem occurs after each clock reset, which is done annually to accommodate "roll-over" of the counter).

The problem leads to relative shifts of 1 s between adjacent PSPC events. Although the problem is not cumulative, throughout the data there may be relative time shifts of the order of 1 second. The effect of the problem is to invalidate some timing analyses which are done on seconds or subsecond time scales. The bug has negligible impact on spectral and spatial analyses. Unfortunately there is no algorithm for correcting bad data. The bug has been corrected in SASS (Version SASS5_7, 1992 April 22, the SASS version numbers in this document refer to the entry on the front page of the SASS paper output and in the PUBLIC_CONTENTS file). Unfortunately, there is no algorithm for correcting bad data. All data will be correct after Rev2 processing.

B.4 HRI Timing Problems

The Space-craft clock onboard the ROSAT satellite has undergone several resets during the first two years of the mission. There has been 2 reasons for a space-clock reset:
1) The satellite is lost or enters safe mode.
2) Annual reset due to an overflow in the on-board counter.

Until recently the processing of these data has introduced an fractional second offset in times assigned to the photons. Below is a list of the clock resets and the fractional seconds by which the times are offset.

1991 January 26 – Satellite Gliche. HRI data taken after this time have event times with an absolute offset of 33/64 seconds.

1991 June 25 – Annual overflow. HRI data taken after this time have event times with an absolute offset of 58/64 seconds.

1992 February 12 – Satellite Gliche. The reset of 63/64 second caused the severe problems in the HRI software. Data taken after this time can have backward times of less than 1 second in duration. Timing analyses for which timescales of a few seconds or less are important may be affected and should be deferred until reprocessed data become available. Fixed in Release SASS5_8 (HRI_4_5).

1992 July 17 – Annual Overflow. Negative fractional reset of -1/64 second. The event times have an absolute offset of -1.0 second. This absolute offset should not inhibit users from searching for periodic behavior. Fixed in SASS HRI_4_5_2.

If an Observation Interval (OBI) processed previous to HRI 4_5 is merged with one run post HRI_4_5, the times in the early OBIs will be offset by a constant fractional second, and the new OBIs will be correct to the fraction. All data run with a software version previous to HRI_4_5 and since the first reset will also be offset by the fractional seconds of the reset. This value will be constant throughout the sequence unless OBIs that were merged were taken at different resets.

B.4.1 HRI Timing Summary

All HRI data processed at GSGC after 1992 October 22 (when HRI_4_5_2 was installed in the on-line processing) are free of timing problems.

B.5 Warning: Unresolved Problems

Recent problems with the "flat fielding" have been reported. Some investigators have claimed that the correction of the PSPC image by the exposure map, produces anomalously high count rates towards the edge of the detector, versus those obtained on-axis. This appears to effect AO4 data. This is currently under investigation.

The PSPC spectral response and gain correction are currently under investigation.

References to Appendix B

Nousek, J., & Lesser, A. 1993 *ROSAT* Newsletter 8, 13.
Prieto, M. A., Hasinger, G., & Snowden, S. L. 1994, MPE TN TBD.

Appendix C

SUMMARY OF ROSAT MEMOS AND CALIBRATION-RELATED PUBLICATIONS

The following list provides a brief summary of each of the MPE technical memos available at Goddard. These memos are mainly informal, sometimes in note form and many are pre-launch documents which will have been rendered obsolete by in-orbit work. Thus, these notes have not been circulated as preprints by MPE. Due to user demand, however, we will provide these on request. This list is intended to provide users with an idea of what information is available, the date relates to the MPE internal release date and gives some guidance as to which are pre-launch calibrations.

1) "Calibration Corrections to Individual PSPC Events"
TN-ROS-ME-ZA00/027, Hasinger & Snowden: 1990 March

This document gives a summary of all calibration corrections to be performed on individual PSPC events, starting out with the raw detector co-ordinates and the event amplitude. The correction algorithms detailed are:
The ADC nonlinearity correction
Gain saturation correction
Temporal gain correction
Electronic position correction
Spatial gain correction
Window correction
Off-Axis correction

2) "PSPC Position Dependant Gain Correction"
TN-ROS-ME-ZA00/025, Hasinger & Briel: 1990 February

This documents the position dependant gain corrections applied to the data during SASS processing. The position-dependant gain variations in the PSPC, which amount to $3 - 5\%$, can be corrected by a position and energy dependant function, yielding residual systematic gain errors of order 1% over the whole sensitive area of the counter.

3) "The Effective Collecting Area of the ROSAT Mirror Assembly and Predictions for the In-Orbit Data"
Aschenbach: 1990 July

A brief note describing the *ROSAT* PSPC effective collecting area as a function of energy and off-axis angle. These plots are based on in-orbit data, and here the effective area is defined as including all sources of obstruction within the XRT mirror assembly *except* the PSPC window support.

4) "The PSPC Deadtime"
TN-ROS-ME-ZA00/026, Hasinger: 1990 March

It is found that the PSPC deadtime per event is energy dependant and changes with incident count rate. There are also differences between the two PSPCs. It is concluded that for most of the time the PSPC deadtime will be dominated by vetoed particle background events. This pre-launch document describes how the necessary calibrations can be performed in-orbit.

5) "The Vignetting Function of the *ROSAT* Mirror Assembly and Comparison with the PANTER Calibration Data"
Aschenbach: 1990 January

The vignetting function is discussed. In particular, the effects of the various hardware components between the mirror assembly rear exit plane and the focal plane are discussed. These are: the magnetic deflector; the apertures of the focal plane housing (which are holes in the sandwich plate and the carousel) and the efficiency of the focal plane detector both on- and off-axis.

6) "Particle Background Analysis"
Plucinsky & Snowden: 1991 March

A discussion of the particle background, now superseded by Snowden *et al.* (1992) and Plucinsky *et al.* (1993), *Astrophysical Journal* papers (see items #7 and #8).

7) "The Particle Background of the *ROSAT* PSPC"
Snowden, Plucinsky, Briel, Hasinger, Pfeffermann 1992, *Astrophys. J.*, **393**, 819.

A detailed description of the *ROSAT* PSPC particle induced background. The PSPC rejection efficiency for these spurious events is exceptionally high with a residual count rate of roughly 5×10^{-6} counts s^{-1} arcmin^{-2} keV^{-1}. About 77% of events enter through the detector while the remainder enter through the counter window. During typical conditions the count rate of the residual counts is well correlated with the Master Veto rate. The spectrum of residual events consists of a flat component, a soft power- law, and an Al Kα line at 1.5 keV. Typically the ratio between the power-law and flat components remains constant to ±4% while the relative Al Kα contribution increases with increasing MV count rate. The distribution of counts over the field is uniform except for a slight radial dependance and shadowing caused by blockage of the externally produced component by the window support structure.

8) "An Updated Calibration of the *ROSAT* PSPC Particle Background"

Plucinsky, Snowden, Briel, Hasinger, Pfeffermann 1993, *Astrophys. J.*, **418**, 519.

An update of the 1992 Snowden *et al.* paper. Includes the post gain change calibration.

9) "The Focal Plane Instrumentation of the *ROSAT* Telescope"

Pfeffermann *et al.*: 1987.

The reference to the published paper is 1987: Proc. SPIE Int. Soc. Opt. Eng., 733, 519. The published paper should be sought directly rather than via the GOF.

10) "X-Ray Calibration of the *ROSAT* Position Sensitive Proportional Counter"

Briel *et al.*: SPIE Proc. 982, 401-408, 1990.

The ground calibration measuring the differential spatial non-linearities caused by the digitizing effects of the anode and cathode grids are discussed. In addition, the bulging of the thin PSPC entrance window and the position dependant gain of the counter are detailed. From those measurements MPE derive tables used to correct individual events in position and pulse height. Presented are the calibration methods and performance achieved for the PSPC.

11) "Spectral Linearity Calibration of the *ROSAT* PSPC"

Snowden: 1988

In this memo the Polya model function (for the spectral response) is discussed, and compared to the empirical model of Jahoda & McCammon (1988, *Nuc. Inst. and Methods*, **A272**, 800).

12) "X-Ray Calibration of the *ROSAT* Position Sensitive Proportional Counter II, The Energy Calibration"

Briel, Burkert, & Pfeffermann SPIE Proc. 1159, 263-267, 1990.

Describes the pre-launch measurements of the anode pulse heights of the PSPC as a function of X-ray energy.

13) "Focal Plane Determination"

TN-ROS-ME-ST00/073, Hasinger & Aschenbach: 1989 December

Reports an update of the focal plane determination procedure compared to a 1989 July write-up

14) "The Physical Composition of the PSPC Flight Entrance Windows and the Flight Boron Filters"

TN-ROS-ME-ZA10/038, Schmitt & Snowden: 1990 May

The transmissions of the entrance windows in the four PSPCs are discussed, plus the boron filters. A physical model is constructed for all known window components.

15) "Determination of Boresight Offsets for *ROSAT* Detectors"

TN-ROS-ME-ZA00/028, Kürster & Hasinger: 1992 May

The boresight corrections, ie the systematic zero point shifts encountered between the measured and known object positions when expressed in detector co-ordinates, are discussed.

16) "Zeitkorrelation"
Predehl: 1991 June

In German — Time correction of the spacecraft clock.

17) "Komponenten Der PSPC"
Hasinger: 1992 February

On-Axis Point Spread Function, this is now written up in full, see #18.

18) "The On-Axis Point Spread Function: In-Flight Comparison with the PANTER results"
CAL/ROS/92-001, Hasinger, Turner, George, Boese: 1992 May

The components of the *ROSAT* PSPC on-axis point spread function (psf) are discussed, and a direct comparison made between the predicted psf from ground calibration measurements and in-flight data obtained during the early part of the mission.

This memo is available on legacy under /caldb/docs/rosat/ as `cal_ros_92_001.tex`

19) "Coordinate systems for the *ROSAT* Data Analysis"
TN-ROS-ME-ED34/002, Hasinger: 1990 January

The relationship between *ROSAT* coordinate systems and celestial coordinates are discussed.

20) "The *ROSAT* PSPC Calibration Guide"
eds: George & Turner

A precursor to this document.

21) "Generation of Energy Dependant Exposure Maps for *ROSAT* PSPC Analysis"
Mendenhall, Snowden, Burrows: Penn State preprint, 1992 June

The importance of energy dependant exposure maps for the analysis of *ROSAT* PSPC data is demonstrated. Although current SASS generated exposure maps, based on a single, band-limited instrument map, are reasonably valid for central energies of the *ROSAT* bandpass, analysis of softer bands(¡0.20 keV) are strongly affected by 'ghost' images. Correction for such effects is critical for studies of extended objects and the diffuse X-ray background, and may also affect the identification of soft point sources. The authors present a method of generating energy dependant exposure maps (7 bands) for any PSPC pointed observation. These maps are based on instrument maps generated from all-sky survey data (similar to the currently used instrument map except for dividing the total PSPC bandpass into additional energy bands). Application of these maps will allow for accurate analysis over the entire PSPC bandpass.

22) "Analysis Procedures for *ROSAT* XRT/PSPC Observations of Extended Objects and the Diffuse Background.

Snowden, McCammon, Burrows, & Mendenhall 1994, Astrophys. J., **424**, 714.

A "Here there be dragons" paper for those interested in reducing PSPC observations in order to study extended objects of the SXRB.

23) "The Scattered Solar X-ray Background of the *ROSAT* PSPC"
Snowden & Freyberg, 1993, Astrophys. J., **404**, 403.

This paper models the scattered solar X-ray background as seen by the *ROSAT* PSPC. The temporal and geometric variation of this background component is modeled and well reproduces the observed light curves. The spectral distribution is also modeled with good results.

24) "Calibration Program for the PSPC Spectral Response"
1993 February 22. No author listed.

Outline of planned calibration of the engineering model at the PANTER facility in late 1993.

25) "The On-Axis Point Spread Function: Addendum - High Signal-to-Noise In-Flight Data"
CAL/ROS/92-001a, Hasinger, Turner, George, & Boese: 1992 May

The authors compare the *ROSAT* PSPC on-axis point spread function *psf* with the best signal-to-noise data obtained to date for a point source. They confirm that the parameterization detailed in CAL/ROS/92-001 does satisfactorily describe the observed *psf* at energies $\gtrsim 0.19$ keV.

This memo is available on legacy under /caldb/docs/rosat/ as `cal_ros_92-001a.tex`

26) "The Off-Axis Point Spread Function"
CAL/ROS/93-015
Hasinger, Boese, Predehl, Turner, Yusaf, George, & Rohrbach: 1993 September

This memo details the extension of the description of the point spread function of the *ROSAT* PSPC to include off-axis effects. The authors present the off-axis *psf* algorithm and compare the model to in-flight data. The limitations of the parameterization are discussed with respect to data analysis.

This memo is available on legacy under /caldb/docs/rosat/cal_ros_93_015

27) "*ROSAT* PSPC: Informal Study Note – Stability of the PSPC Spectral Calibration"
CAL/ROS/93-007, T.J.Turner

The *ROSAT* PSPC data processing software SASS, gain corrects the pulse height analyser (PHA) spectral data to pulse invariant (PI) data. This study note tests the accuracy of those corrections by making a simple ratio comparison between spectra of a constant X-ray source, N132D taken at different epochs. The analysis shows evidence for variations in the N132D spectra which are interpreted as uncalibrated variations in the detector response.

This memo is available on legacy under /caldb/docs/rosat/cal_ros_93_007

28) "Mission Planning with *ROSAT* "
Snowden & Schmitt 1992, in *Data Analysis in Astronomy IV*, eds. V. Di Gesu *et al.* (New York:Plenum), p. 121

The mission planning activities for the *ROSAT* project are discussed.

29) "Study of the *ROSAT* XRT Startracker Problem"
TN-ROS-ME-ZA00/029, Kürster & Hasinger: 1992 October

The possible connection between difficulties in boresight determination and the startracker pixel calibration is discussed.

30) "The Effects of *ROSAT* Orbit Inclination on the All-Sky Survey"
Snowden & Schmitt: 1988 February 16

A pre-launch document discussing the possible orbital inclinations available One of a series of studies aimed at reducing the planned orbital inclination from 57°, eventually 53° was chosen.

31) "In-Orbit PSPC Entrance Window Ablation by Atomic Oxygen Bombardment"
Schmitt: 1987 August

The expected oxygen particle flux in the XRT focal plane was investigated in order to study the possible degradation of the PSPC detector entrance window due to erosion by neutral oxygen atoms.

32) "Data Aquisition and -Evaluation Electronics for the *ROSAT* PSPC's"
Metzner 1986 in *Nuc. Inst. and Methods*, **A242**, 493

Discusses the on-board particle-background vetoing schemes for the PSPC.

33) "Region Selection Bases on Detector Coordinates: A Cautionary Note on Extracted Spectra"
Turner: 1994 April

34) "Assesment of Efforts to Improve the *ROSAT* Attitude Solution"
Kürster & Hasinger: 1993 November 16

Now Appendix D.

35) "*ROSAT* PSPC Calibration: Gain Variations"
Prieto, Hasinger, & Snowden: August 1994

A review of the systematic shifts in the PSPC spectral response.

Appendix D

ASSESSMENT OF EFFORTS TO IMPROVE THE ROSAT ATTITUDE SOLUTION

The causes for the existing deficiencies in the determination of the attitude of the *ROSAT* satellite were investigated by a collaboration of DASA, GSOC, and MPE. In order to develop possible improvements detailed studies of the precision achievable in position measurements by the star trackers on the one hand and by the X-ray system on the other hand were performed. The comparison of the two systems showed that each subsystem by itself fulfills the specification but that the complete *ROSAT* system falls short of fulfilling it. Although only a small improvement of the attitude solution was achieved the performed tasks were essential for an optimal calibration of the X-ray system. The gained insights into the properties of the attitude variations will in some suitable cases make it possible to develop empirical correction procedures for the scientific evaluation of the X-ray data.

D.1 The System Specification

The specification requires that in every pointed observation with the HRI detector ("High Resolution Imager"), 68% of the X-ray photons of an on-axis point source must arrive within a circle with radius $10''$ around the expected source position. (As a comparison: the 68% radius of the XRT point spread function with the HRI in the focal plane is $5''$).

D.2 Assessment

As can be deduced from the following considerations this specification requirement is not completely satisfied. The PSPC and HRI perform in an identical fashion as far as the accuracy of sky position determinations for on-axis X-ray sources is concerned. For 61 suitable bright PSPC sources we studied the deviations of the determined positions from the known optical positions (the latter are accurate to $1''$). For the HRI we only managed to find six suitable sources. This is due to the reduced sensitivity of the HRI and the smaller number of HRI observations carried out so far. A comparison of both distributions revealed the same scatter of the source positions around their corresponding optical positions of $6''$ (*i.e.,* after considering the appropriate boresight offset of the respective detector).

The cumulative histogram of the deviations of the sources from their optical positions is shown in the figure. It can be seen that 7% of the sources deviate by more than $10''$ from their optical positions. Less than 50% of the photons from these sources arrive within the $10''$ radius of the specification. The number of pointing targets which satisfy the specification requirement (68% of the photons within the $10''$-Radius) is even smaller (see Section D.2).

Since the main error source for the attitude inaccuracies could not be spotted the large number of the performed studies resulted in only a small improvement of the attitude solution. However, these efforts constitute an essential contribution to the optimal calibration of the X-ray system. It is in particular the detailed knowledge of the properties of the attitude variations that makes it possible in certain cases to develop suitable correction procedures which can be applied in the scientific evaluation of the X-ray data. The details of these empirical procedures depend on the scientific goal to be achieved. The following section summarizes the performed studies.

D.3 Performed Investigations

Initially, the investigations were based on the assumption that the cause of the observed attitude inaccuracies must be sought in the performance of the star trackers. Later on also the accuracy of the X-ray system was studied. The following tasks were carried out:

1. A theoretical study was made of the effects that errors in the star tracker correction lens have on the spot size in the image, *i.e.*, on the scale factor in the star tracker. Possible errors may be a result of neglecting the diffraction index of air in ground calibrations or manufacturing and positioning inaccuracies (DASA).

2. The effect of a modified spot size on the position determination was estimated analytically (DASA).

3. The scale factor was re-determined (GSOC and DASA).

4. The new scale factor was incorporated into the attitude solution (GSOC).

5. New boresight studies based were performed on observations for which the attitude solution was produced with the new scale factor. No reduction of the attitude inaccuracies was found (MPE).

6. Several studies of the detailed movement of guide stars in the star tracker were carried out. The variation of the separation of pairs of stars was studied as well as the movement of single stars with respect to the mean position of the stars. In particular, correlations with the spacecraft wobble were found and also with the CCD pixel structure (see next item). However, the discovered effects turned out to be much smaller than the attitude inaccuracies (DASA, GSOC and MPE).
7. The shifts which affect the measured star positions in both star trackers were inferred. For this purpose the distribution of a large number of guide star measurements in the sub-pixel range of the star tracker CCD was determined (so called "modulo flatfield"). A characteristic pattern appeared in the distribution which can be explained by a modified scale factor (MPE).
8. A correction procedure for removing the inhomogeneities in the "modulo flatfield" was developed. However, it again turned out that the discovered systematic shifts of single star positions (maximum value $2.5''$) are to small to make a significant contribution to the observed position errors (MPE).
9. The off-axis dependence of the "modulo flatfield" was studied. The shift effects were more clearly apparent, but they are still small. In an extreme case $4''$ were found, but on the average the shifts are much smaller (MPE).
10. Test slews were carried out with *ROSAT* which were specially devised to investigate the star tracker measurement effects and to make a comparison with the gyro measurements. However, these tests turned out to be very difficult for operational reasons so that no significant results could be obtained. Also the accuracy of the gyros measurements was not good enough (DASA).
11. A study of the (otherwise neglected) influence of guide star colour on the derived position of the star in the star tracker. The variation of the spot size with colour results in shifts of the stars by $\approx 1.5''$. So it is by far too small to be a major contributor to the observed error (DASA).
12. Ground measurements with the ASTRO SPASS star tracker. They showed a performance comparable to the *ROSAT* star trackers (DASA).
13. Development of a correction algorithm for the improvement of the attitude solution. This algorithm uses the a priori known separations of the guide stars. No significant improvement was obtained (DASA).
14. An intercomparison of the guide stars observed in both star trackers. The scatter in the measured separations and the scatter in the relative movements of the stars were determined. Both are much smaller than the attitude inaccuracies (DASA).
15. Several studies consisting of a comparison of the positions of the star tracker guide stars with the positions of selected bright X-ray sources in

the X-ray system. This comparison was made for the PSPC as well as for the HRI; for the HRI it was made both with and without wobble. These studies showed the attitude inaccuracies to their full extent (DASA and MPE).

16. Search for a possible time shift between star tracker data and data from the X-ray system which could explain effects correlated with the wobble. No time shift was found (GSOC, DASA and MPE).
17. Extensive studies of the accuracy of the system of X-ray telescope and detectors. Small image rotations were found for PSPC and HRI. However, it turned out that the total error budget of the X-ray system is too small to be considered as the major contributor (systematic errors greater than $3''$ can be excluded (MPE and DASA).
18. An analysis of the precision of the entries in the used star catalogue. The position accuracy turned out to be sufficient and do not lead to significant errors in the attitude solution (GSOC).
19. First evaluation of in-orbit measurements performed with the ASTRO SPASS star tracker indicate comparably small star tracker inaccuracies (DASA).

D.4 Prospect

We recommend to resume these studies again, if new aspects of the instrument calibration become known. It is planned to obtain a better documentation of the behaviour of the attitude errors by suitable end-of-life calibrations performed in orbit.

Appendix E

SUMMARY OF ROSAT ON-LINE DATABASES

ROSAT Centres in Germany, the UK and the USA (at MPE and GSFC for the XRT, at Leicester and AIT for the WFC) offer on-line services, through which users can access ROSAT related information like status reports, timelines, observation lists, software, etc. and retrieve data from the ROSAT Archives.

The following sections give short descriptions of the contents and the access to the services at the time of writing. Please consider that some access possibilities and services may have already changed from the examples given here. Every installation provides on-line help reflecting the actual status.

E.1 On-Line Services at the German RSDC

Mail address	ROSAT Scientific Data Center Max-Planck-Institut für Extraterrestrische Physik Postfach 1603 85740 Garching Germany
fax	(Germany) - (0)89-3299-3569
e-mail address	rosat_svc@mpe-garching.mpg.de (Internet) MPE::ROSAT_SVC (SPAN)
ROSAT Service Area	rosat_svc.mpe-garching.mpg.de
(ftp access)	user is anonymous; give e-mail address as password
(www URL)	http://rosat_svc.mpe-garching.mpg.de/
BROWSE	xray.mpe-garching.mpg.de
(telnet access)	user is xray; give email address as password

E.1.1 Information Services

The German data centre at MPE provides electronic services through the so-called ROSAT Service Area (rosat_svc), accessible via anonymous ftp and World Wide Web services like mosaic (see address header). Entering the Service Area the user finds information and data stored in a tree like directory structure. Each directory contains a file 'contents.doc' listing the available information. The files 'help.doc' and 'updates' in the top level directory provide help and list the names of new or updated files. Information is grouped into the following main directory branches:

archive	archive info, utilities, entry to ROSAT Data Archive
calibration	instrument calibration related info and data
doc	ROSAT project and utility documents
exsas	EXSAS software, updates, bug lists
processing	status, shipping lists, bug lists
general	general items like status, publications, news
timeline	mission timelines, observation logs

```
Example session:

% ftp rosat_svc.mpe-garching.mpg.de   connect to the Service Area
                         user: anonymous; password: e-mail address
ftp> cd general          move to directory general
ftp> get help.doc        copy 'help.doc' to your current directory
ftp> cd ../calibration   change to directory calibration
ftp> get pspc_cal.info   copy file
ftp> bye                 leave the Service Area
```

E.1.2 ROSAT Data Archive (RDA)

The ROSAT Data Archive lies in the subdirectory 'data' of directory 'archive'. The data are stored in compressed form (using the public domain utility gzip) and therefore, after network transfer, have to be decompressed at the users site (subdirectory archive/tools contains help info and gzip code for UNIX and VMS systems).

Data from a specific observation, identified by its sequence number (6 digits) and an additional identifier ('p' for PSPC, 'f' for PSPC with filter and 'h' for HRI data), are stored in a subdirectory of directory 'archive/data'. PSPC data with sequence number 123456, for example, are stored in directory 'archive/data/123456p'. Follow up observation(s) have a postfix of '-1', '-2', ... E.g., the data of the first follow up observation of the above example are in archive/data/123456p-1.

```
Example session (copy data of PSPC observation 200014p):

% ftp rosat_svc.mpe-garching.mpg.de   connect to the Service Area
                         user: anonymous; password: e-mail address
ftp> cd archive/data    go to RDA main directory
ftp> cd 200014p         proceed to proper observation directory
ftp> bin                set binary mode transfer
ftp> prompt             avoid prompting using mget
```

```
ftp> mget *            copy all files from the directory
ftp> bye               leave ftp
% gzip -d *-gz         decompress files
```

Now the data (in FITS format) are ready for input to one of the interactive analysis systems (EXSAS, PROS).

To receive data on tape (cassette), archive requests may also be sent via mail or e-mail to the RSDC. The proper request form is available in directory 'archive'.

E.1.3 Interactive Access (BROWSE)

ROSAT mission logs, timelines, data files, astronomical catalogues, towards the end of 1994 also the ROSAT Result Archive, can be interactively accessed (see address header) via the BROWSE utility (at MPE the version provided by GSFC is installed). An example session is given in chapter 'On-line Services at GSFC: HEASARC Services'.

E.2 On-Line Services at GSFC

Mail address	ROSAT Science Data Center GSFC/NASA Code 631 Green Belt, Maryland 20771 U.S.A.
e-mail address	NDADSA::REQUEST (HEASARC)
OGIP service	legacy.gsfc.nasa.gov
(ftp access)	user: anonymous; password: e-mail address
HEASARC service:	DECnet - node NDADSA, address 15761
(telnet access)	legacy.gsfc.nasa.gov user: xray; no password required
(www URL)	http://heasarc.gsfc.nasa.gov/
MIPS utility:	15576::ROSAT (SPAN) ROSAT.GSFC.NASA.GOV (INTERNET)
phone service:	(USA) - 301-286-3569 or - 301-286-1512
www URL	http://acadia.gsfc.nasa.gov/adf/rosatDC.html

GSFC provides ROSAT Services maintained by the US RSDC, the HEASARC (High Energy Astrophysics Science Archive Research Center), and the OGIP (Office for Guest Investigator Programs) groups.

E.2.1 HEASARC Services

By logging in to the HEASARC on-line services, users can access ROSAT status reports, timelines, the AO proposal list, and an observation log. The captive account XRAY may be accessed via SPAN or telnet (see address header).

ROSAT information is available within the XRAY account through the bulletin board and the database system. To access the bulletin board, simply type 'BULLETIN'; information on the latest HEASARC developments is posted there, as are status reports for ROSAT and GRO.

To access the database system, type 'BROWSE' followed by the name of the database you wish to view. ('BROWSE ?' lists available databases.) BROWSE is a command-driven program which allows users to manipulate, display, and execute analysis tasks on database entries.

```
Example session (search ROSATLOG for a specific PI name):

HEASARC> BROWSE ROSATLOG    load the ROSATLOG database
...> HELP                   get help on browse commands
...> DBHELP                 get help on current database
...> SP PI WHITE            Search the total sample for entries
                            with 'WHITE' as PI. All entries
                            will be displayed.
...> DALL 1                 display all information in entry 1
...> RSAM                   reset the sample to TOTAL again
...> EXIT                   quit browse
```

ROSAT public archive data can be extracted using the BROWSE request command.

```
Example session (obtaining data from the US public archive once data
files are located):

HEASARC> BROWSE ROSUSPSPC   load the US PSPC database
...> SC                     do coordinate search (prompts for values)
...>                        displays all files matching search criterion
...> REQUEST                starts automatic procedure to de-archive the data
                            that user requested as file numbers. Will prompt
                            user for their e-mail address
...> EXIT
```

BROWSE will send a request for data to ARMS (Automated Retrieval Mail System). ARMS will de-archive and place the data in an anonymous FTP area that the user can access for downloading. The system will also notify the user via e-mail when the de-archiving has been completed. For more information see the document 'Using the US Public Data Archive'. It is available via anonymous ftp on the 'legacy' machine in directory rosat/doc/archive. The document describes in detail how to obtain data via BROWSE, ARMS or MIPS.

BROWSE can also be accessed via the www HEASARC home page as given in the header.

E.2.2 The ROSAT Anonymous FTP Account

The Office for Guest Investigator Programs (OGIP) has a multi-mission anonymous ftp account on the Ultrix machine 'legacy' (see address header). At the top level the user sees the directory trees for all OGIP missions and some general directories. The user should move to 'rosat' (cd rosat). Directories available at this level are:

`problems, nra_info, data, timelines, software, publications, doc, calib_data, exp_map, .cache, FAQ.rosatFTP, symposium, FTPmap.txt`

FTPmap.txt describes the directory structure of the 'rosat' ftp area. ROSAT related calibration information can also be found in the 'caldb' area.

ROSAT archival data can also be found under the directory rosat/data/<hri or pspc>/processed_data/<seq-id group>/<seq-id>, where <seq-id group> is one of 100000, 200000, ..., 900000. For example, data associated with the data set having sequence id rp300023 is located in the directory rosat/data/pspc/processed_data/300000/rp300023.

To minimize storage space, the data are stored on the jukebox in UNIX compressed format. Users can uncompress the data automatically when ftp'ing. To do this, simply "get" the file by specifying the filename WITHOUT the .Z extension. An example is shown below:

```
% ftp legacy.gsfc.nasa.gov   user: anonymous; password: e-mail address
ftp> cd rosat/data/pspc/processed_data/300000/rp300023
ftp> ls rp300023.fits.Z
rp300023.fits.Z
ftp> bin
ftp> get rp300023.fits
ftp> quit
```

This automatic uncompression will work for both VMS and UNIX systems. Users should note that automatic uncompression does NOT work with the ftp "mget" command.

E.2.3 MIPS

The Mission Information and Planning System (MIPS) is an on-line information retrieval system (on a VAX computer, see address header) devised for ROSAT guest observers. MIPS contains software tools to:

```
- calculate target viewing windows, to precess coordinates,
  estimate source count rates, ...
- mission, proposal, and investigator information
- bulletin board for ROSAT news and events
- proposal generation and submission software
- downloading archival data via ARMS
```

E.3 On-Line Services at the UK ROSAT Data Archive Centre (UKRDAC)

mail address	UK ROSAT Data Archive Centre Department of Physics and Astronomy University of Leicester Leicester LE1 7RH U.K.
Phone	(UK) - (0)533-523507
Fax	(UK) - (0)533-550182
e-mail	LTVAD::RDAC (SPAN)
on-line access	ltxdb.star.le.ac.uk (Internet, see below) ltxdb (SPAN) user-id is xray; no password required
ftp data retrieval	darc.star.le.ac.uk user: anonymous; password: email address
www URL	http://www.star.le.ac.uk/

E.3.1 Information Services

Connecting to the captive account XRAY the user finds on-line help by typing 'help'. The databases are accessed via the program BROWSE allowing to select and extract data and to use the built-in analysis package. Presently available are:

ROSPUBLIC	list of accessible PSPC and HRI datasets
ROSPIMAGE	list of accessible HDS images of PSPC observations
ROSHIMAGE	list of accessible HDS images of HRI observations
ROSWPUBLIC	list of available pointed WFC datasets
ROSWFC	list of accessible HDS images of WFC observations

Other databases contain information on ROSAT timelines, observation status, etc. (ROSLTL, ROSSTL, ROSAO, ROSPROC) and standard astronomical catalogues.

E.3.2 ROSAT Data Archive

Example session (extract a dataset):

```
set host LTXDB             user-id is xray; no password required
    [Note: RDAC services will switch to the Internet address in
    the near future; the SPAN address LTXDB will be discontinued]
...> browse ROSPUBLIC      start BROWSE with specified database
...> csam cdrom            select datasets which are on CD-ROM
...> request
     Do you want to select all [N]: y
       Enter start entry number [d/f=1]: 1
       Enter end entry number [d/f=2468]: 1
```

```
       Enter your email address:<e-mail address>
...> exit                  exit browse
> logout                   exit from XRAY
```

After the requested data have been copied from the CD-ROM jukebox system to a publicly accessible hard disk, the user will be informed by a message to the e-mail address given in the request. Then the data can be copied via anonymous ftp:

```
% ftp darc.star.le.ac.uk  user: anonymous; password: e-mail address
ftp> cd rosat/data        change to the data main directory
ftp> ls                   list available data directories
ftp> cd 700339h           go to requested data directory
ftp> binary               set binary tranfer mode
ftp> prompt               avoid prompting
ftp> mget *               get all files in directory
ftp> quit                 exit
```

You may also request data by sending an e-mail to 'ukrdac@star.le.ac.uk', specifying the 6-digit ROR number of the observation with a single character appended (p for PSPC, f for PSPC with filter, h for HRI, w for WFC), e.g. 7000111p. The system will respond the same way as with the request from 'BROWSE'.

To receive data on tape fill in the request form (available from directory rosat on darc.star.le.ac.uk) and send it to LTVAD::RDAC.

E.4 On-Line Services at the German XUV Data Center

mail address	XUV Data Center Astronomisches Institut Tübingen
Phone	(+49) - 7071-295471
Fax	(+49) - 7071-293458
e-mail	29382::GXUVDC (Span) gxuvdc@ait.physik.uni-tuebingen.de (Internet)
telnet/ftp access	ait.physik.uni-tuebingen.de user-id is xuv, the password is xuv_archive

The service is available on a VAX cluster at the Astronomisches Institut der Universität Tübingen (AIT) via ftp or telnet.

E.4.1 Information Services

The main directory contains a list of contents (file contents.list), a help file (readme.txt), a listing of all observations processed at the data centre (file observation.list) and information on detected XUV sources (file source.list).

E.4.2 Archived Data

For each (filter-) observation an image (`IMA`), a merged exposure map (`MEX`), and an instrument map (`INS`) can be found on the sub-directories `XUV_ARCHIVE:[XUV.<n>00_ROR]`, where `<n> = 1, 2,...,9,A`, depending on the first digit of the ROR number. All images are 512 x 512 MIDAS images (.bdf), which are converted to FITS and then compressed, using the standard UNIX compress utility. File names are of the form `<ROR-nr>.<type><nn>_Z` where `<type>` is either `IMA, INS, or MEX` and `<nn>` is the number of the filter observation, e.g. `200141.INS01_Z`. Typical sizes of the compressed images are 25-75 kbytes.

UNIX users can apply their usual compress facility to decompress the data. After renaming the extension of the compressed dataset from `_Z` to `.Z` type: `compress -d 200141.ima01`. VMS users can copy the executible COMPRESS.VMS from `XUV_ARCHIVE:[XUV]`. Then, at your home computer, rename it to `COMPRESS.EXE` and to install it, type: `$ COMPRESS := $ <disk>:[path] COMPRESS.EXE`. To decompress a dataset, type: `$ COMPRESS -d 200141.IMA01`.

For the future, it is intended to also keep the photon event files of all sources detected by the WFC (extraction radius TBD) in the on-line archive.

For all public data the complete set of files (including photon files, attitude file etc. in EXSAS compatible FITS format) is available on tape. The request should contain the ROR number of the observation, your postal address and the prefered transport medium (EXABYTE (default) or mag-tape).

Appendix F

SUMMARY OF ROSAT PSPC CALIBRATION FILES

The chapter Summary of *ROSAT* PSPC Calibration Files will be written by W.Voges and included in the near future.

Appendix G

SASS INPUT FILES

The chapter SASS INPUT FILES will be written by W.Voges and included in the near future.